



**This electronic thesis or dissertation has been
downloaded from Explore Bristol Research,
<http://research-information.bristol.ac.uk>**

Author:

Brahma Narzary, Basiram

Title:

Perylene- and Naphthalene-based Porous Polyimide Networks for CO Capture and Conversion

General rights

Access to the thesis is subject to the Creative Commons Attribution - NonCommercial-No Derivatives 4.0 International Public License. A copy of this may be found at <https://creativecommons.org/licenses/by-nc-nd/4.0/legalcode>. This license sets out your rights and the restrictions that apply to your access to the thesis so it is important you read this before proceeding.

Take down policy

Some pages of this thesis may have been removed for copyright restrictions prior to having it been deposited in Explore Bristol Research. However, if you have discovered material within the thesis that you consider to be unlawful e.g. breaches of copyright (either yours or that of a third party) or any other law, including but not limited to those relating to patent, trademark, confidentiality, data protection, obscenity, defamation, libel, then please contact collections-metadata@bristol.ac.uk and include the following information in your message:

- Your contact details
- Bibliographic details for the item, including a URL
- An outline nature of the complaint

Your claim will be investigated and, where appropriate, the item in question will be removed from public view as soon as possible.

Perylene- and Naphthalene-based Porous Polyimide Networks for CO₂ Capture and Conversion

By

Basiram Brahma Narzary



School of Chemistry
University of Bristol

Supervisor
Prof. Charl F. J. Faul

A dissertation submitted to the University of Bristol in accordance with the requirements of the degree of DOCTOR OF PHILOSOPHY in the Faculty of Science.

13th August 2023

Word count: thirty five thousand six hundred twenty-four (35624)

Abstract:

Porous polyimides (pPIs) represent a fascinating class of porous organic polymers (POPs) known for their exceptional thermal and chemical stabilities, as well as high surface areas, and energy storage capabilities. pPIs are synthesised through simple polycondensation reactions utilising a diverse array of linkers (dianhydrides) and cores (amines) to form highly crosslinked networks. The surface areas and pore sizes of pPIs are optimised using the Bristol-X'an-Jiatong (BXJ) approach. This thesis demonstrates how the BXJ approach can be used to optimise the porous network properties to target and tune their ability to capture CO₂. Once optimised, these porous organic frameworks were utilised, for the first time, as metal-free electrocatalysts for the conversion of CO₂. The excellent faradaic efficiencies (FEs) for the electrochemical conversion of CO₂ to formate (91%) and methanol (95%) present exciting opportunities for the generation of useful fuels and feedstocks from CO₂. In addition, the ability to directly address and select the conversion products through tuning of the porous materials' properties highlights the potential of this work, and more generally for a wide range of organic frameworks, as future metal-free CO₂ reduction catalysts. Additionally, pPIs were utilised as a metal-free heterogeneous catalyst for the first time, in synthesising cyclic carbonates from CO₂ and epoxides. pPIs exhibit excellent reusable heterogeneous catalytic activities under very mild and sustainable conditions (solvent- and co-catalyst free) with 99.9% conversion to cyclic carbonate. A wide substrate scope of pPIs for cyclic carbonate synthesis was investigated, making them promising candidates for green and sustainable industrial synthesis.

Dedication

To my beloved parents, Aai and Baba, I am filled with eternal gratitude for your endless sacrifices and tireless efforts that have paved the way for my success. Your unconditional love, guidance, and faith in my abilities have played a pivotal role in shaping the person I am today.

To my dear siblings, Joba and Mahat, you have always been my pillars of strength. I am deeply thankful for your unwavering support and continuous push towards excellence. Your presence in my life has been a constant source of inspiration.

To my extended family, relatives, and close family friends, your words of encouragement, guidance, and unconditional love have been a guiding light throughout my journey. I am profoundly grateful for your unwavering belief in my capabilities.

I extend my heartfelt appreciation to all of you for being my rock, for celebrating my accomplishments, and for providing a safe haven during the most challenging times.

With a grateful heart, I offer my deepest thanks to Bwrai Bathou, for your constant presence, love, and guidance in my life.

Jai Afa Bwrai Bathou!

Acknowledgements

The acknowledgments section is my favourite part whenever I read a thesis. It serves as a humble reflection of the immense teamwork and support, both academically and socially, that contribute to the creation of a thesis. Moreover, it offers a delightful glimpse into the author's personality before delving into the scientific aspects of chemistry. With this in mind, I will make every effort to craft an acknowledgments section that would have brought me joy as a reader.

I would like to express my gratitude to my supervisor, Professor Charl F. J. Faul, for granting me the opportunity to conduct this research. His scientific knowledge, invaluable guidance, unwavering support and encouragement during my tenure in the Faul research group have played a pivotal role in my academic and personal growth. I am also grateful to him for always being available to engage in scientific and non-scientific discussions, which have helped keep me motivated throughout my PhD journey. I am also appreciative of the input and advice generously provided by Dr Sebastien Rochat and Professor David Fermin.

I would like to express my gratitude to all those I have had the pleasure of collaborating with or have otherwise helped me with my research. In particular, I wish to thank Dr. Jean-Charles Eloi for assistance and guidance with electron microscopy and related techniques, Dr Natalie E. Pridmore for X-ray powder diffraction measurements, and Dr. Craig Butts and Dr. Paul Lawrence for assisting with the setup and analysis of NMR measurements. Also, thanks to Tony Roger for technical assistance throughout my project and Duncan Tarling for his skillful glass blowing, which has greatly contributed to the experimental aspects of my research. I would also like to extend my appreciation to the project students, Jerry Mintah and Elizaveta Bejan, with whom I had the opportunity to work and who made significant contributions to this project.

I would also like to extend my gratitude to the past and present members of the Faul Research groups, as well as my friends in Bristol for the stimulating discussions, support, assistance, and the enjoyable experiences we have shared over the past four years. Thank you all for bearing me. I would like to thank Dr Veronica del Angel, Safa Al Siyabi, John Worth, Maximillian Hagemann, Marcos Villeda Hernandez, Ulzhalgas Karatayeva, Xue Fang, Helal Alharbi, Lucy Barden, Connie Hedditch, Pongsathon Boonrod, Sam Deeks, Julia Maxwell, Yubing Wang, Himanshi Mishra, Dr Christian Romero, Dr. Nouf Zaghoul, Dr Henry Symons, Dr Esther Townsend for the help, support, guidance and friendship. Special thanks to Dr Ben Baker for his friendship, support and the respective collaboration projects which were a fundamental part of my thesis and publication. I am particularly grateful for his willingness to work late nights and those shouting/arguing session.

I would also like to express my gratitude to all the amazing friends I had the opportunity to meet in Hodgkin House, individuals who came from various parts of the world and shared a home within the Hodgkin House family. Additionally, I would like to convey my heartfelt appreciation to Jacqui and Joanne for their consistent support and exceptional management of Hodgkin House. Their unwavering dedication and care have greatly contributed to making my time at Hodgkin House truly memorable and enjoyable.

I would like to express my heartfelt appreciation to my friends and family from Assam who have made Bristol feel like home away from home. Despite being far from my family and hometown, their unwavering support and constant presence in my life have meant the world to me. In particular, I would like to extend special thanks to Parag Sharma, Anannya Borthakur, Debarchana Chetiya, Jyotisman Sarma, Adriza Batsah, Shreya Borah, Papu Kalita, and Depankar Borgayari for their exceptional support and friendship. I would also like to thank Pasuporn Po-Ngernnak, Eshita Kasar, Atul Sharma and Tirumala Chakradhar for being always there for me and for their enduring friendship.

I would like to express my sincere gratitude to the Government of India, Ministry of Tribal Affairs, for funding my PhD studies through the National Overseas Scholarship for ST. Additionally, I would like to extend my thanks to the High Commission of India in London for their assistance and support.

I would also like to express my gratitude to the University of Bristol, the Royal Society of Chemistry, Armourous and Brasiers' company, Bristol Collegiate Research Society, American Chemical Society for providing travel grants that have helped support my attendance at various conferences.

Author's Declaration

I declare that the work in this dissertation was carried out in accordance with the requirements of the University's Regulations and Code of Practice for Research Degree Programmes and that it has not been submitted for any other academic award. Except where indicated by specific reference in the text, the work is the candidate's own work. Work done in collaboration with, or with the assistance of, others, is indicated as such. Any views expressed in the dissertation are those of the author.

SIGNED: DATE:

Publications

1. B. B. Narzary, B. C. Baker, N. Yadav, V. D'Elia and C. F. J. Faul, **Crosslinked Porous Polyimides: Structure, Properties and Applications**, *Polymer Chemistry*, **2021**, 12, 6494–6514 (with front cover) doi.org/10.1039/D1PY00997D.

Authors contribution:

B. B. Narzary conceived and designed the study, conducted the literature review and drafted the original manuscript.

B. C. Baker assisted with data analysis and provided critical review and editing to the manuscript.

N. Yadav and V. D'Elia contributed to data interpretation in the heterogeneous catalysis section and participated in manuscript reviewing and editing.

C. F. J. Faul supervised the study and provided overall manuscript review, editing and writing.

All authors have read and approved the final version of the manuscript.

2. B. B. Narzary, B. C. Baker and C. F. J. Faul, **Selective CO₂ electroreduction from tuneable naphthalene-based porous polyimide networks**, *Advanced Materials*, **2023**, 35, 2211795. doi.org/10.1002/adma.202211795

Authors contribution:

B. B. Narzary conceived and designed the research study, conducted the experiments, performed data analysis and drafted the original manuscript.

B. C. Baker provided critical review and editing to the manuscript.

C. F. J. Faul supervised the study and provided overall manuscript review, editing and writing.

All authors have read and approved the final version of the manuscript.

3. B. B. Narzary, U. Karatayeva, J. Mintah, M. Villeda-Hernandez and C. F. J. Faul, **Bifunctional Metal-Free Porous Polyimide Networks for CO₂ Capture and Conversion**, *Mater. Chem. Front.* **2023**, 7, 4473–4481 (with inside cover), doi.org/10.1039/D3QM00639E.

Authors contribution:

B. B. Narzary conceived and designed the research study, conducted the experiments, performed data analysis and drafted the original manuscript.

U. Karatayeva, J. Mintah, and M. Villeda-Hernandez contributed to the chemical conversion section under the guidance of B. B. Narzary and provided critical review and editing.

C. F. J. Faul supervised the study and provided overall manuscript review, editing and writing.

All authors have read and approved the final version of the manuscript.

4. U. Karatayeva, S. A. A. Siyabi, B. B. Narzary, B. C. Baker, C. F. J. Faul, **Conjugated Microporous Polymers for Catalytic CO₂ Conversion**. (accepted for publication in the *Advanced Science*)

Manuscripts under preparation

5. B. B. Narzary, E. Bejan, C. F. J. Faul, **Pyridine containing porous polyimides as a metal-free catalyst for CO₂ conversion**.
6. B. B. Narzary, M. J. L. Hagemann, C. F. J. Faul, **PDI-and NDI-based porous polyimides for CO₂ capture and conversion**

International conferences

1. Oral presentation at the American Chemical Society (**ACS- Spring 2023**), Indianapolis, USA, **2023**
Title: Perylene- and naphthalene-based porous polyimides for CO₂ capture and conversion.
2. Poster presentation at the European Materials Research Society (**EMRS- Fall 2022**), Warsaw, Poland, **2022**
Title: Tuneable naphthalene-based porous polyimide networks for CO₂ capture and conversion
3. Oral presentation at the Materials Research Society (**MRS-Spring 2022**), Honolulu, USA, **2022**
Title: Tuneable naphthalene-based microporous polyimide networks for CO₂ capture and conversion

List of Figures

Figure 1.1: (a) CO₂ concentration measured at Mauna Loa Observatory, Hawaii,¹ and (b) Global land and ocean temperature anomalies (2000-2022).

Figure 1.2: (a) Atmospheric CO₂ concentration, and (b) Global surface temperature, respectively, reported in IPCC Sixth Assessment Report.

Figure 1.3: The three different carbon capture and separation process.

Figure 1.4: Example of COFs structures.

Figure 1.5: Schematic representation of the hyper crosslinking process.

Figure 1.6: Schematic illustration of structures of PAFs.

Figure 1.7: (a) Chemical structure of PIM-1 and (b) Molecular model of PIM-1 showing its highly contorted and rigid structure.

Figure 1.8: Reaction schemes for the synthesis of CMPs adapted from ref.² (a) Sonogashira-Hagihara, (b) Suzuki-Miyaura, (c) Yamamoto, (d) Heck, (e) cyclotrimerization, (f) phenazine ring fusion, (g) Schiff-base, (h) heterocycle linkages, (i) alkyne metathesis, (j) oxidative coupling, (k) Buchwald-Hartwig, (l) electropolymerisation, and (m) hypercrosslinking linear polymers.

Figure 1.9: Porous polyimides (pPis) properties and application.

Figure 1.10: Structure of amine monomers, grouped into different reactive sites/geometries (di-, tri- and tetra- amines), utilised in the formation of pPI networks covered within this chapter.

Figure 1.11: Structure of anhydride monomers utilised in formation of pPI networks covered within this chapter.

Figure 1.12: Preformed diimides **M1–6** (left) and crosslinker units (right) utilised in pPI formation.

Figure 1.13: Various oxidation states of common anhydride linkers **L3–5**.

Figure 1.14: Long-term cycling performance of PI-1 (**B1** and **L4**) and PI-2 (**B1** and **L3**) at 5 A g⁻¹.

Figure 1.15: Schematic representation of heterogeneous Pd catalysts based on porous polyimide networks from ref.³

Figure 1.16: The BXJ approach and the impact of the solvent-polymer compatibility on the porosity of the polymer network.

Figure 1.17: CO₂ uptake capabilities of PTPA (at 273 K) tuned by salts with different (a) anions and (b) cations.

Figure 1.18: Possible structure of adsorbed CO₂ on catalyst (A) Oxygen coordinated, (B) Carbon coordinated and (C) Mixed coordinated.

Figure 1.19: Examples of homogeneous catalysts used in the synthesis of cyclic carbonates from CO₂ and epoxides.

Figure 1.20: Some selected examples of metal-based catalysts (a) salen-based, (b) porphyrin-based, and (c) pyridine-based.

Figure 1.21: Selected structure of metal-free POPs used as a catalyst for cyclic carbonate synthesis.

Figure 1.22. Structures of epoxides used for cycloaddition with CO₂.

Figure 3.1: BNPI-1

Figure 3.2: BNPI-2

Figure 3.3: BNPI-3

Figure 3.4: pPI-1

Figure 3.5: pPI-2

Figure 3.6: pPI-3

Figure 3.7: p-PDI

Figure 3.8: p-NDI

Figure 4.1: (a) Synthetic pathway to synthesise BNPI-1 and BNPI-2, (b) BXJ approach schematic adapted from reference and (c, d) optimisation of surface areas of BNPI-1 and BNPI-2 using the BXJ approach by appropriate salt addition.

Figure 4.2: (a, b) Pore size distribution of BNPI-1 and BNPI-2, synthesised in imidazole or *m*-cresol and DMSO or DMF with NaF additives, respectively, (where PV = Pore Volume) (c, d) PXRD plot of BNPI-1 and BNPI-1, synthesised in imidazole/*m*-cresol and DMSO/DMF with NaF additives, respectively and (e, f) UV-Vis-NIR spectra of BNPI-1 and BNPI-1, synthesised in imidazole or *m*-cresol and DMSO or DMF with NaF additives, respectively.

Figure 4.3: Showing CO₂ capture and electrocatalytic reduction using BNPI-1 and BNPI-2 with (a) the CO₂ uptake in wt% of BNPI-1 and BNPI-2 at 1 bar, 273K, for different synthesis conditions, (b) the schematic of the H-cell setup used to convert CO₂ to formate and methanol, showing the proposed interaction of CO₂-pPIs, (c) the FEs for the formation of CO₂ reduction products (formate and methanol) from H-cell investigations at 298 K, using BNPI-1 and BNPI-2 (from different synthetic conditions optimised by BXJ approach) as catalysts. Products monitored and determined by ¹H NMR analysis.

Figure 4.4: Plot of surface areas (m²/g) vs FEs (%) demonstrating the observed trends across optimised pPIs of BNPI-1 and BNPI-2. All orange symbols represent data for methanol production; all green symbols represent data for formate production.

Figure 4.5: (a-d) Analysis of current densities vs formate and methanol production from CO₂ reduction using BNPI-1 and BNPI-2 as electrocatalysts.

Figure 5.1: (a) FT-IR spectra of starting materials and pPI-1 and pPI-2, (b) TGA plot of pPI-1 and pPI-2 under N₂ atmosphere, (c) PXRD of pPI-1 and pPI-2 (solid line) and after use as a catalyst (dotted line) (peak 2θ 21.5 is from the paraffin wax used to fix samples to the sample holder during our XRD analysis)⁴, (d) UV-Vis-NIR spectra of pPI-1 and pPI-2, (e) SEM of pPI-1 before and after 5 cycles used as a catalyst, and (f) SEM micrographs of pPI-2 before and after 1 cycle used as a catalyst.

Figure 5.2: (a) Time-dependent percentage conversion of ECH at 80 °C for pPI-1. (b) Temperature-dependent conversion for cycloaddition of CO₂ to ECH for pPI-1. (c) pPI-1 catalyst loading for cycloaddition of CO₂ to ECH at 80 °C. (d) Recycling test of pPI-1 for the cycloaddition of CO₂ to ECH at 80 °C.

Figure 5.3: (a) Cyclic voltammogram of pPI-1 and pPI-2 in the applied potential range from -1–1 V vs RHE, scan rate 20mV/s, 20 cycles, (b-c) Chronoamperometry studies (vs RHE) of pPI-1 and pPI-2, respectively in CO₂-saturated electrolytes, and (d-e) Highest obtained faradaic efficiency of pPI-1 and pPI-2, respectively in CO₂ saturated electrolytes for 30 min.

Figure 5.4: (a) FT-IR spectra of starting materials and **BNPI-3** and **pPI-3**, (b) UV-Vis-NIR spectra of starting materials and **BNPI-3** and **pPI-3**, (c) PXRD of **BNPI-3** and **pPI-3**, and (d-e) SEM of **BNPI-3** and **pPI-3**, respectively.

Figure 5.5: (a) The N₂ sorption isotherms of **BNPI-3** and **pPI-3**, (b) Pore size distribution calculated from NLDFT, (c) CO₂ uptake of **BNPI-3** at 273 K and 298 K at 1 bar.

Figure 5.6: The experimental setup for the synthesised cyclic carbonates using gauge CO₂ and epoxides.

Figure 5.7: Time-dependent percentage conversion of SO at 100 °C, 0.25-gauge CO₂ for **pPI-2 (black)** and **pPI-3(blue)**

Figure 6.1: Position of PDI.⁵

Figure 6.2: (a) FT-IR of **p-NDI** and **p-PDI** and (b) UV-Vis-NIR spectra of **p-NDI** and **p-PDI**.

Figure 6.3: (a) PXRD of p-NDI, p-PDI and NaF, and (b) SEM image of p-NDI and p-PDI.

Figure 6.4: (a) BET adsorption-desorption isotherm of N₂ for p-PDI and p-NDI and (b) PSD of p-PDI and p-NDI calculated from NLDFT.

Figure 6.5: CO₂ uptake isotherms of (a) p-NDI and (b) p-PDI, were measured at 273 K and 298 K, respectively, at a pressure up to 1 bar.

Figure 7.1: Various in situ methods to investigate the CO₂ reduction process.

Figure 7.2. A standard GDE set-up for electrochemical CO₂ reduction.

List of Schemes

Scheme 1.1: Schematic showing carbon capture and routes to conversion using pPIs.

Scheme 1.2: Classification of porous materials based on pore sizes and building blocks.

Scheme 1.3: Synthetic pathway of COF-1 and COF-5, respectively.

Scheme 1.4: Examples of synthesised HCPs: **(A)** post-crosslinking of poly(vinylbenzyl chloride)-based precursors,⁶ **(B)** knitting rigid benzene monomers with formaldehyde dimethyl acetal external crosslinkers,⁷ and **(C)** direct one-step polycondensation of benzyl alcohol monomers.⁸

Scheme 1.5: Synthetic route of PAF-1.⁹

Scheme 1.6: Schematic illustration of electrocatalytic CO₂ reduction pathway.

Scheme 1.7: The general scheme depicts the reaction between an epoxide and CO₂.

Scheme 1.8: Generic mechanism for the synthesis of cyclic carbonates through epoxide activation.

Scheme 1.9: Generic mechanism for the synthesis of cyclic carbonates through CO₂ activation.

Scheme 1.10: Generic mechanism for the synthesis of cyclic carbonates through dual activation (substrate and CO₂).

Scheme 2.1: Schematic showing CO₂ capture and conversion using pPIs.

Scheme 2.2: (a) General synthesis pathways for pPIs and (b) Structure of cores and linkers used in this project.

Scheme 3.1: Synthesis of TAPT.

Scheme 3.2: Synthesis of N-TAPT.

Scheme 5.1: Sustainable routes to CO₂ capture and conversion using pPIs.

Scheme 5.2: Synthetic pathway to **pPI-1** and **pPI-2**.

Scheme 5.3: pPI-catalysed, solvent-free cyclic carbonates synthesis from CO₂ and epoxides.

Scheme 5.4: Synthetic pathway to **pPI-3** and **BNPI-3**.

Scheme 5.5: General scheme to synthesised cyclic carbonates using gauge CO₂ and epoxides.

Scheme 6.1: Synthesis of **p-NDI** and **p-PDI** via BH coupling reaction.

Scheme 7.1: Reaction between CO₂ and *o*-phenylenediamine

List of Tables

Table 1.1: Nomenclature for reported pPIs, constituent monomers and references.

Table 1.2: Showing T_{deg} of pPIs from TGA under nitrogen and char yields at 800 °C, where * = estimated by the authors from TGA traces utilising imageJ image analysis software, and # = char yield at 700 °C.

Table 1.3: Porosity properties of pPIs where S_{BET} = surface area from BET, PV = pore volume, Q_{st} = isosteric heat of absorption, A: amorphous; C: crystalline; i: at 195K, 1 bar; ii: at 273K, 1 bar; iii: at 77 K, 1 bar, iv: 77 K, 30 bar, v: 298 K, 1 bar, *only the highest surface areas are reported.

Table 1.4: Gas uptakes from reported pPIs where H₂ = hydrogen, H₂O = water vapor, CH₄ = methane C₆H₆ = benzene, C₆H₁₂ = cyclohexane, A = amorphous; C = crystalline; i = at 77 K, 1 bar; ii = at 195 K, 1 bar; iii = at 273 K, 1 bar, iv = 298 K, 1 bar, v = 77 K, 30 bar, * wt % values were converted for the purpose of this review from published isotherms using the conversion formula wt % = (mmol g⁻¹ * 100 * mol. weight)/1000 where mmol g⁻¹ = (cm³ g⁻¹)/22.414 cm³ mmol⁻¹ .

Table 1.5: Aliphatic VOC absorption by reported pPIs where A: amorphous; C: crystalline; i: at 77 K, 1 bar; ii: at 195 K, 1 bar; iii: at 273 K, 1 bar, iv: 298 K, 1 bar, v: 77 K, 30 bar.

Table 1.6: Possible electrochemical potential for CO₂ reduction reaction in aqueous medium.^{10,11}

Table 5.1: Porosity parameters and CO₂ uptake at 273 K and 298 K at 1 bar.

Table 5.2: Cycloaddition of CO₂ to different epoxide substates for cyclic carbonate synthesis using pPIs (**pPI-1** and **pPI-2**, under balloon pressure).^a

Table 5.3: BET surface area and CO₂ uptake at 273 K and 1 bar of **BNPI-3** and **pPI-3**, respectively.

Table 5.4: Cycloaddition of CO₂ to different epoxide substates for cyclic carbonate synthesis using pPIs (**BNPI-3** and **pPI-3**, under CO₂ gauge pressure).^c

Table 6.1: Elemental analysis results of p-NDI and p-PDI.

Table 6.2: BET surface area and CO₂ uptake at 273 K and 1 bar of **p-NDI** and **p-PDI**.

List of Abbreviations

Ag	silver
Al	aluminium
Ba₂(NO₃)₂	barium nitrate
BDBA	phenyl diboronic acid
BET	Brunauer–Emmett–Teller
BH	Buchwald-Hartwig
BXJ	Bristol–Xi'an Jiaotong
CCUS	carbon capture, utilisation and storage
cm	centimetre
CMPs	conjugated microporous polymers
CO₂RR	carbon dioxide reduction reaction
COFs	covalent organic frameworks
DSC	dynamic scanning calorimetry
e⁻	electron
E°	cell potential
EDLC	electric double layer capacitance
F	Faraday's constant (96485.33 C/mol)
FE	faradaic efficiency
g	gram
h	hour
HCPs	hyper-crosslinked polymers
HSPs	Hansen solubility parameters
IPCC	Intergovernmental Panel on Climate Change
K	Kelvin
LIBs	Li-ions batteries
mA	milliampere
MEA	monoethanolamine
mg	milligram
mmol	millimole

MOFs	metal-organic frameworks
n	number of moles
nm	nanometre
NMR	nuclear magnetic resonance
NOAA	National Oceanic and Atmospheric Administration
NL-DFT	Non-local density function theory
PAFs	porous aromatic frameworks
PIMs	polymers of intrinsic microporosity
POPs	porous organic polymers
pPis	porous polyimide networks
ppm	parts per million
PV	pore volume
Q	total charged passed
Q_{st}	isosteric heat of adsorption
RHE	reversible hydrogen electrode
SA	surface area
SHE	standard hydrogen electrode
T_g	glass transition temperature
TGA	thermogravimetric analysis
UV- Vis	ultraviolet visible
V	volt
VOCs	volatile organic compounds
wt%	weight percentage
XPS	X-ray photoelectron spectroscopy
XRD	X-ray diffraction
z	number of electrons required to produce a given product
Zn	zinc
η	the total cell overpotential

Contents

Chapter 1: Introduction	23
1.1. Climate change and global warming	23
1.2. Carbon capture and conversion	24
1.3. Porous organic polymers (POPs)	26
1.4. Types of POPs	27
1.4.1. Covalent organic frameworks (COFs)	28
1.4.2. Hyper-crosslinked polymers (HCPs)	31
1.4.3. Porous aromatic framework (PAFs)	32
1.4.4. Polymers of Intrinsic microporosity (PIMs)	34
1.4.5. Conjugated microporous polymers (CMPs)	35
1.5. Porous Polyimides (pPIs)	36
1.5.1. Monomer structure	37
1.5.2. Properties	44
1.5.3. Applications	57
1.6. Routes to tuning structure and function in porous materials	67
1.6.1. Hansen Solubility Parameters (HSPs)	67
1.6.2. The Bristol-Xi'an Jiaotong (BXJ) approach	69
1.7. Electrocatalytic conversion	72
1.7.1. Performance target for the CO₂ reduction reactions	76
1.8. Chemical Conversion	78
1.9. Conclusion and Future outlook	85
Chapter 2: Aim and objectives	89
Chapter 3: Experimental Methods	93
3.1. Chemicals	93
3.2. Synthesis	93
a. Monomer synthesis:	93
b. Polymer synthesis:	95
3.3. Characterisation techniques	101
3.3.1. FT-IR Spectroscopy	101
3.3.2. UV-vis-NIR Spectroscopy	101
3.3.3. Powder X-ray Diffraction (P-XRD)	101
3.3.4. Thermogravimetry analysis (TGA)	101
3.3.5. Proton Nuclear Magnetic Resonance (H-NMR)	101
3.3.6. Scanning Electron Microscopy (SEM) and Energy Dispersive X-ray (EDX)	101
3.3.7. X-ray photoelectron spectroscopy (XPS)	102

3.3.8.	Surface area (BET) and CO ₂ uptake Measurements	102
3.3.9.	Electrochemical measurement	102
Chapter 4:	Tuneable naphthalene-based pPIs for CO₂ capture and conversion	105
4.1.	Introduction	105
4.2.	Result and discussion	107
4.2.1.	Optimisation of porous properties through the BXJ approach	107
4.2.2.	CO ₂ capture and conversion	110
4.3.	Conclusion:	116
Chapter 5:	Perylene-based pPIs for CO₂ capture and conversion	117
5.1.	Introduction:.....	117
5.2.	Results and Discussion	119
5.2.1.	pPI-catalysed chemical conversion of epoxides (using balloon pressure)	121
5.2.2.	Electrocatalytic CO ₂ reduction:	125
5.3.	Pyridine-containing pPIs	126
5.3.1.	pPI-catalysed chemical conversion of epoxides (using gauge CO ₂ pressure).....	131
5.4.	Conclusion:	135
Chapter 6:	Naphthalenediimide- (p-NDI) and perylenediimide- (p-PDI) based porous polyimides	137
6.1.	Introduction:.....	137
6.1.	Results and discussion:	139
6.2.	Conclusion:	142
Chapter 7:	Conclusions and Future Outlook	145
7.1.	Conclusion	145
7.2.	Future work	147
References	150
Appendix 1	163
Appendix 2	170
Appendix 3	193

Chapter 1: Introduction

1.1. Climate change and global warming

Since the early 1950s, the concentration of anthropogenic carbon dioxide (CO₂) in our atmosphere is exponentially increasing to reach 424 ppm as of May 2023, as reported by the National Oceanic and Atmospheric Administration (NOAA) (**Figure 1.1a**).¹ The extensive use of carbon-based fossil fuels to meet energy demands are the major source of anthropogenic CO₂ emission. At present coal, natural gas and oil are the most commonly used types of fossil fuels. The global emissions of CO₂ stemming from the combustion of fossil fuels reached 36.8 Gt in the year 2022.¹²

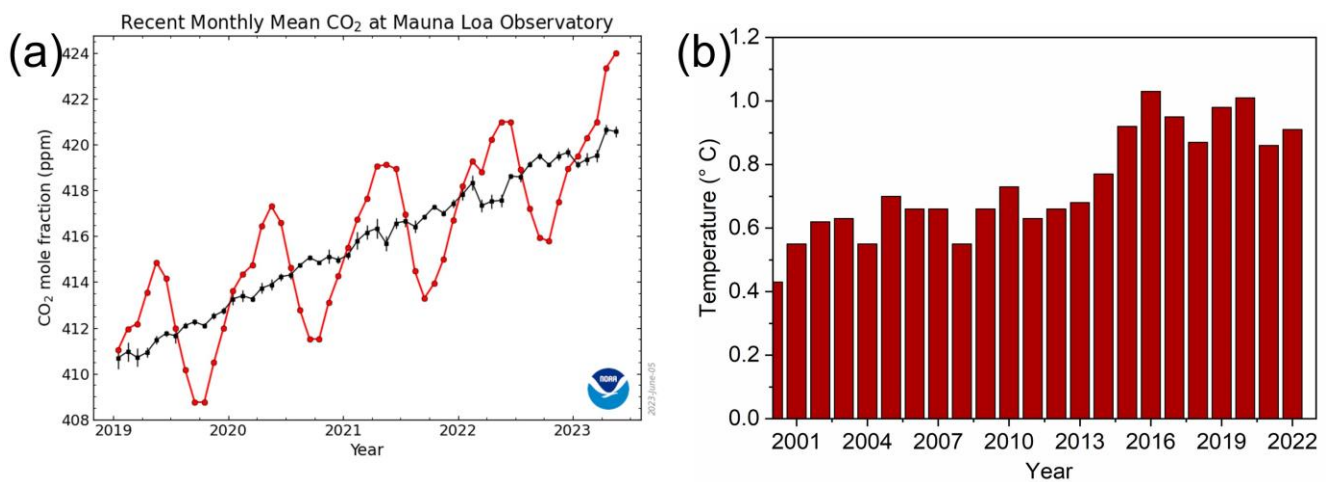


Figure 1.1: (a) CO₂ concentration measured at Mauna Loa Observatory, Hawaii,¹ and (b) Global land and ocean temperature anomalies (2000-2022).¹³

CO₂ is a greenhouse gas - it absorbs a significant amount of reflected solar heat energy from the earth and leads to an increase in global surface temperature. This increase in CO₂ concentration has been considered the major reason for global warming, consequently triggering various environmental issues. Extreme climate change has become a more concerning problem all over the world. The elevated atmospheric CO₂ is directly linked to the rise in the global average temperature of our planet by the greenhouse effect. According to NOAA, the global surface temperature (land and ocean) has already increased by 1 °C relative to the pre-industrial level (**Figure 1.1b**).¹³ The consequences of this increasing temperature, so-called "global warming", are such as diminished agricultural productivity, degradation of forests, loss of biodiversity, shifts in species distribution, rising sea levels, habitat destruction, intensified land degradation, heightened occurrence of cyclones, floods, heat waves, wild fires and more.^{14,15}

As predicted by the Intergovernmental Panel on Climate Change (IPCC) (Sixth Assessment Report), if we continue to emit CO₂ at an exponential rate, the concentration of CO₂ is projected to reach 1200 ppm by the end of 2100 (**Figure 1.2a**).¹⁶ Additionally, with the increased CO₂ concentration, the global average temperature is also predicted to surge up to 8 °C by the end of this century (**Figure 1.2b**).¹⁶ Therefore, there is a need to decrease the emission of CO₂ into the air, adapt to changing climate conditions, and shift towards sustainable and renewable energy sources. Additionally, capturing and converting anthropogenic CO₂ into value added chemicals and fuels, utilising porous materials hold promise for addressing climate change (discussed in **Section 1.2, 1.7** and **1.8**). These measures are crucial in mitigating the potential impacts of climate change and ensuring a sustainable future.

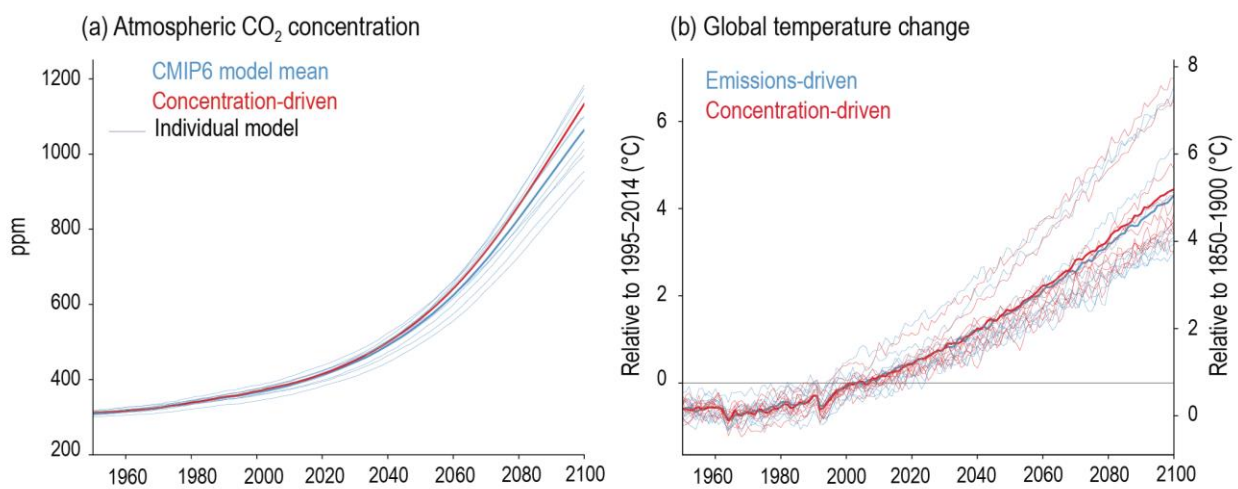


Figure 1.2: (a) Atmospheric CO₂ concentration, and (b) global surface temperature, respectively, reported in IPCC Sixth Assessment Report.¹⁶

1.2. Carbon capture and conversion

Carbon capture, utilisation and storage (CCUS) is a way of reducing the atmospheric CO₂ concentration of our planet, which could be key strategies for tackling climate change. CCUS involves the capture of CO₂ from significant emissions sources for instance industries or power plants that heavily depend on burning fossil fuels.¹⁷ There are ongoing efforts to create renewable and green energy sources as substitutes for conventional fossil fuels, with the objective of minimising CO₂ emissions. However, these renewable energy systems are still in their early stages and necessitate significant financial investments and implementation. As a result, fossil fuels are expected to dominate as the primary energy source for the next century due to their widespread availability and cost-effectiveness.

Given this scenario, the current challenge lies in the advancement and execution of CO₂ capture and conversion technologies for a sustainable future. The goal is to capture emitted CO₂ and utilise it, store it, or convert it to mitigate their impact on the environment.

There are various methods for capturing CO₂, namely post-combustion, pre-combustion, and oxy-combustion.¹⁸ Post-combustion capture employs a solvent to extract CO₂ (15%) from the flue gas emitted by a power plant. In pre-combustion capture, the fuel reacts with air or oxygen and steam to generate a combination of CO₂ (25%–35%) and H₂ (30%–50%). The CO₂ is separated, while the H₂ can be stored as a fuel. On the other hand, Oxy-combustion involves using high purity oxygen (>95%) as a substitute for air in combustion, generating a flue gas that primarily contains CO₂ (55%–65%) and H₂O (25%–35%), making it potentially suitable for storage after condensation and H₂O removal.¹⁸ All three types of carbon capture and separation process are depicted in **Figure 1.3**

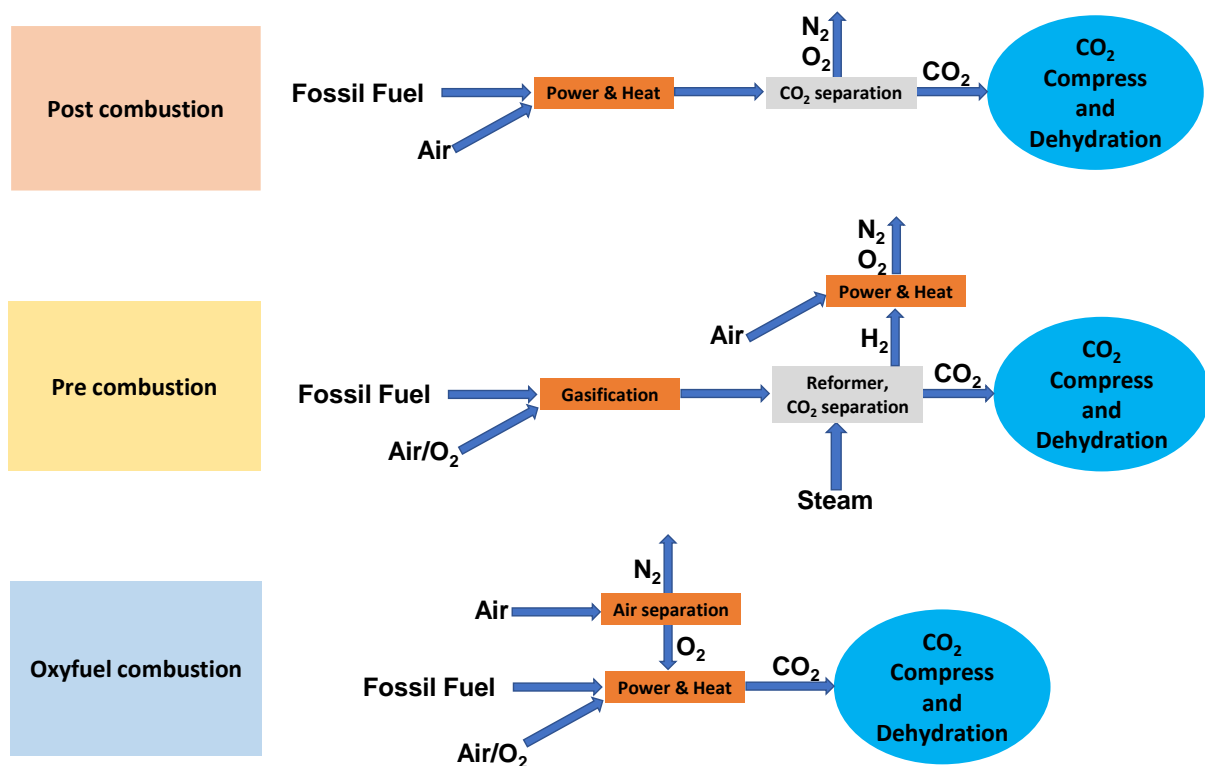
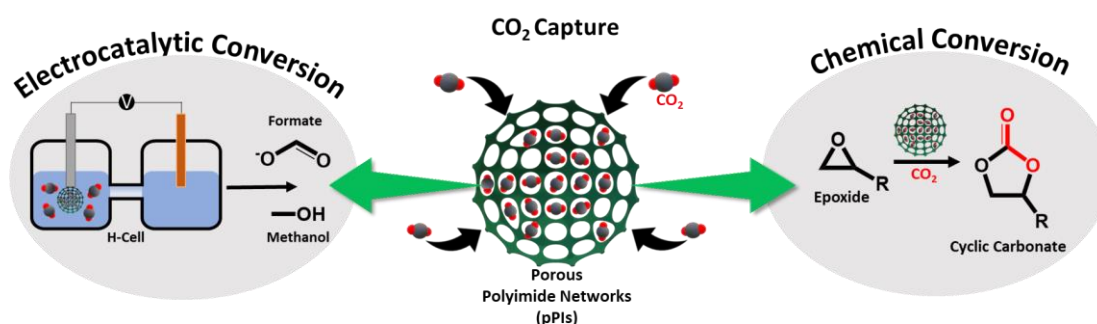


Figure 1.3: The three different carbon capture and separation process.¹⁸

At present, post-combustion capture and separation systems have been extensively employed in large-scale CO₂ capture plants. The majority of these systems utilise aqueous amine solutions, such as monoethanolamine (MEA), diethanolamine (DEA) and aminomethyl propanol.¹⁹ These solutions efficiently absorb CO₂ from flue gas at ambient temperature and subsequently regenerate the amine through water vapor stripping at temperatures between 100 °C and 120 °C.

However, the drawbacks of amine scrubbing include its corrosive nature and the significant energy consumption associated with purification, separation, compression, transportation, and storage processes.^{18,20} Additionally, flue gas often contains very low levels of nitrogen oxides (NO_x) and sulphur oxides (SO_x), that can react with the amine yielding stable and non-regenerable salts, leading to amine loss. As an alternative to address these challenges, porous materials such as porous organic polymers (POPs) have demonstrated their potential as viable media for carbon capture and separation, offering significantly higher energy efficiency and reversibility compared to aqueous amine solutions.²¹

Solid porous sorbents offer several advantages over liquid sorbents, including a wider temperature range and the absence of new chemical bond formation between the sorbates and sorbents.^{22,23} Desorption in solid adsorption is achieved through varying pressure and/or temperature.²⁴ However, the limited CO₂ uptake capacities within the porous structure of solid sorbents can present challenges in terms of storage. A more sustainable approach involves capturing CO₂ using porous organic polymers (POPs) and subsequently converting it into value-added chemical products or feedstocks.



Scheme 1.1: Schematic showing carbon capture and routes to conversion using pPIs.

There are several methods for converting CO₂ into valuable chemicals, including chemical methods,^{25–28} thermochemical catalysis,^{29–31} photocatalytic^{32–34} and electrocatalytic reduction.^{11,35,36} However, this thesis specifically focused on chemical and electrochemical conversion methods utilising pPIs as heterogeneous catalysts as shown in **Scheme 1.1**. A detailed discussion on electrochemical and chemical conversion are discussed in **Section 1.7 and 1.8**.

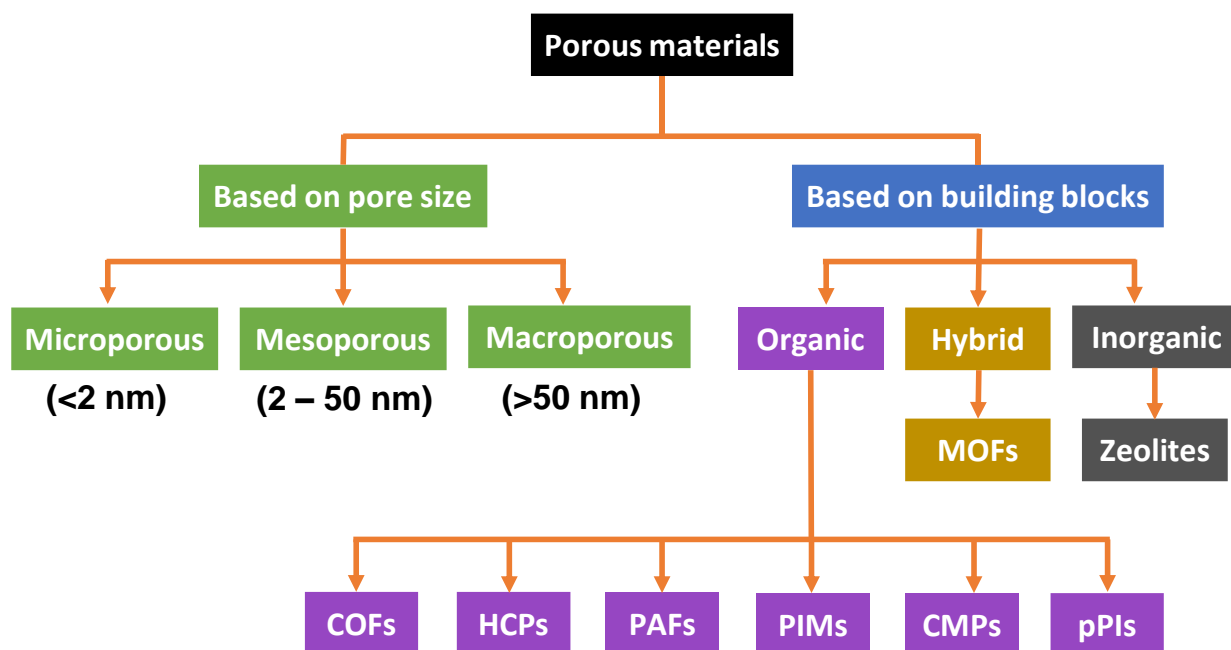
1.3. Porous organic polymers (POPs)

Porous organic polymers (POPs) are multidimensional porous networks that exhibit high crosslinking, comprising exclusively of organic building blocks. POPs are synthesised via strong covalent linkages

between various organic molecules with different geometries.^{37,38} POPs demonstrate excellent physical and chemical stability, enabling them to withstand harsh environmental conditions such as extreme temperatures (>500 °C) and pressures.^{39,40} Over the past few decades, POPs have attracted interest owing to their prospective uses in various applications such as gas storage and separation,⁴¹⁻⁴³ heterogeneous catalysis,^{44,45} drug delivery,^{46,47} energy storage,⁴⁸ and sensing.^{2,49}

1.4. Types of POPs

Porous materials can be classified based on two factors: the size of the pores and the composition of the building framework as shown in **Scheme 1.2**.⁵⁰ In terms of pore size, they are divided into three groups: microporous (pore size <2 nm), mesoporous (2-50 nm) and macroporous (>50 nm).⁵¹ Depending on their building framework, they are classified as organic, hybrid and inorganic porous polymers.⁵⁰ For instance, metal-organic frameworks (MOFs) and zeolites represent examples of hybrid and inorganic porous polymers, respectively. Within the category of POPs, they are further classified into covalent organic frameworks (COFs), hyper-crosslinked polymers (HCPs), porous aromatic frameworks (PAFs), polymers of intrinsic microporosity (PIMs), conjugated microporous polymers (CMPs) and porous polyimides (pPIs). This PhD project specifically focused on POPs that incorporate conjugated building blocks, namely porous polyimide networks (pPIs), as discussed in **Section 1.5**.



Scheme 1.2: Classification of porous materials based on pore sizes and building blocks.

1.4.1. Covalent organic frameworks (COFs)

Covalent organic frameworks (COFs) are crystalline POPs with a highly ordered structure that features widely tuneable pores.^{52,53} In COFs, organic building blocks such as boron, carbon, nitrogen, oxygen and silicon are linked by strong covalent bonds.⁵⁴ The directional nature of covalent bonds facilitates the binding of building blocks in a predetermined manner, resulting in the formation of a pre-designed structure with both crystallinity and porosity (see **Figure 1.4**).⁵⁵

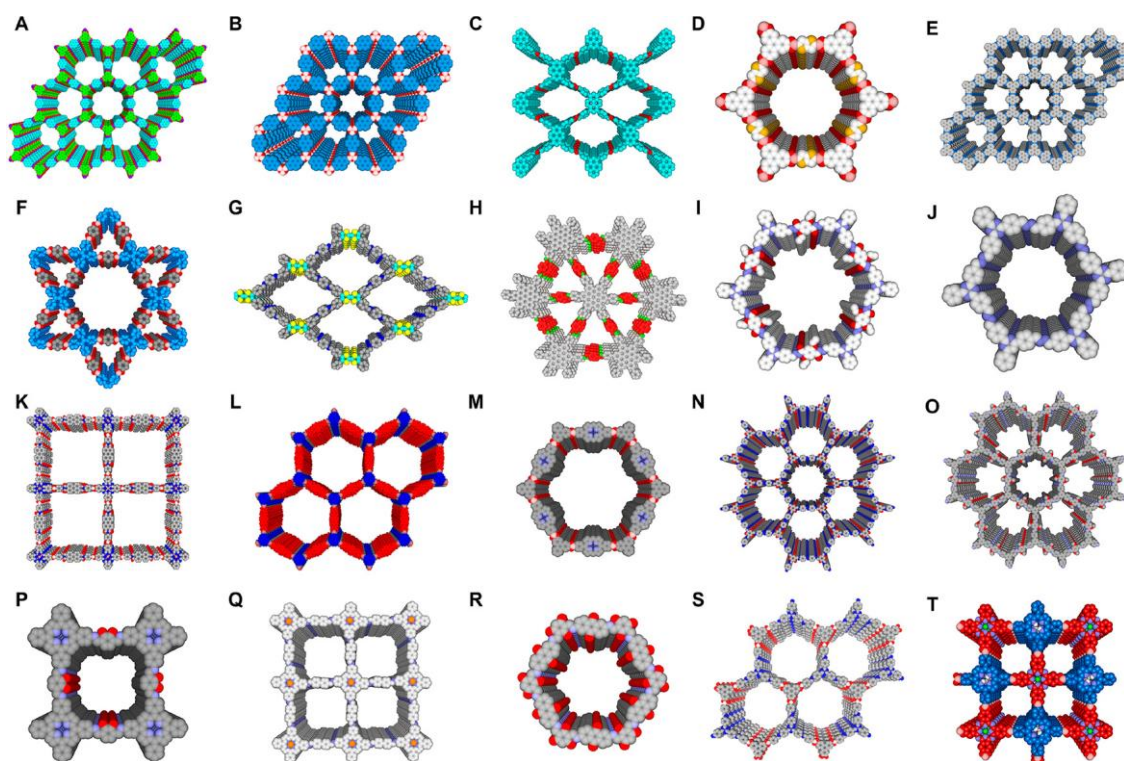
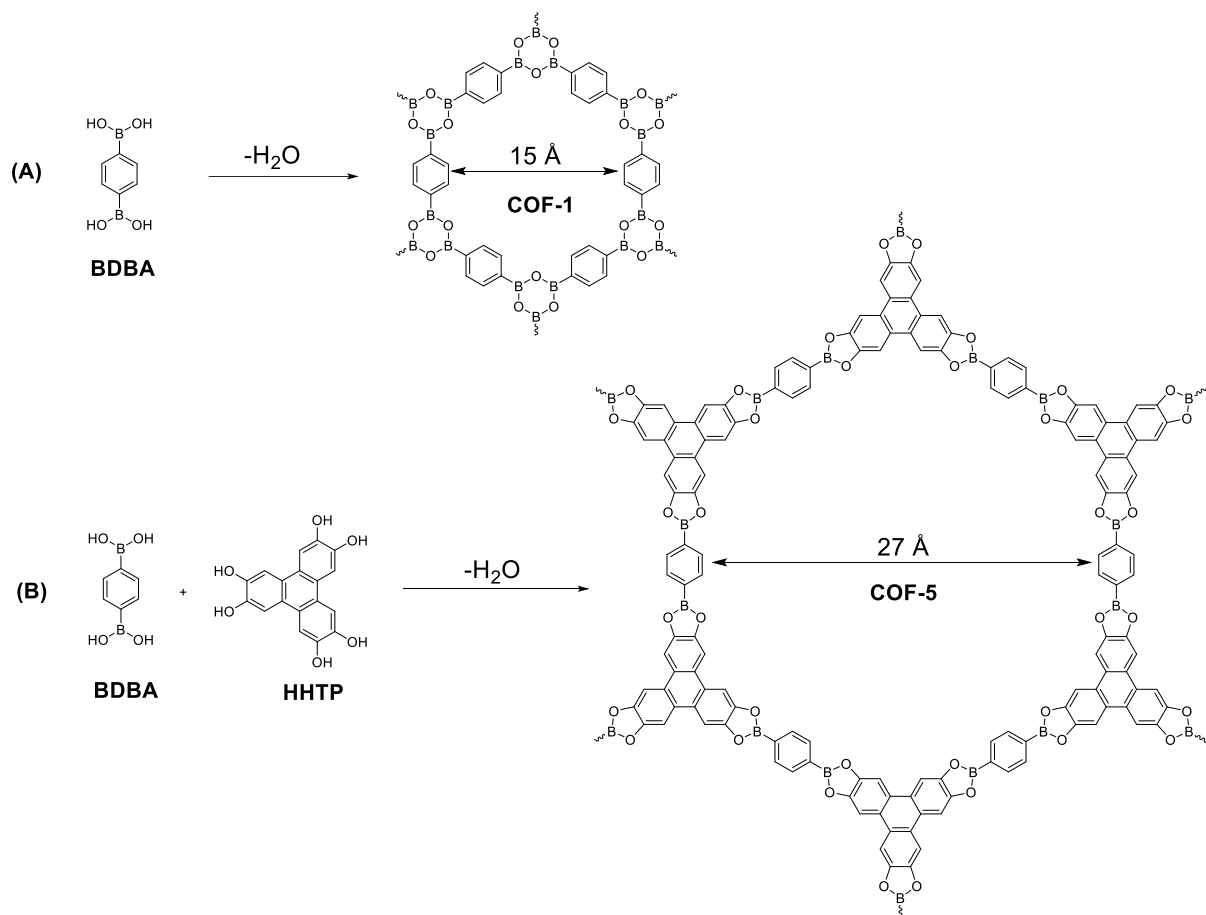


Figure 1.4: Example of COFs structures.⁵⁴

In 2005, Yaghi and co-workers first reported the synthesis of COFs (COF-1 and COF-5).⁵⁶ COF-1 was synthesised through self-condensation reactions of phenyl diboronic acid (BDDBA), while COF-5 was obtained through the co-condensation reaction between BDDBA and hexahydroxy triphenylene (HHTP) (see **Scheme 1.3**).⁵⁶ A poor solvent was chosen for the synthesis of COF-1 and COF-5, which allowed for slow condensation and slower reaction rate, resulting in the nucleation and growth of crystalline and ordered structures. As a result, COF-1 exhibited a surface area of $711 \text{ m}^2 \text{ g}^{-1}$, while COF-5 possessed a surface area of $1590 \text{ m}^2 \text{ g}^{-1}$.

Since their discovery, owing to their advantageous properties such as flexible molecular design, tailored pore size and high surface area,^{57,58} COFs have been widely investigated in various applications, for instance, gas capture and separation,⁵⁹⁻⁶¹ sensing,^{62,63} energy storage,^{62,64} and catalysis.⁶⁵⁻⁶⁷



Scheme 1.3: Synthetic pathway of COF-1 and COF-5, respectively.⁵⁶

1.4.2. Hyper-crosslinked polymers (HCPs)

Hyper-crosslinked polymers (HCPs) are amorphous polymers that exhibit properties such as significant swelling and enhanced stability due to their high degree of cross-linking as shown in **Figure 1.5**.⁶⁸ They offer impressive surface area and high microporosity through secondary cross-linking, thus forming pores after drying.⁶⁹ From a synthetic perspective, HCPs offer several advantages, including mild reaction conditions, monolithic product formation, the use of less expensive reagents, and easy scale-up synthesis.⁷⁰

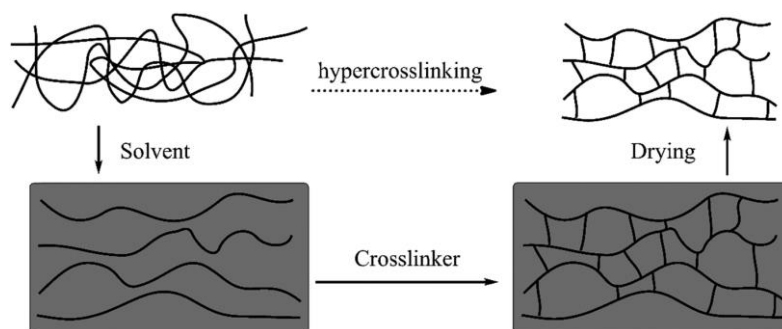
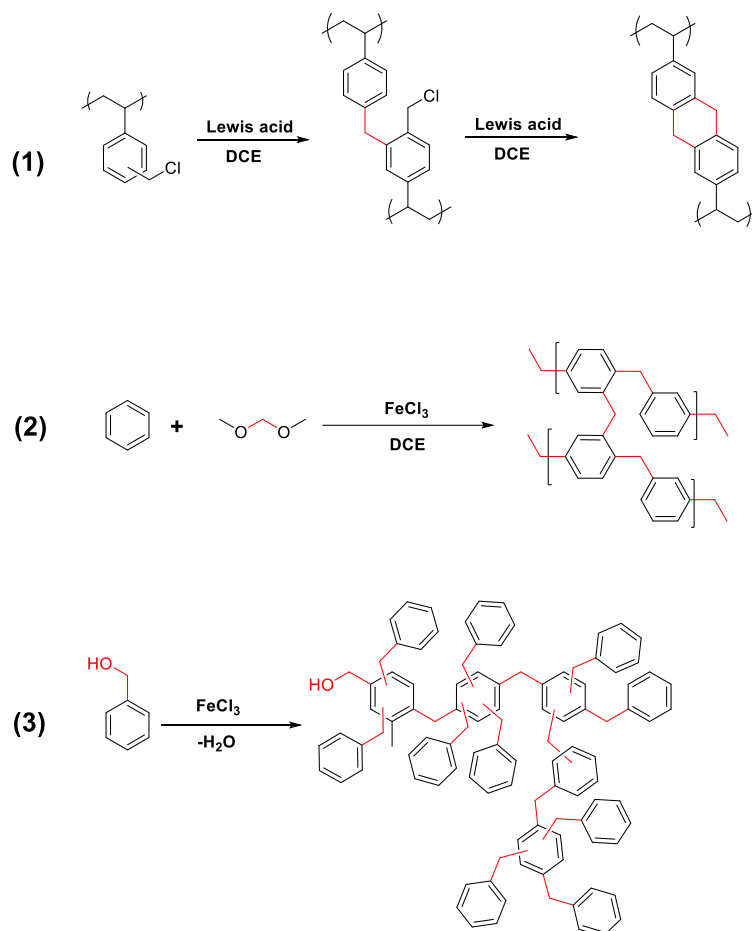


Figure 1.5: Schematic illustration of the hyper crosslinking process, adapted from ref.⁶⁹

HCPs find promising applications in areas such as gas capture and separation, catalysis, and adsorption of aromatic molecules from water.⁷¹ The first example of HCP synthesis was reported by Davankov et al,⁶⁸ in 1969. Friedel-Crafts alkylation reactions are commonly employed for the synthesis of HCPs,^{68,70} and they predominantly involve three approaches as shown in **Scheme 1.4**: (1) post-crosslinking of polymers,^{6,68} (2) direct one-step polycondensation of functional monomers,^{7,68} and (3) knitting rigid aromatic building blocks with external crosslinkers.^{8,68}



Scheme 1.4: Examples of synthesised HCPs: (1) post-crosslinking of poly(vinylbenzyl chloride)-based precursors,⁶ (2) knitting rigid benzene monomers with formaldehyde dimethyl acetal external crosslinkers,⁷ and (3) direct one-step polycondensation of benzyl alcohol monomers.⁸

1.4.3. Porous aromatic framework (PAFs)

Porous aromatic frameworks (PAFs) are rigid aromatic frameworks built by covalently linked carbon-carbon bonds between aromatic-based building blocks.^{72,73} PAFs lack a π -conjugated skeleton but exhibit outstanding surface area with high stability. The arrangements of PAFs can be altered and managed by incorporating a diverse array of functionalities as shown in **Figure 1.6**.⁷⁴ This property makes PAFs a promising material for use as adsorbents in gas storage and separation applications.⁷⁵

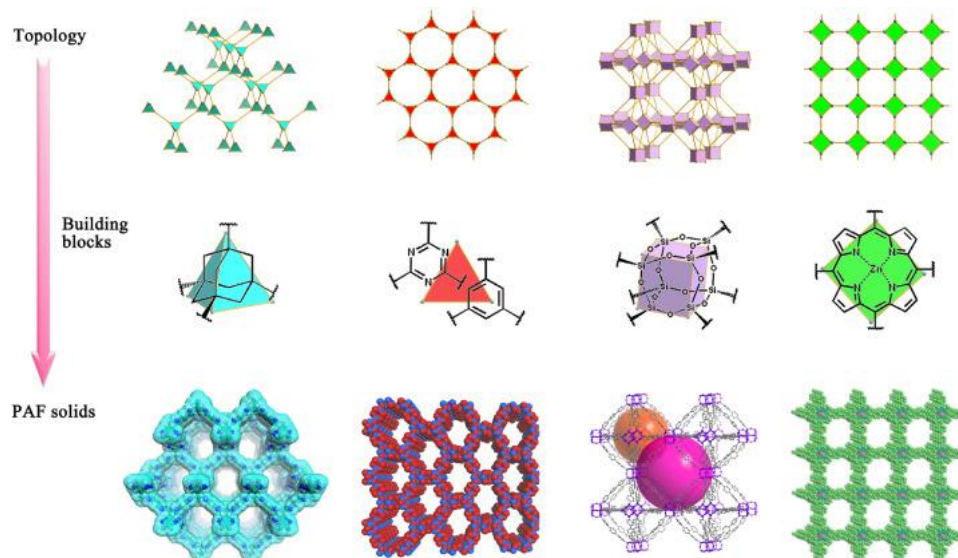
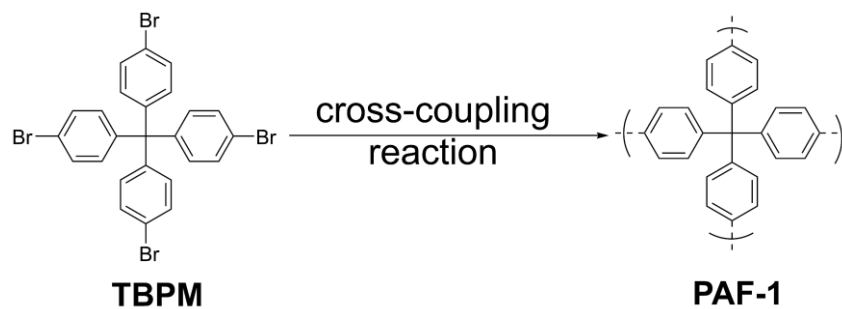


Figure 1.6: Schematic illustration of structures of PAFs.⁷⁴

In the year 2009, Ben and coworkers,⁹ synthesised the first PAFs (PAF-1), which possesses a tetrahedral diamond-like connectivity formed by tetraphenylene methane structural units. Its synthesis was achieved using the Yamamoto-type Ullmann cross coupling reaction involving tetrakis(4-bromophenyl)methane (TBPM) as shown in **Scheme 1.5**. The reported surface area for PAF-1 was 5640 m² g⁻¹.



Scheme 1.5: Synthetic route of PAF-1.⁹

1.4.4. Polymers of Intrinsic microporosity (PIMs)

The polymers of intrinsic microporosity (PIMs) are continuous polymer with highly rigid, nonlinear and contorted molecular backbones that create an interconnected intermolecular void within the polymer backbone.^{76,77} The inherent microporosity of PIMs is referred to as “intrinsic” because it results from the molecular structure and remains unaffected by the processing of the materials.

PIMs exhibits fused cyclic structure with contorted configuration around the spiro-centre and do not possess rotational freedom along the polymer backbone as shown in **Figure 1.7**.⁷⁸ This lack of rotational freedom does not allow polymer chains to rearrange their conformation and pack efficiently, thus their highly contorted shape is fixed.⁷⁹ Moreover, PIMs are solution processable, which is unique among porous materials.

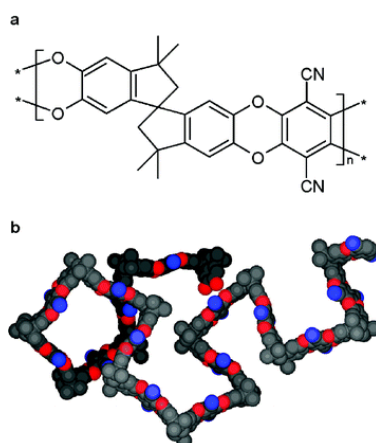


Figure 1.7: (a) Chemical structure of PIM-1 and (b) Molecular model of PIM-1 showing its highly contorted and rigid structure.⁸⁰

In the year 2004, McKeown and co-workers successfully synthesised the first PIMs (PIM-1, as shown in **Figure 1.7**). The PIM-1 was synthesised by the nucleophilic substitution reaction between 5,5',6,6'-tetrahydroxy-3,3,3',3'-tetramethyl-1,1'-spirobisindane (THTMSBI) and tetrafluoroterephthalonitrile (TFTN).⁸¹ The Brunauer-Emmett-Teller (BET) specific surface area (S_{BET}) of PIM-1 was approximately 850 m²/g.

1.4.5. Conjugated microporous polymers (CMPs)

Since the discovery by Cooper in 2007, conjugated microporous polymers (CMPs) have become an significant subgroup within POPs.² CMPs are a distinct class of highly cross-linked POPs that integrate extensive π -conjugation with permanent micropores and possess three dimensional (3D) structures.^{49,82} In CMPs, the rigid aromatic groups are interconnected, either directly or via double/triple bonds, to give π -conjugated skeletons. The conjugation occurs from the alteration of single and double/triple bonds throughout the extended structure.^{82,83} Most of the synthesised CMPs are amorphous, although control over micropore dimensions and surface area is attainable. Poly(aryleneethynylene) networks was the first reported CMPs synthesised by Cooper et al. with S_{BET} of up to 834 m²/g.⁸⁴

CMPs have been constructed in a broad range of architectures, for instance, linear chain polymers, dendrimers hyperbranched and network polymers. CMPs are synthesised via various pathways, such as the reaction between two distinct monomers or, occasionally, by homo-coupling of particular monomers. The commonly employed reaction pathways used for synthesising CMPs are illustrated in

Figure 1.8.²

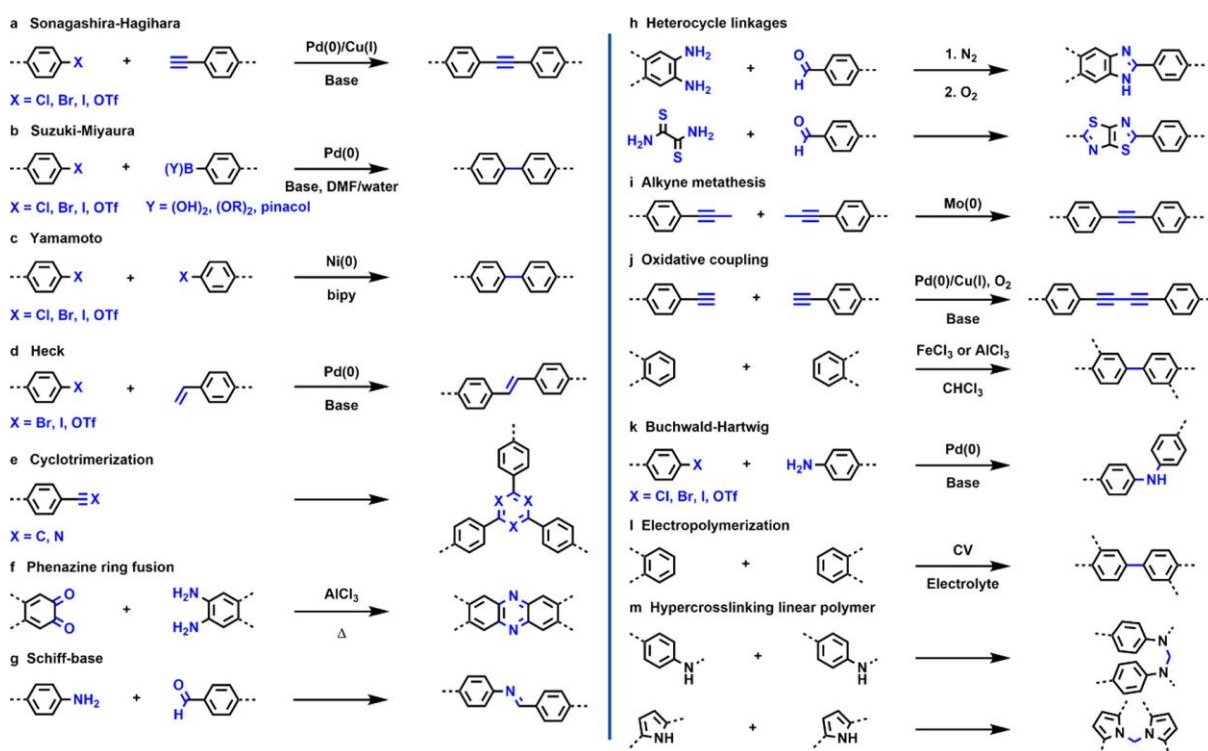


Figure 1.8: Schematic representations showing different reaction approaches applied in the synthesis of CMPs adapted from ref.² (a) Sonogashira-Hagihara, (b) Suzuki-Miyaura, (c) Yamamoto, (d) Heck, (e) cyclotrimerization, (f) phenazine ring fusion, (g) Schiff-base, (h) heterocycle linkages, (i) alkyne metathesis, (j) oxidative coupling, (k) Buchwald-Hartwig, (l) electropolymerisation, and (m) hypercrosslinking linear polymers.

1.5. Porous Polyimides (pPIs)

This Section is published in *Polymer Chemistry*, 2021, 12, 6494-6514; doi.org/10.1039/D1PY00997D; front cover.

Title: **Crosslinked porous polyimides: structure, properties and applications**

Basiram Brahma Narzary, Benjamin C. Baker, Neha Yadav, Valerio D'Elia and Charl F. J. Faul

doi.org/10.1039/D1PY00997D

Polyimide (PI) polymers were first synthesised and reported by Bogart et al. in 1908.⁸⁵ PIs can be divided into two classes, aromatic and aliphatic. The first aromatic PI was developed and commercialised by DuPont™ in 1960 and aliphatic first reported in 1971 by Hirsch et al.^{86–88} Initially aromatic PIs were found to exhibit higher thermal, chemical and mechanical stabilities than aliphatic PIs, whereas, aliphatic PIs possess good solubility, low dielectric constant and high optical transparency owing to their molecular packing and polarisability.⁸⁹ PIs have found general use and application in the fields of aviation, aerospace, micro-electronics, gas separation, membranes, fuel cells, batteries, electronic memory devices, shape memory devices, optical devices, biomedical applications, sensors, aerogels and polymer matrices in composites/hybrid materials.^{90–96}

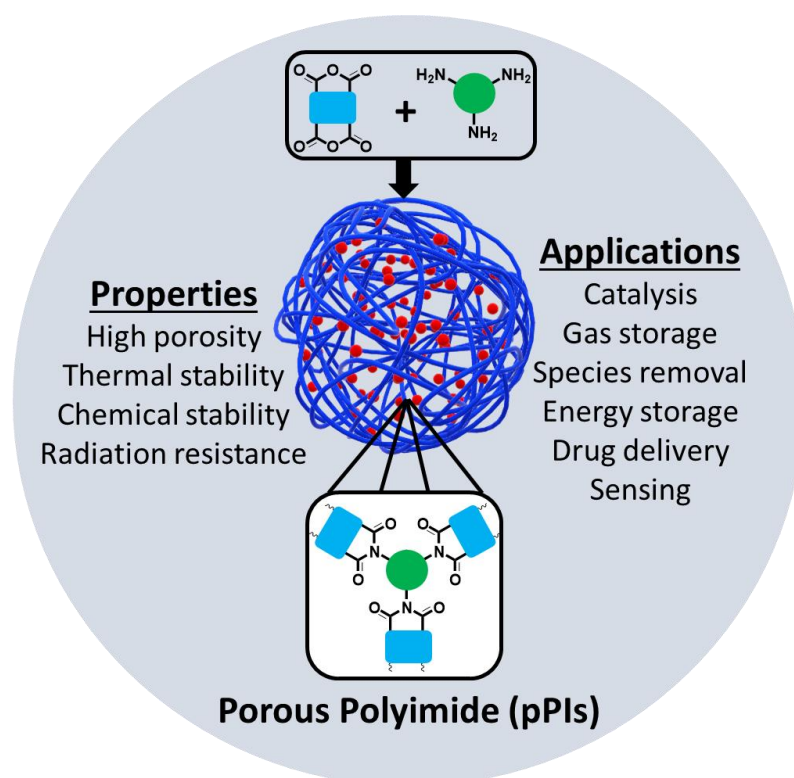


Figure 1.9: Porous polyimides (pPIs) properties and application.

Generally speaking, porous PIs (pPIs) are a class of porous organic polymers (POPs) synthesised by polycondensation reaction between amines and anhydrides (at high temperatures, 180–200 °C). Crosslinking is achieved either by multiple (> 2) reactive sites or cross-linkable groups (e.g. alkylene) present in the starting materials. pPIs offer high flexibility of their molecular design by variation of the monomer units to yield 3D-crosslinked networks. Moreover, pPIs can also be classified according to their initial building blocks: conjugated/aromatic and non-conjugated/aliphatic. Highly crosslinked pPI networks are advantageous over other porous materials owing to the excellent physical and chemical properties such as high mechanical, chemical and thermal stabilities, radiation resistance and high surface areas. Owing to their unique properties, PIs have shown great potential applications for addressing current energy and environmental global challenges. Specifically, pPIs can be utilised in gas adsorption and separation, electrical energy storage, heterogeneous catalysis, drug delivery, sensor, and species removal from aqueous environment (**Figure 1.9**).

This chapter covers the broader field of crosslinked and porous PIs, i.e., pPIs, with a specific focus on the monomer design, synthetic advances and the exploration of function and potential applications. The content covers literatures published since 2010, and considers amorphous, crystalline and gelatinous crosslinked pPIs, thus ensuring a range of applications and properties demonstrated in each are discussed. Non-crosslinked PIs are not discussed in this chapter, and readers are referred to other literature reviews and studies that address this topic in detail.^{89,90,92,97,98}

1.5.1. Monomer structure

The properties of polymers are inextricably related to the choice of monomers used for their synthesis. In the case of polyimides, polytopic amines and anhydrides are reacted exploiting several strategies to produce the desired crosslinked and porous pPIs. The structures of amine monomers are shown in **Figure 1.10.**, organised according to the number of amino moieties in the monomers (and hence the overall geometry of the formed pPIs, see **Section 1.5.2.2.1**), grouped into mono (**D1**), di- (**A1–18**), tri- (**B1–14**) and tetra- (**C1–8**) amine units; the anhydrides are provided in **Figure 1.11. (L1–26)**. To react this wide range of monomers several synthetic strategies have been applied, including solvothermal, ionothermal, interfacial synthetic approaches (exhaustively described in a recent review by Zhang et al.⁹⁹ and, therefore, not discussed in detail here). The authors of the latter work described also how the choice of monomers affected the geometry of the polymeric skeleton, however they only focused on pPIs in covalent organic framework (COFs) states. In this section we will focus on those cases where the rational design and multi-step synthesis of functional monomers allowed control over the properties of the final polymers in crystalline, amorphous and gelatinous pPIs.

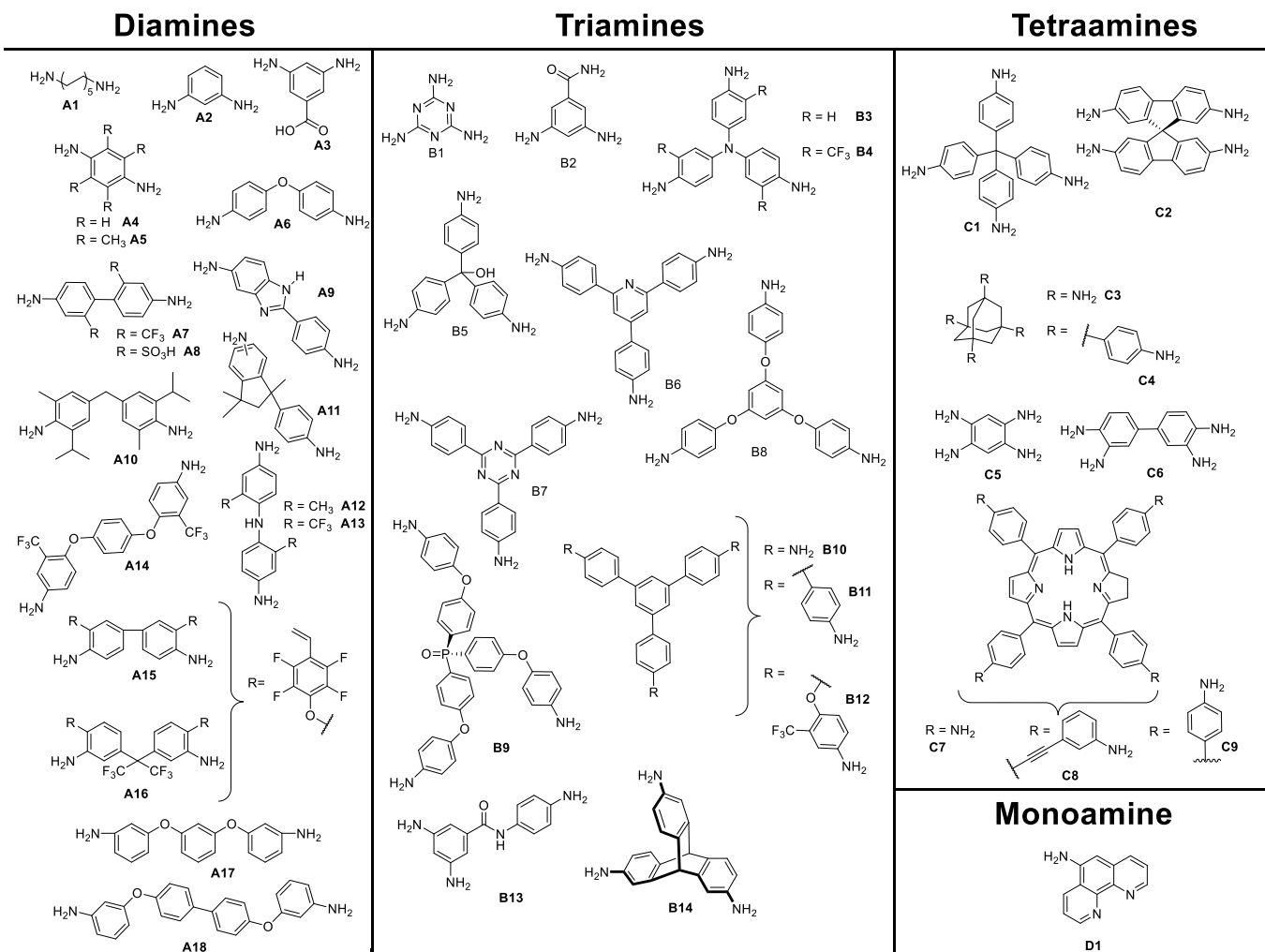


Figure 1.10: Structure of amine monomers, grouped into different reactive sites/geometries (di-,tri- and tetra-amines), utilised in the formation of pPI networks covered within this chapter.

Anhydrides

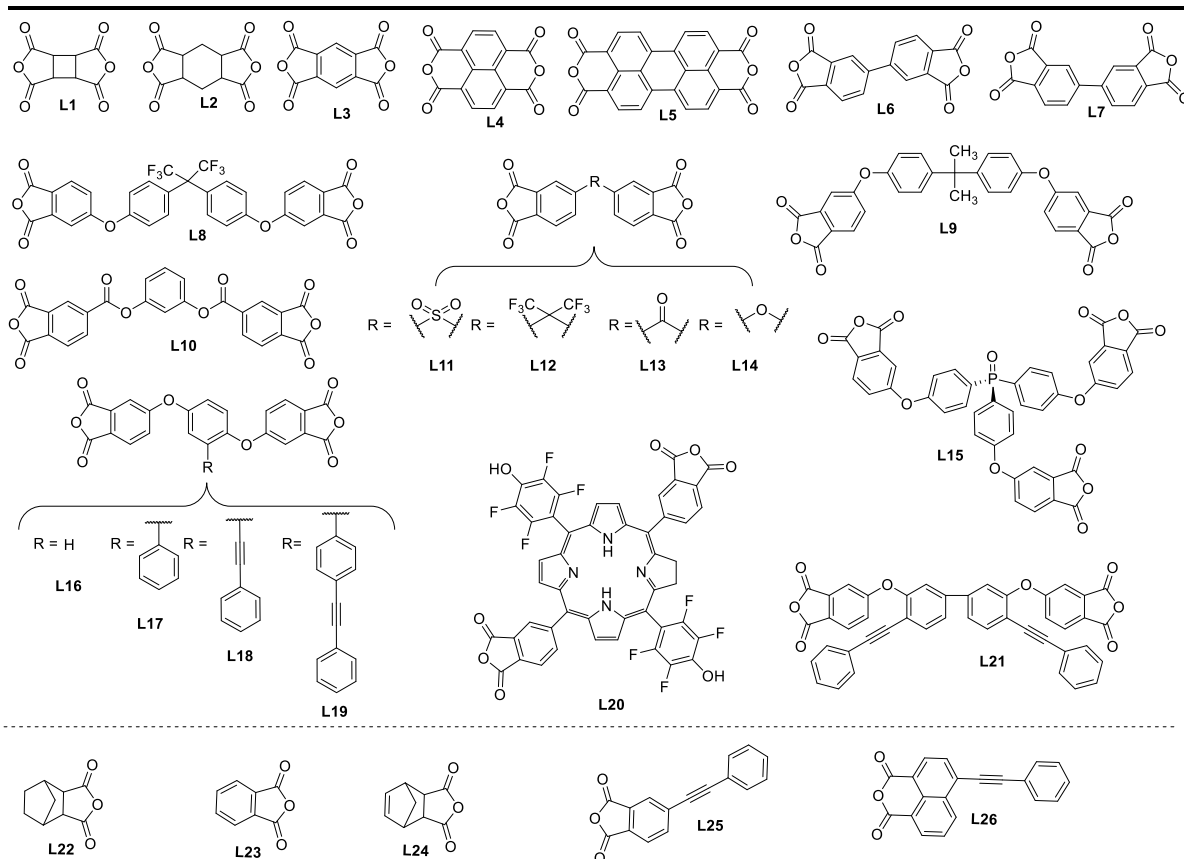


Figure 1.11: Structure of anhydride monomers utilised in formation of pPI networks covered within this chapter.

Most amine monomers reported in the literature for pPI syntheses are commercially available and require little to no synthetic modification. Here we focus on those monomers with rational geometric or functional design targeting specific properties (see **Section 1.5.2 and 1.5.3**). Within the amine monomers reported there are 3 major aspects that are noteworthy:

1. **Amount of reactive amine sites.** We have found that a variety of amine monomers with 2, 3 or 4 reactive amine sites are available, both commercially and synthetically, and are shown in **Figure 1.10**. The number of reactive sites is closely related to the geometry of the amine, e.g., 2 reactive sites = linear (**A1–18**), 3 = trigonal pyramidal or planar (**B1–14**), which has the additional effect of crosslinking (with distinct effects on properties such as surface area and applications such as gas absorption, see **Section 1.5.3.1**). For the creation of 4 reactive amine sites many papers cite the use of tetrahedral starting monomers **C1–6**, or the square planar porphyrin ring (**C7–8**, both synthetically modified specifically for the purpose of creating pPIs).

- 2. Introduction of heteroatoms and functional groups.** The introduction of heteroatoms and functional groups into the imide backbone of the polymers have a variety of impacts on the properties and applications (discussed later in **Sections 1.5.2 and 1.5.3**). In the case of such functionalised amine monomers several are worthy of discussion. With respect to di-reactive amine monomers, the use of commercially available fluorinated aromatic **A7** and the synthetically modified **A13** and **A14** (achieved via a dehydration reaction from the fluorinated ethylene benzene and phenol diamine) are used to include novel functionality. For tri-reactive amine monomers such as **B4**, **B12**, and **B13**, heteroatom-containing functionalities are introduced in the form of CF₃ functionalities or oxygen ether/ketone linkages. For the monomer **B4** multistep synthesis is required; firstly, 4-nitro-3-(trifluoromethyl)aniline and 4-chloro-1-nitro-2-(trifluoromethyl)benzene were coupled and the intermediate reduced in the presence of palladium and hydrazine hydrate by Song et al.¹⁰⁰ In the case of monomers with additional nitrogen heteroatoms (with respect to those involved in the imide linkage), **B7** was synthesised by Liebl et al.³⁸ from a two-step synthetic procedure involving the trimerisation of 1-bromo-4-cyanobenzene in the presence of CF₃SO₃H, followed by a nucleophilic substitution reaction in the presence of Pd(dba)₂.
- 3. Introduction of cross-linkable structures or moieties in the monomers.** Modifications of the monomers, to bear cross-linkable groups, lead to the formation of networks with improved control over their microporous structures (which has a direct effect on sorption and separation applications as discussed in **Section 1.5.3.1**). Perhaps the best examples of these are found in the porphyrin-based tetraamine monomer **C8**, synthesised by Shi et al.¹⁰¹ Here **C8** was functionalised with a cross-linkable ethynyl functionality in a two-step synthetic procedure (condensation and oxidation of 4-bromobenzaldehyde and pyrrole in the presence of acetic anhydride and propionic acid). Further examples can be found in the linear fluorinated diamines **A15** and **A16**, modified with ethylene functionalities for post-polymerisation crosslinking. In the cases of non-alkene or alkyne cross-linkable moieties the triamines **B2** (synthesised from an addition–elimination reaction between 3,5-dinitrobenzoylchloride followed by -NO₂ reduction in the presence of Pd/C) and **B13** (synthesised from an acylation reaction between 3,5-dinitro benzoylchloride and 4-nitroaniline, followed by reduction with hydrazine hydride in the presence of Pd/C by Rangel et al.¹⁰²) have also been employed.

Anhydride monomers typically possess two reactive sites (especially with benzene **L3**, naphthalene **L4** and perylene **L5** linkers). A few exceptions are the use of the mono reactive anhydrides such as **L22**, used as endcaps by Li et al.¹⁰³ to control polymerisation.

The majority of variations for this monomer are seen in the introduction of heteroatom and functional groups and cross-linkable moieties;

1. **Introduction of heteroatoms and functional groups.** The commercially available di-linkers **L8** and **L12** have been used to introduce fluorine (useful for increasing hydrophobicity), whereas the porphyrin-based **L20** was synthesised in a multistep procedure by Shultz et al.¹⁰⁴ (involving the formation of dimethyl 4-carboxaldehydophthalate and cyclisation with 5-pentafluorophenyl dipyrromethane in the presence of $\text{BF}_3 \cdot \text{Et}_2\text{O}$ and DDQ) to introduce fluorine, porphyrin and phenol functionalities.¹⁰⁴ Anhydrides **L9**, **L10**, **L13** and **L14** are commercially available and used to introduce oxygen into the polyimide backbone, an important addition to influence gas absorption (see **Section 1.5.3.1**).
2. **Introduction of cross-linkable structures and moieties in the monomers.** Shi et al.^{101,105} have synthesised a range of anhydride monomers containing two cross linkable pendant alkynyl functionalities, **L18**, **L19** and **L21**, and crosslinked them with amine monomers bearing the alkynyl functionalities (**A15** and **A16**).

Several preformed diimide-containing monomers are documented in the literature and shown in **Figure 1.12**. Roy et al.¹⁰⁶ synthesised a range of aromatic-based diimide monomers **M1–3**, from dianhydrides **L2–4**, respectively, via condensation of 5-aminoisophthalic acid. The formed diimide, functionalised with dicarboxylic acids, was then condensed with the tetra-amine monomers **C5** and **C6** to produce benzimidazole linked pPIs. Lu et al.¹⁰⁷ and Zhu et al.¹⁰⁸ condensed maleic anhydride with the appropriate diamine linker to yield the preformed monomer diimides **M4–6**. Lu et al.¹⁰⁷ then used diimide **M4** and crosslinkers **N1** and **N2** to generate pPIs via click reactions. Finally, Zhu et al.¹⁰⁸ used preformed diimides **M4–6** to generate pPIs via homo-thermal coupling.

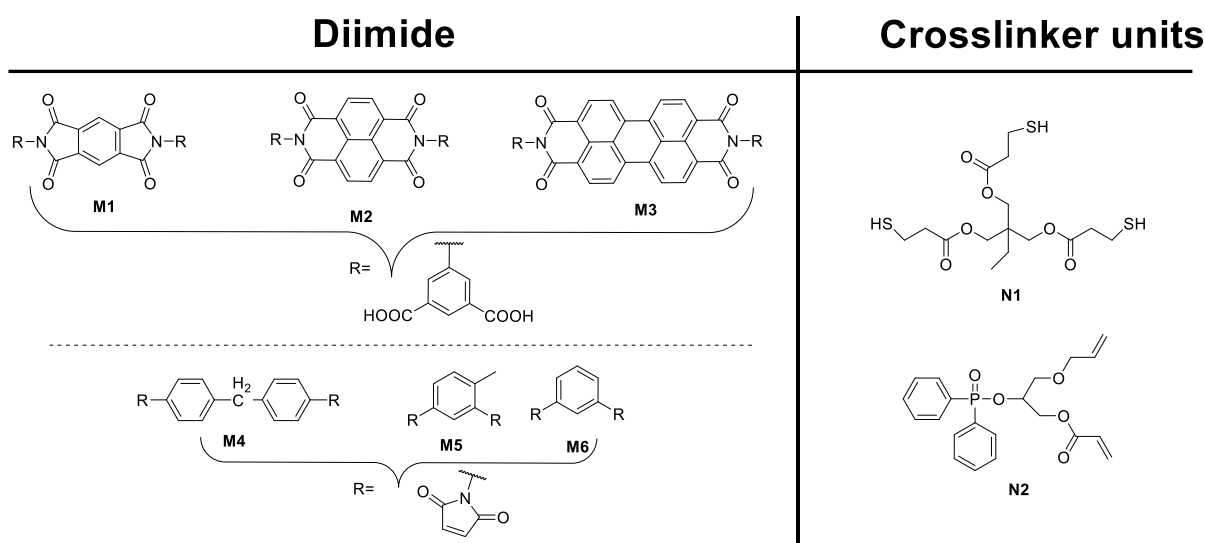


Figure 1.12: Preformed diimides **M1–6** (left) and crosslinker units (right) utilised in pPI formation.

Table 1.1: Nomenclature for reported pPIs, constituent monomers and references.

Name in Paper	Amine	Anhydride	Ref.	Name in Paper	Amine	Anhydride	Ref.
PDI-250	B1	L3	109,110	PI	B1	L3	111
PI0.01-.05	A6, B3	L7	112	PI-COF-201	B1	L3	113
3,5-DABA-TFMB	A7, B2	L3	114	PI-COF-202	B1	L4	113
MPI-Phen/MS/MPI-Phe	B10, D1	L3	115	PEDA-PI	A15	L17	116
NP1	C1	L4	117	PEQDA-PI	A15	L18	116
NP2	B3	L4	117	ODPA PB	B5	L14	118
NP3	B10	L4	117	ODPA TAPA	B3	L14	118
MPI-1	C1	L3	102	ODPA TAPP	B6	L14	118
MPI-2	B3	L3	102	ODPA MDA	A2	L14	118
MPI-3	B10	L3	102	BPADA MDA	A2	L9	118
PI-1	B1	L4	119	BPADA PB	B5	L9	118
PI-2	B1	L3	119	TAPOB-HBPI-CR	B8	L19	120
Tr-PPI	B3	L5	121,122	TAPB-HBPI	B10	L19	123
Td-PPI	C1	L5	121,122	TAPA-HBPI	B3	L19	123
TPI-1	B7	L3	38	TAPM-HBPI	C1	L19	123
TPI-2	B7	L4	38	STPI-1	B14	L3	124
TPI-3	B7	L5	38	STPI-2	B14	L4	124
TPI-4	B7	L13	38	STPI-3	B14	L6	124
TPI-5	B7	L14	38	6FDA-DAPI	A11,A11	L12	125
TPI-6	B7	L12	38	PI (10, 30, 50 wt %)	C1	L3	126
TPI-7	B7	L11	38	PI-COF-4	C3	L3	47
PI-1	B1	L3	127	PI-COF-5	C1	L3	47
PI-2	B1	L7	127	Pristine PI	A5	L12	128
PI-3	B1	L4	127	MMPI	B10	L1	129
BIBDZ	C6	M1	106	MPI-6FA	C1	L12	130

NIBDZ	C6	M2	106	API-6FA	C4	L12	130
PIBDZ	C6	M3	106	MPI-BPA	C1	L6	130
BIBZ	C5	M1	106	MPI-BTA	C1	L13	130
NIBZ	C5	M2	106	PI & CFs	A6	L13,L24	103
PIBZ	C5	M3	106	FPI	A6	L8, L12	131
PPBPI-1-CR	C7	L21	101	FHBPA	B12	L12	131
PPBPI-2-CR	C8	L21	101	BTMP-6-11	M4	N1	107
PPBPI-PM-CR	C8	L3	132	BTMP-6-11- AGDP	BTMP-6-11	N2	107
PPBPI-BP-CR	C8	L7	132	LCP2	A17	L12	133
PPBPI-NT-CR	C8	L4	132	xCP2-Am(1,2,5)	A17, B9	L12	133
PPBPI-PTC-CR	C8	L5	132	xCP2-An(1,2,5)	A17	L12, L15	133
PPBPI-x-CR	C7	L19	105	LPI-BP	A18	L8	133
PPBPI-PA-CR	C7	L19,L23/L25/26	134	SPI-DMDAs	A1, A9, A8	L4	135
FB POPP	C1	L20	104	PPI-1	B10	L3	3
PI/ZIF	A6	L7	136	PPI-2	C1	L3	3
PI nanosheets	B1	L3	137	PI-ADPM	C4	L3	138
B/P/T-0	A4.B8	L7	139	PI-ADNT	C4	L4	140
PI-COF-1	B3	L3	93	TF-PI	A15	L19	141
PI-COF-2	B10	L3	93	6FA-PI	A16	L19	141
PI-COF-3	B11	L3	93	PEQDA-HBPI-CL	C1	L18	142
PI-1	B1	L5	42	PEPHQDA-HBPI-CL	C1	L19	142
TAPB-PTCDA-COF	B10	L5	143	HBPI-TAPP-6FDA	C7	L12	144
TAPB-PMDA-COF	B10	L3	143	HBPI-TAPEPP-6FDA	C8	L12	144
TT-PMDA-COF	B7	L3	143	PI-1	C1	L3	145
TAPA-PMDA-COF	B3	L3	143	PI-2	C1	L4	145
PPI-1	B13	L3	102	PIA-6FDA(0,10,20,30,40,50)	A7, C2	L7, L12	146
PPI-2	B10	L3	102	sPI-A-H	C3	L2	147
PPI-3	B10	L5	102	sPI-M-H	C1	L2	147
CH ₃ -PI	A12	L18	148	sPI-A-B	C3	L1	147
CF ₃ -PI	A13	L18	148	sPI-M-B	C1	L1	147
TAPA-HBPI	B3	L18	100	MPI	C1	L3	149
CF ₃ TAPA-HBPI	B4	L18	100	PBDM	--	M4	108
PI-1	B10	L3	150	PBMP	--	M5	108
PI-2	B10	L4	150	PPDM	--	M6	108
PAF-110	B3	L4	151	PI-3	B10	L5	150
PPPP-1	C9	L3	152	NT-COF	B3	L4	153
PPPP-1	C9	L4	152	PI-COF	C7	L5	154
PIA	B10	L3	155	NDI-COF	B10	L4	156
PIB	B3	L3	155	TP-COF	B7	L3	157
PIC	B10	L4	155	CPI	B10	L4	158
PID	B3	L4	155	PI – 0%6FAPB	A6, A14,B8	L7	159

1.5.2. Properties

1.5.2.1. Thermal stability

Crosslinked pPIs present excellent thermal stabilities, making them suitable for applications such as gas capture in high-temperature environments (e.g. industrial flue-gas outlets), battery and electrode environments or as protective coatings.¹⁵⁹ Weight loss above 400 °C can often be attributed to imidisation of unreacted amic acid groups (from anhydride ring opening but failed imide formation) and water loss.¹²⁷ In many cases in the literature temperatures of degradation (T_{deg}) and char yields (wt% remaining after heating to 800 °C) are not reported. In this chapter we have attempted to calculate those values from thermo gravimetric analysis (TGA) graphs that were not reported in the original literature and display these generated values in **Table 1.2.** alongside those reported.

Table 1.2: Showing T_{deg} of pPIs from TGA under nitrogen and char yields at 800 °C, where * = estimated by the authors from TGA traces utilising imageJ image analysis software, and # = char yield at 700 °C

Name in Paper	T_{deg} (°C)	Char (wt%)	Ref.	Name in Paper	T_{deg} (°C)	Char (wt%)	Ref.
MPI-1	530	57.4	102	TAPA-HBPI-CR	500*	60*	120
MPI-2	530	53.0	102	TAPA-HBPI-GEL	600*	60*	120
MPI-3	530	59.3	102	TAPM-HBPI	450*	60*	120
PI-COF-1	520	60*	93	TAPM-HBPI—CR	530*	60*	120
PI-COF-2	535	60*	93	TAPM-HBPI-GEL	580*	60*	120
PI-COF-3	530	60*	93	TAPOB-HBPI	500*	70*	120
TFMB	537	-	114	TAPOB-HBPI-CR	550*	75*	120
3,5-DABA (20)TFMB (80)	520	-	114	TAPOB-HBPI-GEL	600*	60*	120
3,5-DABA (50)TFMB (50)	489	-	114	STPI-1	610*	5*	124
3,5-DABA (80)TFMB (20)	467	-	114	STPI-2	580*	50*	124
m-PDA (20)TFMB (80)	527	-	114	STPI-3	600*	60*	124
m-PDA (50)TFMB (50)	536	-	114	PI-COF-4	450	40*	47
m-PDA (80)TFMB (20)	532	-	114	PI-COF-5	460	42*	47
PAA0.03	200*	30*	112	BI-PEG2-xPI	510*	--	128
PI0.03	550	50	112	BI-PEG3-xPI	510*	--	128
NPI 1	480	50.0	117	BI-PEG4-xPI	500*	--	128
NPI 2	485	46.7	117	BI-PEG6-xPI	450*	--	128
NPI 3	490	64.7	117	MPI-6FA	550*	50*	130
PI1	400		119	MPI-BTA	560*	55*	130
PI 1	400	45	42	MPI-BPA	610*	58*	130
PI 2	405	45	42	API-6FA	550*	53*	130
PI-1-C		68	42	PI 300	-	-	103
TPI1	419	-	38	CF 600	-	73	103
TPI2	456	-	38	CF 900	-	65	103
TPI3	342	-	38	CF 1200	-	55	103
TPI4	427	-	38	CF 1500	-	47	103

TPI5	421	-	38	FPI	542	60*	131
TPI6	396	-	38	FPI/FHBPI-5%	530	58*	131
TPI7	450	-	38	FPI/FHBPI-10%	528	58*	131
PI1	410	10*	127	FPI/FHBPI-15%	524	57*	131
PI2	350	0*	127	FPI/FHBPI-20%	519	57*	131
PI3	350	30*	127	FPI/FHBPI-25%	516	56*	131
PI – 0%6FAPB	591	T _g 202.1	159	FHBPI	514	55*	131
PI – 25%6FAPB	589	T _g 221.6	159	BTMP-6-AGDP	328	30	107
PI – 37.5%6FAPB	-	T _g 234.3	159	BTMP-9-AGDP	327	32	107
PI – 50%6FAPB	589	T _g 259.2	159	BTMP-11-AGDP	326	34	107
PPI1	560	-	102	PPI-1	570	62*	3
PPI2	570	-	102	PPI-1-NH2	405	54*	3
PPI3	525	-	102	PPI-2	540	65*	3
Tr-PPI	550*	60*	122	PPI-2-NH2	410	35*	3
Td-PPI	450*	60*	122	PI-ADNT	600*	-	140
BIBDZ	100*	70*	106	PI-NO2-1	400*	-	140
PIBDZ	100*	60*	106	PI-NO2-2	400*	-	140
NIBDZ	100*	65*	106	PI-NO2-3	400*	-	140
BIPZ	100*	70*	106	TF-PI	500*	45*	141
PIBZ	100*	60*	106	TF-PI-CL	560*	65*	141
NIBZ	100*	68*	106	6FA-PI	500*	45*	141
PPBPI-H	520*	65*	105	6FA-PI-CL	550*	60*	141
PPBPI-Mn	580*	75*	105	PI-1	588	72*	145
PPBPI-Fe	518*	66*	105	PI-2	519	65*	145
PPBPIR-H CR	522*	66*	105	PIA/6FDA-0	593	60*	146
PPBPI-Mn-Cr	520*	68*	105	PIA/6FDA-10	573	59*	146
PPBPI-Fe-Cr	580*	70*	105	PIA/6FDA-20	565	59*	146
PPBPI-PA	580*	60*	134	PIA/6FDA-30	551	59*	146
PPBPI-PEPA	600*	70*	134	PIA/6FDA-40	550	59*	146
PPBPI_PENA	560*	68*	134	PIA/6FDA-50	536	58*	146
PPBPI-PA-CR	600*	68*	134	sPI_A-H	540*	52*	147
PPBPI-PEPA-CR	560*	70*	134	sPI-M-H	530*	47*	147
PPBPI-PENA-CR	380*	60*	134	sPI_A-B	430*	48*	147
TAPA-HBPI	510*	54*	100	sPI-M-B	420*	48*	147
TAPA-HBPI-CL	610*	65*	100	MMPI	520*	60*	129
CF3TAPA-HBPI	510*	55*	100	LCP2	526	-	133
CF3TAPA-HBPI-CL	600*	65*	100	xCP2-Am1	514	-	133
PI-1	473	-	150	xCP2-Am2	511	-	133
PI-2	502	-	150	xCP2-Am5	518	-	133
PI-3	490	-	150	xCP2-An1	519	-	133
PI	380*	-	111	xCP2-An2	518	-	133
PI-COF 201	380*	10*	113	xCP2-An5	518	-	133
PI-COF 202	420*	10*	113	LPI-BP	--	-	133
PEDA-PI	500*	55*	116	CSPI-DMDA (1:3)	340*	49*	135
PEDA-PI-CL	550*	68*	116	CSPI-DMDA (1:1)	340*	52*	135
PEQDA-PI	480*	50*	116	CSPI-DMDA (3:1)	330*	40*	135
PEQDA-PI-CL	550*	67*	116	PAF-110	530*	5*	151

TAPB-HBPI	520*	75*	123	MPI-0-10	363	55*	160
TAPB-HBPI-CR	570*	75*	123	MPI-30-10	485	60*	160
TAPB-HBPI-GEL	570*	70*	123	MPI-40-10	465	60*	160
TAPA-HBPI	510*	60*	123	MPI-50-10	443	60*	160
PIA	535	65*	155	MPI-60-10	452	60*	160
PIB	525	60*	155	MPI-70-10	476	60*	160
PIC	535	65*	155	MPI-100-10	391	61*	160
PID	520	50*	155	MPI-60-5	--	--	160
CPI	275*	55*	158	MPI-60-7	348	60*	160
NDI-COF	500	60	156	MPI-60-9	490	61*	160
PI-COF	500	60	154	MPI-60-11	492	62*	160
PPPP-1	560	70	152	MPI-60-13	503	63*	160
PPPP-2	570	70	152				

Conjugated pPIs show typical degradation temperatures between 400 – 600 °C (10 wt% loss), with the highest stabilities reported by Shi et al.,^{101,105,132,134} Song et al.,^{100,141,142,148} and Yao et al.^{120,123} (each slightly above 600 °C). Conjugated pPIs quite often exhibit a decrease in T_{deg} when increasing the weight percentage of heteroatoms in the network, as seen, for example, in the studies by Wang et al.^{111,113} with the T_{deg} increasing with increasing carbon-based dianhydride monomer linker units **L3** and **L4** (although the reasons behind this trend were not investigated by the authors). The introduction of post-polymerisation crosslinking units into pPI networks tends to lead to an increase in pPI thermal stability (with respect to T_{deg}) after crosslinking. However, if the crosslinking moieties lead to an increased heteroatom content, a decrease in thermal stability can be observed (see the effect of the introduction of the amide crosslinker unit **B2** by Hasegawa et al.¹¹⁴). Interestingly, very little variation in thermal stabilities of conjugated pPI networks is observed when varying the molar ratio of amine centres on the starting monomers from tri- or tetra-amines (see Rao et al.¹²² utilizing the tetra-armed amine **C1**, and Shi et al.¹⁰⁵ using the porphyrin-based tetramines **C7** and **C8**). Perhaps the most interesting take on control over the thermal properties of conjugated pPI networks is found in the study by Qiao et al.,¹⁵⁹ where they investigated polyimide aerogels. Here frustrated pPI chain growth is found to leave pendant carboxylic acid groups from the anhydride monomer **L8**, that are then crosslinked post polymerisation (by addition of triethyl amine) under supercritical CO₂ to control T_{deg} via the degree of crosslinking.

The majority of conjugated pPIs reported in this chapter are highly crosslinked amorphous materials; thermal analysis such as dynamic scanning calorimetry (DSC) to examine thermal transitions before the T_{deg} are thus largely unreported or unexplored. An exception can be found in the pPIs synthesised by Hasegawa et al.¹⁶¹ where both DSC and dynamic mechanical analysis are used to demonstrate the manipulation of glass transition temperatures (T_g) by post-polymerisation crosslinking of pPIs utilising the amide crosslinker unit **B2**. Further to this exception, Qiao et al.¹⁵⁹ show manipulation of T_g via

introduction of CF₃ side groups (to increase the steric hinderance and free movement of chains, hence increase in T_g), using the amine monomer **A14** into their polyimide aerogels. Song et al.¹⁴⁸ and Shi et al.¹⁰⁵ utilised post-polymerisation cross-coupling of alkynes present in the anhydride monomers **L18** and **L19**. In the majority of cases DSC is primarily used for verification of post-polymerisation crosslinking, with exotherms being recorded in the first heating scan but absent in second.

The properties of pPIs beyond their T_{deg} temperatures were explored by Liao et al.¹⁶² using the charred product after heating beyond T_{deg} to form 'derived carbons' (from pPIs of **B1** and **L5**). They found both increased surface area and CO₂ uptakes for these derived carbons with respect to the non-charred pPIs (see further discussion on gas absorption properties **Section 1.5.3.1**). This leads to the question whether higher T_{deg} is desirable when trying to access char products with enhanced absorption properties efficiently.¹⁶¹ The mechanisms of charring and carbonisation have also been explored by Li et al.^{103,131} using Raman, XPS spectroscopy and XRD diffractometry to analyse the products post carbonisation. They concluded that 'the decomposition of imide rings and the breakage of the ether oxygen in the bridging part of polyimide' are responsible for charring, leading to the proposition that increased heteroatom content can facilitate carbonisation (and hence a decrease in T_{deg}). It is evident that carbonisation (and its beneficial effects on properties such as surface area or gas absorption, specifically CO₂ uptake) are relatively unexplored in the literature to date and is an area for further future exploration and development.

Many of the reported non-conjugated pPIs show similar properties and trends to the conjugated pPIs summarised above. However, there are some aspects to be highlighted in this section. Studies for non-conjugated pPIs tend to conclude that T_{deg} as well as char yields in N₂ tend to be optimised when using pPIs with the least amount of heteroatoms within the network (see, for example, Li et al.^{102,117,163}). Rangel et al.³³ demonstrated that functionalisation of their pPIs with nitro groups (for catalysis applications, see **Section 1.5.3.2**) results in a decrease in thermal stability, from the 540–570 °C to the low 400 °C region. Similar results were observed by Shen et al.¹⁴⁰ tetra-armed pPI with a high thermal stability of 621 °C that experiences a considerably drop in stability after nitration to 370 °C (as a result of C-NO₂ cleavage throughout the pPI). However, in contrast to this behaviour, Wang et al.¹⁴⁵ found that a change in anhydride linker from benzene **L3** to naphthalene **L4** (an increase in carbon percentage as well as conjugation) in their non-conjugated pPIs resulted in a drop in the T_{deg}. Lu et al.¹⁰⁷ also showed how increased thiol linkages in pPIs (present from linker N₂) can result in increased T_{deg} and increased char yields. Finally, Wu et al.¹⁴⁶ found, counterintuitively, a decrease in T_{deg} with increasing crosslinking percentage (and hence increased carbon-carbon bond formation), with no further explanation provided.

The majority of crosslinked pPIs do not demonstrate melts or glass transitions (T_g). However, Lu et al.¹⁰⁷ showed how control over the length of thiol linkages (N_2) in pPIs allow manipulation of the T_g , with a maximum of 59 °C appearing for moieties with 9 thiol linkers per linker unit. It is worth noting that although this polymer is classified here as a pPI, the thiols are used for the formation of the final crosslinked product from the preformed diimide **M2**. The manipulation of the T_g of the final product is important as it has been linked to a deformation temperature. Below this temperature the polymer will hold a deformed shape and above the polymer recovers to its original shape (i.e., displaying shape memory function) due to the high degree of crosslinking and stability. Li et al.¹³¹ use blends of both linear (from **A12** and **L12**) and crosslinked (using **B12** to crosslink) fluorinated pPIs to manipulate both T_{deg} and T_g . A decrease of T_{deg} is observed with increasing crosslinked content in the blend, attributed to the increase in terminal hydrides in the crosslinked structure and hence increased post-polymerisation carbonisation. Both the linear and crosslinked pPIs demonstrate T_g values of approximately 260 °C; mixing provides a route to manipulation of the T_g , with a maximum value of T_g realized at 5 wt% crosslinker (as confirmed by dynamic mechanical analysis).

1.5.2.2. Porosity

Several trends were found in changes in the surface areas of pPIs, and the most relevant and important factors influencing this important property of this class of porous materials is discussed here:

1.5.2.2.1. Effect of geometry of starting material on porosity

Specifically, a number of groups have explored the influence of 3D geometry of the cores of pPIs on surface areas and properties. For example, Li et al.¹¹⁷ synthesised three pPIs with three different core amines; the tetra-amine **C1** (tetrahedral, to give NPI-1) and tri-amines **B3** and **B10** (trigonal pyramidal, NPI-2 and trigonal planar NPI-3, respectively), whilst keeping the dianhydride linker (**L4**) the same. This study found that the highest pore volumes, as well as surface areas, were generated with the tetrahedral core (**C1**) due to its 3D shape, which prevented the pPIs from close packing (surface areas of NPI-1, 2, 3 are 721, 291, and 373 $m^2 g^{-1}$, respectively, See **Table 1.3.**). Similar studies were undertaken by the same author using the same cores but a shorter linker (**L3**). The same trends were observed: the surface area with tetrahedral core was the highest (1454 $m^2 g^{-1}$) followed by the trigonal pyramidal (814 $m^2 g^{-1}$) and the trigonal planar core (586 $m^2 g^{-1}$, see **Table 1.3.**). The lowest surface area with the trigonal planar core was attributed to formation of π -stacking and loss of pore volume, thus resulting in lower surface area compared with the tetrahedral and trigonal pyramidal geometry cores.

Table 1.3: Porosity properties of pPIs where S_{BET} = surface area from BET, PV = pore volume, Q_{st} = isosteric heat of absorption, A: amorphous; C: crystalline; i: at 195K, 1 bar; ii: at 273K, 1 bar; iii: at 77 K, 1 bar, iv: 77 K, 30 bar, v: 298 K, 1 bar, *only the highest surface areas are reported.

Name in Paper	S_{BET} ($m^2 g^{-1}$)	PV ($cm^3 g^{-1}$)	CO ₂ (wt%)	Q_{st} (KJ mol ⁻¹)	Ref.	Name in Paper	S_{BET} ($m^2 g^{-1}$)	PV ($cm^3 g^{-1}$)	CO ₂ (wt%)	Q_{st} (KJ mol ⁻¹)	Ref.
PI-250	16.8 ^A	--	--	--	110	PI-1	--	--	8 ⁱⁱ	--	164
PI-275	7.5 ^C	--	--	--	110	PI-2	--	--	--	--	164
PI-300	6.8 ^C	--	--	--	110	PI-3	--	--	--	--	164
PI-325	5.1 ^C	--	--	--	110	PI	635.5 ^A	0.98	--	--	111
PI-350	4.3 ^C	--	--	--	110	PI-COF-201	3.9 ^C	--	--	--	113
NPI-1	721 ^A	0.51	12.3 ⁱⁱ	33.5	117	PI-COF-202	9.1 ^C	--	--	--	113
NPI-2	291 ^A	0.2	7.3 ⁱⁱ	30.1	117	PEDA-PI	78 ^A	0.09	--	--	116
NPI-3	373 ^A	0.29	8.2 ⁱⁱ	33.3	117	PEDA-PI-CL	399 ^A	0.29	6.32 ⁱⁱ	31	116
MPI-1	1454 ^A	1.07	16.8 ⁱⁱ	34.8	102	PEQDA-PI	64 ^A	0.08	--	--	116
MPI-2	814 ^A	0.59	13.8 ⁱⁱ	30.4	102	PEQDA-PI-CL	607 ^A	0.42	9.88 ⁱⁱ	30.4	116
MPI-3	586 ^A	0.31	9.9 ⁱⁱ	31.4	102	TAPOB-HBPI CR	322	0.33	5.5 ⁱⁱ	30.3	165
Tr-PPI	400 ^A	4.33	45 ⁱ	--	122	TAPB-HBPI-CR	385	0.19	1.23 ⁱⁱ	--	123
Td-PPI	2213 ^A	0.63	31 ⁱ	--	122	TAPA-HBPI-CR	497	0.24	1.01 ⁱⁱ	20.2-28.3	123
TPI-1	809 ^A	0.45	10.78 ⁱⁱ	34.4	38	TAPM-HBPI-CR	492	0.25	1.22 ⁱⁱ	--	123
TPI-2	796 ^A	0.4	10.78 ⁱⁱ	31.4	38	STPI-1	4 ^A	0.16	7 ⁱⁱ	31	124
TPI-3	40 ^A	--	2.99 ⁱⁱ	32.3	38	STPI-2	541 ^A	0.32	14 ⁱⁱ	36	124
TPI-4	245 ^A	0.22	8.1 ⁱⁱ	33.6	38	STPI-3	378 ^A	0.34	10 ⁱⁱ	28	124
TPI-5	201 ^A	0.18	6.9 ⁱⁱ	30	38	PI-COF-4	2403 ^C	--	--	--	47
TPI-6	510 ^A	0.31	9.6 ⁱⁱ	29.2	38	PI-COF-5	187 ^C	--	--	--	47
TPI-7	<10 ^A	--	7.9 ⁱⁱ	32.4	38	MMPI	530 ^A	0.394	--	--	129
PI-1	660 ^A	0.6	7.3 ⁱⁱ	--	166	MPI-6FA	781 ^A	0.53	13.5 ⁱⁱ	--	130
PI-2	265 ^A	0.27	2.7 ⁱⁱ	--	166	API-6FA	752 ^A	0.61	12.4 ⁱⁱ	--	130
PI-3	366 ^A	0.76	6.0 ⁱⁱ	--	166	MPI-BPA	677 ^A	0.53	11.1 ⁱⁱ	--	130
BIBDZ	177 ^A	--	11.33 ⁱ	--	167	MPI--BTA	490 ^A	0.39	10.4 ⁱⁱ	--	130
NIBDZ	118 ^A	--	14.56 ⁱ	--	167	PPI-1	474 ^A	--	--	--	3
PIBDZ	75.35 ^A	--	11.85 ⁱ	--	167	PPI-1-NH2	206 ^A	--	--	--	3
PPBPI-1-CR	682 ^A	0.429	8.8 ⁱⁱ	25.1	101	PPI-2	604 ^A	--	--	--	3
PPBPI-2-CR	693 ^A	0.457	7.3 ⁱⁱ	30.1	101	PPI-2-NH2	274 ^A	--	--	--	3
PPBPI-PM-CR	628 ^A	0.379	10.25 ⁱⁱ	22.2	132	PI-ADPM	868	0.37	14.6 ⁱⁱ	34.4	138
PPBPI-BP-CR	582 ^A	0.573	7.92 ⁱⁱ	24.7	132	PI-ADNT	774	0.415	15 ⁱⁱ	35.2	140
PPBPI-NT-CR	415 ^A	0.425	5.89 ⁱⁱ	19.7	132	PI-NO2-1	286	0.155	17.7 ⁱⁱ	43.3	140
PPBPI-PTC-CR	115 ^A	0.838	2.94 ⁱⁱ	29.6	132	PI-NO2-2	57	0.08	10 ⁱⁱ	37.9	140
PPBPI-H-CR	733 ^A	0.532	9.94 ⁱⁱ	24.5	105	PI-NO2-3	26	0.03	8.6 ⁱⁱ	37.9	140
PPBPI-Mn-CR	144 ^A	0.124	6.33 ⁱⁱ	29.2	105	TF-PI	66	0.22	--	31.9-32	141
PPBPI-Fe-CR	172 ^A	0.135	5.63 ⁱⁱ	31	105	TF-PI-CL	727	0.44	10 ⁱⁱ	--	141
PPBPI-PA-CR	1.8 ^A	0.001	6.02 ⁱⁱ	34.8	134	6FA-PI	67	0.29	--	--	141
PPBPI-PEPA CR	373 ^A	0.267	8.84 ⁱⁱ	27.5	134	6FA-PI-CL	635	0.37	7.28 ⁱⁱ	--	141
PPBPI-PENA CR	633 ^A	0.858	10.43 ⁱⁱ	22.6	134	TF-6FDA-PI	154	0.29	--	--	141
PI-COF-1	1027 ^C	--	--	--	93	TF-6FDA-PI-CL	472	0.33	6.63 ⁱⁱ	--	141
PI-COF-2	1297 ^C	--	--	--	93	PEQDA-HBPI	138	0.79	--	--	142
PI-COF-3	2346 ^C	--	--	--	93	PEQDA-HBPI-CL	339 ^A	0.26	9.82 ⁱⁱ	32.8	142
PI-1	19 ^A	0.043	3 ⁱⁱ	--	162	PEPHQDA-HBPI	155	0.6	--	--	142

PI-2	16 ^A	--	0.9 ⁱⁱ	--	162	PEPHQDA-HBPI-CL	593 ^A	0.35	10.1 ⁱⁱ	32.9	142
PI-opt	--	0.084	5.8 ⁱⁱ	--	162	PI-1	1407 ^A	0.78	--	5.3	145
PI-1-C	13 ^A	0.125	10.3 ⁱⁱ	--	162	PI-2	732 ^A	0.51	--	7	145
PI-opt-C	181 ^A	0.177	15 ⁱⁱ	--	162	PIA/6FDA-50	607	4.34	--	--	146
TAPB PTCDA COF	460 ^C	--	--	--	143	PIA/6FDA-40	604	2.9	--	--	146
TAPB PMDA COF	1250 ^C	--	--	--	143	PIA/6FDA-30	594	2.59	--	--	146
TT-PMDA-COF	706 ^C	--	--	--	143	PIA/6FDA-20	577	2.87	--	--	146
TAPA-PMDA-COF	1592 ^C	--	--	--	143	PIA/6FDA-10	463	1.41	--	--	146
PI – 0%6FAPB	327 ^{gel}	2.69	--	--	159	PIA/6FDA-0	441	1.86	--	--	146
PI – 25%6FAPB	346 ^{gel}	2.43	--	--	159	sPI-A-H	25 ^A	0.02	12 ⁱⁱ	31.7	147
PI – 37.5%6FAPB	368 ^{gel}	2.28	--	--	159	sPI-M-H	492 ^A	0.27	13.24 ⁱⁱ	34	147
PI – 50%6FAPB	402 ^{gel}	2.77	--	--	159	sPI-A-B	620 ^A	0.46	10.69 ⁱⁱ	32.5	147
PPI-1	18 ^A	0.038	--	--	102	sPI-M-B	618 ^A	0.47	11.48 ⁱⁱ	34.3	147
PPI-2	604 ^A	0.285	--	--	102	MPI	1001	0.68	12 ⁱⁱ	32.8	149
PPI-3	707 ^C	1	--	--	102	MPI-S	448	0.31	6.9 ⁱⁱ	36.3	149
CH ₃ -PI	20 ^A	0.09	--	--	148	MPI-Ag	103	0.1	6.4 ⁱⁱ	37.1	149
CH ₃ -PI-CL	33 ^A	0.05	7.3 ⁱⁱ	31.3	148	TAPB-HBPI-CR	385	0.19	1.56 ⁱⁱ	28.6-30.0	123
CF ₃ -PI	21 ^A	0.05	--	--	148	TAPA-HBP-CR	497	0.24	1.68 ⁱⁱ	--	123
CF ₃ -PI-CL	575 ^A	0.43	9.4 ⁱⁱ	33	148	TAPM-HBPI-CR	492	0.25	2.04 ⁱⁱ	--	123
TAPA-HBPI	123 ^A	0.34	--	--	100	PBDM*	954	0.79	13	--	108
TAPA-HBPI-CL	43 ^A	0.045	7.47 ⁱⁱ	27.4	100	PBMP*	1025	0.87	--	--	108
CF ₃ TAPA-HBPI	88 ^A	0.23	--	--	100	PPDM*	930	1.36	--	--	108
CF ₃ TAPA-HBPI-CL	294 ^A	0.2	8.56 ⁱⁱ	32.3	100	MPI-0-10	300	--	--	--	160
NT-COF	1276 ^C	1.23	--	--	153	MPI-30-10	302	--	--	--	160
PI-COF	894 ^C	0.47	--	--	154	MPI-40-10	303	--	--	--	160
PIA	580 ^C	--	10 ⁱⁱ	--	155	MPI-50-10	276	--	--	--	160
PIB	760 ^C	--	12 ⁱⁱ	--	155	MPI-60-10	258	--	--	--	160
PIC	990 ^C	--	11 ⁱⁱ	--	155	MPI-70-10	250	--	--	--	160
PID	1430 ^C	--	13 ⁱⁱ	--	155	MPI-100-10	251	--	--	--	160
PAF-110	910 ^C	0.59	--	--	151	MPI-60-5	--	--	--	--	160
NDI-COF	1138 ^C	0.77	--	--	156	MPI-60-7	202	--	--	--	160
PPPP-1	295 ^C	--	--	--	152	MPI-60-9	226	--	--	--	160
PPPP-2	301 ^C	--	--	--	152	MPI-60-11	262	--	--	--	160
TP-COF	960 ^C	--	--	--	157	MPI-60-13	281	--	--	--	160
CPI	65	--	--	--	158						

Surface area and pore size can also be tuned by the varying the length and size of the monomer linkers and cores. Rao et al.¹²² reported two pPIs consisting of either tetra-amine **C1** (tetrahedral) or tri-amine **B3** (trigonal pyramidal), but with a longer anhydride linker **L5** (when compared with NPI-1–3 synthesised by Li et al.^{102,117}). The surface areas were 2213 m² g⁻¹ (**C1** tetrahedral) and 400 m² g⁻¹ (**B3** trigonal pyramidal), respectively, which were higher than pPIs synthesised with the shorter dianhydride **L4** linker with the same core (see **Table 1.3**).¹¹⁷ Analogously, Fang et al.⁹³ showed that increases in the core size increased the surface area. The condensation of the dianhydride linker **L3** with either **B10** or **B11** (larger core than **B3**) resulted in a doubling of surface area from 1297 m² g⁻¹ to

2346 m² g⁻¹ when the core length was increased to contain an extra benzene moiety. The average pore size also increased from 37 Å to 53 Å with this extended architecture (**Table 1.3**).

1.5.2.2.2. Post-synthesis modification

To ensure the full range of post-synthesis modification strategies are covered, we have included carbonisation, post-polymerisation crosslinking and post-polymerisation chemical functionalisation under the heading of post-synthesis modification. Here we expand on the effects and general trends seen in these three subsections.

A. Carbonisation:

It is important to note that uncontrolled post-polymerisation crosslinking in the form of carbonisation is reported to increase the surface area of most conjugated porous networks. Despite this general observation, the pPIs reported in this chapter have largely not been investigated in regard to the effects of carbonisation on surface area. In the specific case of pPIs we have found that only Liao et al.¹⁶² investigated this effect, with an increase from 19 m² g⁻¹ to 181 m² g⁻¹ after carbonisation of pPI synthesised from **B1** and **L5**. Wu et al.¹³⁶ also used carbonisation to crosslink linear PIs (from **L7** and **A6**) to form pPIs, which were blended, in the linear form (pre-carbonisation), with zeolite imidazolate frameworks (ZIF). However, the surface area decreased significantly after carbonisation (from 200–300 m² g⁻¹ to 10 m² g⁻¹); the reasons behind this decrease were not investigated.

B. Post-polymerisation crosslinking:

Surface areas can be further tuned via controlled post-polymerisation crosslinking. Shi et al.¹⁰⁵ synthesised porphyrin-based pPIs (based on amine **C7**) with a cross-linkable alkynyl group present in the starting anhydride monomer **L19**. The surface area of the pPIs after crosslinking (without metal absorption) were 733 m² g⁻¹, significantly higher than the non-crosslinked pPI (167 m² g⁻¹ see **Table 1.3**). Another study by Wang et al.¹¹⁶ used an amine monomer **A15** bearing a cross-linkable ethynyl group in combination with non-cross-linkable **L17** and cross-linkable alkene-containing **L18** dianhydride, respectively. The surface areas of the pPIs from the non-cross-linkable dianhydride was 78 m² g⁻¹ whilst that using the cross-linkable group was 64 m² g⁻¹. After thermal crosslinking, the surface area increased to 399 m² g⁻¹ and 604 m² g⁻¹, respectively. The increase in surface area was attributed to the crosslinking restricting movement (and hence restricting denser packing) of polymer chains.

C. Post polymerisation chemical functional modification:

Rangel et al.³ utilised dianhydride linker **L3** and triamine **B10** or tetraamine **C1** to synthesize PPI-1 and PPI-2, respectively. PPI-1 and PPI-2 were then functionalised with additional amino groups (via nitration and subsequent reduction), which resulted in a decrease of surface areas from 570 to 405 $\text{m}^2 \text{g}^{-1}$ and 540 to 410 $\text{m}^2 \text{g}^{-1}$, respectively. Shi et al.¹⁰⁵ also reported that the metalloporphyrin-based pPIs (from monomers **C7** and **C8**) have lower surface areas than the materials prepared from metal-free cores. The incorporation of metal ions increased the unit mass and blocked the micropores of the polyimide skeleton, leading to a decrease in their surface area from 733 $\text{m}^2 \text{g}^{-1}$ to 144 $\text{m}^2 \text{g}^{-1}$ for Mn and 172 $\text{m}^2 \text{g}^{-1}$ for Fe, respectively. It is noteworthy that these values were obtained via post-polymerisation crosslinking; the surface areas compared with the non-crosslinked pPIs were higher by a factor of 10). Yan et al.¹⁴⁹ also reported that the post-polymerisation chemical modification of pPI MPI (formed from **C1** and **L3**) decreased the surface area from 1001 $\text{m}^2 \text{g}^{-1}$ to 448 $\text{m}^2 \text{g}^{-1}$ after sulfonation (MPI-S), and further to 103 $\text{m}^2 \text{g}^{-1}$, after forming a silver–pPI ionically bound complex (MPI-Ag).

1.5.2.2.3. Amorphous vs. crystalline

The expected trend is that crystalline (COF) porous pPIs will have higher surface areas than their amorphous counterparts (for a comprehensive review on crystalline polyimides see Zhang et al.⁹⁹), and is indeed apparent in the highest surface area reported for the crystalline pPI synthesised by Fang et al.⁹³ at 2403 $\text{m}^2 \text{g}^{-1}$. This trend is observed where similar pPIs were synthesised with either amorphous or crystalline properties, with the crystalline materials having higher surface areas owing to an increase in uniformity of the pores (see **Table 1.3**). Specifically, this trend is demonstrated in the pPIs synthesised using **B3** and **L3** by Fang et al.⁹³ in 2014 (1027 $\text{m}^2 \text{g}^{-1}$) and Maschita et al.¹⁴³ in 2020 (1592 $\text{m}^2 \text{g}^{-1}$). Crystalline pPIs (in this case, COFs) were produced, yet a similar synthesis by Li et al.¹⁶⁸ in 2013 produced the analogous amorphous pPI with a reduced surface area (814 $\text{m}^2 \text{g}^{-1}$). Furthermore, studies by Jiang et al.¹⁵¹, Lv et al.¹⁵³ and Jagt et al.¹⁵⁵ to form crystalline pPIs from **B3** and **L4** give surface areas of 910 $\text{m}^2 \text{g}^{-1}$, 1276 $\text{m}^2 \text{g}^{-1}$, and 1430 $\text{m}^2 \text{g}^{-1}$, respectively, in comparison with a surface area of 291 $\text{m}^2 \text{g}^{-1}$ found for its amorphous counterpart NPI-2 (Li et al.¹¹⁷). Manipulation of the crystallinity of porous pPIs via synthetic condition variations is clearly demonstrated in pPIs synthesised by Fang et al.⁹³ and Maschita et al.¹⁴³ It was found that ionothermally synthesised pPIs demonstrated higher crystallinity and therefore higher surface areas than the solvothermally synthesised analogous counterparts (with lower crystallinity) in these two studies. The trend of higher surface area of PI-COFs over amorphous pPIs was also observed by Fang et al.,⁴⁷ Li et al.,¹⁶⁸ and Wang

et al.,¹¹⁶ each synthesising pPIs with **L3** and **C1**. They found surface areas of up to 1876 m² g⁻¹ for crystalline materials, with amorphous materials (from the same starting materials) possessing lower surface areas of up to 1407 m² g⁻¹.

Outliers to the trend are found for the pPIs synthesised from **L3** and **B1** by Wang et al.,^{111,113} where the surface area of the amorphous analogue was significantly higher (by a factor of over 70) than that of the crystalline counterpart (i.e., 635 vs 9 m² g⁻¹). Although it is not immediately obvious why higher surface areas were obtained for the amorphous pPI, one of the factors that could contribute to lower surface area for COFs could be the chosen synthesis conditions; specifically, the COF pPI was synthesised by direct heating without any solvent, resulting in potential uncontrolled polymerisation, whereas the amorphous pPI was synthesised in solution (that that might have led to the a higher degree of control in regard to surface area, but less order). A further similar example was presented by Luo et al.¹⁶⁶ with **L4** and **B1** as starting materials, where the surface area of amorphous materials were higher than that of the crystalline COF analogue synthesised by Wang et al.¹¹³ However, it is noteworthy that these were the only two cases found where amorphous pPIs possessed higher surface areas than their COF counterparts.

1.5.2.3. Energy storage capabilities and related properties

Polymers with an extended π -conjugated backbone and high surface area with excellent microporosity (with an average pore size of < 2 nm) are advantageous for electrical energy storage applications.² Conjugation is beneficial with respect to both electrochemical stability and electronic conductivity.¹⁶³ It is to be noted that we are only considering conjugated pPI networks in this section owing to their attractive electronic properties. The electronic properties of non-conjugated pPIs are explored in two recent publications by Tian et al.,¹⁴⁴ and Gao et al.,¹²⁶ highlighting attempts to increase conductivity focusing on increasing pPI conjugation, or via addition of conjugated additives.

Batteries and capacitors, as the most common energy storage devices, operate via electric double layer capacitance and pseudo-capacitance mechanisms. In electric double layer capacitance (EDLC), energy is stored and released by a physical ion adsorption-desorption mechanism at the electrode–electrolyte interface.¹⁶⁹ The EDLC depends on the pore size and surface area of the materials, as well as the electrical conductivity of the electrode.¹⁷⁰ Therefore, high surface areas are crucial for larger numbers of ions or charge accumulation at the electrode-electrolyte interface, i.e., the higher the specific surface area or the micropore volume of the materials the higher the capacitance value (although this relationship is not actively explored in the literature).¹⁷¹ Pseudo-capacitive mechanisms depend on charge storage involving fast surface redox reactions, which consist mainly of surface

electron transfer by the intercalation or adsorption of charge-compensating ions.^{172,173} Therefore, high surface areas as well as redox-active moieties (e.g., carbonyl compounds) are desirable to benefit pseudo-capacitive mechanisms.

The key advantages of porous pPIs are their tuneable molecular structure, e.g. redox-active groups can be introduced within the backbone, allowing manipulation of beneficial properties for electrochemical applications.^{2,49} Highly crosslinked porous pPI networks possess the above properties and create active sites for charge or ions to be stored within the porous surface. In addition, pPIs (as part of the broader class of porous organic polymers) are presented as environmentally friendly, low safety risk (with respect to toxicity) and low-cost electrodes when compared with metal-containing electrode counterparts.¹⁶⁴ Specifically, the major advantage is the presence of carbonyl groups in the polyimide framework structure, which provides redox stability and multi-electron transfer capabilities (see **Figure 1.13**).^{163,164}

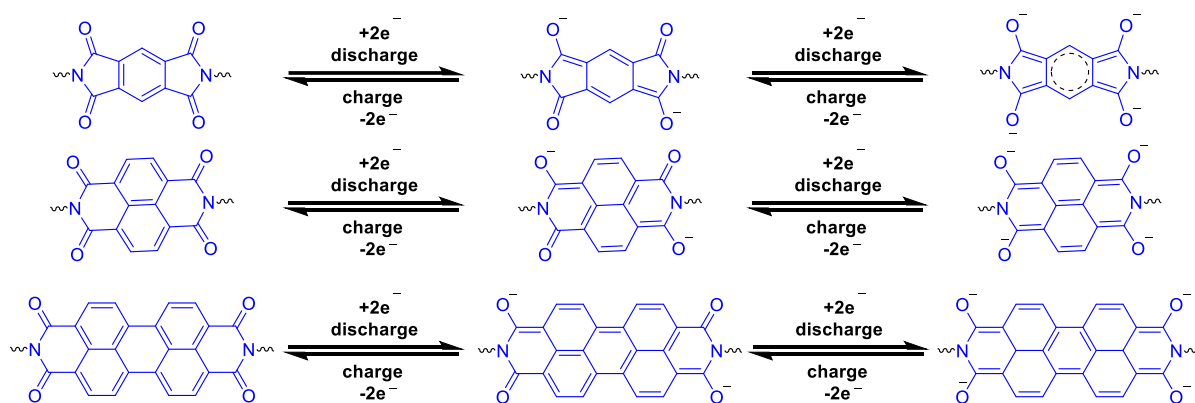


Figure 1.13: Various oxidation states of common anhydride linkers **L3–5**.¹⁶⁴

One major drawback for using porous organic polymers (POPs) as electrode materials is poor bulk conductivity, limiting their effectiveness in electrochemical applications.¹⁷¹ To overcome this challenge, materials can be carbonised, or conductive additives incorporated into the bulk (e.g. carbon nanotubes, graphene or reduced graphene oxide).^{126,157,171,174} pPIs containing aromatic linkers **L3–5** have demonstrated semiconductive properties without the need for additives; however, they can only transfer two electrons in the reversible charge/discharge process as shown in **Figure 1.13**.¹⁶⁴ In an initial study Song et al. employed non-crosslinked linear PIs for redox-active systems (from anhydrides **L3–4** and various diamines). However, dissolution in the electrolyte during cycling resulted in inefficiency as well as degradation of the PI.^{175,176} To overcome this practical problem, Tian et al.¹⁶⁴ utilised triamine **B10** with anhydrides **L3–5** to form crosslinked pPIs as electrode materials (cathodes)

for Li-ions batteries (LIBs). The highly crosslinked networks were able to sustain harsh chemical and thermal environments without degradation or dissolution. These naphthalene- and perylene-based pPIs utilise carbonyl groups within the structure to effectively conjugate with the aromatic rings as well as ionically bonding to Li-ions. The aromatic carbonyl-derived pPIs show high capacity and high cycling stabilities, with those incorporating the perylene linker **L5** giving the best electrochemical performance, around 74% retention of discharge capacity (57.9 mA h g^{-1}) after 65 cycles. A further approach is detailed by Lv et al.¹⁵³ utilizing **B3** and **L4** to form cathodes that are able to exhibit intramolecular charge transfer with lithium anodes to form solar-to-electrochemical energy storage and conversion devices. Finally, Zhao et al.¹⁵⁷ reported atomic-layer modification of pPI COFs used as a cathode material for LIBs. They used a mechanical exfoliation method to create atomic-layered or nano-sheet pPIs (thickness c.a. 2.6 nm) to improve the electrochemical performance (with respect to the bulk material). The dual active site modified atomic-layered pPIs shows initial capacity of 110 mA h g^{-1} (unmodified pPI 25 mA h g^{-1}) with 87.3% retention after 500 cycles.

Li et al.¹⁶³ reported polycondensation of melamine (**B1**) with the benzene (**L3**) and naphthalene (**L4**) linkers to generate pPIs for anode materials for Na ion batteries. When compared to graphitic carbon (used as anodic materials in both Na and Li-ion batteries),¹⁷⁷ these pPI networks facilitate higher mobility of the larger sized Na-ions (owing to increased pore size relative to graphitic carbon). These materials thus performed more effectively as anodes, possessing more reactive sites for electrode-electrolyte interactions and ion transport during the reversible sodiation/desodiation processes. Furthermore, the randomly arranged conjugated systems and larger conjugated units provided higher stability and conductivity than the graphitic carbon. The discharge capacity of PI-1 (using linker **L4**) and PI-2 (using linker **L3**) are 330.8 and $137.02 \text{ mA h g}^{-1}$, respectively, at 100 mA g^{-1} after 20 cycles, when compared with the discharge capacity of graphitic carbon at 31 mA h g^{-1} (see **Figure 1.14**). The higher redox activity and conductivity of PI-1 can be attributed to the higher electron affinity values and the ionisation potential and lower HOMO-LUMO gap as compared to PI-2 (**L3** linker). Effectively, PI-1 is more conjugated than PI-2. The long-term stability of PI-1 and PI-2 are shown in **Figure 1.14**, with minimal capacity degeneration (c.a. 10% for PI-1) even after 1000 cycles.

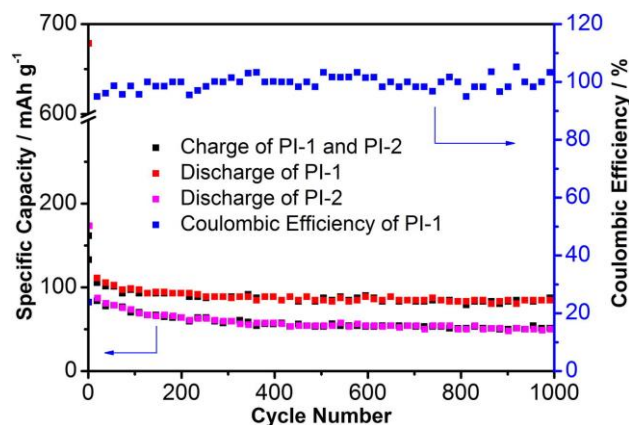


Figure 1.14: Long-term cycling performance of PI-1 (**B1** and **L4**) and PI-2 (**B1** and **L3**) at 5 A g^{-1} .¹⁶³

Roy et al.¹⁶⁷ condensed dicarboxylic acids **M1–3** (containing diimides) with tetra-amines **C5–6** to form polybenzimidazole rings within pPI networks for use as electrode materials for energy storage applications. The incorporation of the polybenzimidazole units (present in **M1–3**) in the pPIs provides dynamic dipolar interactions between the electrolyte cations ($1\text{M H}_3\text{PO}_4$) and the pPI pore walls, facilitating proton storage on the pore walls during the charge-discharge process. In addition, the extended π -conjugation and presence of heteroatoms throughout the pPI networks provide conductivity and enhance the redox activity of the network. The specific capacitance of networks formed from the tetraamine core **C4** and linker **L3** (BIBDZ), **L4** (NIBDZ) and **L5** (PIBDZ) were 88.4 , 66.56 and 5.65 F g^{-1} , respectively, at 5 A g^{-1} . The higher capacitance value of **L3** was attributed to the higher surface area (accommodating larger number of interactions between the electrode–electrolyte interface, assisting EDLC) when compared to **L4** and **L5**, overriding the increased units available for π -conjugation of the other pPIs. Most recently, Royuela et al.¹⁵⁶ reported a crystalline pPI NDI-COF (synthesised from **L4** and **B10**), as an electrocatalyst in the oxygen reduction reaction (ORR). The majority of known ORR catalysts rely on containing metals within their structure, or pyrolysis or addition of conductive materials to achieve conductivity.^{178–180} The NDI-COF for ORR represents one of the first metal-free catalysts in this field that doesn't rely upon pyrolysis or additives. Owing to the increased electroactive area of the NDI-COF vs the bare glassy carbon electrode, the capacitance current increases upon addition of the pPI, as shown by cyclic voltammetry. It is noteworthy that pPI networks are largely unexplored in the field of electrocatalysis and electrocatalytic behaviour.

1.5.3. Applications

1.5.3.1. Gas storage and separation

The high surface areas, high stabilities preventing degradation (as discussed in the previous section), alongside their synthetic simplicity and tunability (including starting materials, chemical make-up, porosity), make pPIs attractive candidates for gas capture in harsh environments. The literature focuses on CO₂, H₂, C₆H₆, CH₄ and CH₃OH (water is considered in a separate section in this Chapter, see **Section 1.5.3.1.2**), and are discussed below:

1.5.3.1.1. Carbon dioxide (CO₂) capture and storage

Crosslinked pPI 3D networks have been widely used for the adsorption and storage of various gases. Porous polyimides are promising for CO₂ capture owing to their compatible pore size with the kinetic diameter of CO₂ (0.33 nm), easy tuneable chemical functionality and ability to combine different properties. The reported CO₂ uptake by pPIs is summarised in **Table 1.3**.

The major factors responsible for high CO₂ uptakes in pPIs are not (solely) reliant on high specific surface areas; for example, the pPIs synthesised by Rao et al.¹²² possess a surface area of 2213 m² g⁻¹ (Td-PPI, synthesised from **C1** and **L5**) and CO₂ uptake of 31 wt% , while Tr-PPI, synthesised from **B3** and **L5**, has as surface are of 400 m² g⁻¹ and uptake of 45 wt% (both measured at 195 K and 1 bar). Direct comparison of the reported pPIs surface areas with CO₂ uptake efficiency is challenging, as the conditions for CO₂ uptake vary greatly between each experiment with little standardisation evident across the studies surveyed in this chapter. For example, the pPIs synthesised by Roy et al.¹⁶⁷ (NIBDZ from **C6** and the dianhydride **M2**) has a low surface area (118 m² g⁻¹) but fair CO₂ uptake (14.56 wt%). In contrast, the pPIs synthesised by Li et al.¹⁶⁸ has far higher surface areas, by a factor of up to 10 (e.g. MPI-1, 1454 m² g⁻¹ synthesised from **C1** and **L3**) but this significant increase is not reflected in an increase in CO₂ uptake, with similar values of 10–16 wt% CO₂ uptake. However, NIBDZ measurements were recorded at a far lower temperature (195 K) than that of MPI-1 (273 K), highlighting the discrepancies mentioned previously.¹⁶⁸

More important than high surface areas are pPIs with high specific surface areas that contain high concentrations of micropores (< 2 nm) or ultramicropores (< 0.7 nm), and ideally without high mesopore (2–50 nm) volumes that will absorb competitive gas species and potentially block the pores.¹⁸¹ The smaller volumes are more compatible with the kinetic diameter of CO₂. As an example, Lou et al.¹⁶⁶ synthesised PI1-3 with mesoporous volumes and poorer CO₂ uptakes (7.3 wt% for 660 m²

g^{-1} surface area), whereas pPIs with similar surface areas (e.g. Shi et al.¹³⁴ PPBPI-PENA-CR, $633 \text{ m}^2 \text{ g}^{-1}$) but with higher overall pore volume and microporous volume exhibited higher CO_2 uptake (10.43 wt%). A further example is found in the linear based PIs from **L7** and **A6** by Wu et al.¹³⁶ Once formed and carbonised with ZIF aerogels the composites formed structures with pore sizes matching that of the kinetic diameter of CO_2 , giving an increased CO_2 capture capacity of 9.81 wt% at 298 K when compared to non-carbonised, though overall still low (however these linear polymers and the effect of ZIF on CO_2 uptake are not investigated individually in this paper). It is important to note that if the pPIs have only ultramicropores ($< 0.7 \text{ nm}$), the CO_2 present may block the pores and so stop further uptake of CO_2 .¹⁸¹

The isosteric heat of adsorption (Q_{st}) provides a general measure of the interactions of gases and porous structures, measuring the heat produced when a gaseous molecule is physisorbed onto the polymeric surface. Higher Q_{st} means stronger interactions and higher absorbance values, though values over 50 kJ mol^{-1} typically indicate chemisorption.^{182,183} Specifically, the interaction of CO_2 and the pore walls in CO_2 -pPI gas uptake studies is of interest here (see **Table 1.3**). The strength of the interactions can be tuned in pPIs via chemical modification of the starting monomers. As an example, NPI-3 (**B10** and **L4**) synthesised by Li et al.¹¹⁷ has similar CO_2 uptake to NPI-1 (**C1** and **L4**) as it has similar Q_{st} , despite having far lower surface area (see **Table 1.3**). A method of affecting the heat of absorption, as a gauge of the strength of CO_2 interactions with the pore walls, is found by the incorporation of heteroatoms or polar groups into the pPIs. Incorporation of heteroatoms and polar groups affects the interactions between the CO_2 and the pore wall via dipole-quadrupole interactions, H-bonding or Lewis acid-base interactions. As an example, the pPI Tr-PPI (**B3** triamine) synthesised by Rao et al.¹²² has a higher N content per repeat unit than the Td-PPI (**C1** tetraamine) and therefore, despite having a far lower surface area, has a higher CO_2 uptake of 45 wt% vs 31 wt% (please note: both these measurements were performed at 195 K and 1 bar).

It is noted that pPIs synthesised by Hossain et al.¹²⁸ from **A5** and **L12** and crosslinked with PEG units are not examined in regard to surface area or CO_2 uptake, but showed promise in CO_2 -selective permeability.

1.5.3.1.2. Uptake of other compounds (gas and vapor)

In addition to CO₂, the uptake of several other volatile organic gas species by pPI crosslinked networks are reported in **Tables 1.4** and **1.5**. The most common of these are hydrogen (H₂), water (H₂O), methane (CH₄), benzene (C₆H₆), and a range of other aliphatic and cycloalkanes and alkenes.

The efficient absorbance and storage of hydrogen gas is important for future fuel applications and a move to net zero emissions.^{184–186} The pPIs reported in **Table 1.4** show hydrogen gas uptake of up to 3 wt% at 77 K and 1 bar, which is low when compared with the published data from high performing MOFs (e.g. Furukawa et al.'s MOF-210, 17.6 wt% at 77 K and 80 bar, although these frameworks rely on potentially scarce metal centres, e.g. zinc).^{187–189} With respect to pPIs, the best uptake was demonstrated by Wang et al.¹⁴⁵ with the tetrahedral core **C1** and dianhydrides **L3** (PI-1) and **L4** (PI-2). These two pPIs possess large surface areas (1407 m² g⁻¹ and 732 m² g⁻¹, respectively) with a higher ultramicroporous pore volume. These ultramicropores are compatible in size with the kinetic diameter of hydrogen (of 0.29 nm), which facilitates increased hydrogen uptake. The authors found that increased π -electron delocalisation groups present in the aromatic linker **L4** (when compared to **L3**) aided Q_{st} values at a range of hydrogen wt% uptakes (0.5–1 wt%) and hence overall hydrogen uptake. Despite the importance of H₂ uptake and storage this remains a largely unexplored area of application for pPIs.

Table 1.4: Gas uptakes from reported pPIs where H₂ = hydrogen, H₂O = water vapor, CH₄ = methane C₆H₆ = benzene, C₆H₁₂ = cyclohexane, A = amorphous; C = crystalline; i = at 77 K, 1 bar; ii = at 195 K, 1 bar; iii = at 273 K, 1 bar, iv = 298 K, 1 bar, v = 77 K, 30 bar, * wt % values were converted for the purpose of this review from published isotherms using the conversion formula wt % = (mmol g⁻¹ * 100 * mol. weight) / 1000 where mmol g⁻¹ = (cm³ g⁻¹) / 22.414 cm³ mmol⁻¹.

Name in Paper	H ₂ (wt%)	H ₂ O (wt%)	CH ₄ (wt%)	C ₆ H ₆ (wt%)	C ₆ H ₁₂ (wt%)	Ref.
NPI-1	--	14.1 ^{iv}	1.35 ⁱⁱⁱ	90.5 ^{iv}	58.1 ^{iv}	117
NPI-2	--	9.5 ^{iv}	0.78 ⁱⁱⁱ	41.5 ^{iv}	17.9 ^{iv}	117
NPI-3	--	10.2 ^{iv}	1.07 ⁱⁱⁱ	59.9 ^{iv}	37.4 ^{iv}	117
MPI-1	--	16.7 ^{iv}	--	119.8 ^{iv}	54.1 ^{iv}	168
MPI-2	--	9.9 ^{iv}	--	76.6 ^{iv}	44.8 ^{iv}	168
MPI-3	--	9.6 ^{iv}	--	54.9 ^{iv}	41.5 ^{iv}	168
PI-1	0.66 ⁱ	--	--	--	--	166
PI-2	0.23	--	--	--	--	166
PI-3	0.58	--	--	--	--	166
BIBDZ	0.75 ^{i*}	--	0.79 ^{iv*}	--	--	167
PPBPI-1-Cr	--	--	1 ^{iii*}	--	--	101

PPBPI-2-CR	--	--	1 ^{iii*}	--	--	101
PPBPI-H-CR	--	--	0.62 ^{iii*}	--	--	105
PPBPI_Fe-CR	--	--	0.24	--	--	105
PPBPI-Mn-CR	--	--	0.37	--	--	105
PPBPI-PA-CR	--	NA	0.6 ^{iii*}	--	--	134
PPBPI-PEPA-CR	--	NA	1.1	--	--	134
PPBPI-PENA-CR	--	19.27 ^{iv*}	1.1	--	--	134
PI-1	0.7 ^{i*}	--	0.5 ^{iii*}	--	--	164
PI-0%6FAPB	--	383.8	--	--	--	159
PI-25%6FAPB	--	12.5	--	--	--	159
PI-37.5%6FAPB	--	9.8	--	--	--	159
PI-50%6FAPB	--	9.5	--	--	--	159
MPI-6FA	--	8.5 ^{iv}	1.42 ^{iv*}	80.9 ^{iv}	44 ^{iv}	130
API-6FA	--	--	1.07	--	--	130
MPI-BTA	--	10.4	1.07	72.8	40.4	130
MPI-BPA	--	13.3	0.78	104.9	60.2	130
PI	1.217 ⁱ	30 ^{iv}	--	99.2 ^{iv}	59.7 ^{iv}	138
PI-1	3.2 ⁱ	--	--	--	--	145
PI-2	2.6	--	--	--	--	145
sPI-A-H	--	--	0.62	--	--	147
sPI_M-H	--	--	0.6	--	--	147
sPI-A-B	--	--	0.56	--	--	147
sPI-m-B	--	--	0.49	--	--	147
MPI	--	--	0.92 ⁱⁱⁱ	--	--	149
MPI-S	--	--	0.59	--	--	149
MPI-Ag	--	--	0.53	--	--	149

Water sorption and harvesting will be an important future application for future proofing water resources, especially in arid environments. The crosslinked conjugated pPIs synthesised by Qiao et al.¹⁵⁹ demonstrate the highest water sorption at 383.8 wt% (**Table 1.4**). This high uptake is attributed to the synthetic conditions employed, forming aerogels from **A6**, **A14** and **L7** owing to the slow reactions at ambient conditions, and slow introduction of crosslinking agent **B8**. However, the exact mechanism of water uptake was not fully explored in this study, leading to interesting avenues for research into future water-harvesting applications of pPIs, potentially fully tuneable by controlling aerogel formation (in addition to controlling chemical content).

High water uptake in other studies are attributed to either the introduction of heteroatoms, especially oxygen-containing linkers such as ester **A6** and ketone **L13** (see Qiao et al.¹⁵⁹ and Li et al.¹³⁰), or a decrease in (hydrophobic) aromaticity of the formed pPI by Shen et al.¹³⁸ Those pPIs synthesised from the hydrophobic monomers **L4** and **L5** show low water uptakes.^{117,130,134} In the case of the materials with the largest water uptake,¹⁵⁹ the introduction of the hydrophobic CF₃-containing monomer **A14**

into the formed pPI aerogels leads to dramatically decreased water absorption capabilities (from 383.8 to 9.5 wt% when the CF₃-containing monomer **A14** content is increased to 50 mol%).

Volatile organic compound (VOC) sorption by pPIs can be separated into two specific focus areas: cyclic (benzene and cyclohexane) and aliphatic hydrocarbon adsorption. In the case of the cyclic hydrocarbons, Li et al.^{48,61,100} synthesised several pPIs based on naphthalene **L4** and pyromellitic (a single benzene ring linker) **L3** anhydrides for successful absorption of cyclic VOCs. With respect to benzene absorption, it was found that the more aromatic the skeleton the higher the benzene absorption (owing to π -interactions). Differences between the individual pPIs in benzene uptake were attributed to differences in surface areas, with lower surface areas leading to lower benzene uptake.¹³⁸ The same pPIs were also used for cyclohexane sorption, though absorbing significantly less (c.a. 40 % lower uptake when compared with benzene) due to the lack of π -interactions.^{117,138,168} The increased absorption of cyclohexane by the pPI synthesised by Shen et al.¹³⁸ from **C4** and **L3** was due to the cycloaliphatic core used – maximizing aliphatic–aliphatic interactions.

Table 1.5: Aliphatic VOC absorption by reported pPIs where A: amorphous; C: crystalline; i: at 77 K, 1 bar; ii: at 195 K, 1 bar; iii: at 273 K, 1 bar, iv: 298 K, 1 bar, v: 77 K, 30 bar.

Name in Paper	C ₂ H ₆ (wt%)	C ₂ H ₄ (wt%)	C ₃ H ₈ (wt%)	C ₃ H ₆ (wt%)	C ₄ H ₁₀ (wt%)	C ₄ H ₈ (wt%)	C ₄ H ₆ (wt%)	Ref
sPI-A-H	4.77 ^{iv}	--	8.8 ^{iv}	11.25 ^{iv}	18.27 ^{iv}	19.82 ^{iv}	25.05 ^{iv}	147
sPI_M-H	4.47 ^{iv}	--	8.44 ^{iv}	10.50 ^{iv}	17.80 ^{iv}	19.60 ^{iv}	25.86 ^{iv}	147
sPI-A-B	3.99 ^{iv}	--	8.05 ^{iv}	9.61 ^{iv}	14.50 ^{iv}	14.95 ^{iv}	19.65 ^{iv}	147
sPI-m-B	3.72 ^{iv}	--	7.61 ^{iv}	9.70 ^{iv}	12.52 ^{iv}	12.99 ^{iv}	18.30 ^{iv}	147
MPI	4.02 ⁱⁱⁱ	4.35 ⁱⁱⁱ	--	--	--	--	--	149
MPI-S	4.16 ⁱⁱⁱ	4.68 ⁱⁱⁱ	--	--	--	--	--	149
MPI-Ag	4.17 ⁱⁱⁱ	4.96 ⁱⁱⁱ	--	--	--	--	--	149
PAF-110	--	4.83 ⁱⁱⁱ	--	--	--	--	--	151

For the case of aliphatic hydrocarbon uptake, methane absorption was reported for a large number of papers (**Table 1.5**); however, the recorded absorbed weight percentages were never higher than 1.42 wt% (Li et al.¹³⁰). This low absorption is theorised to be a result of poor interactions with the pPIs and incompatible kinetic diameters of the CH₄ (0.38 nm) and pPI pore volumes.^{101,105,117,130,132,147,149,164,167} In regards to absorbance of other aliphatic VOCs (alkanes and alkenes), this review only found two papers by Yan et al.^{147,149} that addressed this specific application: a Ag-doped pPI MPI-Ag (from **C1** and **L3**) and its four non-doped pPI counterparts sPI-A-H (**C1** and **L1**), sPI-M-H (**C4** and **L1**), sPI-A-B (**C1** and **L2**) and sPI-M-B (**C4** and **L2**). Interestingly, the pPIs reported were predominantly non-conjugated, which aided interaction with the aliphatic VOCs and their sorption. In

parallel to cyclic VOC (benzene and cyclohexane) sorption studies, the pPIs MPI, MPI-S, and MPI-Ag (from **C1** and **L3**) were able to adsorb unsaturated aliphatic VOCs when Ag was present in the pPI owing to C=C bond and Ag⁺ d-orbital overlap interactions (π -Ag⁺). In contrast, the pPI without Ag⁺ units were better suited to adsorb saturated aliphatic VOCs, although the reasons behind this were not explored in the study. Further studies by Jiang et al.¹⁵¹ show selective adsorption of acetylene from ethylene/acetylene mixtures due to Q_{st} values clearly demonstrating a greater affinity of the material for acetylene (up to 9.0 wt% uptake).

We found several reports of nitrogen sorption, rather than just related to surface area calculations. However, in the majority of cases the level of N₂ gas absorbed was extremely low: in the cases where these values are calculated and reported, or from our own calculations taken from isotherms provided, the values never exceeded 1 wt%, with the majority below 0.2 wt%.

1.5.3.2. Heterogeneous catalysis

Porous organic polymers play an important role in modern catalytic applications.^{45,190} In this context, pPI networks can be applied either by incorporating the active site within the polymeric structure (as pendant group or incorporated into one of the monomers), or by directly exploiting the activity and properties of conjugated pPIs. Nevertheless, application of pPI networks in catalysis has been, thus far, limited to a few examples as discussed below.

In a first application of polyimides in catalysis, Shultz et al.¹⁰⁴ prepared a metalloporphyrin ring functionalised with aromatic moieties (**L20**), two of which bore anhydride functionalities that could be used for the condensation reaction with tetramine **C1**. This reaction generated a polyimide network that was subsequently metalated at the porphyrin rings with iron(II) or manganese(II). The synthesised polyimide performed as recyclable catalyst for the epoxidation of styrene using iodosylbenzene as the oxidant; however, the recyclability was only partially effective as most of the catalytic activity was lost after three reaction cycles. Considering the excellent catalytic activity of Lewis acidic centres in metalloporphyrins for the cycloaddition of CO₂ to epoxides,^{191,192} it is expected that appropriately designed and constructed pPI catalysts would perform well in this reaction;^{193,194} to the best of our knowledge, these promising materials have not yet been explored for this specific application.

A different catalytic application was reported by Chu et al.¹⁰⁹ in the search of organic photocatalysts for hydrogen generation. To this aim, a crystalline pPI network was fabricated from the thermal reaction of melamine (**B1**) and pyromellitic dianhydride (**L3**) at 325 °C. The good crystallinity of the polymer was attributed to the solvent-free, high-temperature synthesis that led to the initial

precipitation of crystals of oligomeric pPI. Whereas the individual monomers were colourless, the produced pPI network displayed a yellow color due to the extended π -conjugation. The pPI displayed attractive optoelectronic properties with a bandgap of 2.7 eV and a spatially separated HOMO (on the melamine moiety) and LUMO (on the pyromellitic moiety), potentially favouring charge separation during photocatalytic processes. The performance of the catalyst in the H_2 evolution reaction (HER) was tested in the presence of methanol as sacrificial reagent and using Pt as co-catalyst under visible light irradiation; 70 mmol of H_2 was produced after 10 h of irradiation. The authors compared the photocatalytic activity of the pPI with that of graphitic carbon nitride ($g\text{-}C_3N_4$) finding that, the two materials displayed similar photocatalytic performance despite the pPI possessing half the surface area of $g\text{-}C_3N_4$. Interestingly, the crystallinity of the pPI was found to play an important role: in a control experiment with a non-crystalline analogue of the pPI no photocatalytic activity was detected. In a subsequent study Chu et al.¹¹⁰ attempted to obtain bandgap modulation and optimize catalytic activity for the pPIs by varying the degree of polymerisation by using different temperatures (in the range from 250–350 °C) during syntheses using the same starting monomers **B1** and **L3** as in the previous example. The increase of the polymerisation temperature above 250 °C had a clear positive effect on crystallinity and on the degree of polymerisation; the UV-Vis optical absorption edge was progressively bathochromically shifted by increasing the polymerisation temperature, with the bandgaps decreasing from 3.39 eV (polymer prepared at 250 °C) to a more application-relevant value of 2.56 eV for the polymer prepared at 350 °C. The latter effect was attributed to achieving stronger orbital overlap by increasing the degree of polymerisation. DFT calculations supported this observation as the bandgap of oligomeric pPIs was found to decrease with chain length.¹⁹⁵ When pPIs produced at different temperatures were tested in hydrogen generation, it was found that the materials produced at intermediate temperatures performed better. Specifically, the material produced at 300 °C was the best catalyst under full arc light whereas that produced at 325 °C was the best photocatalyst under visible light irradiation. This effect was attributed to the balance of several factors contributing to or affecting the photocatalytic activity. Indeed, despite a higher degree of polymerisation, the pPI prepared at the highest temperatures suffered from strong particle aggregation (with consequent decrease of surface area) and decreased redox power. Overall, this investigation highlighted a promising route worthy of further exploration, showing that the reaction conditions, and thus the degree of polymerisation of pPIs, can be used to engineer and modulate the bandgap of polymeric photocatalysts.

Kim et al.¹¹⁵ synthesised pPI networks from the triamine **B10**, anhydride **L3** and the mono amine **D1**, (yielding MPI-Phen), showing catalytic activity in the Suzuki reactions. These pPI networks were synthesised both on and without a melamine sponge support, allowing ease of handling under

catalytic conditions, placing in or removal from reaction vessels, whilst still allowing access to high surface areas ($723 \text{ m}^2 \text{ g}^{-1}$ without the sponge and $524 \text{ m}^2 \text{ g}^{-1}$ on the sponge support). The catalytic activity of the networks was observed upon coordination of Pd(II) ions to the mono amine **D1**, and activity evaluated for the Suzuki coupling reaction between bromobenzene and phenylboronic acid in toluene (and other solvents) at 95°C , to give a maximum yield of 83.3%. The recycling results showed a slight decrease in yields, which could be attributed to the leaching of Pd(II) ions from the network. Zhu et al.¹⁵² reported porphyrin-based pPI networks synthesised from dianhydride **L3** and **L4** with tetraamine porphyrin **C9** monomer (PPPP-1 and PPPP-2, respectively). The major advantage of porphyrin-based pPIs in heterogeneous catalysis applications is found in the large size of the porphyrin linker ($\sim 2 \text{ nm}$), creating large pores inside the framework. Furthermore, catalytically active sites can be modified by binding various metal ions to the porphyrin linker (strong π -metal orbital coupling also enhances the heterogeneous binding of the ions). The authors also loaded the porphyrin-based pPI networks with Pd nanoparticles (to form Pd@PPPP-1 and Pd@PPPP-2 from PPPP-1 and PPPP-2 respectively) to catalyse the Suzuki-Miyaura coupling reaction. Pd@PPPP-1 and Pd@PPPP-2 were utilised to catalyse substituted phenylboronic acid and aryl halides to form C-C bonds with high catalytic activity and product yield greater than 90%. Furthermore, the pPI catalytic networks were recovered and reused 5 times without any loss of catalytic activity of Pd@PPPP-1 and Pd@PPPP-2.

Rangel et al.³ synthesised 2 different pPI networks with triamine **B10** and tetraamine **C1** with dianhydride **L3**, respectively. The networks were nitrated with $\text{HNO}_3/\text{H}_2\text{SO}_4$ and subsequently reduced with SnCl_2 to yield amine-decorated aromatic cores (**B10** or **C1**). These modified networks were then reacted with picolinaldehyde to yield iminopyridine ligands for coordination with palladium (**Figure 1.15**). It is noteworthy that these modifications resulted in a significant decrease in thermal stability of the final network structures (as discussed in **Section 1.5.2.1**). The catalytic activity was monitored using the Suzuki coupling reaction of halobenzenes with various aryl boronic acids; when compared to the palladium ligand only (*i.e.*, not bound to the pPI networks) the pPI was found to yield on average twice the efficiency (calculated from GC and GCMS of the Suzuki coupling reaction). The increase in efficiency is related to the hydrophobicity of the pPI and the products from the coupling, as well as increased surface area for contact. Furthermore, the pPIs' excellent catalytic activity in aqueous media provide very useful greener alternatives to other heterogeneous palladium catalyst systems.

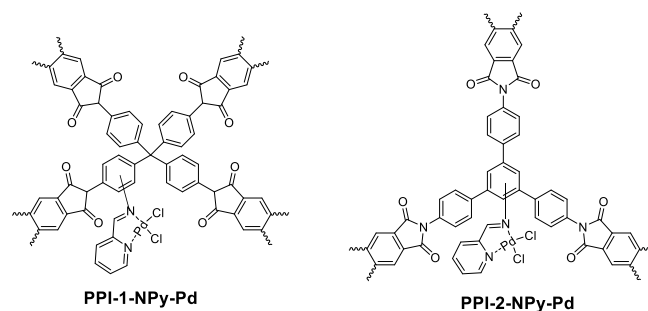


Figure 1.15: Schematic representation of heterogeneous Pd catalysts based on porous polyimide networks from ref.³

1.5.3.3. Drug delivery

There are several documented porous materials that have been utilised in drug delivery applications,^{47,196,197} however pPIs have been largely ignored in this field. One example found was for the pPIs synthesised by Fang et al.⁴⁷ Here the pore sizes (1.0–1.5 nm) of the pPIs were found to be compatible with the commercially available drugs ibuprofen (of similar size, 0.5–1.0 nm), captopril (utilised for the treatment of hypertension and congestive heart failure) and caffeine. Controlled release over a 6-day period was demonstrated, with up to 95% release recorded for ibuprofen. Significant opportunities exist for further exploration of this field of study.

1.5.3.4. Removal of organic pollutants from aqueous environment

Several pPIs have been utilised for the removal of organic small molecules from aqueous systems. Fang et al.⁹³ synthesised pPIs capable of absorbing Rhodamine B (up to 17 wt%, determined by TGA). The dye could be recovered from the networks by washing with methanol. The absorbance of the Rhodamine B excitation peak bound in the network in aqueous environments decreased linearly in dependence of temperature, showing promise for temperature sensing devices; however, the mechanisms behind the quenching were not explored in this study.

Wang et al.¹¹¹ used a pPI synthesised from **B1** and **L3** to investigate the removal of organic pollutants (the dye methyl orange and the antibiotic tetracycline) from aqueous solutions. Removal was monitored by UV/Vis spectroscopy and further investigated with IR spectroscopy to show how the amino groups of the pPI could interact ionically with the sulfonic groups of methyl orange, leading to adsorption. These pPIs absorbed methyl orange and tetracycline at 555.6 and 122.2 mg g⁻¹, respectively, at 298 K from aqueous solutions.

A further good example of the potential of crosslinked pPIs for the removal of undesired species from aqueous systems is found in the study by Simón-Herrero et al.¹¹² Here linear polyimides from **L7** and **A6** with hydrophobic properties were used to separate oil from water (please note: the crosslinked pPI formed via addition of **B3** was not studied in this investigation, despite the potential for separation enhancement). In contrast, Qiao et al.¹⁵⁹ reported on high surface area CF₃-functionalised pPI-based aerogels with high water repulsion for the adsorption of organic species from aqueous systems. The pPI aerogels removed both chloroform and toluene from aqueous mixtures. However, the investigation only reported empirical observations, with no quantification of the performance of the materials presented. Although a range of other CF₃-containing water-repellent pPIs have been synthesised,^{100,101,105,132,134,141,142} they have not been exploited for solvent removal from water.

With respect to metal ion removal from aqueous systems, mention is only made of one study related to the porphyrin-containing materials prepared by Shi et al.^{101,105,132,134} Here iron and manganese binding capabilities were demonstrated but not explored in regards to species removal. Binding studies focused on either blocking or increasing pore sizes and surface areas rather than the removal of metal ions from aqueous systems, leaving this aspect wide open for further exploration.

1.5.3.5. Sensing

Predominantly, sensing studies with pPI materials focus on metal ion sensing in both organic and aqueous systems. Liao et al.¹⁶² utilised pPIs derived from **B1** and **L5** that demonstrate strong yellow-green fluorescence (here a reduction in π - π stacking of the synthesised pPIs hinders self-quenching and hence gives amplified fluorescence) in simple quenching studies. Fluorescence quenching was tested for a range of ions, with only Fe³⁺ eliciting significant quenching (greater than 50%). Wang et al.¹¹³ also employed a melamine-**B1** based pPI (with both **L3** and **L4**) that fluoresced in DMF (as well as other solvents) to detect Fe³⁺ via fluorescence quenching. Here the quenching was attributed to effective energy transfer from the emission level of pPI to the unoccupied d-orbitals of Fe³⁺. Other metals also showed fluorescent enhancement and linear shifts in excitation wavelengths but were not investigated in any further detail in these studies.

Further sensing of heavy metal ions by fluorescence quenching was demonstrated by Xiao et al.,¹⁹⁸ specifically sensing Cr³⁺ ions. It was theorised that the strong binding of Cr³⁺ ions to the triazine nitrogen atoms (**B1**), as well as oxygen atoms from the imide bonds within the pPI framework, led to a reduction in antenna efficiency and hence an increase in quenching of the luminescence.

Beyond heavy metal sensing, Zhang et al.¹⁵⁴ demonstrated a porphyrin (**C7**) and perylenetetracarboxylic dianhydride (**L5**) derived pPI for 2,4,6-trinitrophenol (TNP) detection, an explosive with higher efficacy than its counterpart 2,4,6-trinitrotoluene (TNT), via fluorescence dampening. Interestingly, the pPI shows selectivity for TNP detection over other nitroaromatics, which was tentatively attributed to a reduction in π - π stacking (although not explored in any detail).

1.5.3.6. Functionalised coating

Where crosslinked polyimides can be manipulated into processable materials (either by blending or direct casting) a few examples were found for coating applications. Li et al.¹³¹ synthesised fluorinated crosslinked polyimides for UV screening applications. They showed how films containing the pPI could reduce the photocatalytic degradation of methylene blue (18% degradation over 1 hr compared to above 90% for the control films with no pPI incorporated), whilst still retaining transparency (80% at 800 nm).

Further applications of pPIs as coatings can be found in the work by Qiao et al.,¹⁵⁹ who prepared fluorinated pPIs as water-repellent coatings. They found that increasing the content of the CF₃-functionalised monomers of the pPI from 0 to 50 wt% increased the water contact angle from 87.7° to 112.1°, allowing optimisation of water repulsion.

Finally, it is noted that the majority of publications do not investigate the chemical stability of pPIs in great detail. One example of stability investigations can be found in Jagts et al.¹⁵⁵, submerging pPIs PIC and PID (see **Table 1.1**) for 14 days in organic (1 M NaClO₄ in ethylene carbonate (EC)/dimethylcarbonate (DMC)) and aqueous (1 M Na₂SO₄ in neutral water) electrolytes, both of which are representative electrolytes used in energy storage application. Both crystalline pPIs (PIC and PID) were found to have identical powder XRD spectra before and after, used as a proof of stability of these highly crosslinked materials in these application-relevant environments.

1.6. Routes to tuning structure and function in porous materials

1.6.1. Hansen Solubility Parameters (HSPs)

The choice of a solvent holds a crucial character in the synthesis of various compounds, and understanding substance solubility is of great importance for numerous industrial applications. In general, the principle of "like dissolves like" or "like likes like" can be used to describe the solubility behaviour of substances in solvents. Many researchers rely on "trial and error methods" for solvent selection during synthesis.

In 1949, Hildebrand and Scott first introduced the term “solubility parameters”.^{199,200} The solubility parameter is an important concept that finds various applications, including the rational selection of solvents for synthesis. Therefore, when the intermolecular forces between the molecules of a solvent and the molecules of a solute are of comparable strength, become more compatible with each other.²⁰¹ Solubility parameters are alternatively referred to as cohesion energy parameters, established based on the energy needed to transform a liquid into a gas, such as the total energy of vaporisation.²⁰² The Hildebrand solubility parameter (δ) is characterised as the square root of the cohesive energy densities and given by **Equation 1.1**.²⁰³

$$\delta = \sqrt{(E/V)} \quad (1.1)$$

Here, E represents the cohesive energy of the liquid, which corresponds to the molal energy required for vaporisation into gas at zero pressure, and V denotes the molal volume of the liquid.

The units of solubility parameter are commonly expressed in $(\text{cal}/\text{cm}^3)^{1/2}$ or $\text{MPa}^{1/2}$. The polymer community often uses the unit Hildebrand (H). In SI units, it is measured as $\text{J}^{1/2} \text{m}^{-3/2}$, which is equivalent to $\text{pascal}^{1/2}$. It is important to note that 1 calorie is equal to 4.184 J and the detailed unit conversion is shown in **Appendix 1**.

However, a limitation of Hildebrand solubility parameters is that they are confined to regular solutions and do not account for the association between molecules, including the interactions resulting from polarity and hydrogen bonding.

Charles Hansen proposed the concept of Hansen solubility parameters (HSPs), which builds upon the Hildebrand solubility parameters. He stated that the total energy of vaporisation of a liquid is composed of three distinct components such as dispersion force (atomic), permanent dipole-permanent dipole force (molecular) and hydrogen bonding (electron exchange).²⁰²

The dispersion interaction (E_D) is known as nonpolar interaction and arises from atomic forces. Since molecules are composed of atoms, these forms of attraction are universally present among all molecules. Another type of cohesion energy, known as polar interactions (E_P), is attributed to permanent dipole–permanent dipole interactions. These molecular interactions exist to some degree in the majority of molecules and are characteristic of their nature. Hydrogen-bonding interactions, representing the third prominent source of cohesive energy, can be described as an electron-exchange parameter. Hydrogen-bonding is a form of molecular interaction that shares similarities with polar interactions. It occurs due to the attractive forces between molecules resulting from hydrogen bonds. The three individual cohesion energy are as follows:

- i. Dispersion (E_D) interactions (nonpolar)
- ii. Polar cohesive energy (E_P) (permanent dipole-dipole) interactions

iii. Hydrogen-bonding (E_H) interactions

The HSPs states that the overall cohesion energy (E) must be the sum of the individual energies contributing it (dispersion (E_D)-, polar(E_p)- and hydrogen(E_H)-bonding interactions), given as

$$E = E_D + E_p + E_H \quad \mathbf{1.2}$$

Dividing **Equation 1.2** by the molar volume gives the square of the total solubility parameters (or Hildebrand) as the sum of the squares of the Hansen D, P and H components (**Equation 1.4**).

$$E/V = E_D/V + E_p/V + E_H/V \quad \mathbf{1.3}$$

$$\delta_T^2 = \delta_D^2 + \delta_P^2 + \delta_H^2 \quad \mathbf{1.4}$$

HSPs offers a useful framework for understanding, predicting and improving the solubility, compatibility, stability and efficacy between the solute and the solvent.²⁰⁴ Materials sharing similar HSP exhibit a strong affinity or attraction towards one another.

1.6.2. The Bristol-Xi'an Jiaotong (BXJ) approach

The Bristol–Xi'an Jiaotong (BXJ) method was developed in 2019 by Dr Jie Chen in the Faul research group at the University of Bristol.^{43,205} This approach utilises HSPs, as discussed in **Section 1.6.1**, to identify suitable synthetic solvents for the synthesis of high surface area materials. In the BXJ method, the materials are initially synthesised using a common synthesis method. Subsequently, the synthesised materials are used to calculate their respective HSPs. These calculated HSPs are then compared with the known HSPs of organic solvents to determine compatible solvents for the synthesis of high surface area materials. According to the BXJ approach, solvents that exhibit low thermodynamic compatibility and poorly match HSPs with the resulting porous polymers, may lead to the formation of microgels and early phase separation during the polymerisation process. This can result in the formation of non-uniform pores and lower BET surface areas. On the other hand, solvents that demonstrate good compatibility with the polymers tend to induce late-phase separation during the polymerisation process. As a result, uniform pore formation, a high degree of polymerisation, and consequently, a high surface area are achieved, as depicted in **Figure 1.16**. Furthermore, the presence of inorganic salts can adjust the HSP parameters by virtue of their ionic strength. The addition of salts can bring the HSPs of the solvent and polymers closer together, enhancing compatibility. However,

excessive addition of salts can lead to an overadjustment, resulting in a mismatch of HSPs and potentially leading to a decrease in surface area.

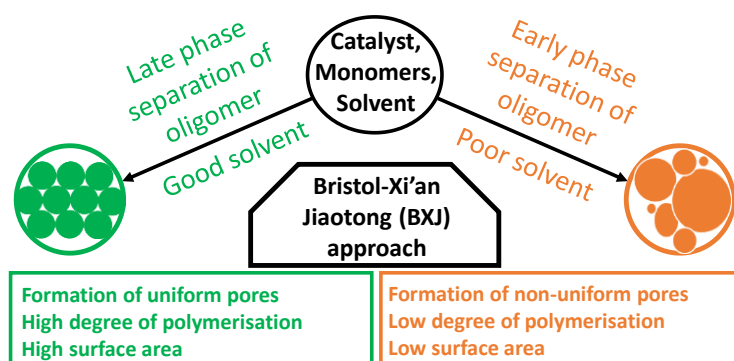


Figure 1.16: The BXJ approach and the impact of the solvent-polymer compatibility on the porosity of the polymer network.

The HSPs of the polymers were determined through a dilution method. In this method, the polymers were dispersed in different solvents, and the absorbance of the resulting supernatant/suspension was recorded using a UV-Vis spectrometer. The highest absorbance intensity in each solvent was recorded. Subsequently, the absorbance intensities were fitted using the B-Spline method with the respective individual HSP parameters (δ_D , δ_P , δ_H) of the solvents. For a more detailed calculation of the HSPs of the polymer, refer to **Appendix 1**, which provides further information and specific procedures regarding the calculation process. The limitation of the BXJ approach is that it measures the absorbance of the dispersed polymers rather than dissolved polymers as the crosslinked polymers do not dissolve in any solvents. It is still unclear whether the systems measure the HSPs of oligomers or polymers. There are several other factors that limit the application of the BXJ approach. For instance, even if the BXJ approach predicts a compatible solvent for the synthesis of polymers, the starting materials may not be soluble in that particular compatible solvent with polymers, and thus might be yielding with no products. Furthermore, if the reaction system required a catalyst or other additive, they may alter the HSPs of the compatible solvent and make it an incompatible solvent for the synthesis. Therefore, the BXJ approach may not always provide accurate information on the HSPs of the polymers and hinders its applicability.

The effectiveness of the BXJ approach was demonstrated in the formation of conjugated microporous polymers (CMPs) through Buchwald-Hartwig (BH) coupling.⁴³ The control polymer, referred to as PTPA, was synthesised using tris(aminophenyl)amine (TAPA) and phenylene diamine (PDA), resulting in an S_{BET} of 50 m²/g. However, by calculating the HSPs of the PTPA polymers and synthesising them

in a compatible solvent with the addition of salt (sodium fluoride (NaF)), the surface area increased by a remarkable factor of 20 ($1134 \text{ m}^2/\text{g}$) compared to PTPA synthesised using the standard synthetic procedure ($50 \text{ m}^2/\text{g}$). The author explored the effects of various inorganic salts such as sodium chloride (NaCl), sodium bromide (NaBr), sodium iodide (NaI), lithium nitrate (LiNO_3), sodium nitrate (NaNO_3), potassium nitrate (KNO_3) and barium nitrate ($\text{Ba(NO}_3)_2$) to improve the surface area of the PTPA. Among these salts, NaF yielded the most favourable results with respect to enhancing the surface area of PTPA. This enhanced surface area also resulted in improved CO_2 uptake capabilities of PTPA as shown in **Figure 1.17**.

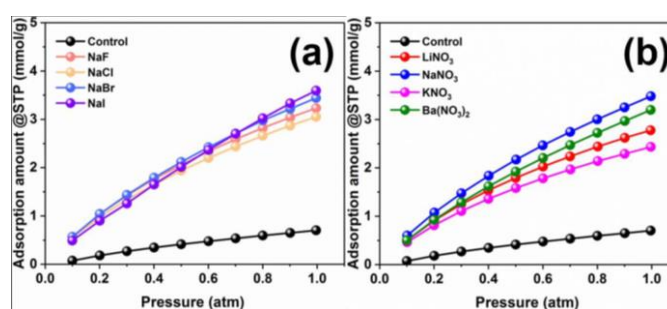


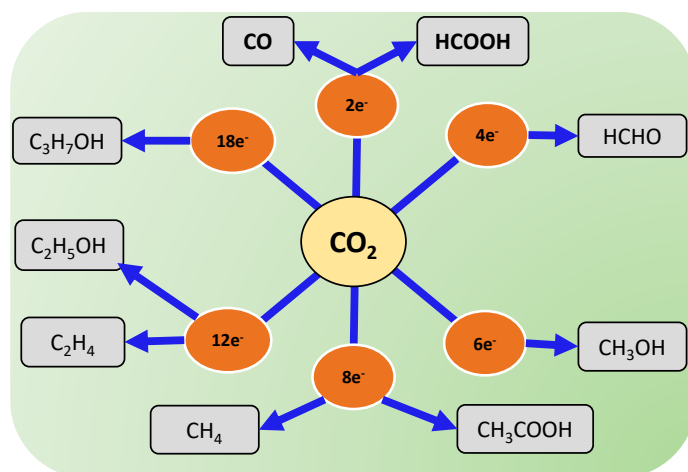
Figure 1.17: CO_2 uptake capabilities of PTPA (at 273 K) tuned by salts with different (a) anions and (b) cations.⁴³

The same author demonstrated another example where the BXJ approach was successfully applied to the synthesis of CMPs using Sonogashira-Hagihara, Suzuki cross-coupling and oxidative coupling reactions.²⁰⁵ Similarly, the surface area of the resulting materials was improved, along with enhanced CO_2 uptake capabilities. However, an interesting observation was made that the surface area gradually decreased with an increase in the ionic radius of the salts used.

In conclusion, the BXJ approach provides a straightforward and effective method to optimise and fine-tune the properties and functionality of porous polymers in a controlled manner. It also offers a systematic and versatile framework for designing innovative porous materials. This approach holds great potential for developing efficient methodologies that establish design principles for optimising and refining HSPs, with the ultimate goal of achieving fully adjustable porous materials that can be finely tuned for diverse applications.

1.7. Electrocatalytic conversion

The electrocatalytic reduction of CO₂ presents a highly promising strategy for converting CO₂ into storable fuels and valuable chemical products as shown in **Scheme 1.6**.^{10,206,207} This method becomes particularly advantageous when the electricity used is sourced from sustainable energy sources like solar and wind energy. The reduction of CO₂ helps in recycling CO₂, facilitating a carbon-neutral energy resource by utilising waste CO₂ and preventing its rising concentration in the atmosphere.



Scheme 1.6: Schematic illustration of electrocatalytic CO₂ reduction pathways.

The CO₂ reduction reaction (CO₂RR) predominantly occurs in a liquid electrolyte, where CO₂ enters the electrolyte solution, leading to the formation of a three-phase reaction system involving gas, liquid and solid phase.²⁰⁸ The process of CO₂RR comprises a series of four stages:²⁰⁸

- In the first stage, the interaction of CO₂ molecules onto the surface of the catalyst by Lewis-acid–base interaction is shown in **Figure 1.18**.
- In the second stage, electrons and protons are transported to the adsorbed CO₂ molecules, resulting in the cleaving of C=O bonds.
- In the subsequent step, the intermediates undergo reduction by continuously receiving electrons or protons. In certain scenarios, neighbouring intermediates might additionally merge, resulting in alterations in configuration and leading to the production of the final products.
- Finally, the formed products desorb the catalyst surface.

These steps collectively define the reaction processes involved in the CO₂RR, which occurs within the liquid electrolyte system. However, despite ongoing research, the mechanism underlying the CO₂RR remains unclear, and there are various challenges that must be addressed to enhance the efficiency

of this process. These obstacles include limited reaction selectivity, inadequate energy efficiency, and overall low conversion rates of CO₂.²⁰⁹

The electrochemical reduction of CO₂ could proceed through various pathways involving the transfer of multiple electrons (**Table 1.6**), *i.e.*, 2-, 4-, 6-, 8-, 12- or 18-electrons. In an aqueous medium, with the presence of a suitable electrocatalyst, this process can produce various gaseous and liquid products as shown in **Scheme 1.6**.¹¹ As reported in the literature, 2-electron transferred products are carbon monoxide (CO) and formic acid (HCOOH). Furthermore, multiple electron transfer can lead to the production of other higher carbon products such as methanol (CH₃OH), acetic acid (CH₃COOH), methane (CH₄), ethylene (C₂H₆), ethanol (C₂H₅OH), and propanol (PrOH) as shown in **Table 1.6**.^{206,210} It is quite probable that instead of yielding a single product, the result would involve a combination of gaseous products (CO, CH₄, etc.) as well as liquid products (CH₃OH, PrOH, etc).

The electrochemical reduction of CO₂ has many advantages over other conversion processes.^{211–214} For instance, the reaction conditions can be directly controlled such as redox potential, reaction temperature, electrolyte and the reaction can be driven by green energy resources.¹¹ Moreover, through the optimisation of the electrocatalyst, the efficiency and selectivity could be enhanced.

Table 1.6: Possible electrochemical potential for CO₂ reduction reaction in aqueous medium.^{10,11}

Possible half-cell electrochemical CO ₂ reduction reaction	Electrode potential (E° (V) vs SHE) at pH 7
$\text{CO}_{2(\text{g})} + 2\text{H}^+ + 2\text{e}^- \rightarrow \text{CO}_{(\text{g})} + \text{H}_2\text{O}_{(\text{l})}$	-0.53
$\text{CO}_{2(\text{g})} + 2\text{H}^+ + 2\text{e}^- \rightarrow \text{HCOOH}_{(\text{l})}$	-0.61
$\text{CO}_{2(\text{g})} + 4\text{H}^+ + 4\text{e}^- \rightarrow \text{HCHO}_{(\text{l})} + \text{H}_2\text{O}_{(\text{l})}$	-0.48
$\text{CO}_{2(\text{g})} + 6\text{H}^+ + 6\text{e}^- \rightarrow \text{CH}_3\text{OH}_{(\text{l})} + \text{H}_2\text{O}_{(\text{l})}$	-0.38
$\text{CO}_{2(\text{g})} + 8\text{H}^+ + 8\text{e}^- \rightarrow \text{CH}_{4(\text{g})} + 2\text{H}_2\text{O}_{(\text{l})}$	-0.24
$2\text{CO}_{2(\text{g})} + 8\text{H}^+ + 8\text{e}^- \rightarrow \text{CH}_3\text{COOH}_{(\text{g})} + 2\text{H}_2\text{O}_{(\text{l})}$	-0.26
$2\text{CO}_{2(\text{g})} + 12\text{H}^+ + 12\text{e}^- \rightarrow \text{C}_2\text{H}_5\text{OH}_{(\text{g})} + 3\text{H}_2\text{O}_{(\text{l})}$	-0.32
$2\text{CO}_{2(\text{g})} + 12\text{H}^+ + 12\text{e}^- \rightarrow \text{C}_2\text{H}_4_{(\text{g})} + 4\text{H}_2\text{O}_{(\text{l})}$	-0.34
$3\text{CO}_{2(\text{g})} + 18\text{H}^+ + 18\text{e}^- \rightarrow \text{C}_3\text{H}_7\text{OH}_{(\text{l})} + 5\text{H}_2\text{O}_{(\text{l})}$	-0.31
$2\text{H}^+ + 2\text{e}^- \rightarrow \text{H}_{2(\text{g})}$	-0.42

The thermodynamic stability and linear geometry of CO₂ make its reduction kinetically challenging, often necessitating a substantial overpotential.^{215,216} Therefore, the effectiveness of electrocatalytic CO₂ reduction primarily relies on the catalyst's selectivity and activity. To design a robust electrocatalyst with superior activity and efficiency, a few factors need to be considered such as thermodynamic stability of the catalyst, catalyst–CO₂ interactions, pore size, overall and microporous surface area.²¹⁷ Due to its possession of a substantial quadrupole moment, CO₂ exhibits electrophilic characteristics. Therefore, introducing electron-rich elements (O, N, S) into the backbone of POPs proves to be an effective strategy for enhancing the selectivity towards CO₂.^{217,218} Thus, linear molecules of CO₂ can be physisorbed through interaction with the surface of the materials. Likewise, CO₂ can be chemisorbed as a partially charged CO₂^{δ-} species with the surface of the materials.²¹⁹ Considering the exceptional stability of CO₂, characterised by high dissociation energy (750 kJ/mol), it is challenging to break the C=O bond to facilitate the formation a new bond.²²⁰ Nevertheless, the interaction with a catalyst and the formation of bent CO₂^{δ-} species induce a disruption in the linear symmetry of the CO₂ molecules. The bent configuration of molecules reduces the hurdle for electron acceptance because the LUMO energy decreases as the molecules bend.^{10,221} The proposed CO₂–catalyst interactions are mentioned below and illustrated in **Figure 1.18**.

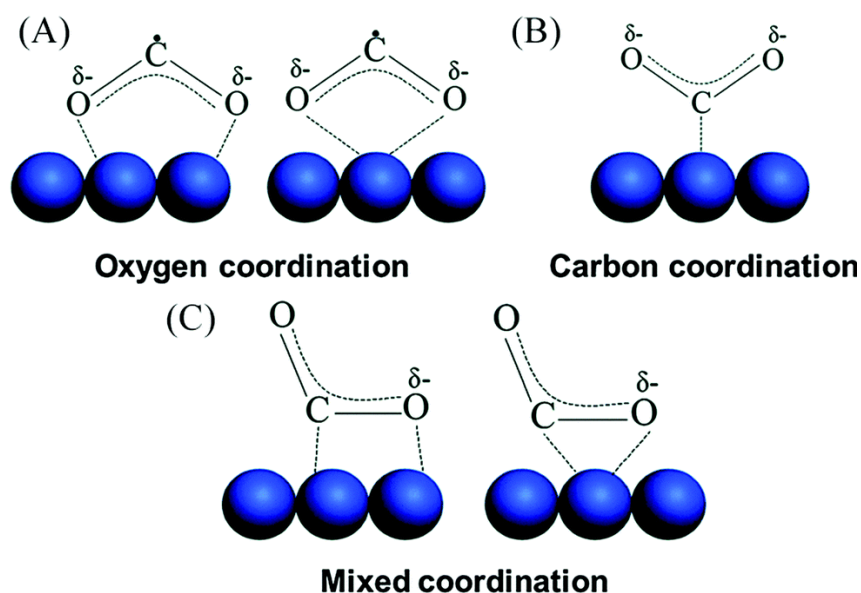


Figure 1.18: Possible configuration of adsorbed CO₂ on catalyst (A) Oxygen coordinated, (B) Carbon coordinated and (C) Mixed coordinated.¹⁰

- (A) CO₂ has two oxygen atoms, the lone pair of electrons of the oxygen atoms could be donated to a Lewis acid surface.
- (B) The carbon atom of CO₂ could also act as Lewis acid and could receive electrons from the Lewis base centres.
- (C) Both the oxygen and carbon atoms have the potential to function as electron acceptors and donors, respectively, thereby leading to the formation of a hybrid coordination structure.

Alternative ways to improve CO₂ reduction is surface functionalisation with some CO₂-philic groups, for instance, amine groups or electron rich heteroatoms. CO₂ is considered as a Lewis acid, which could lead to enhanced interactions by means of Lewis acid–Lewis base interactions.¹⁰ It is worth noting that the CO₂ reduction pathway depends on binding intermediates on the catalyst surface. Thus, the binding should be optimised, as excessive affinity between the catalyst and the substrate could induce catalyst poisoning, whereas insufficient binding might prevent CO₂ reduction reactions.

Various metal-containing porous polymers such as MOFs^{222–224} and metal-containing COFs^{222,225–227} have been extensively investigated in the electrochemical CO₂ reduction.

Zhang et al,²²⁸ utilised bismuth-based MOFs (Bi-BTC-D) for electrocatalytic CO₂ reduction to formate achieving a FE up to 95.5% at -0.86 V vs RHE. Another example was demonstrated by Jiang et al,²²⁹ they utilised zinc-containing MOFs (ZIF-8) as an electrocatalyst for the conversion of CO₂ to CO obtaining FE of 81% at -1.1 V vs RHE. Several other MOFs that contain copper (Cu),^{230,231} iron (Fe),²³² rhenium (Re),²³³ cobalt (Co),²³⁴ and silver (Ag)²³⁵ in their building blocks have been successfully utilised for the reduction of CO₂ into value-added products such as CO, CH₄, C₂H₄, CH₃OH, and C₂H₅OH.

Similar to MOFs, various COFs have been investigated for the electroreduction of CO₂ to useful chemical feedstocks.²²⁶ In 2015, Lin et al,²³⁶ demonstrated for the first time, the use of Co-based COFs (COF-367-Co) for electrocatalytic conversion of CO₂ to CO with 90% FE. Cheung et al,²³⁷ utilised Fe-porphyrin-based COFs for the conversion of CO₂ to CO, achieving 80% FE. It is worth noting that only metal-porphyrin or phthalocyanine-based COFs were investigated in electrochemical CO₂ reduction.^{237,238} For instance for instance Cu-, Co-, Ni-, and Fe-porphyrin/phthalocyanine-based COFs have been widely used electrocatalyst.²³⁹

However, MOFs and metal-containing COFs lack stability, poor conductivity and functionality limiting their applications in electrocatalytic CO₂ reduction.²⁴⁰ Moreover, the active metal sites may leach after repeated use, thus limiting their recyclability.²⁴¹ Taking into consideration, all the factors and properties discussed above, pPIs would be the best metal-free electrocatalyst for electrocatalytic CO₂

reduction. Owing to their advantageous properties (discussed in **Section 1.5**), including their high surface area, abundant heteroatoms, and conjugated chemical structure utilising well-known organic semiconductor linkers such as PTCDA and NTCD, make them highly suitable for electrocatalytic CO₂ reduction.

1.7.1. Performance target for the CO₂ reduction reactions

To evaluate the performance of the electrochemical process, several key factors are employed, including current density, faradaic efficiency, energy efficiency, and stability.²¹⁰ These figures of merit provide a comprehensive characterisation of the electrochemical process and enable an assessment of its effectiveness and reliability.

1.7.1.1. Current density

The current density is defined as the amount of current flowing per unit geometric area of the electrode at a specific potential.^{206,210} It represents the rate of the electrochemical reaction per electrode area, indicating the catalytic activity of the electrode. The current density serves as a means to determine the required size of the electrolyser for achieving a desired production rate. Moreover, it is influenced by various factors including catalyst loading, catalyst utilisation, reactant and product transport rates (back and forth) at the electrode. Therefore, achieving a high current density is crucial for minimising the overall size of the electrolyser and reducing capital investment while attaining the desired production rate for the CO₂ reduction reaction.

1.7.1.2. Faradaic efficiency

Faradaic efficiency (FE) plays a pivotal role in assessing the performance of catalysts, serving as a key metric.^{206,210} It provides a measure of the proportion of power effectively utilised in producing desired products, in relation to the total power transmitted through the electrode within a specified time period. The FE is defined as the current efficiency toward the generation of a specific CO₂ reduction product and is given by **Equation 1.5**. A substantial FE reduces the need for extensive separation prerequisites and decreases the overall current needed to achieve a desired production rate.²⁴²

$$\epsilon_{Faradaic} = \frac{z \cdot n \cdot F}{Q} \quad \mathbf{1.5}$$

z: number of electrons required to produce a given product

n: number of moles of the given product

F: Faraday's constant (96485.33 C/mol)

Q: total charge passed (C)

1.7.1.3. Energy efficiency

Energy efficiency is defined as the proportion of energy contained within the targeted products in relation to the overall energy input required for their synthesis.^{206,210} The energy efficiency can be determined using the subsequent equation (**Equation 1.6**).

$$\varepsilon_{energy} = \sum \frac{E^\circ \varepsilon_{Faradaic}}{E^\circ + \eta} \quad \mathbf{1.6}$$

Where, E° : the equilibrium cell potential for the product.

$\varepsilon_{Faradaic}$: the faradaic efficiency

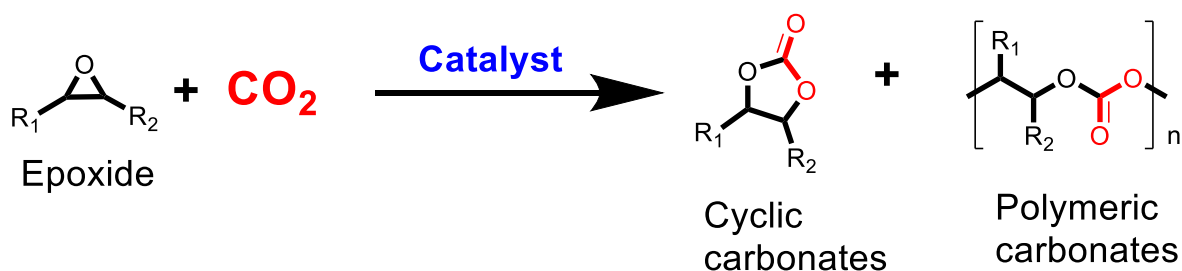
η : the total cell overpotential

1.7.1.4. Stability

The CO₂ electrolyser must exhibit long-term stability and meet predetermined performance criteria, including FE, current density and energy efficiency.^{206,210} For instance, industrial water electrolyzers have exhibited consistent operation for over 80,000 hours.²⁴³ Ensuring long-lasting stability is essential in order to minimise maintenance and replacement costs. It is worth noting that even slight impurities in the catalyst or electrolyte can have an impact on CO₂ reduction reactions. However, the study of CO₂ reduction reactions for extended periods of time has been limited in the existing literature, typically lasting less than 100 hours.

1.8. Chemical Conversion

The chemical conversion approach for converting CO₂ into valuable chemicals has garnered increasingly interested owing to its potential to transform industrial waste (*i.e.*, CO₂) and generate a cost-effective, readily available, non-toxic, and renewable carbon feedstock.^{244,245} From a sustainability perspective, this approach shows great potential in efficiently harnessing and utilising CO₂ as a valuable and abundant carbon resource. Therefore, there has recently been a growing interest in chemical reactions that utilise CO₂ as a chemical feedstock. Specifically, the cycloaddition reaction between CO₂ and epoxides produces various cyclic carbonates or polymeric carbonates (**Scheme 1.7**). Cyclic carbonates are industrially important and utilised in a diverse range of applications, including as building blocks for polymeric materials,²⁴⁶ solvents,²⁴⁷ and, importantly, as electrolytes for lithium-ion batteries.²⁴⁸

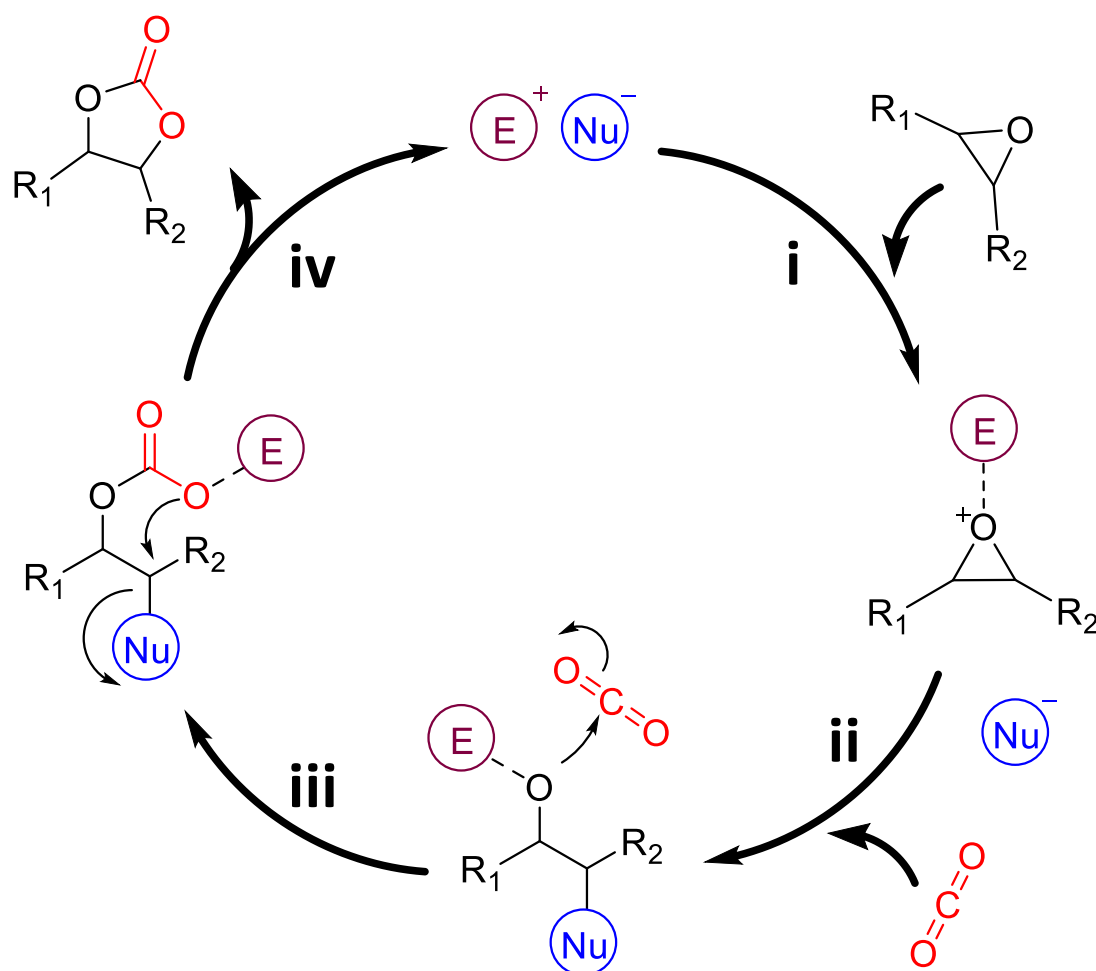


Scheme 1.7: The general scheme depicts the reaction between an epoxide and CO₂.

The production of cyclic carbonates from epoxides and CO₂ encompasses various mechanistic pathways, offering multiple potential catalytic cycles. They can be mainly categorised into three types: (1) epoxide activation, (2) CO₂ activation and (3) activation of both CO₂ and epoxide.^{26,28}

(1) Epoxide activation

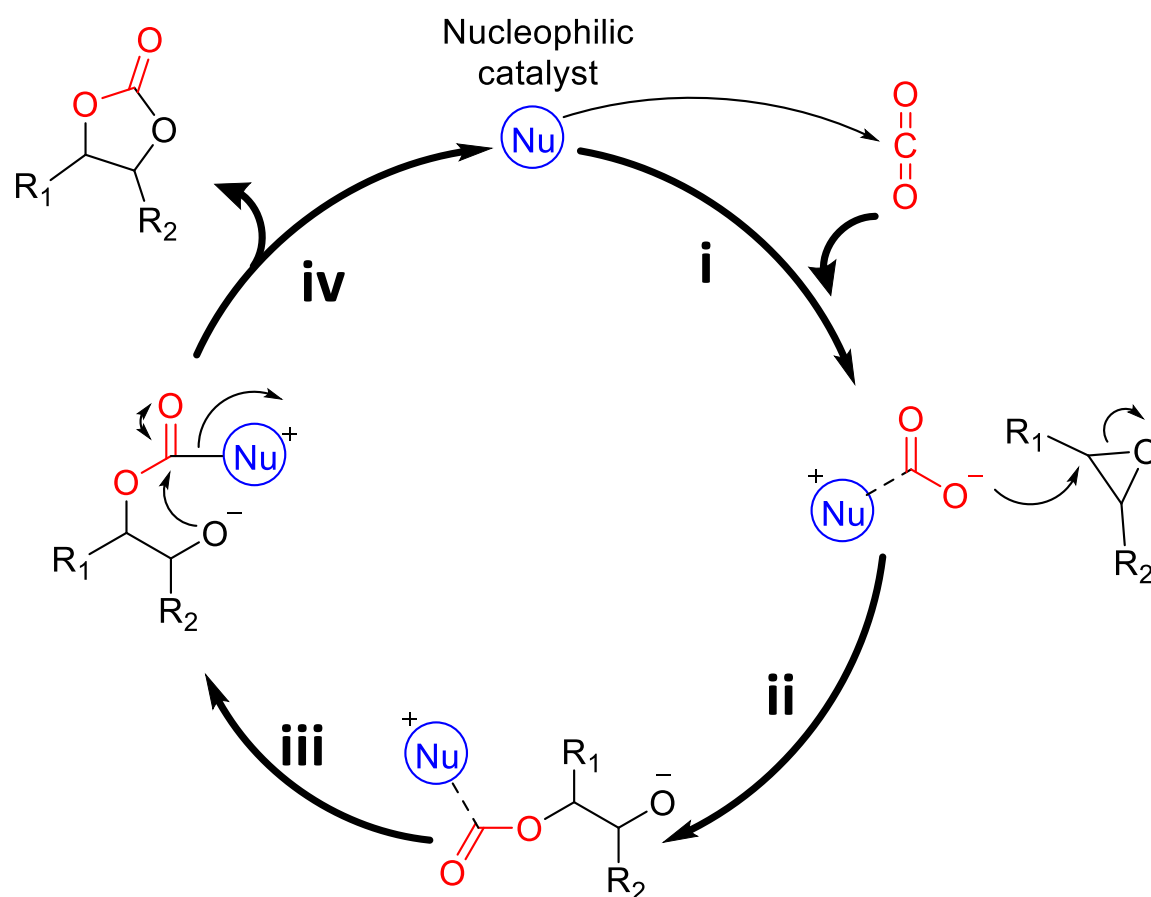
The catalyst that activates epoxides should act as a Lewis or Bronsted acid or be functionalised with Lewis or Bronsted acids. The electrophile (E) (Lewis acid center or hydrogen-bond donor) initially coordinates with the epoxide (step i), thereby activating it for ring-opening by a nucleophile (Nu).²⁴⁹ This is followed by the insertion of the CO₂ (step ii), where the oxygen (O) atom of the epoxide attacks the electron-deficient carbon atom of CO₂ (step iii) and forms a carbonate intermediate. The final step is intramolecular cyclisation of the carbonate intermediate (step iv) to yield corresponding cyclic carbonates and reuse the catalyst simultaneously. The catalytic process involved in activating epoxides is illustrated in **Scheme 1.8**.



Scheme 1.8: Generic mechanism for the synthesis of cyclic carbonates through epoxide activation.

(2) CO₂ activation

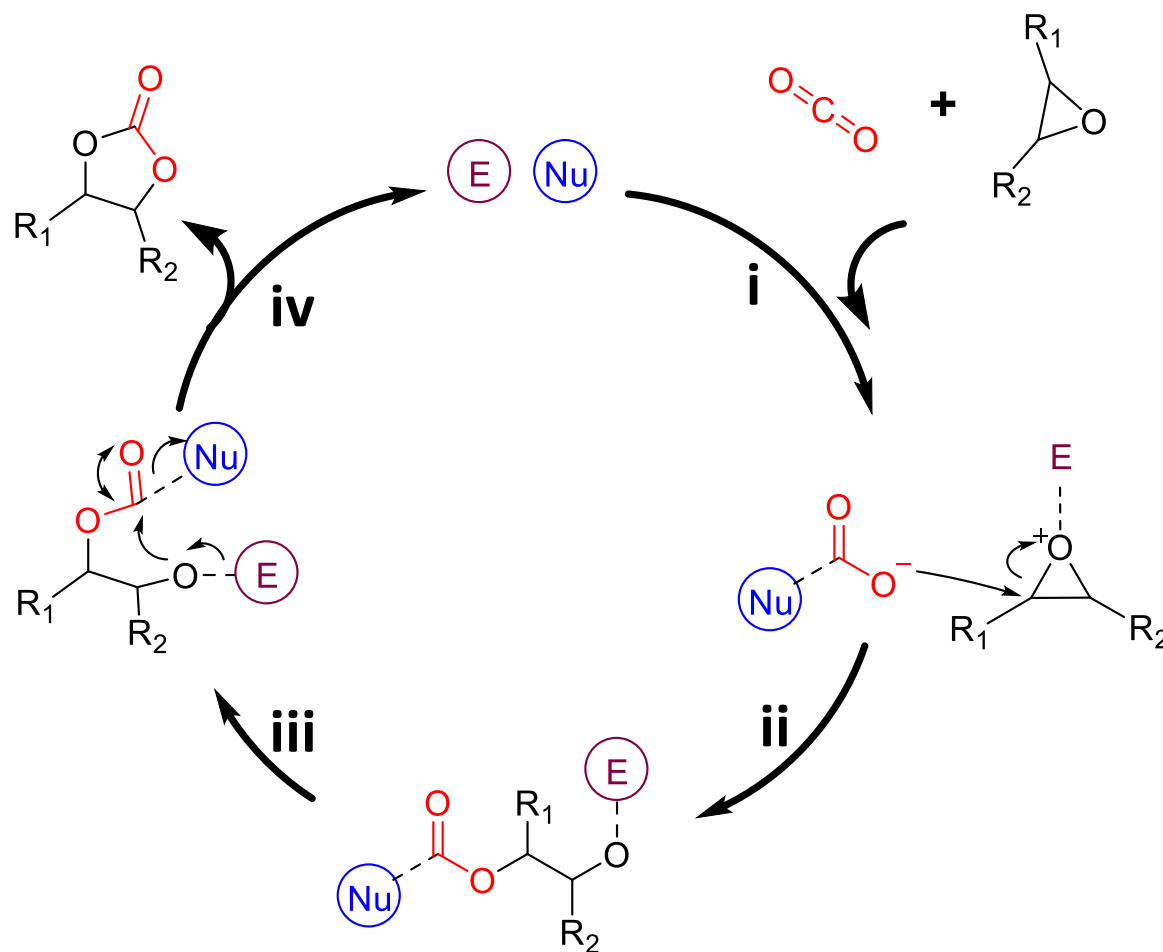
It is recognised that CO₂ is a nonpolar molecule with two polar C=O bonds and cancelling each other out, resulting in the carbon site being a relatively weak electrophile. Therefore, catalysts that are nucleophilic towards CO₂ but not towards epoxides can activate CO₂ by coordinating or bonding with the electron-deficient carbonyl carbon of CO₂ (step **i**).²⁵⁰ The epoxide is then attacked to open the ring by the oxygen anion intermediate formed after CO₂ activation (step **ii**). Similarly, the final step is intramolecular cyclisation (step **iii**) of the intermediate to form corresponding cyclic carbonates (step **iv**) and reuse the catalyst simultaneously. The general mechanism for cyclic carbonate synthesis via CO₂ activation (**Scheme 1.9**).



Scheme 1.9: Generic mechanism for the synthesis of cyclic carbonates through CO₂ activation.

(3) Activation of both CO₂ and epoxide

Typically, a catalyst having dual or multiple active sites can effectively activate CO₂ and epoxide simultaneously.^{251,252} A particularly effective approach involves employing well designed bifunctional catalysts, whether in a single-catalyst or two-catalysts system. The general mechanism for CO₂ and epoxide activation and thus forming corresponding cyclic carbonates are shown in **Scheme 1.10**.



Scheme 1.10: Generic mechanism for the synthesis of cyclic carbonates through dual activation (substrate and CO₂).

Following these three approaches for synthesising cyclic carbonates from epoxide and CO₂, there are multiple catalysts have been developed to date such as homogeneous catalysts,^{253,254} metal-based catalysts²⁵⁵ and POP-based catalysts.²⁵ These catalysts have been efficiently used in the synthesis of corresponding cyclic carbonates from CO₂ and various epoxide substrates (shown in **Figure 1.22**).

Ionic organic halides^{253,254} and ionic liquids (ILs)²⁵⁶ such as quaternary ammonium salts, phosphonium salts, imidazolium and pyridinium, are examples of homogeneous catalysts that exclusively consist of an ionic nucleophile. Additionally, Lewis bases like strong organic bases are also employed as homogeneous catalysts. However, drawbacks of homogeneous catalysts are reusability and difficulties in separation.

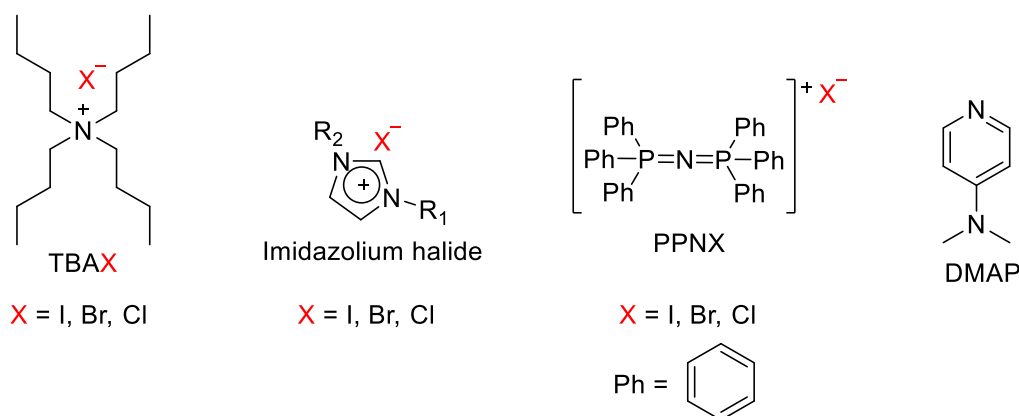


Figure 1.19. Examples of homogeneous catalysts used in the synthesis of cyclic carbonates from CO_2 and epoxides.

In order to address the challenges of separation and reusability, many researchers have attempted to convert homogeneous catalysts into heterogeneous catalysts by incorporating them onto high-surface-area material or metal complex supports. Liao et al.,²⁵⁷ have synthesised hypercrosslinked ionic polymers with multi-ionic sites and utilised them in the synthesis of cyclic carbonates. They also examined the impact of surface area and successfully reused the catalyst six times without observing significant decreases in catalytic activities and selectivity. Another example was demonstrated by Kim et al.²⁵⁸ in which they attached quaternary ammonium salts onto nanoporous covalent organic polymers and utilised them for the same application.

There are several metal-based catalysts utilised for the cycloaddition of CO_2 to epoxides.^{27,245,259} Few examples of metal-based catalyst are salen-, porphyrin-, and pyridine-metal-based catalyst as shown in the **Figure 1.20**.

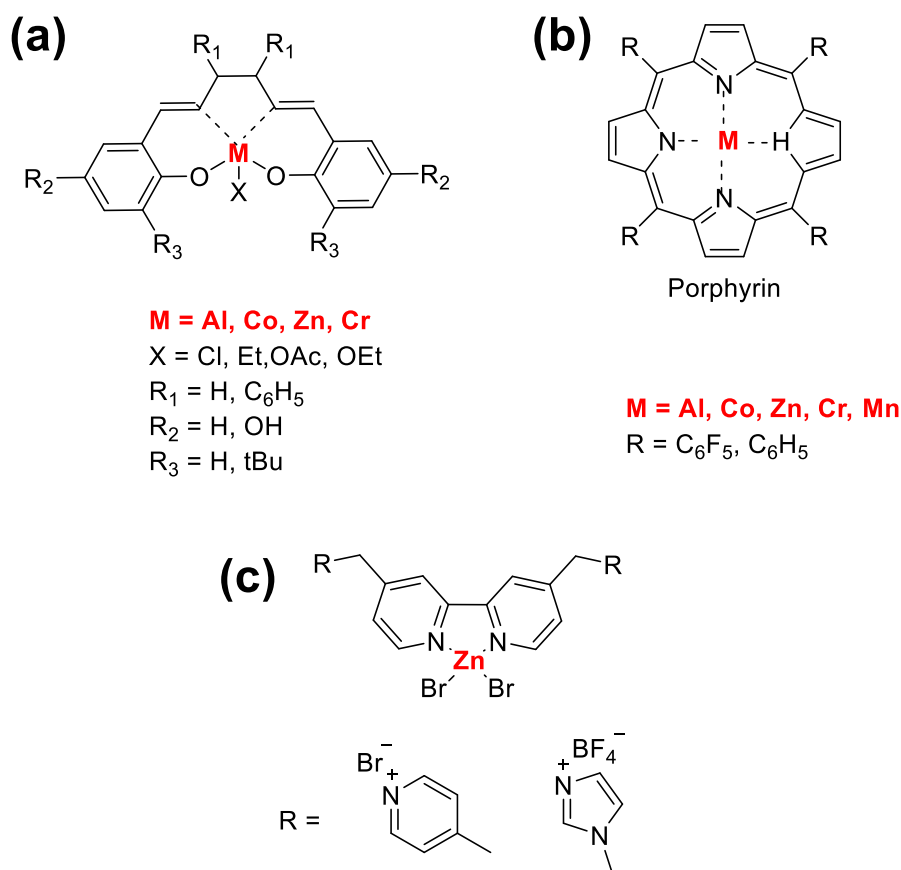


Figure 1.20: Some selected examples of metal-based catalysts (a) salen-based,²⁶⁰ (b) porphyrin-based,²⁷ and (c) pyridine-based.²⁶¹

Considering the beneficial characteristics of porous polymers discussed in **Chapter 1**, different types of porous materials, both metal-based and metal-free, have been employed as heterogeneous catalysts for converting CO₂ into cyclic carbonates. Since this project concentrates on metal-free pPIs as a catalyst, this chapter will exclusively cover metal-free porous organic polymers (POPs) heterogeneous catalysts used in the cycloaddition process of CO₂ to generate cyclic carbonates.

Zhang et al.,²⁶² successfully synthesised a range of metal-free triazine-based POPs (MOPs) using a simple one-pot polycondensation between melamine and monoaldehydes (**Figure 1.21a**). These POPs were then employed as a recyclable, metal-free heterogeneous catalysts for the conversion of CO₂ and epoxides (**Figure 1.22 (2, 6, 7, 8,10, 11, 19, 22)**) into corresponding cyclic carbonates. The catalytic activity was ascribed to the hydrogen-bonding interaction facilitated by the POPs. Ravi et.,²⁶³ also reported amino functionalised triazine-based POPs (CTP-1-NH₂) via Friedel–Crafts arylation (**Figure 1.21b**). However, in the case of CTP-1-NH₂, although it had the ability to form hydrogen bonds with epoxides (**Figure 1.22 (2, 12, 17, 21,22)**), the successful conversion to corresponding cyclic carbonates

required the existence of a co-catalyst, namely tetrabutylammonium bromide ($n\text{-Bu}_4\text{NBr}$). This conversion took place under moderate reaction conditions ($40\text{ }^\circ\text{C}$ and 1 bar) without the need for a solvent, and it was completed within 36 hours of reaction time. Ma et al.,²⁶⁴ synthesised pyridine-containing metal-free POPs (**Figure 1.21c**) and they performed a post-synthetic modification of the POPs with the Brønsted acidic site provided (carboxylic acid) and the Br^- anion, resulting in POF-PNA- Br^- . These modified POF-PNA- Br^- were then successfully employed as bifunctional metal-free heterogeneous catalysts for the cycloaddition reaction of CO_2 to epoxide (**Figure 2.4 (6, 7, 10, 17,22)**). Remarkably, this reaction was carried out under a moderate reaction setting without the need for any co-catalyst.

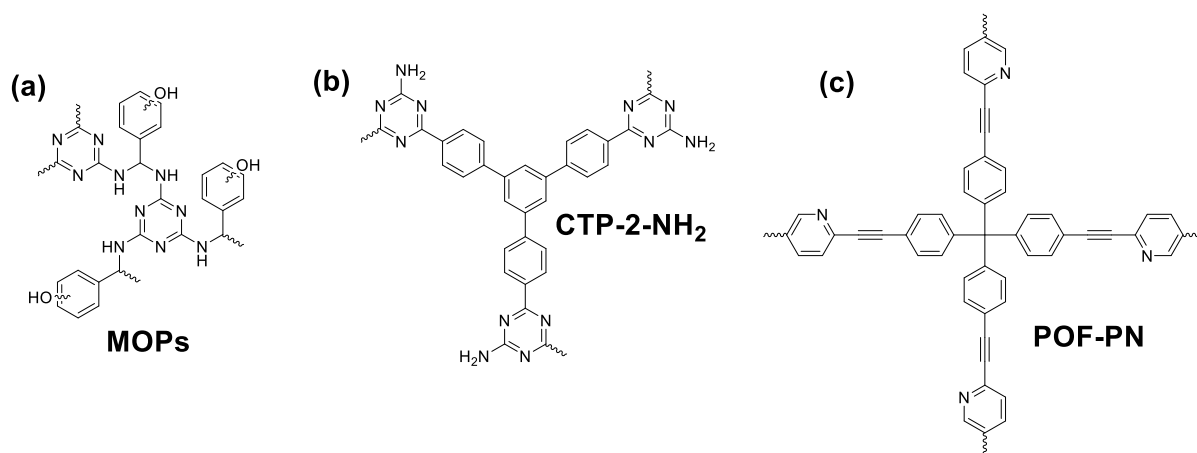


Figure 1.21: Selected structure of metal-free POPs used as a catalyst for cyclic carbonate synthesis.

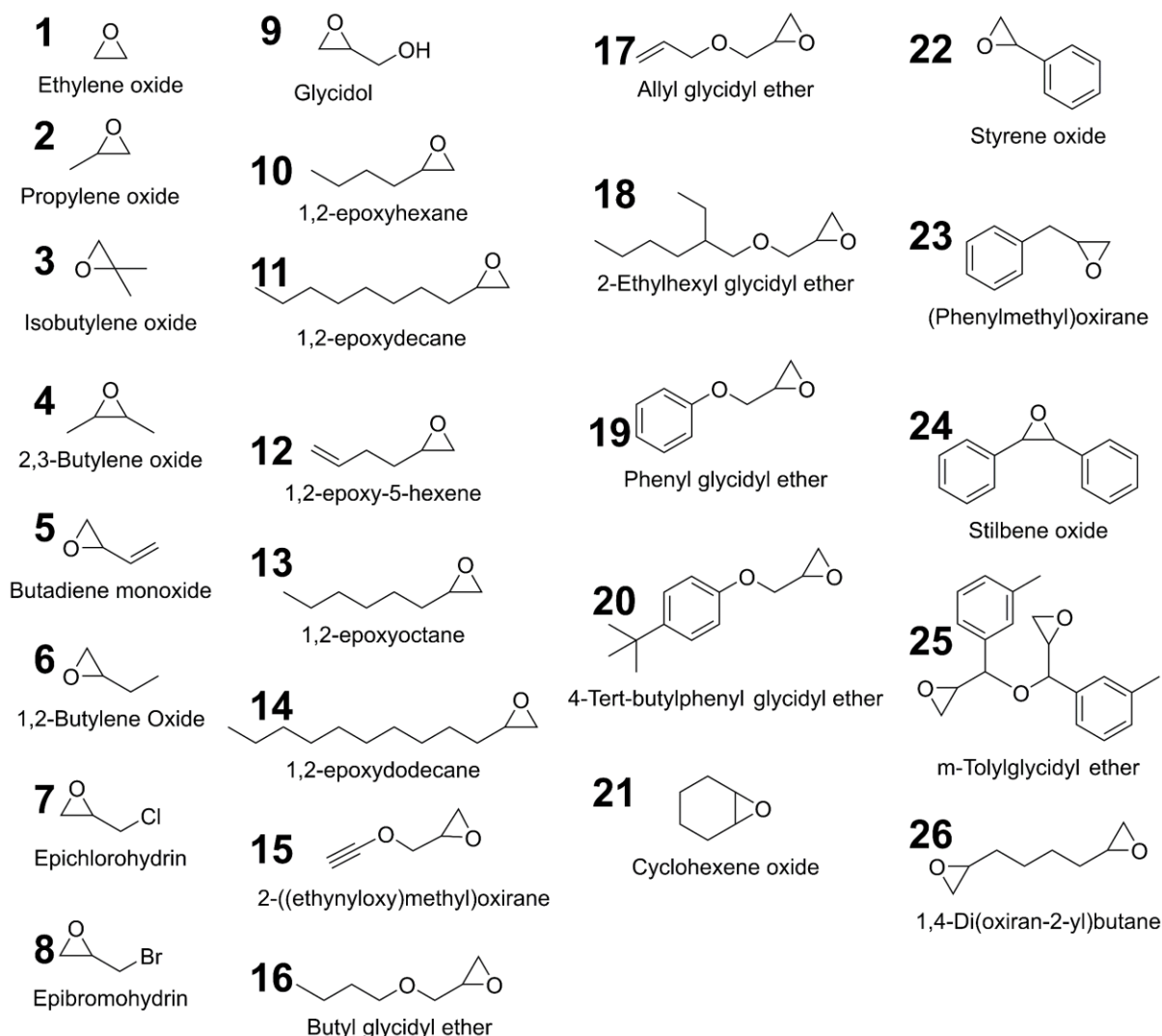


Figure 1.22. Various epoxide substrates used for cycloaddition to CO₂.

1.9. Conclusion and Future outlook

One common theme throughout the studies cited in this chapter was centred around the ability and opportunities available to control the properties and the function of the prepared pPIs. We have endeavoured to highlight aspects of deliberate design, where encountered and attempted to show the influence of careful choice of starting materials and their functionality, and synthesis conditions on the chosen areas of applications. There are however a number of challenges that the broader field of porous functional materials, and certainly also pPIs, face that are connected to fine control of properties and function.

Although pPIs can be synthesised solvent-free to avoid issues with insolubility and the incompatibility of the growing and crosslinked polymer chains with reaction solvents, Chen et al.^{43,205} have recently

explored tuning Hansen solubility parameters (HSPs) in the preparation of CMPs through the addition of simple inorganic salts to reaction mixtures. They showed that this approach, the so-called Bristol-Xi'an Jiaotong (BXJ) approach, provides a novel route to accurately match the HSPs of the growing polymer construct with that of the reaction solvent, thus exerting fine control over the properties and functionality (as expressed through increased CO₂ uptake) in the obtained porous materials. Significant opportunities, therefore exist, especially when keeping **Tables 1.1** and **1.3** in mind in terms of the scope of materials, to apply the BXJ approach for the production of optimised and fully tuned functional pPI networks.

In terms of application areas as potential future growth areas, especially those with environmental applications are of global interest. Given the current world shortages in water (for safe human consumption, but also for wider agricultural use), the use of pPIs as water harvesting motifs presents a significant opportunity. Although pPIs synthesised by Wu et al.¹⁴⁶ demonstrate large water uptake (over 300 wt%), and while many other systems were reported as having the capability (**Table 1.4**), water harvesting remains largely unexplored in the majority of papers where gas absorption is presented as an application (**Table 1.3**). It is expected that significant increases in performance would be possible with focused efforts in this area of importance, thus leading to a significant global socio-economic impact on local communities where water is a precious commodity.

To the best of our knowledge biocompatibility of pPIs has not been reported in the literature. This omission is especially worthy of attention when one considers the potential of these networks as controlled drug delivery or drug removal motifs (as discussed in **Sections 1.5.3.3**), as potential scaffolds for cell culture and growth (for biocompatible implants), as well as the possibility for in-vitro drug detection, **Section 1.5.3.3**.

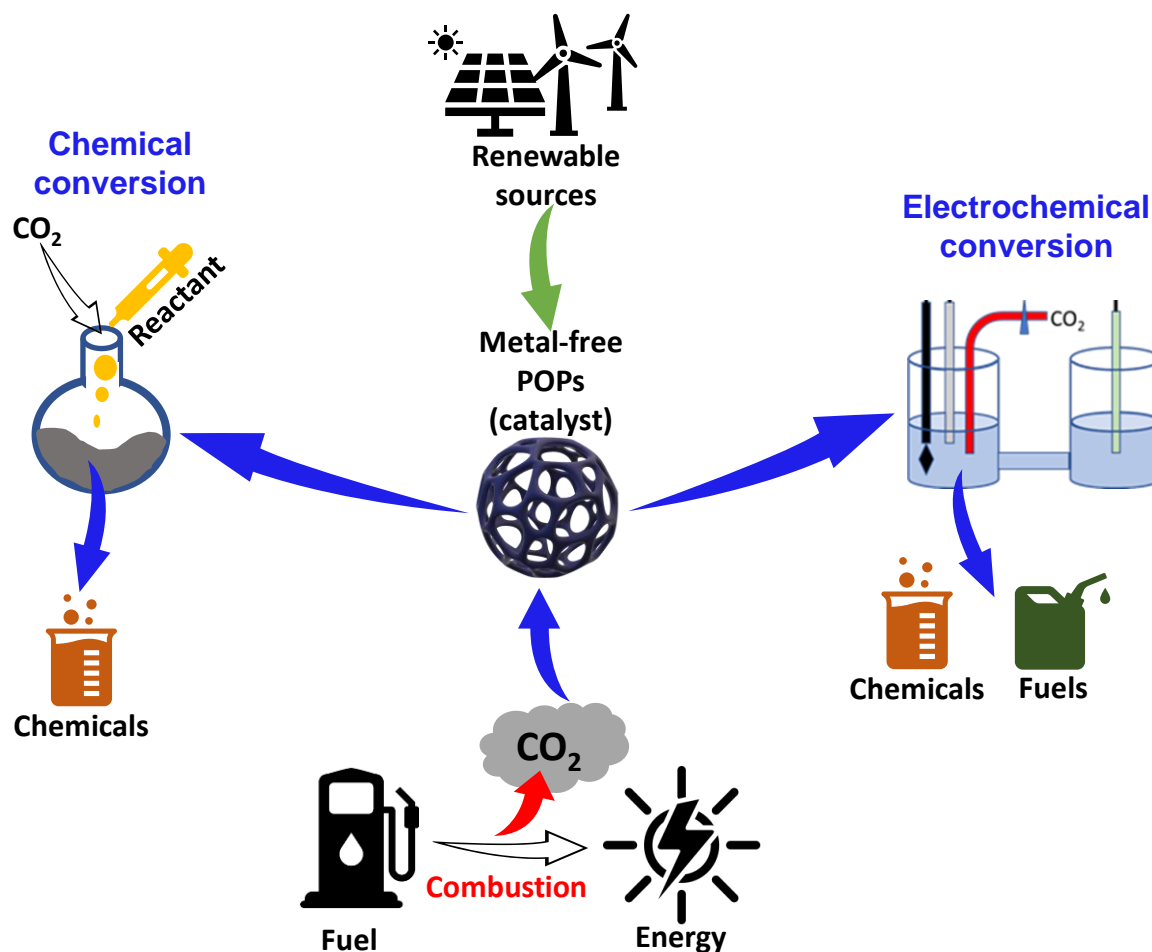
Finally, the excellent surface areas reported, high wt% of CO₂ capture, and tuneable conductivity of the reported pPIs make them excellent candidates for CO₂ capture and conversion. The remarkable properties of pPIs, including their high surface area, tuneable porosity achieved through the BXJ approach, and conjugated chemical structure utilising well-known organic semiconductor linkers such as PTCDA and NTCDA, make them highly suitable for electrocatalytic CO₂ reduction. Furthermore, the unique structural features and inherent chemical functionality of pPIs provide active sites for the synthesis of cyclic carbonates from CO₂ and epoxides in an environmentally friendly and sustainable manner.

The multifunctionality of pPIs, as both efficient CO₂ sorbent and metal-free catalysts, positions them as valuable materials in addressing the challenges of CO₂ capture and utilisation. Their versatility and

potential for large-scale implementation make pPIs a promising avenue for advancing CO₂ conversion technologies and contributing to a more sustainable future.

Chapter 2: Aim and objectives

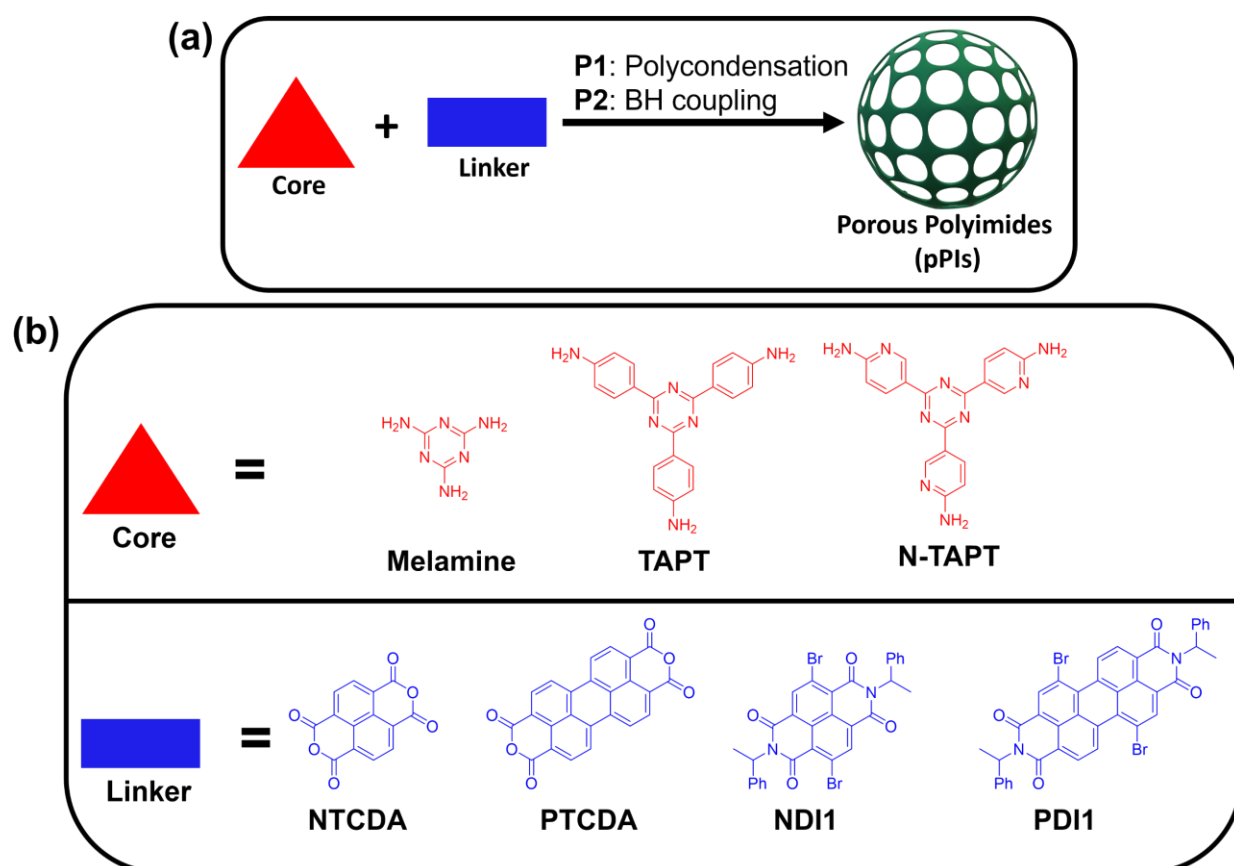
This thesis is predominantly focused on the synthesis of conjugated porous polyimide (pPIs) and explores their application not only for capturing CO₂ but also utilising them as the heterogeneous catalysts for the reduction of CO₂ to valuable chemical feedstocks and fuels as shown in **Scheme 2.1**.



Scheme 2.1: Schematic of CO₂ capture and conversion using pPIs.

The overall aim of this project is to explore naphthalene- and perylene-based pPIs, which are a type of POP (discussed in **Chapter 1 Section 1.6**). Naphthalene- and perylene-based pPIs offer great potential for CO₂ capture and conversion owing to their porous nature and excellent redox behaviour. This aim is to be achieved by investigating the three following objectives:

- The first objective is the optimisation of synthesis pathways to achieve naphthalene- and perylene-based polyimide networks. Two synthetic pathways were employed in this study to synthesise highly crosslinked pPIs: polycondensation (**P1**) and BH coupling (**P2**).
 Pathway 1 (**P1**), polycondensation of dianhydride (PTCDA and NTCDA) with triamines (melamine, TAPT and N-TAPT, respectively) as shown in **Scheme 2.2**.
 Pathway 2 (**P2**), Buchwald–Hartwig (BH) cross coupling reaction between bay brominated perylene diimide (PDI1) and naphthalene diimide (NDI1) with triamine, respectively (see **Scheme 2.2**).



Scheme 2.2: (a) General synthesis pathways for pPIs and (b) Structure of cores and linkers used in this project.

Generally, these types of polycondensation reactions require a catalyst to form cyclic imide linkage and achieve highly cross-linked products and only water as a side product. However, in this work we have demonstrated catalyst free polycondensation pathways, resulting in highly crosslinked pPIs.

- 2.** The second objective is to fine-tune the properties and functionalities of pPIs by implementing the BXJ approach, discussed in **Chapter 1 (Section 1.6.2)**. This will be achieved by calculating the Hansen Solubility Parameters (HSPs) of pPIs and comparing them with the HSPs of various common reaction solvents to identify suitable solvents for optimised synthesis conditions. Additionally, inorganic salts will be employed to adjust the HSPs to enhance the surface area by modifying the compatibility of the reaction solvent during pPI growth. The BXJ approach offers a valuable means to precisely adjust the surface area and pore size distribution (PSD) of the porous polymers. Further information on HSPs and their calculation can be found in **Chapter 1, (Section 1.6.1)** and **Appendix 1**.
- 3.** Finally, the third objective is to utilise pPIs not only for the capture of CO₂ but also as a heterogeneous catalyst for CO₂ conversion. There are several approaches for CO₂ conversion, but this thesis only focuses on electrocatalytic and chemical conversion as shown in **Scheme 2.1** and discussed in detail in **Chapter 1 (Sections 1.7 and 1.8)**.

Chapter 3: Experimental Methods

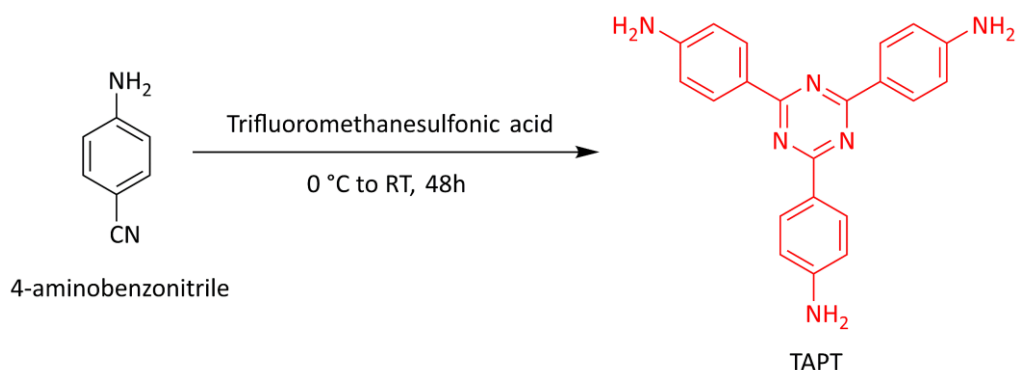
3.1. Chemicals

All chemicals were used as received.

4-aminobenzonitrile, xylene, toluene, dioxane, 6-amino-3-pyridinecarbonitril, trifluoromethanesulfonic acid, methanol (MeOH), ethanol (EtOH), acetone, melamine, 1-methylimidazole (NMI), perylene-3,4,9,10-tetracarboxylic dianhydride (PTCDA), 2-dicyclohexylphosphino-2',4',6'-triisopropylbiphenyl (XPhos), maleic acid (NMR quality), tetrafluoroethylene-perfluoro-3,6-dioxa-4-methyl-7-octenesulfonic acid copolymer (Nafion™ perfluorinated ion-exchange) resin (5 wt%, in a mixture of lower aliphatic alcohols and water, containing 45% water), sodium fluoride (NaF), sodium iodide (NaI), styrene oxide, barium sulfate ($\text{Ba}(\text{SO}_4)_2$) were purchased from Merck. Lithium fluoride (LiF), potassium fluoride (KF), sodium nitrate (NaNO_3), potassium bicarbonate (KHCO_3), sodium tert-butoxide (NaOtBu), 1,4,5,8-naphthalenetetracarboxylic dianhydride (NTCDA), sodium hydroxide (NaOH), were purchased from Thermo Fisher Scientific. Epibromohydrin, deuterium oxide (D_2O), chloroform-D (CDCl_3), glycerol, bis(dibenzylideneacetone)palladium(0) ($\text{Pd}(\text{dba})_2$), propylene carbonate were purchased from Scientific Laboratory supplies. Epichlorohydrin, dimethyl formamide (DMF), m-cresol, chloroform, dimethyl sulfoxide (DMSO), quinoline, dimethylacetamide, N-Methyl-2-pyrrolidone (NMP), acetonitrile were purchased from VWR chemicals.

3.2. Synthesis

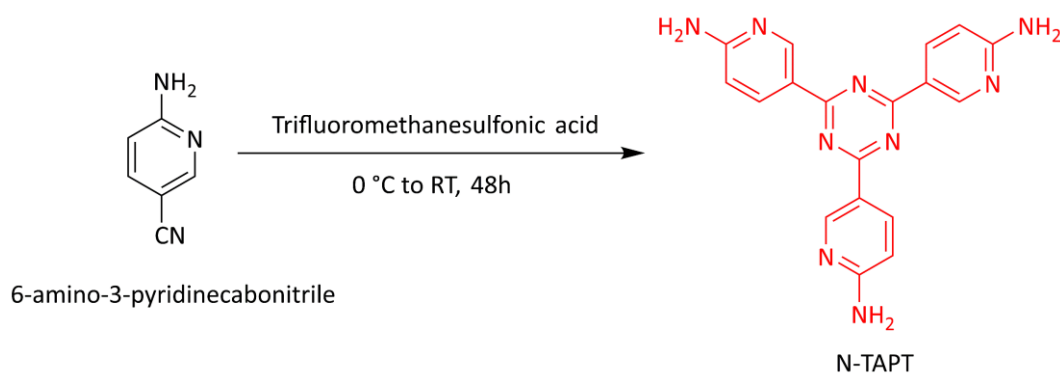
a. Monomer synthesis:



Scheme 3.1: Synthesis of TAPT.

Synthesis of 1,3,5-tris-(4-aminophenyl)triazine (TAPT):

A dried 100 mL two-neck round bottom flask was charged with 4-aminobenzonitrile (772.0 mg, 6.5 mmol) and placed in an ice bath at 0 °C under inert atmosphere. Trifluoromethanesulfonic acid (2 mL) was added dropwise over 20 minutes, maintaining the temperature at 0 °C under an inert atmosphere. The resultant mixture was stirred for 48 h at room temperature. Distilled water (20 mL) was added, and the reaction mixture neutralized by 2 M NaOH solution. Initially, with an increase in pH, an orange precipitate dissolved to give a bright orange solution, which upon further increase in the pH gave a pale-yellow precipitate. The resultant product was filtered and washed with distilled water (3 x 250 mL) and ethanol (3x 50 mL). Yield: 80%.



Scheme 3.2: Synthesis of N-TAPT.

Synthesis of 5,5'-(6-(5-aminopyridin-2-yl)-1,3,5-triazine-2,4-diyl)bis(pyridin-2-amine) (N-TAPT):

In a dried 100 mL two-neck round bottom flask charged with 6-amino-3-pyridinecarbonitrile (1547 mg, 13 mmol) and placed in an ice bath at 0 °C under inert atmosphere. Trifluoromethanesulfonic acid (4 mL) was added dropwise for 20 minutes, maintaining the temperature at 0 °C under an inert atmosphere. The resultant mixture was then stirred for 24 h at room temperature. Distilled water (40 mL) was added, and the reaction mixture was neutralized by 2 M NaOH solution. Initially, with an increase in pH, an orange precipitate dissolved to give a bright orange solution, which upon further increase in the pH gave a pale-yellow precipitate. The resultant product was filtered and washed with distilled water (3 x 250 mL) and ethanol (3x 50 mL). Yield: 80%.

b. Polymer synthesis:

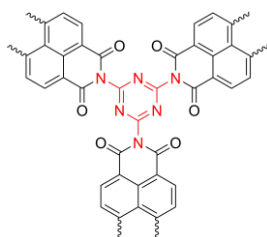


Figure 3.1: BNPI-1

Synthesis of BNPI-1:

A dried round-bottomed flask equipped with mechanical stirring, nitrogen inlet, Dean-Stark trap and a reflux condenser and charged with DMSO (40 ml) and melamine (100 mg, 0.79 mmol). After 5 min of stirring 1,4,5,8,-naphthalenetetracarboxylic dianhydride (321 mg, 1.19 mmol) and salt (0.33, 0.66 and 0.99 mmol, respectively), were added and the reaction mixture stirred at room temperature for 30 min. The temperature was raised gradually to 180 °C and held for 72 hours in a drysyn or high temperature oil bath. The reaction must be carried out in an open Schlenk under N₂ to prevent pressure buildup, with the formation of water (H₂O) as a side product. After cooling to 70 °C, MeOH (50 ml) was added and the precipitate collected and washed with additional DMF and methanol, warm water and acetone (50ml x 3, each). The resulting product was dried at 80°C under vacuum for 24 hours. Yield 40-50%

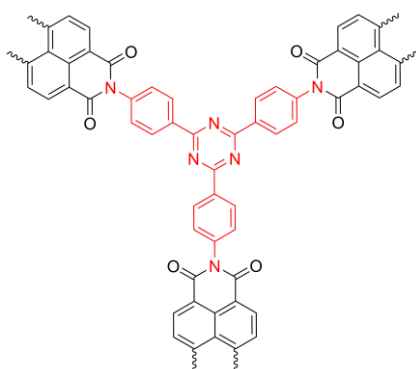


Figure 3.2: BNPI-2

Synthesis of BNPI-2:

A dried round-bottomed flask equipped with mechanical stirring, nitrogen inlet, Dean-Stark trap and a reflux condenser was charged with DMF (50 mL), tris(4-aminophenyl)triazine (280 mg, 0.79mmol) and salt (0.33, 0.66, and 0.99 mmol, respectively). After 5 min of stirring 1,4,5,8,-

naphthalenetetracarboxylic dianhydride (321 mg, 1.19 mmol) was added and the reaction mixture stirred at room temperature for 30 min. The reaction must be carried out in an open Schlenk under N₂ to prevent pressure buildup, with the formation of water (H₂O) as a side product. The temperature was raised gradually to 150°C and held for 72 hours in a drysyn or high temperature oil bath. After cooling to 70°C, MeOH (50 mL) was added and the precipitate collected and washed with additional DMF and methanol, water and acetone (3 x 50 mL each). The resulting product was dried at 80°C under vacuum for 24 h hours. Yield: 70-80%

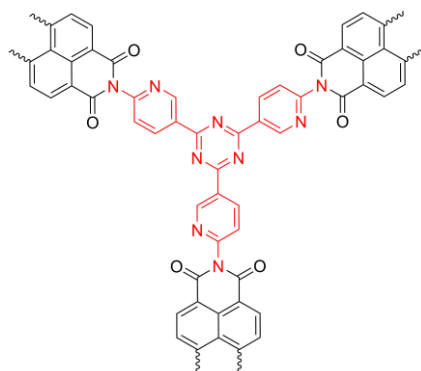


Figure 3.3: BNPI-3

Synthesis of BNPI-3:

A dried round-bottomed flask equipped with mechanical stirring, nitrogen inlet, Dean-Stark trap and a reflux condenser was charged with 1-methyl-imidazole (50 mL), and N-TAPT (280 mg, 0.79mmol). After 5 min of stirring 1,4,5,8,-naphthalenetetracarboxylic dianhydride (321 mg, 1.19 mmol) was added and the reaction mixture stirred at room temperature for 30 min. The reaction must be carried out in an open Schlenk under N₂ to prevent pressure buildup, with the formation of water (H₂O) as a side product. The temperature was raised gradually to 150 °C and held for 72 hours in a drysyn or high temperature oil bath. After cooling to 70°C, MeOH (50mL) was added and the precipitate collected and washed with additional DMF and methanol, water and acetone (3 x 50 mL each). The resulting product was dried at 80°C under vacuum for 24 h hours. Yield: 50-60%

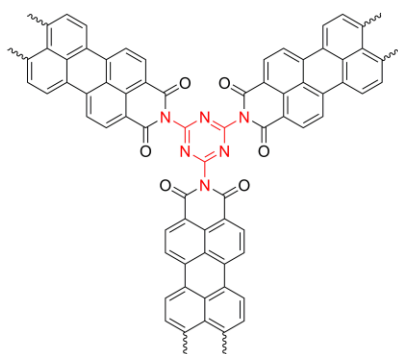


Figure 3.4: pPI-1

Synthesis of pPI-1:

A dried round-bottomed flask equipped with mechanical stirring, nitrogen inlet, Dean-Stark trap and a reflux condenser was charged with 1-methyl-imidazole (40 ml), and perylene-3,4,9,10-tetracarboxylic dianhydride (PTCDA) (466 mg, 1.19 mmole). After 30 min of stirring in room temperature melamine (100 mg, 0.79 mmol) was added and the reaction mixture stirred at 180°C and held for 72 hours. The reaction must be carried out in an open Schlenk under N₂ to prevent pressure buildup, with the formation of water (H₂O) as a side product. After cooling to 70°C, MeOH (50 ml) was added and the precipitate was collected and washed with additional DMF and methanol, warm water and acetone (50ml x 3, each). The resulting product was dried at 80°C under vacuum for 24h. Yield: 60-70%

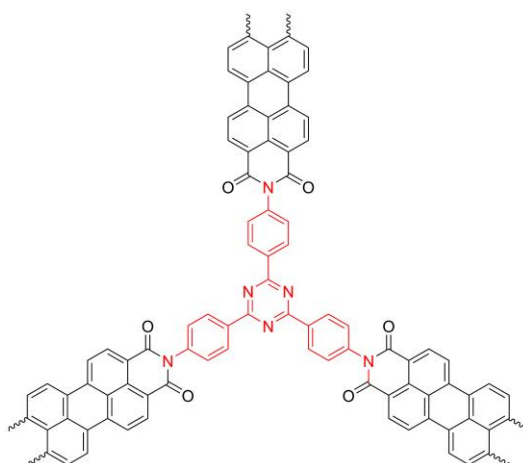


Figure 3.5: pPI-2

Synthesis of pPI-2:

A dried round-bottomed flask equipped with mechanical stirring, nitrogen inlet, Dean-Stark trap and a reflux condenser was charged with 1-methyl-imidazole (40 ml), and perylene-3,4,9,10-

tetracarboxylic dianhydride (PTCDA) (297 mg, 0.76 mmol). After 30 min of stirring in room temperature TAPT (135 mg, 0.38 mmol) was added and the reaction mixture stirred at 180°C and held for 72 hours. The reaction must be carried out in an open Schlenk under N₂ to prevent pressure buildup, with the formation of water (H₂O) as a side product. After cooling to 70°C, MeOH (50 ml) was added and the precipitate was collected and washed with additional DMF and methanol, warm water and acetone (50ml x 3, each). The resulting product was dried at 80°C under vacuum for 24h. Yield: 80-90%

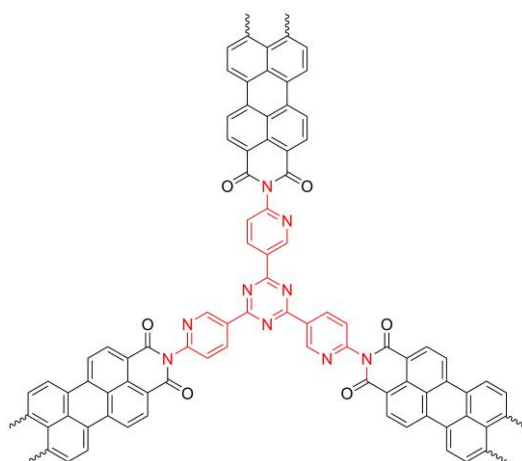


Figure 3.6: pPI-3

Synthesis of pPI-3:

A dried round-bottomed flask equipped with mechanical stirring, nitrogen inlet, Dean-Stark trap and a reflux condenser was charged with 1-methyl-imidazole (50 mL), and N-TAPT (280 mg, 0.79mmol). After 5 min of stirring perylene-3,4,9,10-tetracarboxylic dianhydride (PTCDA) (446 mg, 1.19 mmol) was added and the reaction mixture stirred at room temperature for 30 min. The reaction must be carried out in an open Schlenk under N₂ to prevent pressure buildup, with the formation of water (H₂O) as a side product. The temperature was raised gradually to 150 °C and held for 72 hours in a drysyn or high temperature oil bath. After cooling to 70°C, MeOH (50mL) was added and the precipitate collected and washed with additional DMF and methanol, water and acetone (3 x 50 mL each). The resulting product was dried at 80°C under vacuum for 24 h hours. Yield: 60-70%

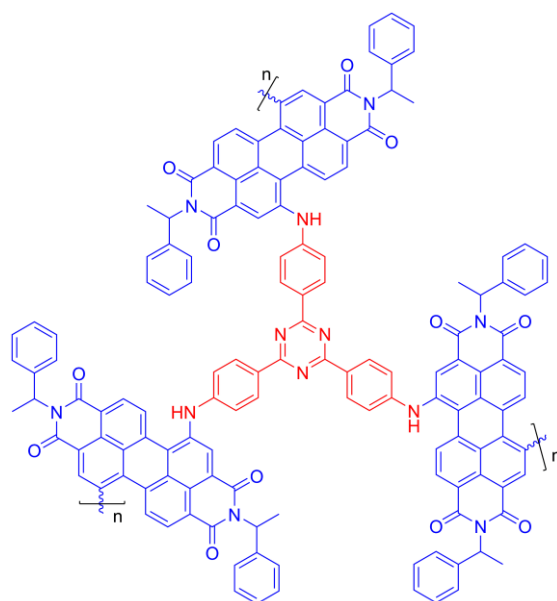


Figure 3.7: p-NDI

Synthesis of p-PDI:

A Schlenk tube was charged with TAPT (0.42 mmol, 150 mg, 1 equivalent), PDI-1 (0.63 mmol, 476 mg, 1.5 equivalent), Pd(dba)₂ (40.0 mg, 0.07 mmol), XPhos (50.1 mg, 0.045 mmol), NaOtBu (461.3 mg, 4.8 mmol, 8 equivalent), and NaF (15 mg, 0.33 mmol) and placed under a nitrogen atmosphere. DMF (40 mL) was added, and the reaction mixture was heated under stirring to 150 °C. After 24 h, the reaction was cooled to room temperature and the products were separated by centrifugation. Yield: 50-60%

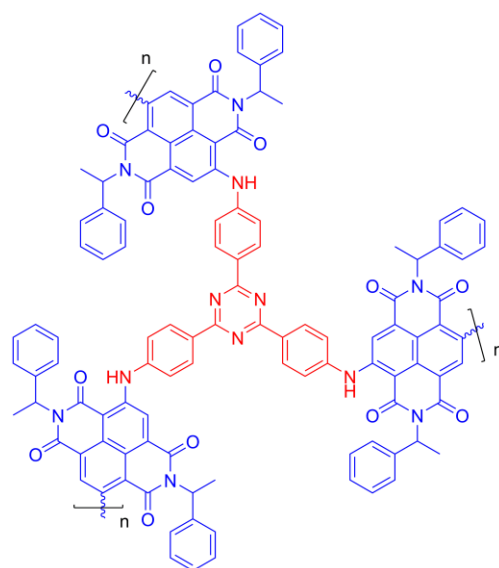


Figure 3.8: p-NDI

Synthesis of p-NDI:

A Schlenk tube was charged with TAPT (0.42 mmol, 150 mg, 1 equivalent), NDI-1 (0.63 mmol, 400 mg, 1.5 equivalent), Pd(dba)₂ (40.0 mg, 0.07 mmol), XPhos (50.1 mg, 0.045 mmol), NaOtBu (461.3 mg, 4.8 mmol, 8 equivalent) and NaF (15 mg, 0.33 mmol) and placed under a nitrogen atmosphere. DMF (40 mL) was added, and the reaction mixture was heated under stirring to 150 °C. After 24 h, the reaction was cooled to room temperature and the products were separated by centrifugation. Yield: 50-60%

3.3. Characterisation techniques

3.3.1. FT-IR Spectroscopy

The Fourier transform infrared (FT-IR) spectra of the pure powder samples were recorded using a PerkinElmer Spectrum Two IR Spectrometer equipped with a UATR Single Reflection Diamond attenuated total reflectance attachment. The spectra were recorded in the wavenumber range of 4000 cm^{-1} to 400 cm^{-1} .

3.3.2. UV-vis-NIR Spectroscopy

The UV-vis-NIR spectra of starting materials and pPIs (3 wt%) mixed with barium sulfate ($\text{Ba}(\text{SO}_4)_2$) were recorded using a Shimadzu UV2600 spectrophotometer equipped with an ISR2600Plus integrating sphere attachment. The spectra were recorded in the wavelength range of 220 nm to 1400 nm.

3.3.3. Powder X-ray Diffraction (P-XRD)

The PXRD patterns were acquired using a Bruker D8 Advance diffractometer equipped with a PSD LynxEye detector. The instrument operated at 40 kV and 40 mA, utilizing $\text{Cu K}\alpha$ radiation with a wavelength of 1.540600 Å. The angle range examined was from 5° to 50° (2θ), with a step size of 0.02° and a step time of 1 second. The diffractometer rotated at a rate of 60 rpm, resulting in a total measurement time of 30-45 minutes.

3.3.4. Thermogravimetry analysis (TGA)

Thermogravimetric analyses (TGA) were carried out on a TA TGA Q500 apparatus in a nitrogen atmosphere (flow rate 30 mL/ min) in the temperature range of 30–800 °C (heating rate 20 °C/min).

3.3.5. Proton Nuclear Magnetic Resonance (H-NMR)

NMR experiments were performed in deuterated solvents such as D_2O , CDCl_3 , and DMSO-d_6 using a Bruker 500, cryo500 or 600 MHz NMR and analysed using commercially available software MestreNova x64.

3.3.6. Scanning Electron Microscopy (SEM) and Energy Dispersive X-ray (EDX)

SEM images were captured using a JSM-IT300 scanning electron microscope (SEM) from JEOL, Japan, operating at 15 kV. The SEM was equipped with an X-Max 80 mm² energy dispersive X-ray (EDX) detector from Oxford Instruments, UK. The analysis software used was AZtec, also from Oxford

Instruments. The samples were coated with a layer of silver using a sputter coater from Agar Scientific, with a silver target of 99.99% purity.

3.3.7. X-ray photoelectron spectroscopy (XPS)

X-ray photoelectron spectroscopy (XPS) measurements were conducted at the Bristol NanoESCA Facility. Powdered samples were pressed into indium foil, subsequently loaded onto carbon tape, and mounted on a Ta plate for analysis. The XPS analysis employed monochromatic Al K α radiation at 270 W. To counteract the charging effects on non-conducting pPIs, a charge neutraliser was employed. The electron analyser used was an Argus analyser, operating at a pass energy of 100 eV for the survey scans and 50 eV for high-resolution scans. The emission angle was set at 35°.

3.3.8. Surface area (BET) and CO₂ uptake Measurements

The samples underwent a drying process on a Schlenk line at a temperature of 180 °C under vacuum conditions for a duration of 24 hours. Gas sorption measurements were conducted using either a Quantachrome Autosorb-1MP or a Quantachrome NovaTouch instrument. Prior to the sorption measurements, the samples were subjected to a three-step degassing process under a high vacuum. Initially, the sample was heated at a rate of 1 °C per minute to 50 °C and held at that temperature for 45 minutes. Subsequently, the temperature was increased to 100 °C at a rate of 2 °C per minute, and the sample was held at this temperature for 100 minutes. Finally, the sample was heated to 180 °C at a rate of 2 °C per minute and held at this temperature for 600 minutes.

The measurements of nitrogen adsorption-desorption were conducted at a temperature of 77.4 K. The isotherms for CO₂ adsorption-desorption were recorded at 1 bar and 273 K and 298 K, respectively. To determine the specific surface areas, the Brunauer Emmett Teller (BET) model was applied to the adsorption or desorption branches of the nitrogen isotherms at 77.4 K. The calculations were performed using the QuadraWin 5.05 software package. Furthermore, the pore sizes were analysed using the commercial Non-Local Density Functional Theory (NLDFT) implemented in the QuadraWin 5.05 software package.

3.3.9. Electrochemical measurement

All the electrochemical performances were investigated with an EG&G Princeton Applied Research Potentiostat Model 273A in a three electrode H-cell setup, using a glassy carbon working electrode

(0.38 cm² contact area of electrode), platinum (Pt) counter electrode and silver chloride (Ag/AgCl) reference electrode. All potentials were converted to the reversible hydrogen electrode (RHE) using $E_{\text{RHE}} = E_{\text{Ag/AgCl}} + 0.059 \times \text{pH} + E^0_{\text{Ag/AgCl}}$, where E_{RHE} is the converted potential vs RHE, $E^0_{\text{Ag/AgCl}} = 0.1976$ at 25 °C, and $E_{\text{Ag/AgCl}}$ is the experimentally measured potential against Ag/AgCl reference.²⁶⁵

Electrolyte preparation (0.1 M KHCO₃):

In a clean 1000 ml volumetric flask, KHCO₃ (10.0114 g) was dissolved in deionised water. Once the solid is completely dissolved, dilute the solution with deionised water to a final volume, resulting in a 0.1 M solution of KHCO₃.

Electrode preparation:

pPis (1.5 mg) were ground to a fine powder and sonicated in isopropanol (500 µL) for 2-3 hours. Nafion (10 µL) was added to the suspension and sonicated for 30 min. The suspension (20 µL) was drop-cast on a clean glassy carbon working electrode. The electrode was dried at a room temperature vacuum oven overnight and used for electrochemical studies.

Electrolyte preparation for NMR analysis after electrochemical reduction of CO₂ experiments

After the chronoamperometry (CA) experiments, the electrolyte (600 µL) was collected from the cathodic side of the H-cell and product detection was undertaken using cryo500 ¹H NMR spectroscopy for methanol and formate, respectively. To determine the amount of methanol and formate produced, which in turn allows the determination of the FE for each product in the system, 1 mM maleic acid (10 µL) was added along with D₂O (180 µL) and the mixture was analysed using ¹H NMR. FEs were calculated using the formula **Equation 1.5 in Chapter 1 (Section 1.7.1)**:

Standard deviation (σ) was calculated using the equation:

$$\sigma = \sqrt{\frac{\sum(x_i - \mu)^2}{N}} \quad \mathbf{1.7}$$

Where N=3, x_i = the faradic efficiencies calculated for methanol and formate respectively and μ = the mean value of the calculated faradic efficiencies for methanol and formate respectively.

Chapter 4: Tuneable naphthalene-based pPIs for CO₂ capture and conversion

This chapter is published in *Advanced Materials*, **2023**, 35, 2211795 (Title: **Selective CO₂ Electroreduction from Tuneable Naphthalene-Based Porous Polyimide Networks**)

Authors: Basiram Brahma Narzary, Benjamin C. Baker and Charl F. J. Faul

(doi.org/10.1002/adma.202211795)

4.1. Introduction

In the past two decades, several strategies have been developed for carbon dioxide (CO₂) capture and storage technologies, including chemical and physical adsorption onto porous organic polymers (POPs).²⁶⁶ However, these strategies incur (significant) additional energy costs for capture, storage and release.²⁶⁷ A promising approach to overcome these limitations is to capture/adsorb gas on porous polymers and utilise the same material as a heterogeneous catalyst for subsequent conversion to valuable chemicals.²⁶⁸ However, CO₂ is inert, has a high C=O dissociation energy (~750 kJ/mol) and is a fully oxidised structure with linear geometry, requiring significant energy input for transformation into new species.^{11,269} Although there are efficient metal-containing covalent organic framework catalysts reported,^{270–272} designing robust and efficient and, ideally, metal-free catalysts (to ensure long-term sustainability) with high surface areas is crucial for the development of future CO₂ capture and conversion technologies to yield products other than CO. The higher surface area materials provide opportunities for enhanced CO₂ storage and electrochemical performance.^{48,273,274} In addition, close interaction between the catalytic surface and CO₂ is necessary to form a bent reactive CO₂^{•-} intermediate – crucial for further reaction by lowering the lowest unoccupied molecular orbital (LUMO) energy and increasing the electron acceptance capacity.^{275,276} A combination of these catalyst properties will allow for successful conversion to more valuable carbon products, such as carbon monoxide (CO), formate, methane (CH₄), methanol (CH₃OH) and, potentially, also higher alcohols and hydrocarbons, depending on the number of electrons and protons involved in the transformation.¹¹

The catalytic conversion of CO₂ can be achieved by chemical, photochemical, electrochemical and biological processes.^{11,213,277,278} As reported in the literature, the electrochemical reduction of CO₂ has many advantages over other conversion processes. For example, reaction parameters such as redox potential, reaction temperature and electrolyte can be directly controlled. In addition, these reactions can be driven by green energy resources, especially if with low energy requirements.²¹² Porous polyimides (pPIs), a class of POPs, are excellent candidates for CO₂ capture and catalysts for electrochemical conversion with beneficial properties such as high surface area, abundant

heteroatoms (especially oxygen and nitrogen) and a wide variety of building blocks.²⁷⁹ pPIs have already been explored for various applications such as gas capture and storage,^{42,280} energy storage,^{106,150,153,155} heterogeneous catalysis,^{115,152} sensing,^{42,137} drug delivery⁴⁷ and functionalised coatings.¹³¹ However, performance of pPIs for both CO₂ capture and electrocatalytic conversion, using the same material, has, to the best of our knowledge, not been explored to date. For state-of-the-art literature comparison for electrocatalytic CO₂ reduction using porous materials, refer **Chapter 1, Section 1.7**.

Two pPIs, BNPI-1 and BNPI-2, were synthesised using two N-containing planar core molecules (melamine and tris(4-aminophenyl)triazine [TAPT]) and a linear linker molecule 1,4,5,8-naphthalenetetracarboxylic dianhydride (NTCDA) via a metal-free polycondensation reaction (**Figure 4.1a**). Surface areas and porosities were tuned using the BXJ approach (**Figure 4.1b**), providing a platform to explore materials with carefully tuned properties for the electrochemical reduction of CO₂.

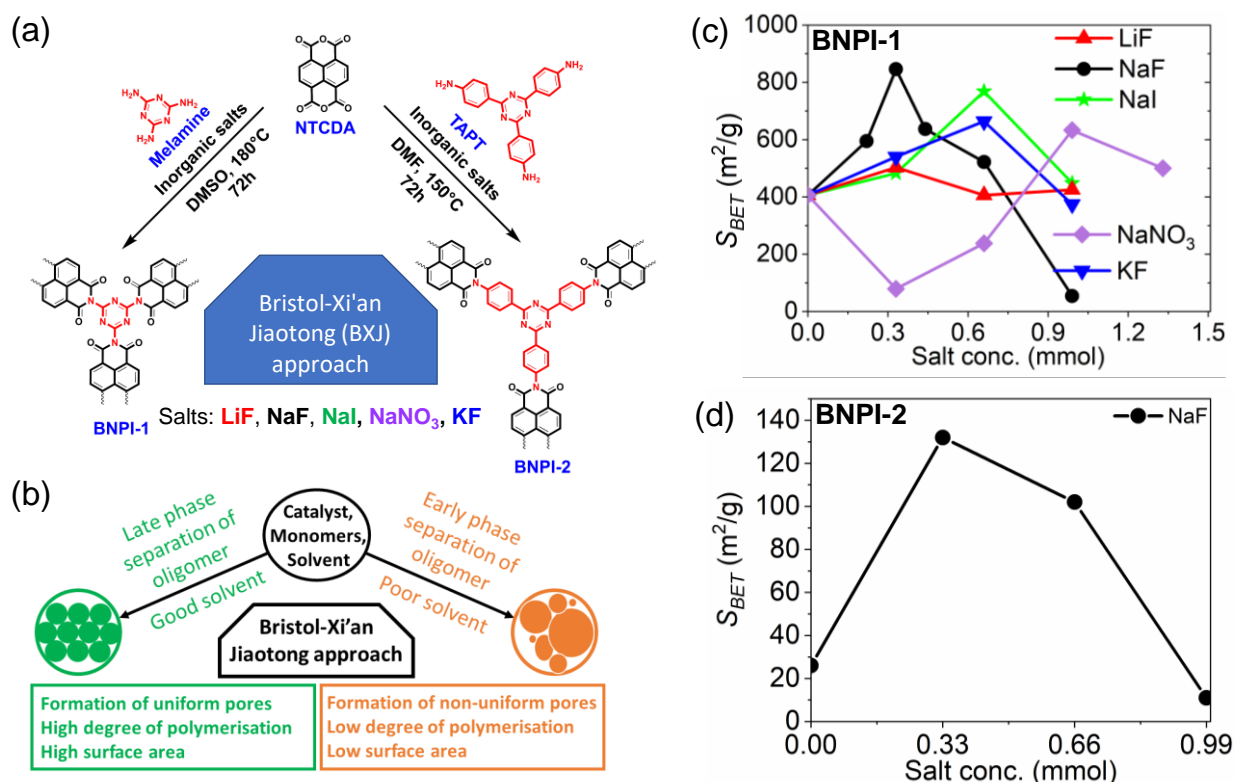


Figure 4.1: (a) Synthetic pathway to synthesise BNPI-1 and BNPI-2, (b) BXJ approach schematic adapted from reference⁴³ and (c, d) optimisation of surface areas of BNPI-1 and BNPI-2 using the BXJ approach by appropriate salt addition.

4.2. Result and discussion

4.2.1. Optimisation of porous properties through the BXJ approach

In the first part of the reaction optimisation utilising the BXJ approach, both pPIs were first synthesised in imidazole (BNPI-1) and *m*-cresol (BNPI-2), respectively, in the absence of salt as control materials; their HSPs were calculated according to the reported literature procedure (see **Appendix 1** for further details of the calculations).^{43,205} The HSPs of BNPI-1 and BNPI-2 were a close match with those of the solvents DMSO and DMF, respectively (see **Appendix 2 Figure A2S9** and **Table S3**); therefore, these two solvents were selected to further tune and optimise synthetic conditions. The individual dipole–dipole interactions (δ_p) and hydrogen-bonding (δ_h) HSP values were further tuned by addition of various inorganic salts.^{43,205} Selected inorganic salts included lithium fluoride (LiF), potassium fluoride (KF), sodium fluoride (NaF), sodium iodide (NaI), and sodium nitrate (NaNO₃). It was demonstrated that addition of various salt concentrations and types allowed tuning and optimisation of the surface areas of both pPIs (see **Figure 4.1c** and **d**). With respect to increased anion size of salts used during BNPI-1 synthesis: as the anion size increased, a higher concentration was required to achieve higher surface areas, as already found in previous studies.^{43,205}

The porosity analyses of the BNPI-1 and BNPI-2 materials produced under these varied synthetic conditions were performed using standard N₂ sorption methods at 77 K and 1 bar (**Appendix 2 Figure A2S6, A2S7** and **Section 1** for calculation methods). The BET surface area of BNPI-1 synthesised in an incompatible solvent (imidazole) was 16 m²/g, while synthesis in the compatible solvent DMSO (as calculated above) yielded a surface area of 406 m²/g (22.5 times higher, see **Appendix 2 Table A2S1**). Further tuning of HSPs utilising BXJ salt addition proved the additional flexibility of our approach, leading to optimisation of surface areas. The highest surface area of BNPI-1 (846 m²/g) was obtained with NaF (0.33 mmol), which is 52 times higher than the unoptimized synthetic conditions (imidazole, without salt) in this study and 2.3 times higher than the best previously reported values for this pPI.¹²⁷ BNPI-1-NaF(0.33) was also analysed in the lower relative pressure region (P/P_0 10e⁻⁷ to 1) to compare analysed in relative pressure range (P/P_0 10e⁻⁵ to 1), showing minimal impact of ultramicropores (< 0.7 nm) range (**Appendix 2 Figure A2S6 g** and **A2S7 g**) on overall properties. Different salts were tested and NaF was found to provide the widest range of tuneability in regard to surface area (see **Figure 4.1c**). The NaF series was therefore selected for further exploration (although all other mentioned salts were also investigated, see **Figure 4.1c** and **Appendix 2 Figure A2** for these additional results). Results from the BNPI-2 optimisation followed a similar trend, with the highest surface area of 132 m²/g obtained with 0.33 mmol of NaF addition in DMF (**Figure 4.1d**). In each case the highest recorded surface area was reported; results from repeat surface area analysis (n=3) of selected high performing pPIs can be found in **Appendix 2 Table A2S2**.

The pore size distribution (PSD) (**Figure 4.2a** and **b** for the NaF series, **Appendix 2 Figure A2S7** for other salts) was calculated from non-local density function theory (NLDFT) and, as found for our PTPA-type materials, revealed that the PSD can be modified with varying salt species and concentration. For BNPI-1 with increasing salt concentration to 0.99 mmol, the PSD was also narrowed towards the microporous region (**Figure 4.2a**, **4.2b** and **Appendix 2 Figure A2S7**), following trends reported in previous studies.^{43,205} The other investigated salts follow similar trends as found for NaF (**Appendix 2 Figure A2S7**).

Powder X-ray powder diffraction (PXRD) data show that both BNPI-1 and BNPI-2 are amorphous in nature (as opposed to the starting materials, see **Appendix 2 Figure A2S4**). Both the pPIs do not lose their amorphous structures with salt additives (NaF shown as a control in **Figure 4.2c**, **4.2d** and see **Appendix 2 Figure A2S4** for other mentioned salts). Interestingly, BNPI-1 synthesised in the incompatible solvent imidazole exhibits a broad peak around 26° (in 2 θ), which corresponds to commonly observed π -stacking of conjugated (and in this case, naphthalene-based) materials ($d = 0.35$ nm). The π -stacking leads to decreased freedoms of growth in network formation, thus reducing the overall surface area.¹⁶⁸ It is noted that the same trend was observed for BNPI-2, see **Figure 4.2d**. As clearly seen from XRD data, syntheses in compatible solvents reduce the π -stacking during the network formation, resulting in significantly higher surface areas. Similar effects were observed during the optimisation of BNPI-2 (**Figure 4.2b**).

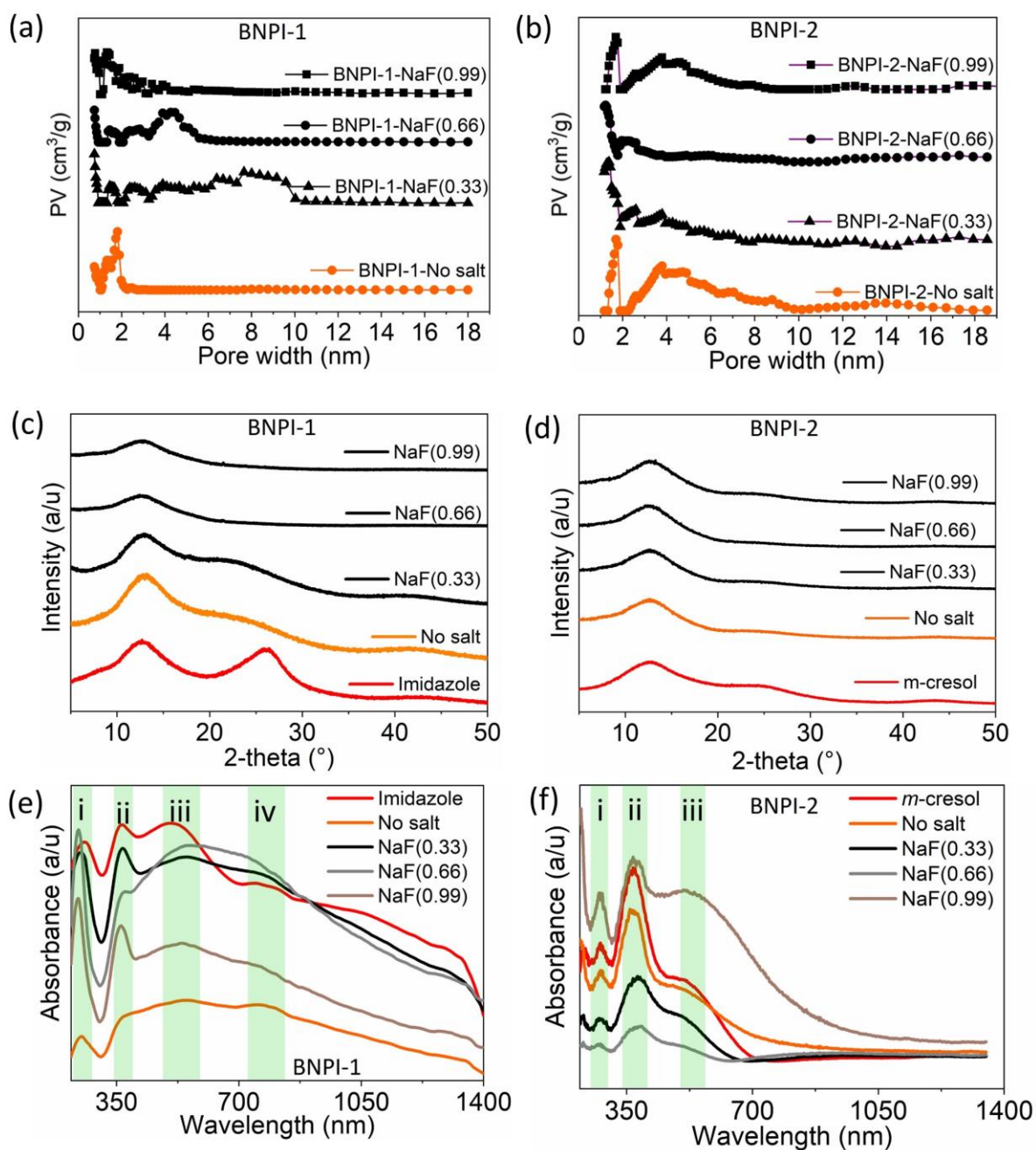


Figure 4.2: (a, b) Pore size distribution of BNPI-1 and BNPI-2, synthesised in imidazole or *m*-cresol and DMSO or DMF with NaF additives, respectively, (where PV = Pore Volume) (c, d) PXRD plot of BNPI-1 and BNPI-1, synthesised in imidazole/*m*-cresol and DMSO/DMF with NaF additives, respectively and (e, f) UV-Vis-NIR spectra of BNPI-1 and BNPI-1, synthesised in imidazole or *m*-cresol and DMSO or DMF with NaF additives, respectively.

UV-Vis-NIR investigations revealed features present in the formed polymers from the starting materials, including absorbances at 250nm (triazine) and 400nm (naphthalene) (i and ii, respectively, in Figure 4.2e and f). The extended conjugation found in the imidazole synthesis by the XRD

investigation is also reflected in the strong absorptions in the visible 450-850 nm region and beyond (iii and iv **Figure 4.2e** and **f**). Red-shifted absorption features into the NIR of the pPIs are attributed to longer conjugation of the formed polymer backbone structures (as the starting materials do not show absorption beyond 500 nm, see **Appendix 2 Figure A2S4**).

Successful formation of the desired polymers was further confirmed by the presence of six-membered polyimide rings ($1680\text{-}1750\text{ cm}^{-1}$) and the absence of the characteristic primary amine -NH stretching ($3460\text{-}3213\text{ cm}^{-1}$), indicating complete imidisation (see **Appendix 2 Figure A2S3** for details). Thermogravimetric analyses (TGA) further confirmed the presence of highly cross-linked products, with degradation temperatures for both BNPI-1 and BNPI-2 $> 350\text{ }^{\circ}\text{C}$ (See **Appendix 2 Figure A2S5**).

4.2.2. CO_2 capture and conversion

The CO_2 uptake was investigated at 273 K and 1 bar as shown in **Figure 4.3a** for selected NaF salt concentrations for BNPI-1 and BNPI-2 (0.33mM, 0.66mM and 0.99 mM). Data recorded at 298 K is shown in **Appendix 2 Figure A2S8** and **Table A2S2**. Results revealed the applicability of our BXJ approach to tune pore sizes, surface areas, and thus CO_2 uptake of the polymers. Exploring the properties of BNPI-1 in the presence of different salt concentrations yielded the highest surface area ($846\text{ m}^2/\text{g}$) and, concomitantly, the highest CO_2 uptake at 11 wt%. The materials synthesized in DMSO (good solvent, but without any salt, yielded lower surface areas ($406\text{ m}^2/\text{g}$) with lower CO_2 uptake (6 wt%). For the BNPI-1 NaF series, trends for CO_2 uptake at both 273 and 298 K mirrored that of the surface areas, each increasing to 0.33 mM of NaF, then decreasing to 0.99 mM of NaF. Further CO_2 uptake experimentation was undertaken on BNPI-1 synthesised with different salts, i.e., where both the anion and cation species were systematically varied (LiF, NaI, NaNO_3 , KF). For these variations only those materials with the highest surface areas, (see **Figure 4.1b** and **c** and **Appendix 2 Figure A2S6** and **Table A2S2**) with respect to each salt were selected for CO_2 uptake studies. The highest CO_2 uptake of 14 wt% was found for BNPI-1 with a surface area of $728\text{ m}^2/\text{g}$, synthesised in the presence of 0.66 mmol NaI, showing the subtle possibilities for tuning and optimising the property-structure-function relationship for these fully crosslinked (and therefore intractable) porous polymers.

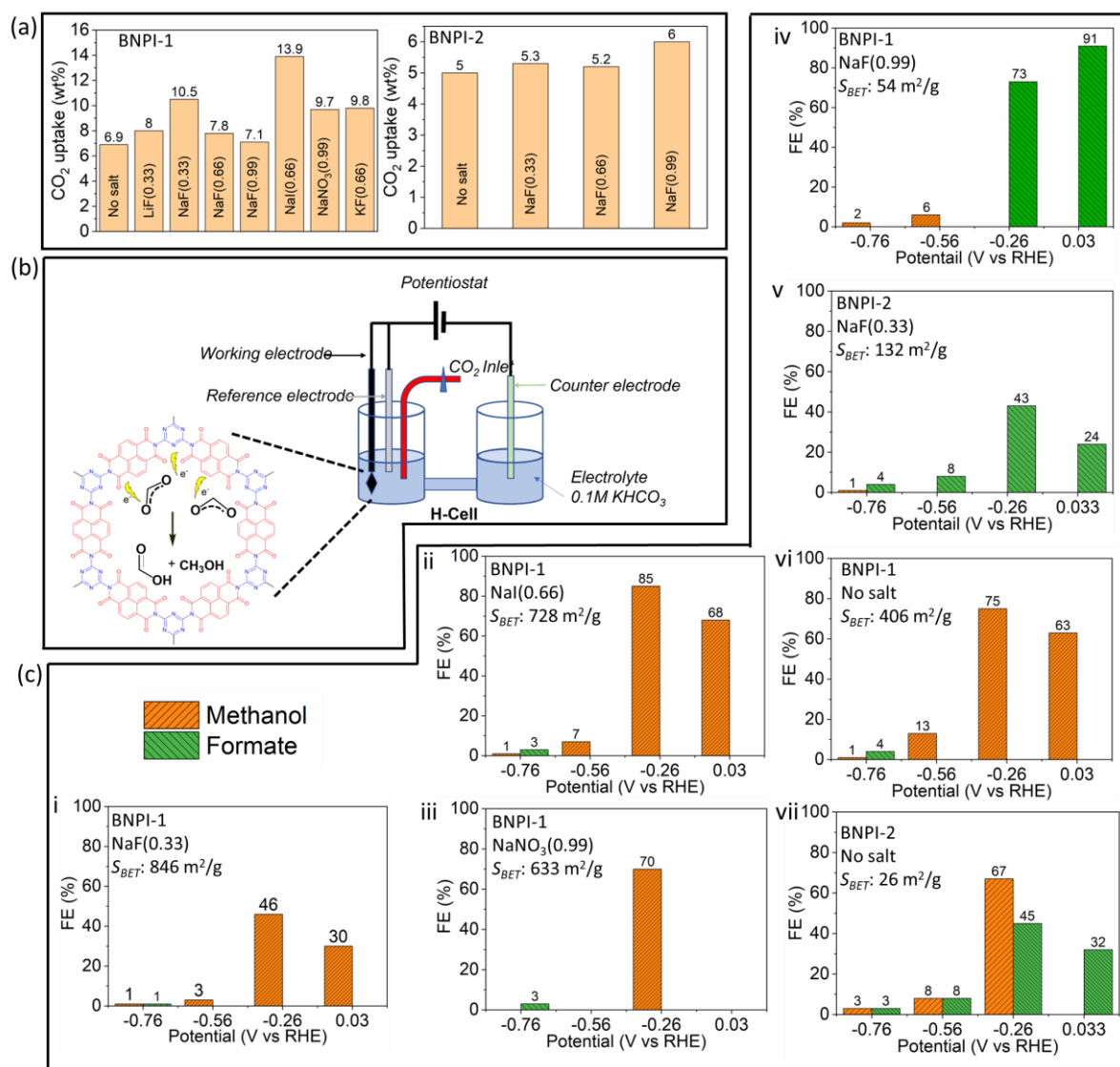


Figure 4.3. Showing CO₂ capture and electrocatalytic reduction using BNPI-1 and BNPI-2 with (a) the CO₂ uptake in wt% of BNPI-1 and BNPI-2 at 1 bar, 273K, for different synthesis conditions, (b) the schematic of the H-cell setup used to convert CO₂ to formate and methanol, showing the proposed interaction of CO₂-pPis^{11,275,276}, (c) the FEs for the formation of CO₂ reduction products (formate and methanol) from H-cell investigations at 298 K, using BNPI-1 and BNPI-2 (from different synthetic conditions optimised by BXJ approach) as catalysts. Products monitored and determined by ¹H NMR analysis.

To investigate the electrocatalytic performance of our pPis towards CO₂ reduction, electrochemical measurements were performed in CO₂-saturated 0.1M KHCO₃ in an H-cell setup (see **Figure 4.3b** and **Appendix 2 Section 6** for details). For these investigations BNPI-1 (NaF 0.33 mmol, NaI 0.66mmol and NaNO₃ 0.99mmol) and BNPI-2 (NaF 0.33 mmol) were selected as potential catalysts, primarily based on the fact that these systems possessed the highest surface area in their respective series (see **Figure**

4.1 c and d). As comparison, further samples were selected: BNPI-1 (NaF 0.99 mmol) as it possessed the lowest surface area, BNPI-1 (NaI 0.66 mmol) was selected as it had the highest CO₂ uptake (14 wt%), and BNPI-1 and BNPI-2, prepared with no salt, were investigated as controls.

Cyclic voltammetry (CV) studies of these selected pPIs performed in argon- and CO₂-saturated 0.1M KHCO₃ electrolyte solution in the potential range -1 to 1 V vs RHE demonstrate that the materials are catalytic active for the reduction of CO₂. Although the CV curves of BNPI-1, from all synthetic conditions, do not show any distinct redox peaks in the potential range -1 to 1 V vs RHE, the current density in the argon-saturated electrolyte investigations is higher than the CO₂-saturated electrolyte at higher negative potential (i.e., at -1 V vs RHE). The increased current density is attributed to higher hydrogen evolution taking place in the argon-saturated electrolyte at higher negative potential (-1 V vs RHE), which confirms the catalytic activity of our materials.²⁶⁸

Interestingly, BNPI-2 shows a shift in the position of the redox peak with a change in saturation gas, and thus pH of the electrolytes (the pH for CO₂-saturated and argon-saturated 0.1M KHCO₃ is 7.21 and 9.36, respectively). The shift in the redox peak positions, from 0.3 to 0.1 V vs RHE (oxidation) and from 0.14 to 0.02 V vs RHE (reduction) could be attributed to more facile oxidation and reduction processes under acidic conditions.^{281,282}

Chronoamperometric (CA) analyses of both pPI systems under the different synthetic conditions highlighted previously (BNPI-1; no salt, 0.33 NaF, 0.99 NaF, 0.66 NaI, 0.99 NaNO₃ and BNPI-2; no salt and NaF 0.33mmol) were carried out at constant potentials of -0.76, -0.56, -0.26, and 0.03 V vs RHE for 1800 s in CO₂-saturated 0.1 M KHCO₃ (**Appendix 2 Figure A2S11**). The liquid products obtained after electrocatalysis was analysed by ¹H NMR (see **Appendix 2** for experimental details). The signals at 8.45 and 3.36 ppm in NMR spectra confirm that the highlighted pPIs electrocatalytically reduced CO₂ to formate and methanol, respectively (**Appendix 2 Figure A2S 12-18**). It is proposed in the literature that the Lewis acid–base interaction of pPIs with CO₂ weaken the linear symmetry of the CO₂ molecules, thus forming a bent CO₂^{δ-} species with decreased LUMO energy, which increases the electron acceptance capability.^{275,283} Interestingly only lower electron reduction products were formed, due to the weak semiconducting nature of the pPIs (no obvious semiconductor characteristics observed in UV-vis-NIR spectra, although related materials were used as conducting electrode materials in various battery applications.^{119,153,278}). It is proposed that the interaction of CO₂ with heteroatoms of the pPIs favour predominantly formate and methanol production, ascribed to the bent nature of the CO₂ when coordinating with the polymer framework (see reported electro-reduction pathways^{11,275,276}). We further speculate that the smaller pore sizes inhibit dimerization (necessary for giving C₂ and beyond products). It is noted that when CA investigations were undertaken in argon-

saturated 0.1 M KHCO₃ no reduction products were detected by ¹H NMR. These results confirmed the need for CO₂ to be present to generate the observed products, and further indicating stability of the catalysts under these conditions. In addition, the highly cross-linked nature of the pPIs (ensuring stable thermal and chemical properties, see **Appendix 2 Figure A2S5**) and the functional stability of the loaded catalysts (from CA analysis) demonstrates the overall stability of our pPIs.

The faradaic efficiencies (FEs) were calculated for 2- and 6-electron pathways for CO₂ reduction to formate and methanol (shown in **Figure 4.3c**, pathways shown in the **Appendix 2 Table A2S3**, calculation methods shown in **Appendix 2 Section 1**). Using BNPI-1 (NaI 0.66 mmol), with the highest CO₂ uptake (14 wt%, surface area 728 m²/g), the highest FE of 85% was achieved for methanol production at -0.26V vs RHE. Interestingly BNPI-1 (NaF 0.99 mmol), with the lowest surface area (54 m²/g) gave a high FE for formate of 91% at 0.03 V vs RHE. The other pPI with a very low surface area (BNPI-2 no salt, 26 m²/g) showed a FE for methanol of 67% at -0.26V vs RHE and FE of 45% for formate. (The sum of the faradaic efficiency (methanol 67%, formate 45%) exceeding 100% at -26 V vs RHE in the **Figure 4.3c, vii**. The possible reasons for this anomaly may be due an overestimation of sampled volume, sampling pre-concentrated products, or spontaneous generation of product through a chemical reactions like corrosion or degradation.²⁸⁴) However, it is noteworthy that the BNPI-2 sample with higher surface area (NaF 0.33 mmol, 132 m²/g) exclusively produced formate (FE of 43% at -0.26V vs RHE).

To clarify the influence of the tuneable physical properties of these pPIs, we also investigated the influence of surface area and PSDs on CO₂ reduction product formation. For BNPI-1 (for each of the synthetic conditions selected for **Figure 4.3c**) the general trends observed were that higher surface areas (> 400 m²/g) gave increased FE for methanol formation (FE of up to 85% at -0.26 V vs RHE), while lower surface area materials (< 54 m²/g) gave increased FE for formate production at lower overpotentials (FE of up to 91% at 0.03 V vs RHE) (see **Figure 4.4**). For BNPI-1 at higher negative potentials (-0.56 and -0.76 V vs RHE) formate production was observed (at very low FE of 3-4%) for catalysts with surface areas of > 406 m²/g, with no formate production observed for the lower surface area BNPI-1 NaF (0.99 mmol, 54 m²/g) at the same potentials. Comparisons of PSD (**Figure 4.2a**) of the BNPI-1 products showed that increased pore widths (into the mesoporous region) gave an increased tendency to form methanol.

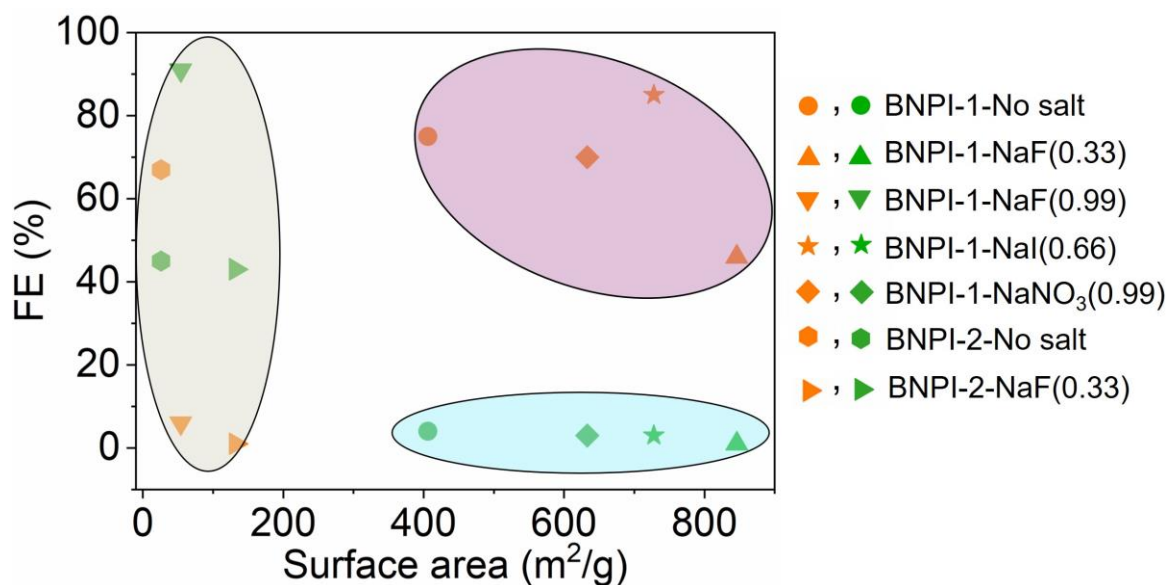


Figure 4.4. Plot of surface areas (m^2/g) vs FEs (%) demonstrating the observed trends across optimised pPIs of BNPI-1 and BNPI-2. All orange symbols represent data for methanol production; all green symbols represent data for formate production.

Recorded surface area of BNPI-2 ($132 \text{ m}^2/\text{g}$ after optimisation, $26 \text{ m}^2/\text{g}$ before) was significantly lower than BNPI-1. Despite this lower surface area, BNPI-2 reduced CO_2 to both formate and methanol. BNPI-2 with a surface area of $132 \text{ m}^2/\text{g}$ yielded high FEs for formate production (up to 43%), while BNPI-2 with surface area of $26 \text{ m}^2/\text{g}$ yielded a mixture of formate and methanol (FEs of 45 and 67%, respectively), as shown in **Figure 4.3** and **4.4**. These results suggests that the pathway of CO_2 reduction to product formation is strongly influenced by the material's surface area, with higher surface areas exhibiting better electrocatalytic performance for methanol production, as seen in recent studies.^{274,285} However, these initial studies would need further refinement for a wider range of conditions, and materials, before more general trends can be established.

Further electrocatalytic analysis, with regard to CO_2 reduction, was undertaken on various BNPI-1 and BNPI-2 materials to calculate current densities (**Appendix 2 Figure A2S10 b** and **c**). Although little difference was observed in current densities vs potential of the various pPIs analysed, further investigation showed that the highest FEs, for both formate and methanol in BNPI-1 and BNPI-2, was observed at low current densities ($< 50 \mu\text{A}/\text{cm}^2$) (**Figure 4.5 a-d**). These low current densities demonstrate the very promising effectiveness of our materials as electrocatalysts for CO_2 reduction.^{286,287}

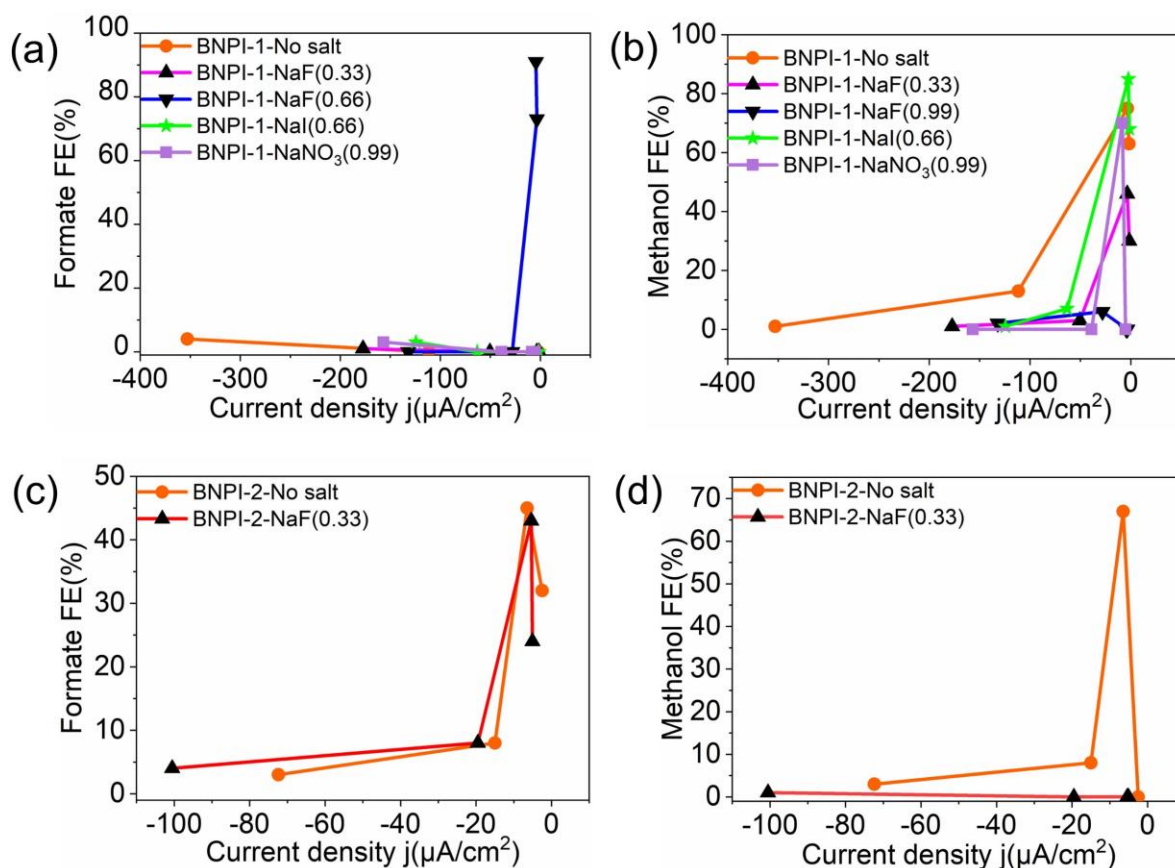


Figure 4.5: (a-d) Analysis of current densities vs formate and methanol production from CO_2 reduction using BNPI-1 and BNPI-2 as electrocatalysts.

pPIs demonstrated best metal-free porous electrocatalysts for producing formate and methanol with high FE (91% and 85%, respectively) from CO_2 via electrocatalytically. To the best of my knowledge, metal-free POPs have not been explored for electrocatalytic CO_2 reduction. However, several metal-containing POPs (such COFs and covalent triazine frameworks (CTFs), functionalised with metal (Fe, Co, Ni, Cu, Mn, or Re) through building blocks metalation or post-synthetic modification, have been investigated for electrochemical CO_2 reduction. Nevertheless, these catalysts exhibit high selectivity for CO production with high FE (96% and 97% with Co-phthalocyanine COF^{288} and Ni-porphyrin-based CFT^{289} , respectively). Recently, only Raja et al,²⁹⁰ reported methanol production with the CTF-Cu-SACs electrocatalyst, achieving a FE up to 72%, which is lower than pPIs (this work). MOFs have been extensively explored for electrocatalytic CO_2 reduction, successfully converting CO_2 to formate (Bi MOF,²²⁸ FE 95.5%) and methanol (HKUST-1(Cu, Ru),²⁹¹ FE 47%).

In this study, pPIs outperformed various metalated POPs in methanol and formate production and showed more effective in methanol production compared to MOFs. However, MOFs outperformed

pPIs in formate production and demonstrated the ability to produce higher carbon (C2) reduction products.^{224,292} The drawbacks of metal-containing catalyst have been discussed in **Chapter 1, Section 1.7**. Compared with various metalated POPs and MOFs, pPIs offer a promising avenue for effective metal-free electrocatalyst, particularly in cost-effectiveness (ca. \$30-35 per gram of pPIs), stability and environmental sustainability are considered. Moreover, fine-tuneable porosity properties allow directly control and select the conversion products is advantage over other porous materials. However, long-term performance should be investigated for industrial utilisation and further research and optimisation are needed for producing C2 and higher carbon reduction products.

4.3. Conclusion:

In the search for scientific solutions to global challenges, porous materials are well known for their ability to capture CO₂. Tuneability of properties, and also CO₂ capture as function, is a challenge that has engaged the scientific community extensively. We have shown that through our developed BXJ approach we can now carefully tune properties (with significant increases in surface areas and narrowing of PSDs) and the ability of our investigated pPIs to capture CO₂ (up to 14 wt%). In an exciting step forward, we have now showed in this study that our pPI materials (prepared metal-free) are also catalytically active under electrocatalytic conditions, converting CO₂ to economically important chemical feedstocks. Combining these two approaches (i.e., BXJ tuneability and this new-found function), we have demonstrated a new route to tuning the production of two distinct reduced C1 species – formate and methanol. With the ability to tune HSPs, properties and function of these pPI materials, and with that the ability to selectively produce valuable feedstocks from CO₂, we envisage that our approach will find wide application and contribute significantly to solutions for global challenges related to CO₂ capture and conversion.

Experimental section: Appendix 2

Chapter 5: Perylene-based pPIs for CO₂ capture and conversion

Part of this section is accepted for publication in the RSC's *Materials Chemistry Frontiers* (13th August 2023).

Title: **Bifunctional Metal-Free Porous Polyimide Networks for CO₂ Capture and Conversion**

Basiram Brahma Narzary, Ulzhalgas Karatayeva, Jerry Mintah, Marcos Villeda-Hernandez, and Charl F. J. Faul

5.1. Introduction:

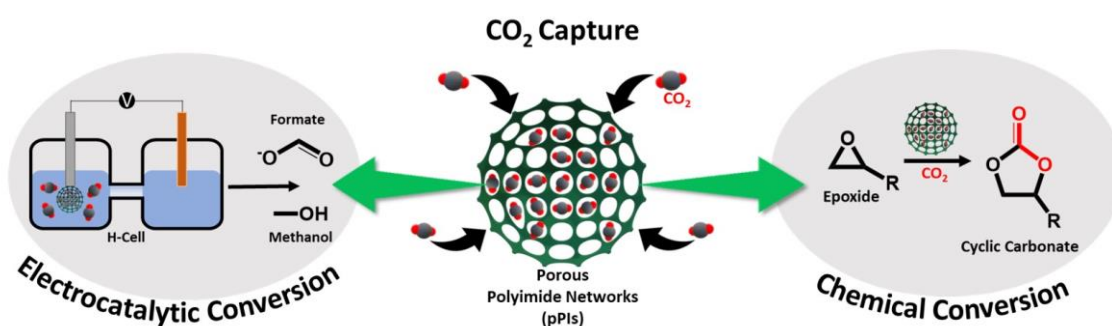
Climate change is the most significant challenge humanity is facing in the 21st century, caused by continuously increasing human activity, leading to excessive anthropogenic CO₂ emissions. However, CO₂ has the potential to be used as a very abundant, inexpensive, and non-toxic source of carbon for industrial utilisation.^{293,294} Therefore, capturing and converting CO₂ into useful chemical feedstocks offer an important emerging approach to developing a carbon-neutral alternative to fossil fuel resources.^{295,296}

From a sustainability perspective, CO₂ can be transformed into cyclic carbonates via the cycloaddition reaction between carbon dioxide and epoxides,²⁵⁹ and be photochemically²⁹⁷ and electrocatalytically²⁹⁸ reduced to valuable chemicals and fuels. Cyclic carbonates are industrially important and utilised in diverse applications, including as building blocks for polymeric materials,²⁴⁶ solvents,²⁴⁷ and, importantly, as electrolytes for lithium-ion batteries.²⁴⁸ Additionally, photochemical and electrochemical reduction of CO₂ can lead to the production of highly desirable C1, C2, and higher carbon products.^{297,298} To date various heterogeneous catalytic systems, including transition metals, have been developed and extensively researched for CO₂ conversion.^{11,299} However, the use of metal catalysts are limited due to their high cost, uncertainty in terms of long-term availability and sustainability, poor selectivity, low durability, susceptibility to gas poisoning, and negative environmental impact, hindering their application in the industry.³⁰⁰ To overcome the limitations of traditional metal catalysts, a variety of metal-containing porous materials, specifically covalent-organic frameworks (COFs),^{271,301} and metal-organic frameworks (MOFs),^{302,303} have been widely explored as effective CO₂ sorption materials, and, more recently, also as materials for conversion. For state-of-the-art literature comparison for chemical conversion of CO₂ using porous materials, refer **Chapter 1, Section 1.8**. However, many obstacles remain in the development of the CO₂ capture and conversion processes, including the design of stable and metal-free materials with high CO₂ adsorption abilities and selectivity, effective CO₂ conversion under benign conditions, affordability and recyclability.

pPIs are an interesting class of metal-free highly cross-linked porous materials that have shown promising results for CO₂ capture owing to their high porosity, synthetic flexibility, and excellent physical and chemical properties.²⁷⁹ Based on these attractive properties, the application of pPIs has been extensively explored in the fields of gas capture and storage,^{38,42} energy storage,^{106,150,153,155} sensing,^{42,137} drug delivery⁴⁷ and functionalised coatings.¹³¹

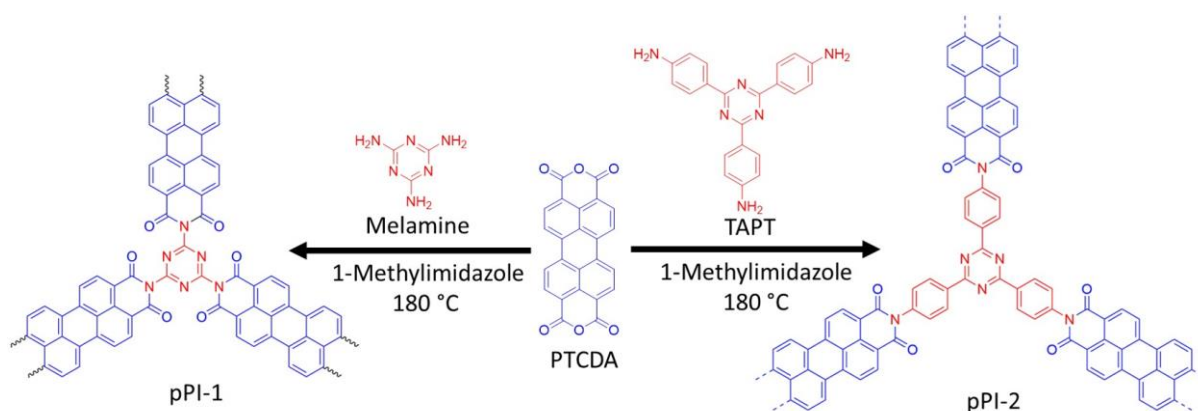
Post-synthetic modification of pPIs with metal species (Pd and Cu) have been explored for use as heterogeneous catalysts, including for Suzuki coupling reactions,^{115,152} and aerobic oxidation of benzyl alcohol.³⁰⁴ However, the route to transforming CO₂ (chemically and electrocatalytically) into value-added chemicals has not been explored to date for metal-free pPIs, despite their high CO₂ affinities. These high affinities, stemming from abundant heteroatomic active sites in their structure, have been shown to yield enhanced interactions in both electro- and chemo-catalytic processes.^{181,275} The mobility of electrons, required for such catalytic processes, can furthermore be facilitated by the presence of conjugated structures within the backbone, especially if an organic semiconductor is incorporated. We have recently shown the validity of this approach for the case of poly(naphthalene imide)s, specifically for the electrocatalytic reduction of CO₂ to formate and methanol.³⁰⁵ Here we explore the use of perylene tetracarboxylic dianhydride (PTCDA) as a further well-known example of suitable conjugated materials for such approaches.³⁰⁶

In this investigation we explore the use of perylene-based pPIs, for the first time, at standard pressures as metal-free heterogeneous catalysts for incorporating CO₂ in epoxides to form cyclic carbonates, as well as for electrocatalytic CO₂ conversion into valuable fuels and feedstocks (see **Scheme 5.1**).



Scheme 5.1: Sustainable routes to CO₂ capture and conversion using pPIs.

5.2. Results and Discussion



Scheme 5.2: Synthetic pathway to **pPI-1** and **pPI-2**.

pPI-1 and **pPI-2** were obtained by polycondensation of PTCDA with melamine and tris-(4-aminophenyl)triazine (TAPT), respectively (**Scheme 5.2**). The successful formation of both pPIs was confirmed by Fourier-transform infrared spectroscopy (FT-IR), ultraviolet–visible–near infrared spectroscopy (UV-Vis-NIR), thermogravimetric analysis (TGA), powder X-ray diffraction (PXRD), scanning electron microscope (SEM) and energy-dispersive X-ray spectroscopy (EDX), as shown in **Figure 5.1(a-f)** and **Appendix 3 Figure A3S9 and Table A3S1**. The characteristic FT-IR absorption signals at 1773 and 1707 cm^{-1} are attributed to the symmetric and asymmetric vibrations, characteristic of carbonyl groups in the newly formed six-membered polyimide rings of **pPI-1** and **pPI-2**. Additionally, the absence of -NH stretching signals (3460–3213 cm^{-1}) from the starting material shows complete condensation of amine moieties to form the respective pPI. The signal at 1446 cm^{-1} confirms the presence of triazine units in both polymers. The maximum UV-Vis-NIR absorption wavelength (λ_{max}) of **pPI-1** and **pPI-2** are 733 and 764 nm, respectively, with absorption features extending beyond 1400 nm, indicating the formation of new products (**Figure 5.1d**). The amorphous nature of **pPI-1** and **pPI-2** were confirmed by PXRD measurements, with broad peaks at 12.5°, commonly observed for POPs.⁴² A further broad peak centred around 26° originates from π -stacking between the aromatic units (**Figure 5.1c**).⁴² Thermogravimetric studies under nitrogen (N_2) atmosphere revealed degradation temperatures (T_{dec}) of 400 °C and 590 °C, with 45% and 70% char yields at 800 °C, respectively, for **pPI-1** and **pPI-2**, confirming the excellent thermal stability of these pPIs.

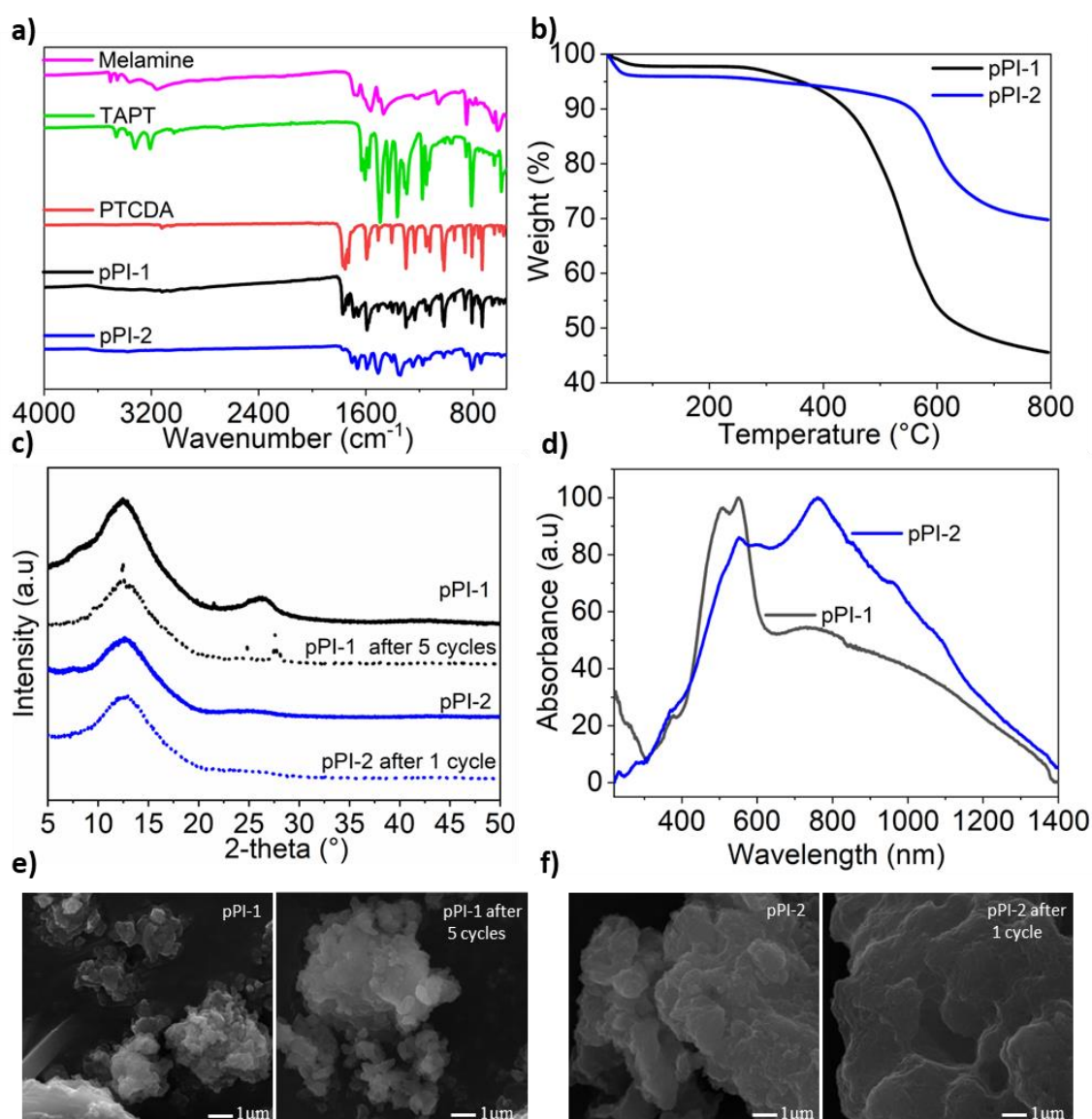


Figure 5.1: (a) FT-IR spectra of starting materials and **pPI-1** and **pPI-2**, (b) TGA plot of **pPI-1** and **pPI-2** under N_2 atmosphere, (c) PXRD of **pPI-1** and **pPI-2** (solid line) and after use as a catalyst (dotted line) (peak 2θ 21.5 is from the paraffin wax used to fix samples to the sample holder during our XRD analysis)⁴, (d) UV-Vis-NIR spectra of **pPI-1** and **pPI-2**, (e) SEM of **pPI-1** before and after 5 cycles used as a catalyst, and (f) SEM micrographs of **pPI-2** before and after 1 cycle used as a catalyst.

The porosity properties of pPIs were investigated by recording N_2 sorption isotherms at 77 K (see **Appendix 3 Figure A3S4**). The isotherms show no significant N_2 -uptake at lower relative pressures (P/P_0), with some uptake observed at higher relative pressures (P/P_0). This behaviour indicates the presence of micro- and macropores, as confirmed in pore size distribution (PSD) calculations using the non-local density functional theory (NL-DFT) method (see **Appendix 3 Figure A3S4**).⁴² These isotherms could be described as typical Type II isotherms according to the IUPAC classification,³⁰⁷ with the specific surface areas (S_{BET}) of **pPI-1** and **pPI-2** 20 and 342 m^2/g , respectively. Additionally, the CO_2

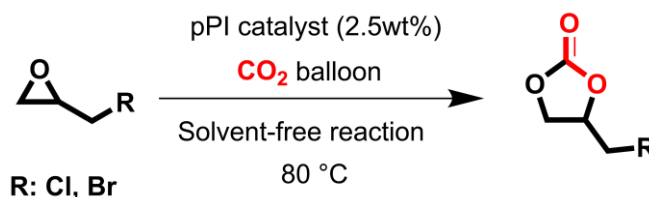
uptake capabilities of the pPIs were investigated at 273 K (2 wt% and 5 wt% for **pPI-1** and **pPI-2**, respectively) and 298 K (0.8 wt% and 3 wt% for **pPI-1** and **pPI-2**, respectively) at 1 bar pressure (see **Table 5.1** for full details). Even though **pPI-1** exhibits poor S_{BET} surface area, the relatively high CO₂ uptake of this polymer may be attributed to the strong affinity between its constituent heteroatoms and CO₂.^{308,309} To quantify the interaction between the pPIs and CO₂, the isosteric heats of adsorption (Q_{st}) were calculated from the absolute adsorption isotherms recorded at 273 and 298 K (**Table 5.1**). The highest adsorption enthalpies of **pPI-1** and **pPI-2** are 39 kJ/mol and 30 kJ/mol, respectively, as shown in **Table 5.1**. These values indicate physisorption processes and interactions for both of these polymers with CO₂. Interestingly, **pPI-1** has stronger CO₂–surface interactions (Q_{st} 39 kJ/mol), thus resulting in moderate CO₂ uptake, even with a surface area (20 m²/g) 17 times lower when compared with **pPI-2** (342 m²/g).

Table 5.1: Porosity parameters and CO₂ uptake at 273 K and 298 K at 1 bar.

Polymer	S_{BET} (m ² /g)	PV (cm ³ /g)	CO ₂ uptake (wt%)		Q_{st} (kJ/mol)
			273 K	298 K	
pPI-1	20	0.07	2.0	0.8	39
pPI-2	342	1.21	4.9	3.0	30

5.2.1. pPI-catalysed chemical conversion of epoxides (using balloon pressure)

The cycloaddition of CO₂ to epoxides to yield cyclic carbonates is commonly performed using potentially unsuitable metal-containing catalysts (e.g., Zn@SBMMP and Bp-Zn@MA) and under undesirable, energy intensive high temperatures (160 °C) and pressure (~20 bar) environments.^{310–314} The presence of a co-catalyst (e.g., tetrabutylammonium bromide (TBAB)) is also required in most cases, increasing cost and molecular economy.^{315,316} The primary driving force behind the cyclic carbonate synthesis from CO₂ and epoxide is substrate activation. Several studies have already shown that there are three distinct mechanistic pathways: CO₂ activation, epoxide activation, or simultaneous activation of both CO₂ and epoxide.^{249–251} The catalyst must have the capability to interact with the substrate and activate it accordingly. Considering the abundant N heteroatoms present in pPIs, we propose that the activation of CO₂ occurs via Lewis-acid base interactions (for detailed plausible mechanisms, refer to **Appendix 3, Scheme A3S1**). In-situ chemical characterisation and computational simulation studies would be beneficial to precisely understand the exact mechanism and interaction between pPIs with CO₂ and epoxide, which however fall outside the scope of this study.



Scheme 5.3: pPI-catalysed, solvent-free cyclic carbonates synthesis from CO₂ and epoxides.

Here we showed the successful application of our pPIs, prepared in the absence of any metal-containing catalysts, for the metal-free, solvent-free cycloaddition of CO₂ to epoxides under standard pressure (*i.e.*, using a balloon filled with CO₂). We furthermore find that no co-catalysts are required for quantitative transformation, with all reactions also performed in the absence of solvent (**Scheme 5.3**). The well-studied cycloaddition of CO₂ to epichlorohydrin (ECH) was chosen as a benchmark reaction for optimisation. As shown in **Table 5.2**, both pPIs efficiently converted ECH to (chloromethyl)ethylene carbonate (CMEC) with a yield of 98% (using **pPI-1**) and 90% (using **pPI-2**), respectively, at 80 °C and after 72 h, in the absence of solvent. Time-dependent analysis of the conversion for both **pPI-1** and **pPI-2** confirmed high conversions only after 72h, as shown in **Figure 5.2a** and **Appendix 3 Figure A3S5**, respectively.

The higher conversion of **pPI-1** could be attributed to the stronger surface interactions with CO₂, as reflected by the Q_{st} value of **pPI-1** (39 kJ/mol) vs that of **pPI-2** (30 kJ/mol). To explore the effect of temperature on the resulting yield, the catalysed reaction was carried out at 60, 80 and 100 °C; with the yields plateauing at 98% as shown in **Figure 5.2b**. The catalyst loading used in the cycloaddition transformation was initially fixed at 2.5wt% (30 mg) of catalyst for 1 mL of neat ECH, giving the highest conversion (**Figure 5.2c**). Subsequently, the catalyst loading was increased to 4.8 wt% (60 mg) and 10 wt% (125 mg). Interestingly, even with increased catalyst loading, the transformation of ECH (at 80°C, over a 72-hour duration) remained unaltered or equivalent to the conversion achieved with 2.5 wt% catalyst loading. Decreased catalyst loading (1.2 wt%) yielded lower transformation (57%). Therefore, 2.5 wt% catalyst loading was selected as the optimum catalyst loading during this investigation.

One of the important considerations of heterogeneous catalysts for industrial applications is recyclability.^{44,317} Thus, we investigated the recyclability of **pPI-1** in the model reaction, using ECH and CO₂ as reactants. In each cycle, **pPI-1** was recovered by centrifugation, washed and dried before being reused in a repeat reaction with a fresh batch of the ECH substrate. The catalyst was found to be recyclable and reusable for up to five cycles without significant loss in catalytic activity, as shown in **Figure 5.2d**. It was also observed that **pPI-1** retained its amorphous structure after going through 5

catalytic cycles as shown by XRD (Figure 5.1c), SEM (Figure 5.1e) and chemical composition (see Appendix 3 Table A3S1 and Figure A3S9). EDX revealed an increase in oxygen and carbon content within both pPIs (pPI-1 and pPI-2) after catalysis, indicating the binding of CO₂ to the catalyst. X-ray photoelectron spectroscopy (XPS) supported these findings, showing changes in the oxygen content of the pPIs after catalysis, implying an increase in C-O and/or O-C=O bonds, originating from the reactive CO₂ species (see the ESI Figure S10 for XPS results). Cl signals were detected after catalysis, suggesting that the catalyst also interacted with the epoxide substrate (ECH). To gain a more precise and detailed understanding of the nature of these interactions between the catalyst, CO₂ and the epoxide, in-situ chemical characterisation will be part of our future investigations. The potential of using these catalysts in industrial settings is underlined by the physical, chemical and thermal stability, recyclability and lack of obvious changes in catalytic activity or morphology, as also confirmed by additional SEM images recorded post-catalysis (see Figure 5.1 e and f).

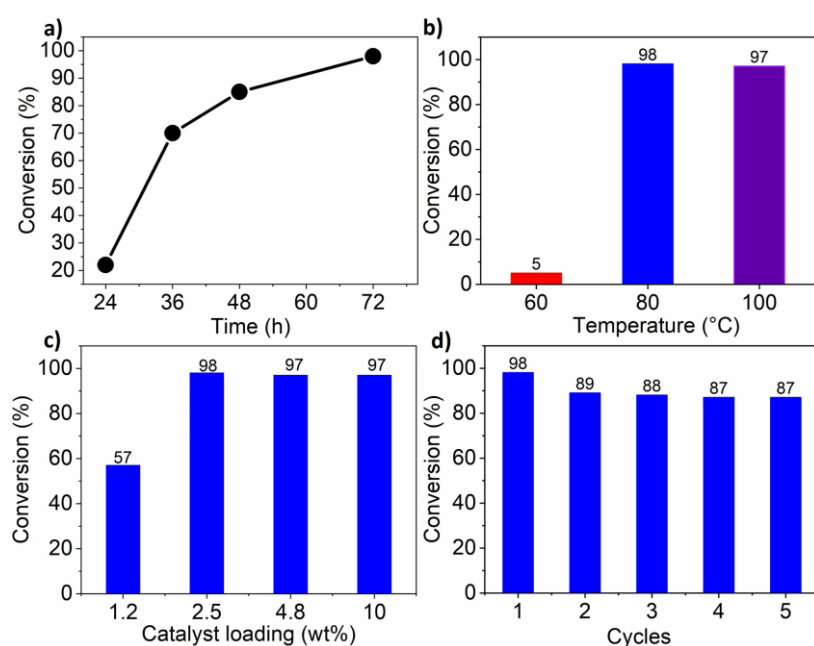


Figure 5.2: (a) Time-dependent percentage conversion of ECH at 80 °C for pPI-1. (b) Temperature-dependent conversion for cycloaddition of CO₂ to ECH for pPI-1. (c) pPI-1 catalyst loading for cycloaddition of CO₂ to ECH at 80 °C. (d) Recycling test of pPI-1 for the cycloaddition of CO₂ to ECH at 80 °C.

After proving the excellent catalytic activity and stability of pPIs for the cycloaddition of CO₂ to ECH, we tested the catalytic performance on a different substrate, epibromohydrin (EBH), under the same reaction conditions (see Table 5.2). Both pPIs gave excellent conversion (89% and 72%, respectively) of EBH to the corresponding cyclic carbonate.

A number of investigations have been directed towards the production of metal-based catalysts aimed at optimising the conversion of CO₂ into cyclic carbonates.²⁹⁶ For instance, Zhang et al.³¹⁸ successfully fabricated cobalt-containing conjugated microporous polymers (CMP) for the cycloaddition of CO₂ and epoxides resulting in 83.6% and 82.5% conversion yields for epichlorohydrin and epibromohydrin, respectively. The same research group later prepared porphyrin-based cobalt-coordinated CMPs for the synthesis of cyclic carbonates from CO₂ and epoxides (with a conversion yield of 74.2% for epichlorohydrin).³¹⁹ In both studies, the well-known co-catalyst TBAB was used. Zhou et al.³²⁰ reported zinc (Zn)-containing a catalyst for CO₂ transformation, their Zn-salen-CMP successfully converted epichlorohydrin into the corresponding cyclic carbonate with a yield of 89% in the presence of TBAB. Notably, the cycloaddition reaction was carried out at 120°C and under 3.0 MPa pressure for 1 hour. Another example of using a Zn-containing catalyst, now containing quaternary phosphonium bromide salts, was reported by Lu et al.³²¹ The salts acted in synergy with the zinc porphyrin (Lewis acid) and opened the epoxide ring, eliminating the need for co-catalysts. Reported conversion yields for epichlorohydrin were 93% under high CO₂ pressure (2.5 MPa) at 90°C. In comparison with metal-based catalysts, there are only a few metal-free POPs for CO₂ fixation via cycloaddition of CO₂ with epoxides (but not without a co-catalyst). Ding et al.³¹⁵ developed a microporous polymeric spheres catalyst, which together with TBAB as a co-catalyst gave an 89% conversion yield with epichlorohydrin as a substrate. In contrast to other studies, our results presented here highlight a greener (lower temperatures, pressures and absence of solvents), safer, metal-free alternative for the fixation of CO₂ using a cycloaddition process, using organic-based pPIs only.

Table 5.2: Cycloaddition of CO₂ to different epoxide substrates for cyclic carbonate synthesis using pPIs (pPI-1 and pPI-2, under balloon pressure).^a

Entry	Epoxide	Catalyst	Product	Yield ^b (%)
1		none	none	0
2		pPI-1		98
3		pPI-2		90
4		pPI-1		89
5		pPI-2		72

^a Reaction conditions: Epoxide (1 ml, neat), pPIs (2.5wt%), CO₂ (balloon), 80 °C, and 72 h. ^b Determined by ¹H-NMR spectroscopic analysis.

5.2.2. Electrocatalytic CO₂ reduction:

To further expand the scope and usage of our pPIs, the electrocatalytic reduction of CO₂ was investigated using a two-compartment H-cell (0.1 M potassium bicarbonate (KHCO₃) as electrolyte in the potential range from -1 – 1 V vs a reversible hydrogen electrode (RHE)). Cyclic voltammetry (CV) studies show that both pPIs exhibit redox activity in the investigated potential range. The CV data (**Figure 5.3a**) shows the current density in the argon-saturated electrolyte is higher than that of the CO₂-saturated electrolyte. The higher current density may be attributed to a higher hydrogen evolution reaction in the argon-saturated electrolyte.³²² Therefore, this data helped to confirm that our pPIs are electrocatalytically active.³²² The chronoamperometric (CA) analyses of these pPIs were carried out at constant potentials of -0.26, -0.56 and -0.76 V vs RHE for 0.5 h (see **Figure 5.3b and c**).

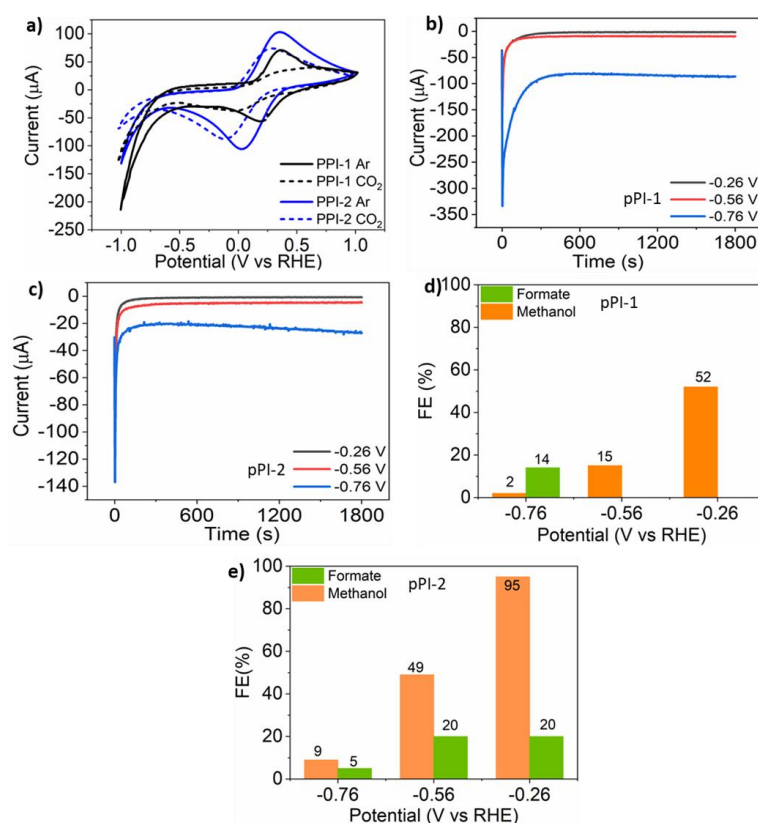
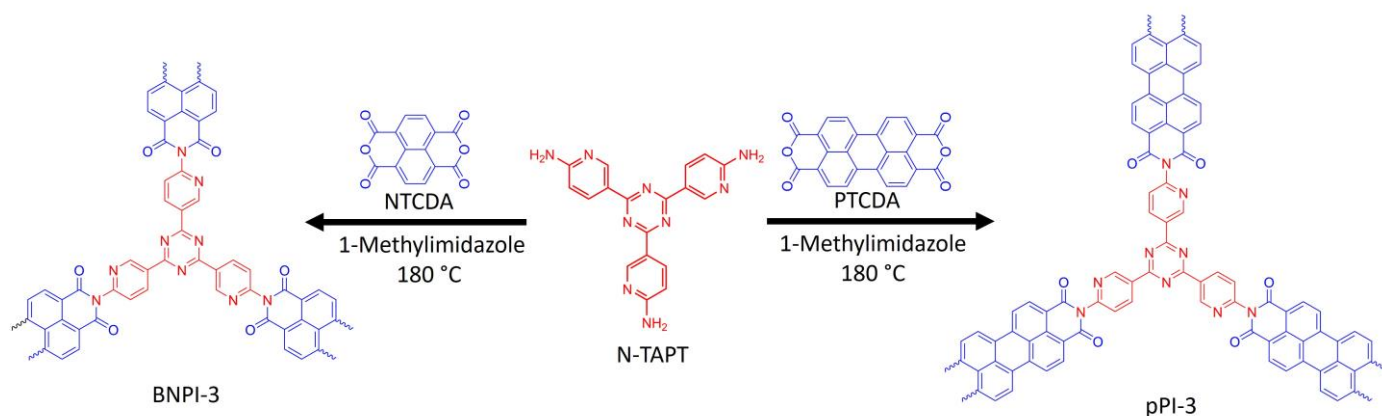


Figure 5.3: (a) Cyclic voltammogram of **pPI-1** and **pPI-2** in the applied potential range from -1–1 V vs RHE, scan rate 20mV/s, 20 cycles, (b-c) Chronoamperometry studies (vs RHE) of **pPI-1** and **pPI-2**, respectively in CO₂-saturated electrolytes, and (d-e) Highest obtained faradaic efficiency (obtained in three run, see **Table S2** in **Appendix 3**) of **pPI-1** and **pPI-2**, respectively in CO₂ saturated electrolytes for 30 min.

The electrolytes were analysed after electrolysis by cryo- ^1H NMR, with data shown in **Appendix 3 Figure A3S14 and A3S15**. The measurements showed that formate and methanol are the primary products present in the CO_2 -saturated electrolyte. In the argon-saturated electrolyte, no product signal was detected from samples at the same applied potential as those saturated with CO_2 . The signals at 3.36 ppm and 8.50 ppm in the ^1H NMR spectra confirm the reduction of CO_2 to methanol and formate, respectively. The stronger Lewis acid–Lewis base interaction of the heteroatoms in the pPIs with CO_2 contributes to increasing the rate of reduction of the gas by stabilising intermediates formed during the conversion.³²² The highest obtained faradaic efficiency (FE) values are reported in **Figure 5.3 d and e** for **pPI-1** and **pPI-2**, respectively (for full data sets, with error bars, see **Appendix 3 Figure A3S13**). **pPI-1** demonstrates a FE of up to 52% for methanol and 14% for formate at -0.26 and -0.76 V vs RHE, respectively, as illustrated in **Figure 5.3d**. For detailed FE calculations, please refer to **Section 4 of Appendix 3**. **pPI-2**, in contrast, exhibits the highest FE for methanol, reaching up to 95% at -0.26 V vs RHE (**Figure 5.3e**). However, the FE gradually decreases with increasing potential, with values of 49% at -0.56 V and 9% at -0.76 V, as shown in **Figure 5.3e**. Moreover, **pPI-2** was also capable of reducing CO_2 to formate at -0.26 V (FE =20%), -0.6 V (FE =20%) and -0.76 V (FE =5%). The higher FE of **pPI-2** for methanol could be attributed to the higher surface area and broad PSD, leading to higher carbon product formation. This observation aligns with the findings from our previous study.³⁰⁵ Additionally, we assume that gaseous products, such as CO and CH_4 , formed during the electroreduction process. However, this assumption could not be confirmed since the reaction setup was not coupled with a GCMS instrument. Investigating this further in future research would be of great interest. Multiple metal-based COF and MOF catalysts systems have been used in electrocatalytic CO_2 reduction, reporting outstanding FEs for CO (97% at -0.9 V vs RHE).^{289,323} To the best of our knowledge, selectively reducing CO_2 electrocatalytically to methanol using metal-based porous materials has not been achieved to date. In contrast, the pPIs herein reported show superior results for methanol production, and in some cases matching with other traditional transition-metal electrocatalysts (FEs of 87% and 98% for methanol and formate, respectively).^{324,325} Our new approach here points towards the exciting development of metal-free porous polymers as electrocatalysts for the wide and sustainable utilisation of CO_2 .

5.3. Pyridine-containing pPIs

Considering the effectiveness of pPIs as a heterogeneous catalyst for the conversion of CO₂ and the incorporation of heteroatom to enhance the CO₂-catalyst interactions (as discussed in **Chapter 1**). The new core was synthesised 5,5',5''-(1,3,5-triazine-2,4,6-triyl)tris(pyridin-2-amine) (N-TAPT) with the basic pyridinic group in it via trimerization of 6-amino-3-pyridinecarbonitrile. N-TAPT was reacted with PTCDA and NTCDA, respectively to yield pyridine-containing pPIs (**pPI-3** and **BNPI-3**) as shown in **Scheme 5.4**.



Scheme 5.4: Synthetic pathway to **pPI-3** and **BNPI-3**

The successful formation of **BNPI-3** and **pPI-3** was confirmed by FT-IR, UV-Vis-NIR, PXRD and SEM as shown in **Figure 5.4**. The FT-IR spectra exhibited similar characteristic peaks as those observed for **BNPI-1** and **BNPI-2** (discussed in **Chapter 4**) and **pPI-1** and **pPI-2** (discussed in this study), respectively, indicating the formation of the desired products. The characteristic peaks at 1575 and 1592 cm⁻¹ are attributed to the vibration of carbonyl groups in the newly formed six-membered polyimide rings of **BNPI-3** and **pPI-3**, respectively. The presence of triazine units in both polymers was confirmed by the signal observed at 1498 cm⁻¹. Additionally, the absence of -NH stretching signals (3460–3213 cm⁻¹) from the starting material (N-TAPT) shows complete condensation of amine moieties (N-TAPT) to form the respective pPI. The UV-Vis-NIR further supported the formation of the new products with extended conjugation, a bathochromic shift of λ_{\max} from 365 and 556 to 1091 and 770 nm for **BNPI-3** and **pPI-3**, respectively, as shown in **Figure 5.4c** were observed. Interestingly, a higher bathochromic shift was observed in **BNPI-3**, which could be attributed to longer conjugated structure formation than **pPI-3**. Furthermore, PXRD reveals the amorphous nature of the polymers as no sharp diffraction peaks were observed. However, the broad peak was observed at 26° (2-theta), which is attributed to π -stacking which was observed in both polymers (**Figure 5.4b**). The SEM image reveals an aggregated morphology observed in both polymers as shown in **Figure 5.4 d-e**. After the successful

characterisation of **BNPI-3** and **pPI-3**, their surface area and CO₂ uptake capabilities were evaluated and presented in **Table 5.3** and **Figure 5.5**.

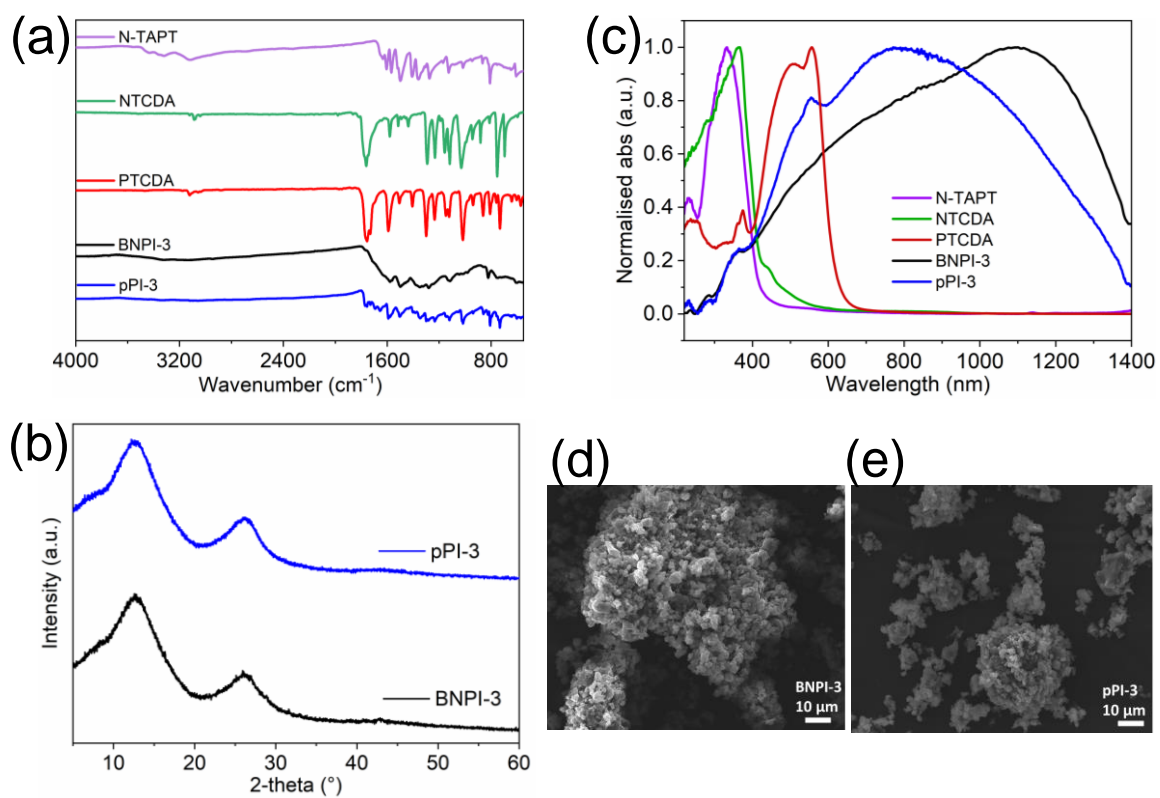


Figure 5.4: (a) FT-IR spectra of starting materials and **BNPI-3** and **pPI-3**, (b) UV-Vis-NIR spectra of starting materials and **BNPI-3** and **pPI-3**, (c) PXRD of **BNPI-3** and **pPI-3**, and (d-e) SEM of **BNPI-3** and **pPI-3**, respectively.

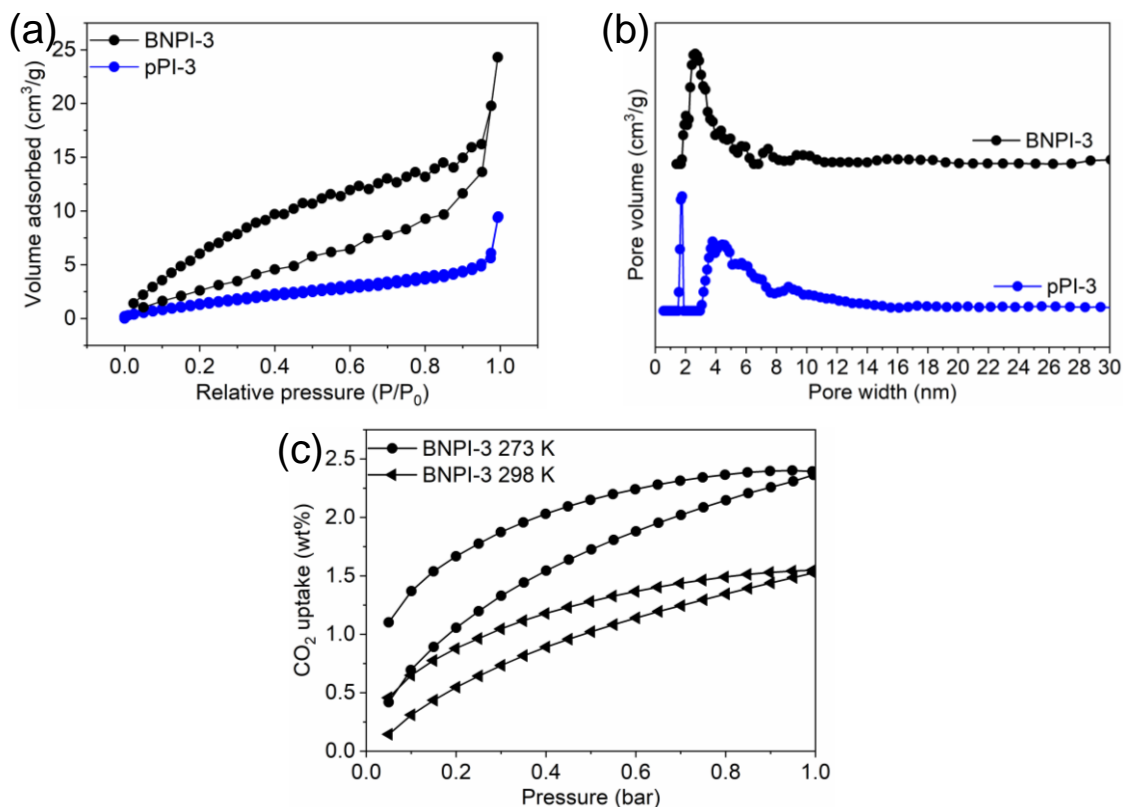


Figure 5.5: (a) The N₂ sorption isotherms of **BNPI-3** and **pPI-3**, (b) Pore size distribution calculated from NLDFT, (c) CO₂ uptake of **BNPI-3** at 273 K and 298 K at 1 bar.

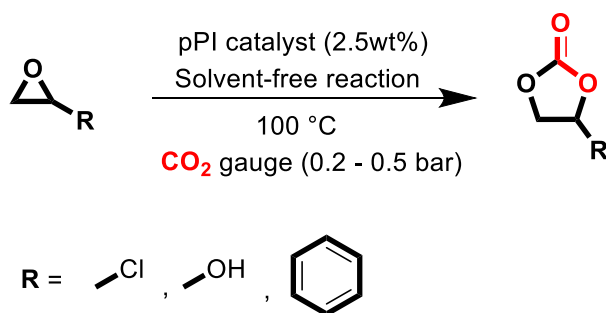
The N₂ sorption isotherms at 77 K were conducted to investigate the porosity properties of **BNPI-3** and **pPI-3** as shown in **Figure 5.5a**. The isotherms exhibited a significant N₂ uptake at lower relative pressures (P/P_0), indicating monolayer adsorption. As the pores became filled, there was a gradual increase in uptake at higher relative pressures (P/P_0), suggesting a multilayer adsorption process. The pore size distribution (PSD) calculations performed using the NL-DFT method (as depicted in **Figure 5.5b**) confirms the presence of both micro and mesopores. The isotherms were classified as typical Type II isotherms according to the IUPAC classification. The specific surface areas (S_{BET}) of **BNPI-3** and **pPI-3** were found to be 13 and 7 m²/g, respectively, as shown in **Table 5.3**. Furthermore, the CO₂ uptake capacities of **BNPI-3** were investigated at 273 K and 298 K under a pressure of 1 bar, as shown in **Table 5.3**. **BNPI-3** exhibited a notable CO₂ uptake of 2.4 wt%. It is worth noting that despite its low surface area, **BNPI-3** displayed relatively high CO₂ uptake. This behaviour can be attributed to the high interactions between its surface constituent (heteroatoms) and CO₂, substantiated by the considerable Q_{st} value of 51 kJ/mol. (Due to an instrument breakdown, **pPI-3** was not subjected to CO₂ uptake analysis.)

Table 5.3: BET surface area and CO₂ uptake at 273 K and 1 bar of **BNPI-3** and **pPI-3**, respectively.

Name	SBET (m ² /g)	CO ₂ uptake (wt%)		Q _{ST} (kJ/mol)
		273 K	298 K	
BNPI-3	13	2.4	1.5	51
pPI-3	7	<i>not analysed</i>	<i>not analysed</i>	--

5.3.1. pPI-catalysed chemical conversion of epoxides (using gauge CO₂ pressure)

BNPI-3 and **pPI-3** (pyridine-containing pPIs), along with **pPI-2** (without pyridine-containing pPI), were employed as heterogeneous catalysts for the synthesis of cyclic carbonates from CO₂ and epoxides. However, in this method, the supply of CO₂ was regulated under gauge pressure (0.25 to 0.50 bar), as illustrated in **Scheme 5.5**. Furthermore, other reaction conditions, such as the absence of solvents and co-catalysts, were kept unaltered as shown in **Scheme 5.3**. The experimental setup for the reaction is illustrated in **Figure 5.6**.



Scheme 5.5: General scheme to synthesised cyclic carbonates using gauge CO₂ and epoxides.

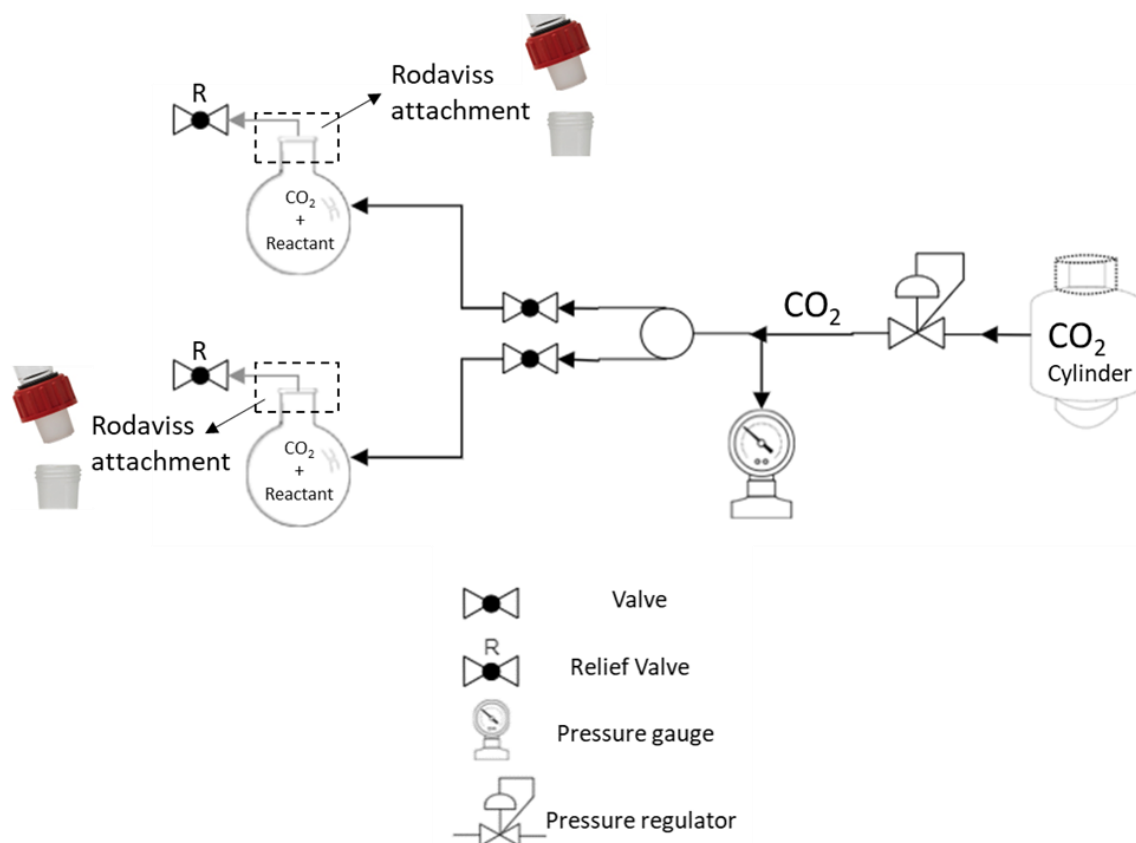


Figure 5.6: The experimental setup for the synthesis of cyclic carbonates using gauge CO₂ and epoxides.

In the initial stage of the experiment, **pPI-3** was chosen as a heterogeneous catalyst for the cycloaddition reaction between CO₂ to styrene oxide, conducted under a gauge pressure (0.50 bar), and at 100° C for 72 hours. Interestingly, **pPI-3** demonstrated a conversion of styrene oxide into styrene carbonate with a yield of 56%. Subsequently, the gauge pressure of CO₂ was decreased to 0.25 bar, while maintaining a constant temperature (100° C), time (72 h) and using the same catalyst (**pPI-3**). Under these conditions, a conversion of 58% styrene carbonate was observed. Therefore, 0.25 bar gauge pressure of CO₂ was established as the optimum pressure in this work. Furthermore, the reaction was extended to a duration of 96 hours, and it was observed that the conversion efficiency improved to 90% (styrene carbonate).

To assess the significance of the basic pyridinic group, **pPI-2** catalyst lacking the pyridinic group was employed in the same reaction (styrene oxide and CO₂). Interestingly, the conversion observed with **pPI-2** was lower (2.7%) compared to the catalyst containing the pyridinic group (**pPI-3**). To further illustrate this comparison, a time-dependent analysis of the conversion for both **pPI-2** and **pPI-3**, spanning up to 96 hours, is depicted in **Figure 5.7**.

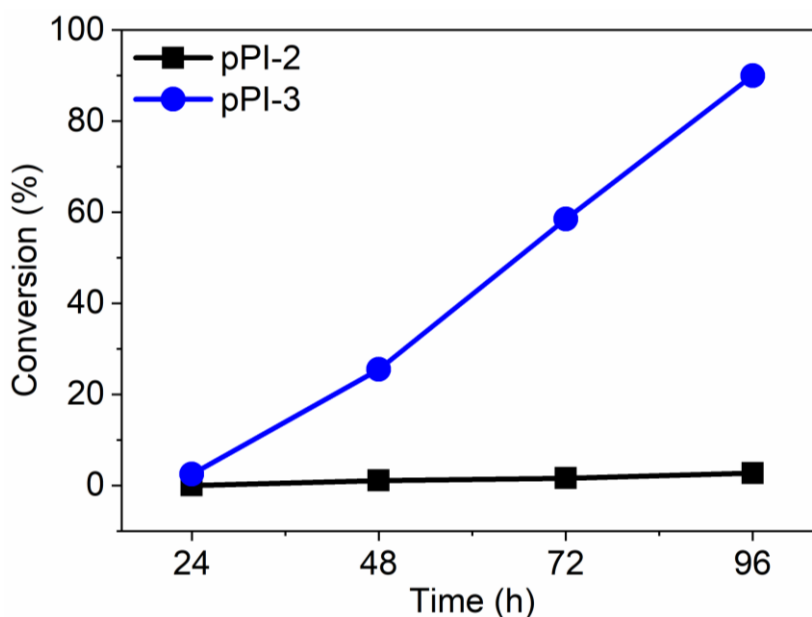
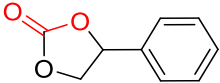
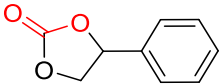
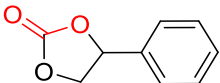
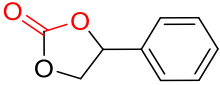
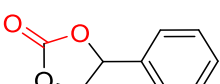
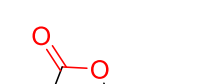
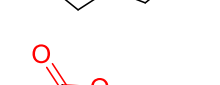
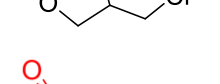
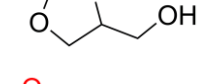


Figure 5.7: Time-dependent percentage conversion of SO at 100 °C, 0.25-gauge CO₂ for **pPI-2 (black)** and **pPI-3(blue)**

Additionally, the same reaction (between CO₂ and styrene oxide) was investigated using **BNPI-3** for the conversion of styrene carbonate: 76% conversion was observed after 96 hours. These results clearly demonstrate that the presence of the basic pyridinic group and increased heteroatom concentration in the catalyst significantly enhances the interaction of CO₂ molecules with the catalyst via Lewis acid–base interactions as discussed in **Chapter 1 (Figure 1.18)**, thereby leading to improved catalytic performance and higher conversion products. Furthermore, both catalysts (**BNPI-3** and **pPI-3**) were investigated for various epoxide substrates as shown in **Table 5.4**, while keeping the reaction parameters constant such as catalyst loading (2.5wt%), reaction time (96 h), and temperature (100 °C). Interestingly, both pyridine-containing pPIs were found to be effective in converting epoxides (ECH), styrene oxide (SO) and glycidol) to the corresponding cyclic carbonates.

However, due to time constraints, electrocatalytic CO₂ reduction using **BNPI-3** and **pPI-3** were not investigated. Their potential electrocatalytic activity should be explored in future work.

Table 5.4: Cycloaddition of CO₂ to different epoxide substrates for cyclic carbonate synthesis using pPIs (BNPI-3 and pPI-3, under CO₂ gauge pressure).^c

SI	Catalyst	CO ₂ gauge pressure (bar)	Temperature (° C)	Yield ^b (%) [h]	Product
1	pPI-2	0.25	100	2.7 [96]	
2	pPI-3	0.50	100	56 [72]	
3	pPI-3	0.25	100	58 [72]	
4	pPI-3	0.25	100	90 [96]	
5	BNPI-3	0.25	100	76 [96]	
6	BNPI-3	0.25	100	98 [72]	
7	pPI-3	0.25	100	99.9 [72]	
8	BNPI-3	0.25	100	85 [96]	
9	pPI-3	0.25	100	85 [96]	

^c Reaction conditions: Epoxide (1 ml, neat), pPIs (2.5wt%), CO₂ gauge (0.25 – 0.50 bar), 100 °C, and [h] = hour.

^b Determined by ¹H-NMR spectroscopic analysis.

pPIs exhibits superior catalytic performance in terms of conversion percentage to yield cyclic carbonates, reaching up to 99.9% (ECH, 72 h, 100 °C) without the need for a co-catalyst and solvent. However, when considering reaction time, pPIs appear to have sluggish kinetics as compared to metal-based and metal-free porous catalysts, requiring 72 h for the reaction to complete. Buyukcakir et al,³¹³ demonstrated a 95% conversion of ECH to corresponding cyclic carbonates in 12 h at 90 °C and 1 MPa. Under the same reaction conditions, only a 36% conversion of SO was observed (90% in this work at 100 °C, 96 h). Liu et al,³²⁶ also reported 99% conversion of ECH in 48 h at 60 °C and 0.1 MPa. There are several other catalysts that require higher temperatures, pressures and the addition of co-catalyst. For instance, Zhang et al,³²⁷ synthesised Al-Por-POPs and utilised in cyclic carbonate synthesis with the addition of a co-catalyst addition (TBAB), reporting a 96% (ECH) and 72% (SO) conversion at 1 bar, 100 °C for 48 h. Roeser et al,³¹⁴ reported 100% conversion of ECH at 130 °C, 6.9 bar in 4 h. Considering all the reaction conditions, including co-catalyst, CO₂ pressure, temperature and reaction time, pPIs performed excellent catalytic activity compared to metal-free and metal-containing POPs without requirement for solvent and co-catalyst and with a minimal CO₂ pressure (0.25 bar), thereby aligning with a more sustainable approach. Nevertheless, additional optimisation of reaction conditions and research are vital to enhance the kinetics of pPIs for cyclic carbonate synthesis from CO₂.

5.4. Conclusion:

In this work, perylene-based pPIs (**pPI-1** and **pPI-2**) and pyridine-containing pPIs (**BNPI-3** and **pPI-3**) were successfully synthesised via polycondensation reactions. The synthesised pPIs were shown to be versatile materials, showing interesting porosity properties and CO₂ uptake capabilities of up to 4.9 wt% (for **pPI-2**). The synthesised pPIs were furthermore successfully utilised, not only to capture CO₂, but also to act as a metal-free heterogeneous catalysts for the utilisation of CO₂ under mild and sustainable conditions. **pPI-1** and **pPI-2** showed excellent catalytic performance for cyclic carbonates synthesis from CO₂ and epoxides (at very slight CO₂ overpressures using balloon, in the absence of solvents and co-catalysts), with up to 98% conversion (ECH) and outstanding recyclability. Additionally, pyridine-containing pPIs (**BNPI-3** and **pPI-3**) showed outstanding catalytic performance for the cyclic carbonate synthesis from CO₂ (under 0.25 bar gauge CO₂ pressure). A range of epoxides were investigated with excellent conversion (99.99% for ECH, 90% for SO and 85% for glycidol), showing the wide applicability of these novel pPI materials.

Further exploring their versatility, these pPIs (**pPI-1** and **pPI-2**) were used in electrocatalytic conversion of CO₂ to form methanol and formate. FEs of 20% for formate and 95% for methanol were achieved in the applied potential range from 0 to -1 V vs RHE. pPIs therefore provide an exciting, metal-free

solution, at low potentials, for the electrocatalytic conversion and fixation of CO₂ to produce useful fuels and chemical feedstocks.

pPIs should therefore continue to be explored to produce efficient and recyclable heterogenous catalysts for chemical and electrocatalytic conversion of CO₂. Further investigations, based on our earlier work on exploiting and optimising HSPs in the BXJ approach, will be useful to explore the influence of the formation of highly optimised conjugated microporous polymers (CMPs). Applying this approach, we will be able to tune porosities and pore size distributions, thereby further improving catalytic efficiency and functionality, and potentially also tune product formation.^{43,205} This metal-free, solvent-free approach will ensure a step-change in the approaches and tools available to address the significant global challenges faced today.

Experimental section: Appendix -3

Chapter 6: Naphthalenediimide- (p-NDI) and perylenediimide- (p-PDI) based porous polyimides

6.1. Introduction:

Over the past few years, perylene diimides (PDIs) and naphthalene diimides (NDIs) have gained increasing attention owing to their distinctive planar molecular structure, remarkable chemical and physical properties, impressive electron mobility, and high molar absorption coefficients.^{328–330} PDIs and NDIs are widely recognised as organic n-type semiconductor.^{331–334} This attractive properties makes them a desired materials for multiple applications, e.g. fluorescence sensing such as metal ion and organic pollutant detections,^{42,335,336} photocatalysis^{337,338} and electrocatalysis.^{338–340} The electronic properties of PDIs and NDIs can be altered by manipulating the energy levels of the HOMO-LUMO through two approaches: the attachment of electron-withdrawing or electron-donating groups in the bay, ortho or imide position as shown in **Figure 6.1**, and the extension of conjugation (bay, ortho or imide position).³⁴¹ These strategies are widely used for the precise tuning and optimisation of the redox properties of PDIs and NDIs, facilitating their broader applications.^{5,342}

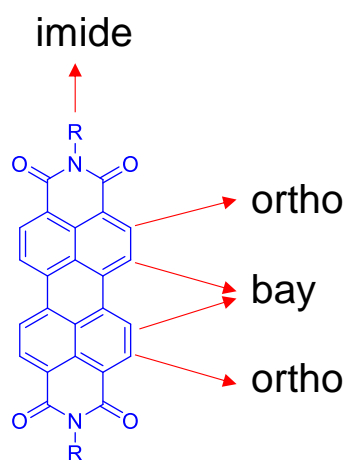


Figure 6.1: Position of PDI.⁵

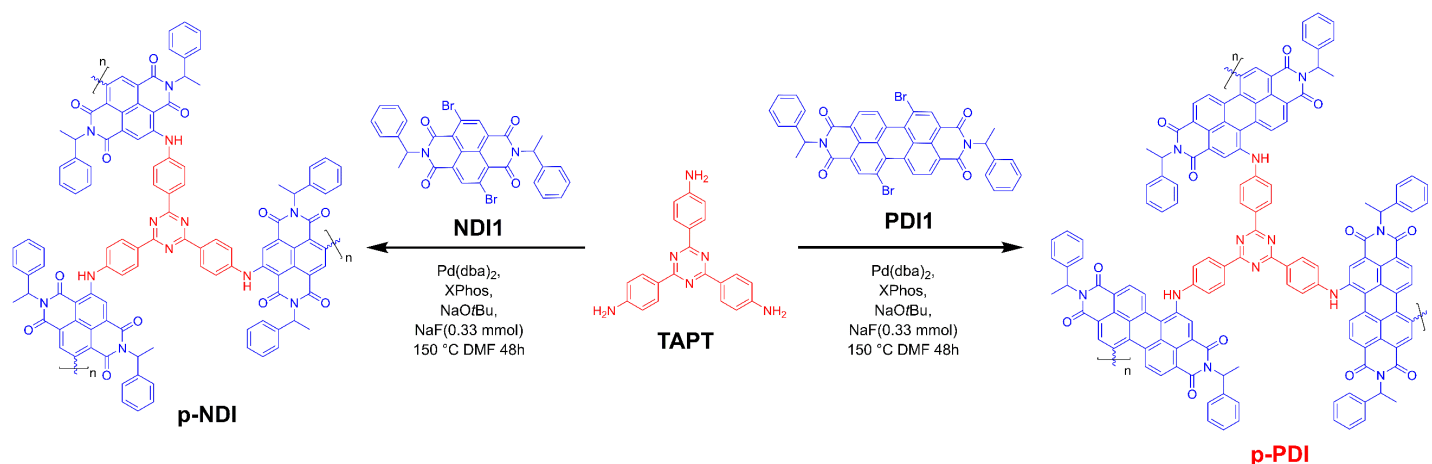
The strong π -stacking observed between planar perylene- or naphthalene-units significantly contributes to efficiently reducing the overall surface area of the materials.^{145,343} However, the π - π stacking between PDI and NDI units can be minimised through various modifications, such as introducing bulky substituents at the bay, ortho, or imide positions of PDI and NDI, thus introducing steric hindrance.^{344–347} Zong et al,³⁴⁸ demonstrated the successful attachment of bulky substituent to the bay position of NDI (NDI-8), resulting in the absence of undesirable π - π stacking interactions. Royackers et al,³⁴⁹ achieved π -stacking suppression by the molecular encapsulation of PDI. In their approach, PDI was initially ortho-substituted with 1,3-dimethoxybenzene, followed by demethylation

to yield PDI with ortho-substituted 1,3-hydroxybenzene (PDI-OH). Finally, PDI-OH was doubly encapsulated with 1,8-dibromooctane leading to suppression of the π stacking.

Furthermore, the extended conjugation within the PDI and NDI could potentially result in the reduction of the energy gap existing between HOMO-LUMO, thus providing enhanced electronic conduction and electron mobilities.^{176,350} Wang et al,³⁴⁴ synthesised PDI-based materials by employing fluorene as a core and attached two terminal PDI units. The two PDI units used are mono brominated PDI units (PDI1) or fused PDI dimers (2PDI1). They investigated photovoltaic and electrochemical properties of these PDIs derivatives and found that the extended conjugation led to improved current density (9.54 mA/cm² for FPDI-I and 11.56 mA/cm² for F2PDI-II) and FE% (52.92 for FPDI-I and 62.80 for F2PDI-II). Similar example was demonstrated by Yu et al,³⁵¹ where an extension of the conjugation length of PDIs exhibited enhanced electron mobility.

The improved conductivity and enhanced surface area hold promising potential for electrocatalytic applications of **p-NDI** and **p-PDI** and further enhanced the established electrocatalytic behaviour for CO₂ reduction. In the preceding chapters (**Chapters 4 and 5**), the formation of pPIs was through the imide position and their energy storage properties were discussed in **Chapter 1**.

However, in this chapter, pPIs were synthesised via Buchwald-Hartwig (BH) cross coupling reaction occurring at the bay position of the linkers (**PDI1** and **NDI1**) to ensure extended conjugation across multiple monomeric units and minimise the π - π stacking between PDI- and NDI-units. Firstly, linkers were prepared as diimide and subsequently brominated at the bay position (**PDI1** and **NDI1**). It is noteworthy that the brominated versions of PDI (referred to as **PDI1**) and NDI (referred to as **NDI1**) were synthesised by Maximilian Hagemann of the Faul research group. These brominated derivatives, **PDI1** and **NDI1**, were subsequently coupled with TAPT through a BH coupling reaction as shown in **Scheme 6.1**.



Scheme 6.1: Synthesis of **p-NDI** and **p-PDI** via BH coupling reaction.

6.1. Results and discussion:

p-NDI and **p-PDI** were synthesised via a palladium (Pd)-catalysed BH cross-coupling reaction between bay-brominated **NDI1** and **PDI1** with TAPT, respectively, thus forming extended conjugated structure through these formed C-N bonds (**Scheme 6.1**). The successful formation of both pPIs was confirmed by FT-IR, and UV-Vis-NIR as shown in **Figure 6.2**. The distinctive FT-IR amine peak observed at 3470 and 3420 (-NH_2 stretching) and 1650 cm^{-1} (-NH_2 deformation) in the starting material TAPT and C-Br (651 cm^{-1}) from the linkers (**NDI1** and **PDI1**) were absent in the spectra of both **p-NDI** and **p-PDI**. Instead, the appearance of a peak corresponding to the triazine ($1415\text{-}1430 \text{ cm}^{-1}$) moiety confirms the presence of the triazine unit in both pPIs. Bathochromic shifts of UV-Vis-NIR absorption wavelength (λ_{max}) of **p-NDI** and **p-PDI** from 358 and 547 to 479 and 722 nm, respectively, indicate the formation of new products with extended conjugation.

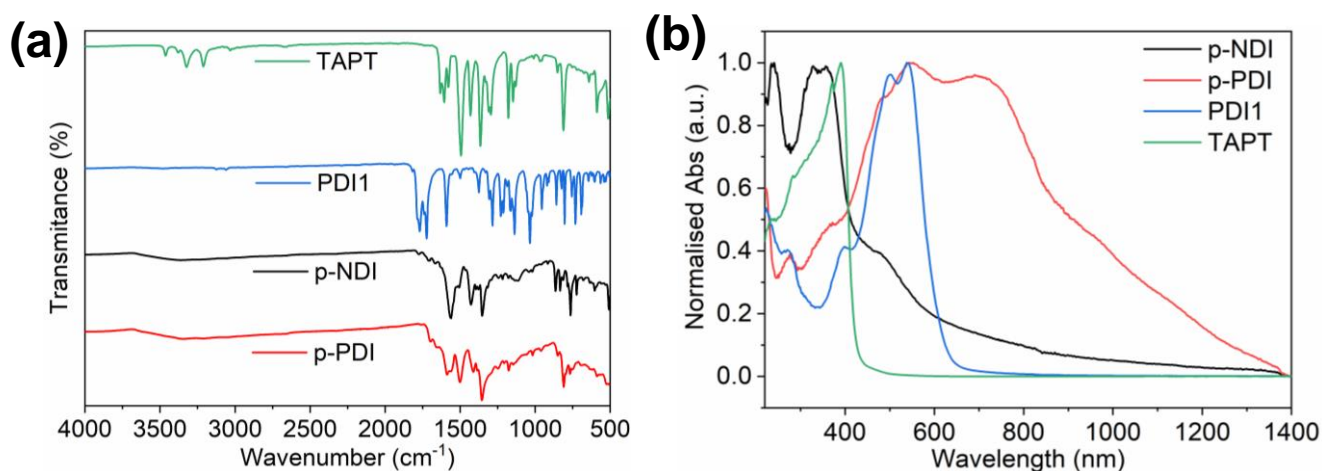


Figure 6.2: (a) FT-IR of **p-NDI** and **p-PDI** and (b) UV-Vis-NIR spectra of **p-NDI** and **p-PDI**.

Furthermore, PXRD reveals the amorphous nature of the polymers as no sharp diffraction peaks was observed as shown in **Figure 6.3a**. Additionally, strong π -stacking peak around 26° (2-theta) was absent in both polymers. However, the peaks observed at 40° (2-theta), which could be attributed to NaF trapped in pores of pPIs. EXD elemental analysis confirm the presence of Na in both samples (see **Table 6.1**). Additionally, the SEM image reveals an aggregated morphology observed in both polymers (**Figure 6.3b**).

Table 6.1: Elemental analysis results of p-NDI and p-PDI.

Name	C%	N%	O%	Na%
p-NDI	60.7	4.8	26.2	7.8
p-PDI	76.9	6.2	13.4	3.3

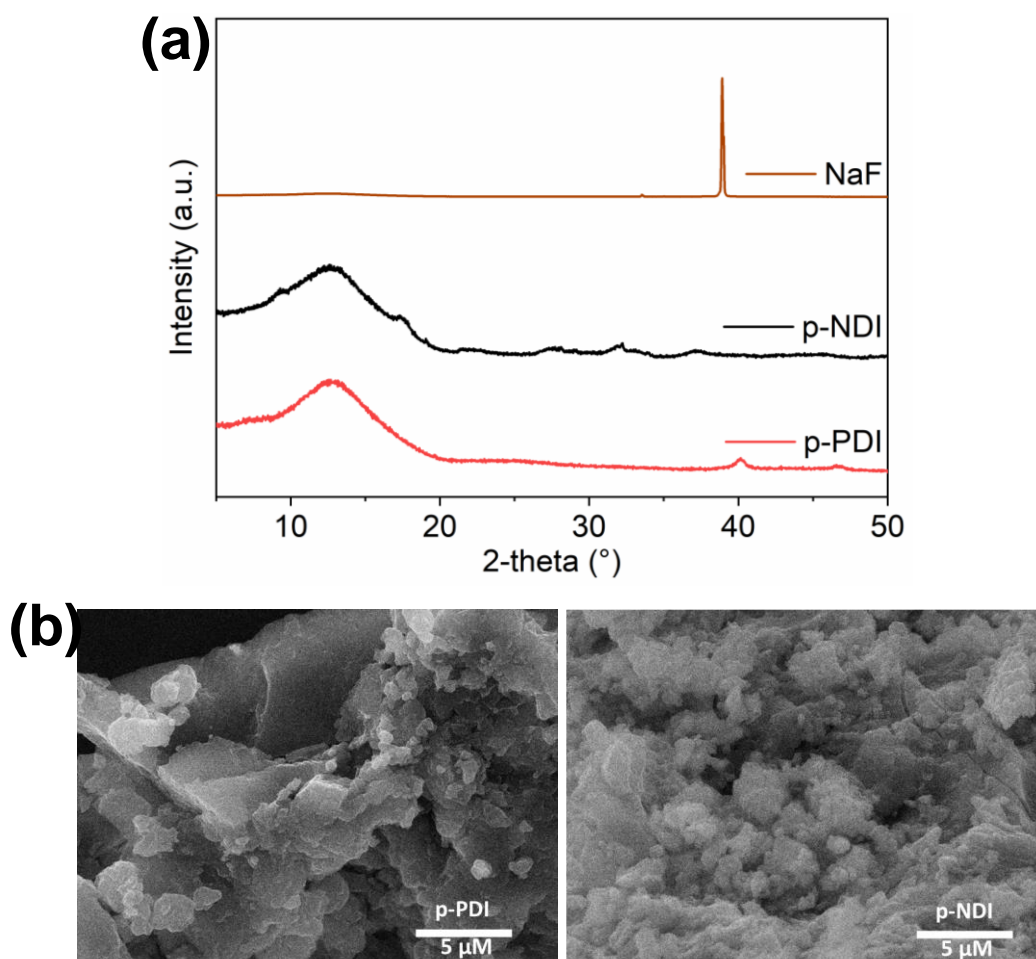


Figure 6.3: (a) PXRD of p-NDI, p-PDI and NaF, and (b) SEM image of p-NDI and p-PDI.

Regrettably, due to the limitations and availability of instruments encountered within the scope of this study, the characterisations such as TGA analyses was not viable, hindering the acquisition of the desired insights of the material's thermal properties. The investigation of the properties of the synthesised **p-NDI** and **p-PDI** through comprehensive analyses would have presented intriguing prospects.

The porosity properties of **p-NDI** and **p-PDI** were explored by recording N₂ sorption isotherms at 77 K (see **Figure 6.3**). The isotherms demonstrate a notable uptake of N₂ at lower relative pressures (P/P_0), which is indicative of monolayer adsorption. Furthermore, as the pores become filled, there is a

gradual increase in uptake observed at higher relative pressures of 0.9 (P/P_0), suggesting a multilayer adsorption process.³⁵² This behaviour provides evidence for the existence of both micro and macropores, as corroborated by pore size distribution (PSD) calculations conducted using the NL-DFT method (as shown in to **Figure 6.3**). These isotherms could be described as a typical Type II isotherms according to the IUPAC classification, with the specific surface areas (S_{BET}) of **p-NDI** and **p-PDI**, 45 and 75 m^2/g , respectively, as shown in the **Table 6.2**. However, it would be intriguing to explore the application of the BXJ approach to fine-tune the porosity properties and pore size distribution (PSD) of these materials. The BXJ approach has proven to be well-established in BH coupling reactions, and its utilisation in optimising porosity properties could yield promising results.^{43,205}

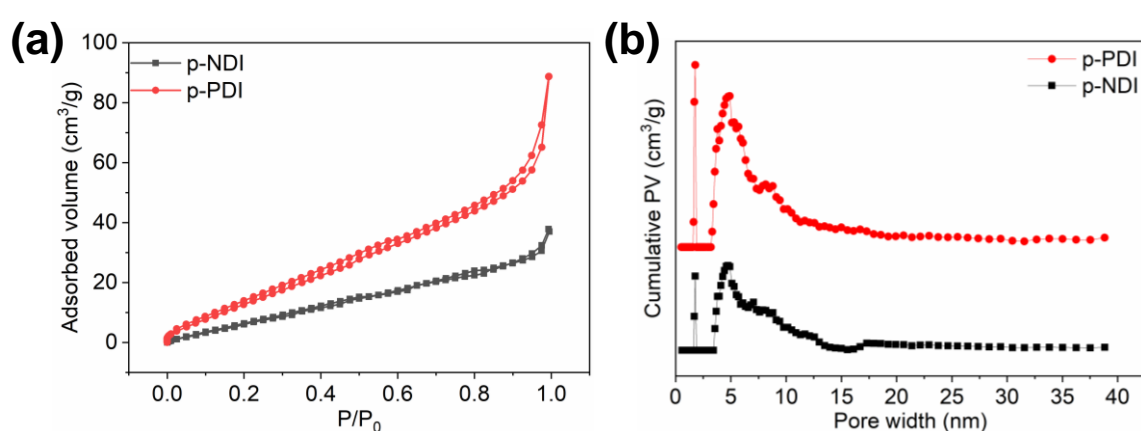


Figure 6.4: (a) BET adsorption-desorption isotherm of N_2 for p-PDI and p-NDI and (b) PSD of p-PDI and p-NDI calculated from NL-DFT.

Table 6.2: BET surface area and CO_2 uptake at 273 K and 1 bar.

Name	S_{BET} (m^2/g)	CO_2 uptake (wt%)		Q_{ST} (kJ/mol)
		273 K	298 K	
p-NDI	45	2.6	1.9	39.13
p-PDI	75	6.0	3.3	32.08

The CO_2 uptake capacities of both pPIs were examined at temperatures of 273 K and 298 K, under a pressure of 1 bar (**Figure 6.5**). At 273 K, p-NDI demonstrated a CO_2 uptake of 2.6 wt%, whereas at 298 K, it exhibited a lower CO_2 uptake of 1.9 wt%. In contrast, p-PDI displayed higher CO_2 uptake than p-NDI, with values of 6 wt% at 273 K and 3.3 wt% at 298 K. The increased uptake for p-PDI can be attributed to its larger surface area of 75 m^2/g , compared with p-NDI, which has a surface area of 45 m^2/g . However, despite the lower surface area, p-NDI exhibits higher adsorption enthalpies (Q_{ST}) of

39 kJ/mol, indicating a stronger interaction between p-NDI and CO₂ than p-PDI, which has an adsorption enthalpy of 32 kJ/mol. It is crucial to highlight that both measurements lie within the physisorption range,³⁵³ suggesting that only physical adsorption of CO₂ is occurring in both cases.

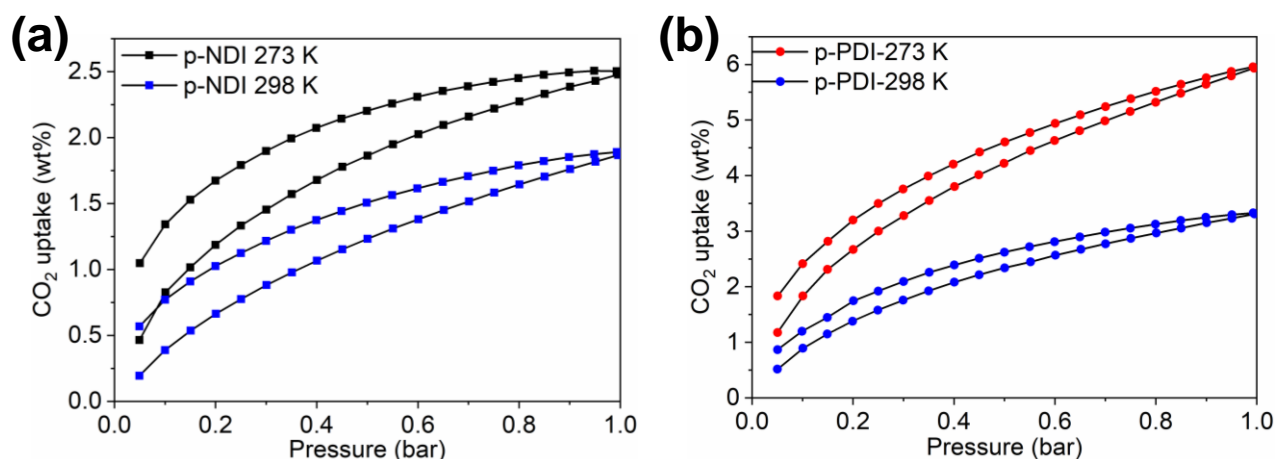


Figure 6.5: CO₂ uptake isotherms of (a) p-NDI and (b) p-PDI, were measured at 273 K and 298 K, respectively, at 1 bar.

6.2. Conclusion:

In this study, we have successfully synthesised porous **p-PDI** and **p-NDI** materials for the first time, to the best of our knowledge. These materials were synthesised via BH coupling between semiconducting PDI and NDI (linkers) with TAPT (core), respectively. The reaction occurs at the bay position of PDI1 and NDI1, to establish C-N bonds with TAPT, ensuring extended conjugation across multiple monomeric units. Also, this approach effectively minimises π - π stacking between PDI- and NDI-units and leads to an improvement in the surface area. These novel materials exhibit interesting porosity characteristics (45 m²/g for **p-NDI** and 75 m²/g for **p-PDI**) and moderate CO₂ adsorption capabilities (2.6 wt% for **p-NDI** and 6 wt% for **p-PDI**). However, regrettably, due to time constraints, the exploration of these materials especially CO₂ conversion applications was not carried out in this study.

As the BXJ approach has been widely utilised in BH coupling reactions and has shown effectiveness in optimising porosity properties,^{43,205} it would be of great interest to investigate the application of the BXJ approach in fine-tuning the porosity properties and PSD of these synthesised materials, as well as exploring its impact on CO₂ uptake capability. Incorporating this strategy in our research could lead to promising results in terms of enhancing the desired properties of these materials (such as high surface area and enhancing CO₂ capture performance).

The further exploration of these synthesised materials for potential applications, such as their use as heterogeneous catalysts for electrocatalytic CO₂ reduction and in the chemical conversion of epoxide with CO₂ to generate cyclic carbonates, has the potential to provide routes to exciting new materials to address global challenges.

Experimental section:

The synthesis of p-NDI and p-PDI can be found in the **Chapter 3**.

Chapter 7: Conclusions and Future Outlook

7.1. Conclusion

The overall aim of the work described in this thesis was to investigate perylene- and naphthalene-based pPIs with dual functionalities. The targeted functionalities were CO₂ capture and conversion as a metal-free heterogeneous catalyst for electrochemical and chemical conversion. To set the scene, a comprehensive literature review on pPIs was conducted, focusing on their design, synthesis, advantageous properties, and various applications that have been extensively explored.²⁷⁹ The literature review provides an in-depth understanding of how the monomer structure and geometry influence the porosity and gas-uptake properties of pPIs. Furthermore, the essential properties and functionalities required for the effective electrocatalytic and chemical conversion of CO₂ to useful chemicals and fuels were highlighted.

Owing to the highly crosslinked networks, conjugated backbone, abundant heteroatoms, and the incorporation of well-known organic semiconductors (PTCDA and NTCDA) into the polymeric backbone, perylene- and naphthalene-based pPIs have been considered as potential candidates for research in the field of CO₂ capture and conversion.

The first objective of this thesis was to synthesise perylene- and naphthalene-based pPIs. This objective was successfully achieved by utilising two different established synthetic approaches. Firstly, pPIs were synthesised via polycondensation reactions between dianhydrides (PTCDA and NTCDA) and various triamines, respectively. Secondly, pPIs were synthesised through BH coupling reactions involving bay brominated PDI (PDI1) and NDI (NDI1), respectively, with triamines.

The second objective of this work was the utilisation of the well-established BXJ approach for the first time in the polycondensation of pPIs to fine tune their properties and functionalities. Through the BXJ approach a remarkable increase in surface area of multiple polymers, e.g. up to 52 times higher than the conventional synthetic approach (BNPI-1, from 18 m²/g to 846 m²/g), was achieved.³⁰⁵ Moreover, the PSD was controlled utilising various inorganic salts (with different ion sizes). This approach showed precise control over the porosity properties of pPIs, and the ability to achieve tunability of surface areas and PSDs of these materials.

The third objective of this thesis was to investigate the optimised pPIs for their CO₂ capture and conversion capabilities. The optimised pPIs possess remarkable CO₂ capture performance, with an impressive uptake capacity of up to 14 wt% (2 times higher than earlier reported values). Furthermore, pPIs were, for the first time, used as metal-free electrocatalysts for the electrochemical reduction of CO₂ to formate and methanol.³⁰⁵ Impressively, pPIs exhibited high FE (91% with BNPI-1 and 95% with

pPI-2) for the respective products at low overpotentials of 0.03 V and -0.56 V vs RHE, respectively. By combining the control achieved through the BXJ approach with this newfound catalytic function of pPIs, this thesis successfully established a novel pathway for tailoring the production of two distinct reduced C1 species: formate and methanol. The ability to selectively produce these valuable feedstocks from CO₂, by simply fine-tuning the properties and function of pPI materials, holds great potential for addressing global challenges related to CO₂ capture and conversion in a sustainable fashion.

Additionally, pPIs were also utilised as metal-free heterogeneous catalysts for the first time, to the best of our knowledge, in the synthesis of cyclic carbonates from CO₂ and epoxides. The reaction was, importantly, conducted in the absence of solvents and co-catalysts while CO₂ was supplied using balloon pressure. The pPIs demonstrated exceptional performance, achieving up to 98% conversion to corresponding cyclic carbonates and outstanding recyclability. Furthermore, the versatility of these pPIs was explored through functional modification, incorporating pyridinic groups into the pPIs. The pyridine-containing pPIs exhibited excellent catalytic activity for other stable epoxide such as styrene oxide and glycidol to corresponding cyclic carbonates with conversion up to 90% and 85%, respectively. However, in this approach, reaction parameters such as the absence of solvent and co-catalyst remain unaltered, except that CO₂ was supplied using gauged pressures in the 0.2 to 0.5 bar range. The obtained results show the wide substrate scope of pPIs for cyclic carbonate synthesis. These findings demonstrate the remarkable capabilities of pPIs as an easy-recyclable, heterogeneous catalyst for synthesising cyclic carbonate from epoxides without the need for solvents and co-catalyst, making them promising candidates for green and sustainable industrial syntheses.

Through this research, the dual functionality of pPIs in capturing CO₂ and acting as a versatile metal-free heterogeneous catalyst for the conversion of CO₂ into valuable chemicals and fuels was successfully demonstrated. By combining the tunability of pPIs with the BXJ method, further optimisation of their performance in CO₂ capture and conversion processes could be achieved – most importantly, it was demonstrated that product selectivity of the catalytic processes can be influenced by tuning the physical properties of the pPIs. The research work presented in this thesis opens up new areas of research for the development of POPs-based metal-free, heterogeneous catalysts for CO₂ capture and conversion, addressing the significant challenge of global climate change.

7.2. Future work

pPIs have shown great potential for sustainable chemical synthesis and addressing globally important issue of capturing atmospheric CO₂ and converting to useful feedstocks. Considering the remarkable properties of pPIs discussed in this thesis, several areas of research are identified for further exploration:

1. In-situ electrochemical CO₂ reduction.

In order to consider the ability of pPIs to reduce CO₂ to formate and methanol, it is crucial to understand the active sites of pPIs, explore and detect any intermediates formed during the electroreduction process, and follow the generation of all products. Utilising in-situ electrochemical reduction coupled with detailed localised analyses is crucial to gain insights into the complex reaction mechanism and optimising the catalyst, also for higher C reduction carbon products.

There are several real-time in-situ characterisation techniques that can be coupled with the electrocatalytic CO₂ reduction methods to monitor the reaction in real-time, for instance, in-situ UV-Vis, in-situ FT-IR, in-situ Raman, in-situ X-ray photoelectron (XPS), in-situ X-ray absorption spectroscopy (XAS), in-situ XRD, in-situ electron spin resonance (ESR), in-situ transmission electron microscopy (TEM), and in-situ mass spectrometry (MS).³⁵⁴⁻³⁵⁸

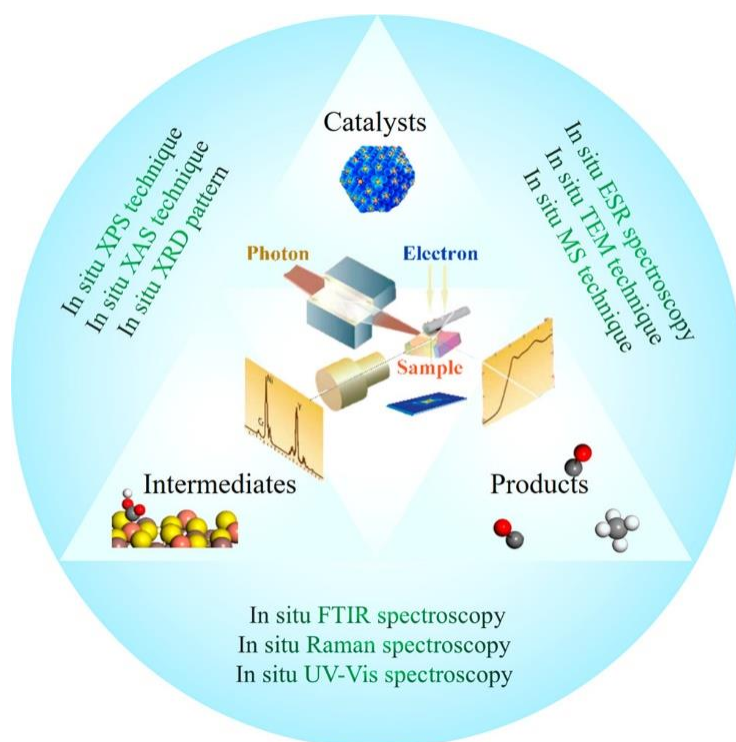


Figure 7.1: Various in situ methods to investigate the CO₂ reduction process.³⁵⁴

Investigating these novel pPIs for CO₂ conversion, coupled with real-time in-situ techniques would allow for the exploration and understanding the fundamentals of this exciting new green and sustainable approach to address the growing CO₂ problem. This study will significantly contribute to the advancement of and gaining knowledge into processes related to the development of more efficient metal-free electrocatalysts, providing sustainable and eco-friendly solutions for mitigating climate change.

2. Designing gas diffusion electrolyser (GDEs)

An electrochemical CO₂ reduction using an H-cell set-up is the preliminary step to investigate the electroactivity of a catalyst. Despite the effectiveness of pPIs in the electrochemical conversion of CO₂ to formate and methanol, the H-cell setup used in this work was not coupled with a gas chromatography mass spectrometry (GCMS) to hindering the detection of any potential gaseous products formed (CO, CH₄, C₂H₄) during the electrochemical reduction process. Therefore, it would be of great interest to perform CO₂ reduction in an H-cell coupled with GCMS to identify the gaseous product formed.

Electrocatalytic CO₂ reduction is a promising method for recycling CO₂ into valuable commodity chemicals and fuels. To facilitate the scaling up of the electroreduction of CO₂ using pPIs, gas diffusion electrolyser (GDEs), a type of flow reactor, appears to be a promising approach as shown in **Figure 7.2**. Implementing GDEs has the potential to enhance efficiency, achieve higher yields and scale-up of the electroreduction process.^{359–361}

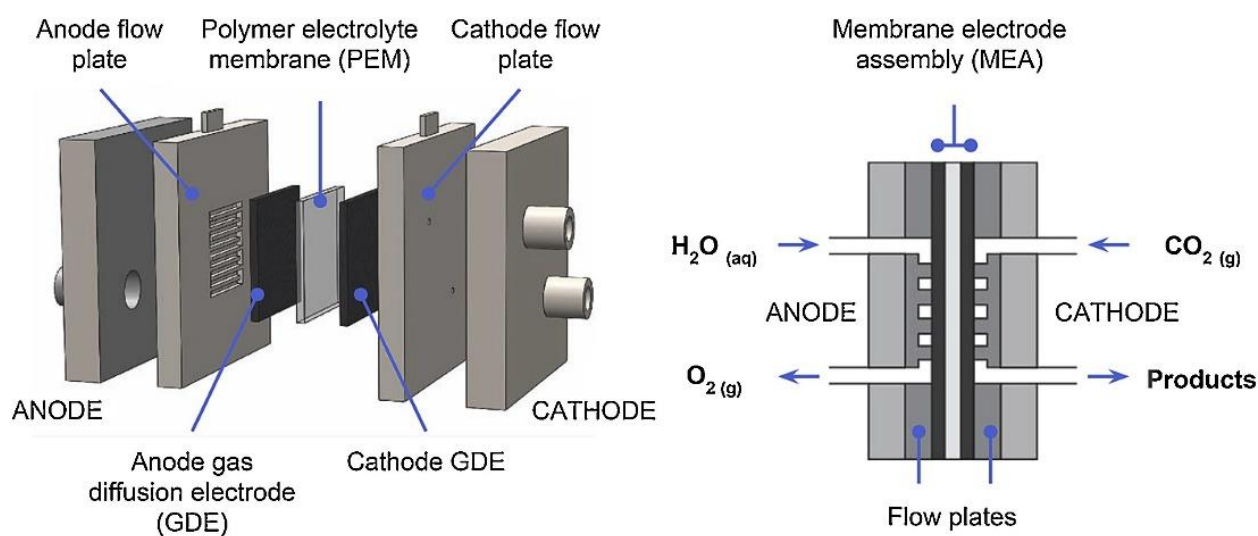
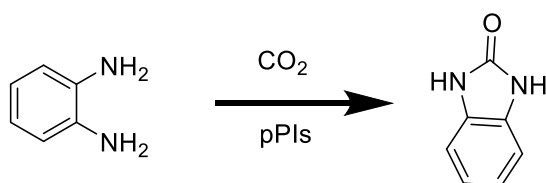


Figure 7.2. A standard GDE set-up for electrochemical CO₂ reduction.³⁶⁰

3. Exploring substrate scope in chemical conversion

pPIs have reusable heterogeneous catalytic capabilities for forming cyclic carbonate from epoxides without the need for solvents and co-catalyst, making it a promising field for industrial synthesis. Given the development of a CO₂ pressure reactor, exploring the conversion of other epoxides mentioned in **Chapter 1 (Figure 1.22)** using pPIs as catalysts is of significant interest. Additionally, this setup provides an opportunity to optimise the synthetic conditions for cyclic carbonate production.

Furthermore, considering the advantageous catalytic properties of pPIs, they should be explored as heterogeneous catalysts for cyclic urea synthesis^{362,363} using CO₂ and diamines (**Scheme 7.1**).



Scheme 7.1: Reaction between CO₂ and *o*-phenylenediamine.

References

- 1 NOAA, Global Monitoring Laboratory, Carbon Cycle Greenhouse Gases: Trends in Atmospheric CO₂, <https://gml.noaa.gov/ccgg/trends/>, (accessed 9 June 2023).
- 2 J. S. M. Lee and A. I. Cooper, *Chem. Rev.*, 2020, **120**, 2171–2214.
- 3 E. Rangel Rangel, E. M. Maya, F. Sánchez, J. G. De La Campa and M. Iglesias, *Green Chem.*, 2015, **17**, 466–473.
- 4 Y. Li, Y. A. Samad, K. Polychronopoulou, S. M. Alhassan and K. Liao, *J. Mater. Chem. A*, 2014, **2**, 7759–7765.
- 5 T. T. Clikeman, E. V. Bukovsky, X. Bin Wang, Y. S. Chen, G. Rumbles, S. H. Strauss and O. V. Boltalina, *European J. Org. Chem.*, 2015, 6641–6654.
- 6 J. H. Ahn, J. E. Jang, C. G. Oh, S. K. Ihm, J. Cortez and D. C. Sherrington, *Macromolecules*, 2006, **39**, 627–632.
- 7 B. Li, R. Gong, W. Wang, X. Huang, W. Zhang, H. Li, C. Hu and B. Tan, *Macromolecules*, 2011, **44**, 2410–2414.
- 8 Y. Luo, S. Zhang, Y. Ma, W. Wang and B. Tan, *Polym. Chem.*, 2013, **4**, 1126–1131.
- 9 T. Ben, H. Ren, M. Shengqian, D. Cao, J. Lan, X. Jing, W. Wang, J. Xu, F. Deng, J. M. Simmons, S. Qiu and G. Zhu, *Angew. Chemie - Int. Ed.*, 2009, **48**, 9457–9460.
- 10 L. Wang, W. Chen, D. Zhang, Y. Du, R. Amal, S. Qiao, J. Wu and Z. Yin, *Chem. Soc. Rev.*, 2019, **48**, 5310–5349.
- 11 W. Zhang, Y. Hu, L. Ma, G. Zhu, Y. Wang, X. Xue, R. Chen, S. Yang and Z. Jin, *Adv. Sci.*, 2018, **5**, 1700275.
- 12 IEA, CO₂ Emissions in 2022 – Analysis - IEA, <https://www.iea.org/reports/co2-emissions-in-2022>, (accessed 11 June 2023).
- 13 Global Time Series | Climate at a Glance | National Centers for Environmental Information (NCEI), https://www.ncei.noaa.gov/access/monitoring/climate-at-a-glance/global/time-series/globe/land_ocean/ann/12/2000-2022, (accessed 12 June 2023).
- 14 S. Mariappan, A. David Raj, S. Kumar and U. Chatterjee, *Global Warming Impacts on the Environment in the Last Century*, Springer Nature, 2022.
- 15 N. Jones, *Nature*, 2023, **618**, 20–20.
- 16 Climate Change 2021: The Physical Science Basis | Climate Change 2021: The Physical Science Basis, <https://www.ipcc.ch/report/ar6/wg1/>, (accessed 12 June 2023).
- 17 J. F. D. Tapia, J. Y. Lee, R. E. H. Ooi, D. C. Y. Foo and R. R. Tan, *Sustain. Prod. Consum.*, 2018, **13**, 1–15.
- 18 L. Zou, Y. Sun, S. Che, X. Yang, X. Wang, M. Bosch, Q. Wang, H. Li, M. Smith, S. Yuan, Z. Perry and H. C. Zhou, *Adv. Mater.*, 2017, **29**, 1700229.
- 19 S. Saha and A. Chakma, *Energy Convers. Manag.*, 1992, **33**, 413–420.
- 20 A. Basile, A. Gugliuzza, A. Iulianelli and P. Morrone, *Membrane technology for carbon dioxide (CO₂) capture in power plants*, Elsevier, 2011.
- 21 A. Samanta, A. Zhao, G. K. H. Shimizu, P. Sarkar and R. Gupta, *Ind. Eng. Chem. Res.*, 2012, **51**, 1438–1463.
- 22 P. Bhanja, A. Modak and A. Bhaumik, *ChemCatChem*, 2019, **11**, 244–257.
- 23 F. Björnerbäck, Stockholm University, 2018.
- 24 K. B. Lee, M. G. Beaver, H. S. Caram and S. Sircar, *Ind. Eng. Chem. Res.*, 2007, **46**, 5003–5014.
- 25 R. Luo, M. Chen, X. Liu, W. Xu, J. Li, B. Liu and Y. Fang, *J. Mater. Chem. A*, 2020, **8**, 18408–18424.

- 26 L. Guo, K. J. Lamb and M. North, *Green Chem.*, 2021, **23**, 77–118.
- 27 B. Grignard, S. Gennen, C. Jérôme, A. W. Kleij and C. Detrembleur, *Chem. Soc. Rev.*, 2019, **48**, 4466–4514.
- 28 A. Velyt and A. Corma, *Chem. Soc. Rev.*, 2023, **52**, 1773–1946.
- 29 X. Y. Wu and A. F. Ghoniem, *Prog. Energy Combust. Sci.*, 2019, **74**, 1–30.
- 30 M. Kosari, A. M. H. Lim, Y. Shao, B. Li, K. M. Kwok, A. M. Seayad, A. Borgna and H. C. Zeng, *J. Mater. Chem. A*, 2023, **11**, 1593–1633.
- 31 K. Atsonios, K. D. Panopoulos and E. Kakaras, *Int. J. Hydrogen Energy*, 2016, **41**, 792–806.
- 32 S. Qiao, M. Di, J. X. Jiang and B. H. Han, *EnergyChem*, 2022, **4**, 2589–7780.
- 33 E. Gong, S. Ali, C. B. Hiragond, H. S. Kim, N. S. Powar, D. Kim, H. Kim and S. Il In, *Energy Environ. Sci.*, 2021, **15**, 880–937.
- 34 K. Li, B. Peng and T. Peng, *ACS Catal.*, 2016, **6**, 7485–7527.
- 35 D. H. Yang, Y. Tao, X. Ding and B. H. Han, *Chem. Soc. Rev.*, 2022, **51**, 761–791.
- 36 S. Wang, L. Wang, D. Wang and Y. Li, *Energy Environ. Sci.*, 2023, **16**, 2759–2803.
- 37 T. Zhang, G. Xing, W. Chen and L. Chen, *Mater. Chem. Front.*, 2020, **4**, 332–353.
- 38 M. R. Liebl and J. Senker, *Chem. Mater.*, 2013, **25**, 970–980.
- 39 M. G. Rabbani and H. M. El-Kaderi, *Chem. Mater.*, 2012, **24**, 1511–1517.
- 40 D. S. Ahmed, G. A. El-Hiti, E. Yousif, A. A. Ali and A. S. Hameed, *J. Polym. Res.*, 2018, **25**, 1–21.
- 41 Y. Liao, J. Weber, B. M. Mills, Z. Ren and C. F. J. Faul, *Macromolecules*, 2016, **49**, 6322–6333.
- 42 Y. Liao, J. Weber and C. F. J. Faul, *Macromolecules*, 2015, **48**, 2064–2073.
- 43 J. Chen, W. Yan, E. J. Townsend, J. Feng, L. Pan, V. Del Angel Hernandez and C. F. J. Faul, *Angew. Chemie Int. Ed.*, 2019, **58**, 11715–11719.
- 44 Y. Zhang and S. N. Riduan, *Chem. Soc. Rev.*, 2012, **41**, 2083–2094.
- 45 P. Kaur, J. T. Hupp and S. T. Nguyen, *ACS Catal.*, 2011, **1**, 819–835.
- 46 Y. Tang, A. Varyambath, Y. Ding, B. Chen, X. Huang, Y. Zhang, D. G. Yu, I. Kim and W. Song, *Biomater. Sci.*, 2022, **10**, 5369–5390.
- 47 Q. Fang, J. Wang, S. Gu, R. B. Kaspar, Z. Zhuang, J. Zheng, H. Guo, S. Qiu and Y. Yan, *J. Am. Chem. Soc.*, 2015, **137**, 8352–8355.
- 48 K. Amin, N. Ashraf, L. Mao, C. F. J. Faul and Z. Wei, *Nano Energy*, 2021, **85**, 105958.
- 49 Y. Xu, S. Jin, H. Xu, A. Nagai and D. Jiang, *Chem. Soc. Rev.*, 2013, **42**, 8012–8031.
- 50 H. Bildirir, V. G. Gregoriou, A. Avgeropoulos, U. Scherf and C. L. Chochos, *Mater. Horizons*, 2017, **4**, 546–556.
- 51 B. D. Zdravkov, J. J. Čermák, M. Šefara and J. Janků, *Cent. Eur. J. Chem.*, 2007, **5**, 385–395.
- 52 N. Keller and T. Bein, *Chem. Soc. Rev.*, 2021, **50**, 1813–1845.
- 53 Y. Li, W. Chen, G. Xing, D. Jiang and L. Chen, *Chem. Soc. Rev.*, 2020, **49**, 2852–2868.
- 54 K. Geng, T. He, R. Liu, S. Dalapati, K. T. Tan, Z. Li, S. Tao, Y. Gong, Q. Jiang and D. Jiang, *Chem. Rev.*, 2020, **120**, 8814–8933.
- 55 W. T. Chung, I. M. A. Mekhemer, M. G. Mohamed, A. M. Elewa, A. F. M. EL-Mahdy, H. H. Chou, S. W. Kuo and K. C. W. Wu, *Coord. Chem. Rev.*, 2023, **483**, 215066.
- 56 A. P. Côté, A. I. Benin, N. W. Ockwig, M. O’Keeffe, A. J. Matzger and O. M. Yaghi, *Science*, 2005, **310**, 1166–1170.
- 57 D. G. Wang, T. Qiu, W. Guo, Z. Liang, H. Tabassum, D. Xia and R. Zou, *Energy Environ. Sci.*, 2021, **14**, 688–728.

- 58 X. Guan, F. Chen, Q. Fang and S. Qiu, *Chem. Soc. Rev.*, 2020, **49**, 1357–1384.
- 59 M. A. Rahman, C. J. Dionne and A. Giri, *ACS Appl. Mater. Interfaces*, 2022, **14**, 21687–21695.
- 60 H. Fan, H. Wang, M. Peng, H. Meng, A. Mundstock, A. Knebel and J. Caro, *ACS Nano*, 2023, **17**, 7584–7594.
- 61 J. Li, Z. Cheng, Z. Wang, J. Dong, H. Jiang, W. Wang, X. Zou and G. Zhu, *Angew. Chemie Int. Ed.*, 2023, **62**, e2022166.
- 62 R. Xue, Y.-S. Liu, S.-L. Huang and G.-Y. Yang, *ACS Sensors*, 2023, **8**, 2124–2148.
- 63 B. Mohan, R. Kumari, Virender, G. Singh, K. Singh, A. J. L. Pombeiro, X. Yang and P. Ren, *Environ. Int.*, 2023, **175**, 107928.
- 64 X. Gao, Y. Dong, S. Li, J. Zhou, L. Wang and B. Wang, *Electrochem. Energy Rev.*, 2020, **3**, 81–126.
- 65 S. Liu, M. Wang, Y. He, Q. Cheng, T. Qian and C. Yan, *Coord. Chem. Rev.*, 2023, **475**, 214882.
- 66 W. Zhou, Q. Deng, H. He, L. Yang, T. Liu, X. Wang, D. Zheng, Z. Dai, L. Sun, C. Liu, H. Wu, Z. Li and W. Deng, *Angew. Chemie Int. Ed.*, 2023, **62**, e202214143.
- 67 R. Zhao, T. Wang, J. Li, Y. Shi, M. Hou, Y. Yang, Z. Zhang and S. Lei, *Nano Res.*, 2023, **16**, 8570–8595.
- 68 L. Tan and B. Tan, *Chem. Soc. Rev.*, 2017, **46**, 3322–3356.
- 69 J. Germain, J. M. J. Fréchet and F. Svec, *J. Mater. Chem.*, 2007, **17**, 4989–4997.
- 70 B. S. Ghanem, M. Hashem, K. D. M. Harris, K. J. Msayib, M. Xu, P. M. Budd, N. Chaukura, D. Book, S. Tedds, A. Walton and N. B. McKeown, *Macromolecules*, 2010, **43**, 5287–5294.
- 71 S. Das, P. Heasman, T. Ben and S. Qiu, *Chem. Rev.*, 2017, **117**, 1515–1563.
- 72 T. Ben and S. Qiu, *CrystEngComm*, 2013, **15**, 17–26.
- 73 Y. Tian and G. Zhu, *Chem. Rev.*, 2020, **120**, 8934–8986.
- 74 Y. Yuan, Y. Yang and G. Zhu, *EnergyChem*, 2020, **2**, 100037.
- 75 T. Ben, C. Pei, D. Zhang, J. Xu, F. Deng, X. Jing and S. Qiu, *Energy Environ. Sci.*, 2011, **4**, 3991–3999.
- 76 N. B. McKeown, *Polymer (Guildf.)*, 2020, **202**, 122736.
- 77 N. B. McKeown, *ISRN Mater. Sci.*, 2012, **2012**, 1–16.
- 78 D. Ramimoghadam, E. M. Gray and C. J. Webb, *Int. J. Hydrogen Energy*, 2016, **41**, 16944–16965.
- 79 N. B. McKeown, *ISRN Mater. Sci.*, 2012, **2012**, 1–16.
- 80 P. M. Budd, N. B. McKeown and D. Fritsch, *J. Mater. Chem.*, 2005, **15**, 1977–1986.
- 81 P. M. Budd, B. S. Ghanem, S. Makhseed, N. B. McKeown, K. J. Msayib and C. E. Tattershall, *Chem. Commun.*, 2004, **4**, 230–231.
- 82 J.-S. S. M. Lee and A. I. Cooper, *Chem. Rev.*, 2020, **120**, 2171–2214.
- 83 A. I. Cooper, *Adv. Mater.*, 2009, **21**, 1291–1295.
- 84 J. Jiang, F. Su, A. Trewin, C. D. Wood, N. L. Campbell, H. Niu, C. Dickinson, A. Y. Ganin, M. J. Rosseinsky, Y. Z. Khimyak and A. I. Cooper, *Angew. Chemie Int. Ed.*, 2007, **46**, 8574–8578.
- 85 M. T. Bogert and R. R. Renshaw, *J. Am. Chem. Soc.*, 1908, **30**, 1135–1144.
- 86 C. E. Sroog, *Prog. Polym. Sci.*, 1991, **16**, 561–694.
- 87 United States Patent Office, 1953, 387038, US2710853A.
- 88 L. T. C. Lee, E. M. Pearce and S. S. Hirsch, *J. Polym. Sci. Part A-1 Polym. Chem.*, 1971, **9**, 3169–3174.

- 89 Y. Zhuang, J. G. Seong and Y. M. Lee, *Prog. Polym. Sci.*, 2019, **92**, 35–88.
- 90 D. J. Liaw, K. L. Wang, Y. C. Huang, K. R. Lee, J. Y. Lai and C. S. Ha, *Prog. Polym. Sci.*, 2012, **37**, 907–974.
- 91 M. Hasegawa and K. Horie, *Prog. Polym. Sci.*, 2001, **26**, 259–335.
- 92 M. Ding, *Prog. Polym. Sci.*, 2007, **32**, 623–668.
- 93 Q. Fang, Z. Zhuang, S. Gu, R. B. Kaspar, J. Zheng, J. Wang, S. Qiu and Y. Yan, *Nat. Commun.*, 2014, **5**, 4503.
- 94 M. C. Fu, T. Higashihara and M. Ueda, *Polym. J.*, 2018, **50**, 57–76.
- 95 M. Hasegawa, *Polymers (Basel)*, 2017, **9**, 520.
- 96 L. Y. Jiang, Y. Wang, T. S. Chung, X. Y. Qiao and J. Y. Lai, *Prog. Polym. Sci.*, 2009, **34**, 1135–1160.
- 97 K. Vanherck, G. Koeckelberghs and I. F. J. Vankelecom, *Prog. Polym. Sci.*, 2013, **38**, 874–896.
- 98 E. P. Favvas, F. K. Katsaros, S. K. Papageorgiou, A. A. Sapolidis and A. C. Mitropoulos, *React. Funct. Polym.*, 2017, **120**, 104–130.
- 99 Y. Zhang, Z. Huang, B. Ruan, X. Zhang, T. Jiang, N. Ma and F. C. Tsai, *Macromol. Rapid Commun.*, 2020, **41**, 2000402.
- 100 N. Song, T. Ma, T. Wang, K. Shi, Y. Tian, H. Yao, Y. Zhang and S. Guan, *Microporous Mesoporous Mater.*, 2020, **293**, 109809.
- 101 K. Shi, N. Song, Y. Zou, S. Zhu, H. Tan, Y. Tian, B. Zhang, H. Yao and S. Guan, *Polymer (Guildf)*, 2019, **169**, 160–166.
- 102 E. Rangel Rangel, E. M. Maya, F. Sánchez, J. de Abajo and J. G. de la Campa, *J. Memb. Sci.*, 2013, **447**, 403–412.
- 103 J. Li, Y. Ding, N. Yu, Q. Gao, X. Fan, X. Wei, G. Zhang, Z. Ma and X. He, *Carbon N. Y.*, 2020, **158**, 45–54.
- 104 A. M. Shultz, O. K. Farha, J. T. Hupp and S. B. T. Nguyen, *Chem. Sci.*, 2011, **2**, 686–689.
- 105 K. Shi, H. Yao, S. Zhang, Y. Wei, W. Xu, N. Song, S. Zhu, Y. Tian, Y. Zou and S. Guan, *Ind. Eng. Chem. Res.*, 2019, **58**, 14146–14153.
- 106 A. Roy, S. Mondal, A. Halder, A. Banerjee, D. Ghoshal, A. Paul and S. Malik, *Eur. Polym. J.*, 2017, **93**, 448–457.
- 107 Y. F. Lu, Y. M. Wang, X. D. Chen, M. H. Miao and D. H. Zhang, *Express Polym. Lett.*, 2020, **14**, 192–204.
- 108 T. Zhu, Q. Yu, L. Ding, T. Di, T. Zhao, T. Li and L. Li, *Green Chem.*, 2019, **21**, 2326–2333.
- 109 S. Chu, Y. Wang, Y. Guo, P. Zhou, H. Yu, L. Luo, F. Kong and Z. Zou, *J. Mater. Chem.*, 2012, **22**, 15519–15521.
- 110 S. Chu, Y. Wang, C. Wang, J. Yang and Z. Zou, *Int. J. Hydrogen Energy*, 2013, **38**, 10768–10772.
- 111 Y. Wang, Q. Gao, Q. You, G. Liao, H. Xia and D. Wang, *React. Funct. Polym.*, 2016, **103**, 9–16.
- 112 C. Simón-Herrero, X. Y. Chen, M. L. Ortiz, A. Romero, J. L. Valverde and L. Sánchez-Silva, *J. Mater. Res. Technol.*, 2019, **8**, 2638–2648.
- 113 T. Wang, R. Xue, H. Chen, P. Shi, X. Lei, Y. Wei, H. Guo and W. Yang, *New J. Chem.*, 2017, **41**, 14272–14278.
- 114 M. Hasegawa, R. Tokunaga, K. Hashimoto and J. Ishii, *React. Funct. Polym.*, 2019, **139**, 181–188.
- 115 J. G. Kim, J. Lee, J. Lee, S. I. Jo and J. Y. Chang, *Macromol. Res.*, 2017, **25**, 629–634.
- 116 T. Wang, H. Yao, N. Song, Y. Yang, K. Shi and S. Guan, *Ind. Eng. Chem. Res.*, 2020, **59**,

- 2953–2959.
- 117 G. Li and Z. Wang, *J. Phys. Chem. C*, 2013, **117**, 24428–24437.
- 118 J. Wu, L. Xia, S. Zhang and X. Liu, *Mater. Today Commun.*, 2020, **24**, 101030.
- 119 Z. Li, J. Zhou, R. Xu, S. Liu, Y. Wang, P. Li, W. Wu and M. Wu, *Chem. Eng. J.*, 2016, **287**, 516–522.
- 120 H. Yao, N. Zhang, K. Shen, N. Song, K. Shi, S. Zhu, Y. Zhang and S. Guan, *Polymer (Guildf.)*, 2017, **115**, 176–183.
- 121 K. V. Rao, R. Haldar, T. K. Maji and S. J. George, *Polymer (Guildf.)*, 2014, **55**, 1452–1458.
- 122 K. V. Rao, R. Haldar, C. Kulkarni, T. K. Maji and S. J. George, *Chem. Mater.*, 2012, **24**, 969–971.
- 123 H. Yao, N. Zhang, N. Song, K. Shen, P. Huo, S. Zhu, Y. Zhang and S. Guan, *Polym. Chem.*, 2017, **8**, 1298–1305.
- 124 C. Zhang, T. L. Zhai, J. J. Wang, Z. Wang, J. M. Liu, B. Tan, X. L. Yang and H. B. Xu, *Polymer (Guildf.)*, 2014, **55**, 3642–3647.
- 125 M. E. Dose, M. Chwatko, I. Hubacek, N. A. Lynd, D. R. Paul and B. D. Freeman, *Polymer (Guildf.)*, 2019, **161**, 16–26.
- 126 H. Gao, B. Tian, H. Yang, A. R. Neale, M. A. Little, R. S. Sprick, L. J. Hardwick and A. I. Cooper, *ChemSusChem*, 2020, **13**, 5571–5579.
- 127 Y. Luo, B. Li, L. Liang and B. Tan, *Chem. Commun.*, 2011, **47**, 7704–7706.
- 128 I. Hossain, A. Z. Al Munsur, O. Choi and T. H. Kim, *Sep. Purif. Technol.*, 2019, **224**, 180–188.
- 129 J. Lee and J. Y. Chang, *Chem. Commun.*, 2016, **52**, 10419–10422.
- 130 G. Li, B. Zhang, J. Yan and Z. Wang, *J. Mater. Chem. A*, 2016, **4**, 11453–11461.
- 131 Q. Li, R. Chen, Y. Guo, F. Lei, Z. Xu, H. Zhao and G. Liao, *Polymers (Basel)*, 2020, **12**, 88.
- 132 K. Shi, H. Yao, Y. Zou, Y. Wei, N. Song, S. Zhang, Y. Tian, S. Zhu, B. Zhang and S. Guan, *Microporous Mesoporous Mater.*, 2019, **287**, 246–253.
- 133 D. H. Wang and L. S. Tan, *ACS Macro Lett.*, 2019, 546–552.
- 134 K. Shi, H. Yao, Y. Zou, Y. Wei, S. Zhang, Y. Song, N. Song, T. Wang, Y. Tian, S. Zhu and S. Guan, *Microporous Mesoporous Mater.*, 2020, **292**, 109739.
- 135 L. Yu, L. Wang, L. Yu, D. Mu, L. Wang and J. Xi, *J. Memb. Sci.*, 2019, **572**, 119–127.
- 136 T. Wu, J. Dong, K. De France, P. Zhang, X. Zhao and Q. Zhang, *Chem. Eng. J.*, 2020, **395**, 124927.
- 137 J.-D. Xiao, L.-G. Qiu, Y.-P. Yuan, X. Jiang, A.-J. Xie and Y.-H. Shen, *Inorg. Chem. Commun.*, 2013, **29**, 128–130.
- 138 C. Shen, Y. Bao and Z. Wang, *Chem. Commun.*, 2013, **49**, 3321–3323.
- 139 H. Zhou, H. Lei, J. Wang, S. Qi, G. Tian and D. Wu, *Polymer (Guildf.)*, 2019, **162**, 116–120.
- 140 C. Shen and Z. Wang, *J. Phys. Chem. C*, 2014, **118**, 17585–17593.
- 141 N. Song, T. Wang, H. Yao, T. Ma, K. Shi, Y. Tian, Y. Zou, S. Zhu, Y. Zhang and S. Guan, *Polym. Chem.*, 2019, **10**, 4611–4620.
- 142 N. Song, H. Yao, T. Ma, T. Wang, K. Shi, Y. Tian, Y. Zou, S. Zhu, Y. Zhang and S. Guan, *Chem. Eng. J.*, 2019, **368**, 618–626.
- 143 J. Maschita, T. Banerjee, G. Savasci, F. Haase, C. Ochsenfeld and B. V. Lotsch, *Angew. Chemie Int. Ed.*, 2020, **59**, 15750–15758.
- 144 Y. Tian, K. Shi, H. Yao, T. Wang, H. Liu, Y. Song, Y. Zhang and S. Guan, *J. Phys. Chem. C*,

- 2020, **124**, 2872–2878.
- 145 Z. Wang, B. Zhang, H. Yu, L. Sun, C. Jiao and W. Liu, *Chem. Commun.*, 2010, **46**, 7730–7732.
- 146 Z. Wu, B. Han, C. Zhang, D. Zhu and Z. Yang, *Polymer (Guildf.)*, 2019, **179**, 121605.
- 147 J. Yan, B. Zhang and Z. Wang, *ACS Appl. Mater. Interfaces*, 2018, **10**, 26618–26627.
- 148 N. Song, T. Ma, T. Wang, Z. Li, H. Yao and S. Guan, *J. Colloid Interface Sci.*, 2020, **573**, 328–335.
- 149 J. Yan, B. Zhang, L. Guo and Z. Wang, *J. Phys. Chem. C*, 2019, **123**, 575–583.
- 150 D. Tian, H.-Z. Zhang, D.-S. Zhang, Z. Chang, J. Han, X.-P. Gao and X.-H. Bu, *RSC Adv.*, 2014, **4**, 7506–7510.
- 151 L. Jiang, Y. Tian, T. Sun, Y. Zhu, H. Ren, X. Zou, Y. Ma, K. R. Meihaus, J. R. Long and G. Zhu, *J. Am. Chem. Soc.*, 2018, **140**, 15724–15730.
- 152 W. Zhu, X. Wang, T. Li, R. Shen, S.-J. Hao, Y. Li, Q. Wang, Z. Li and Z.-G. Gu, *Polym. Chem.*, 2018, **9**, 1430–1438.
- 153 J. Lv, Y.-X. Tan, J. Xie, R. Yang, M. Yu, S. Sun, M.-D. Li, D. Yuan and Y. Wang, *Angew. Chemie Int. Ed.*, 2018, **57**, 12716–12720.
- 154 C. Zhang, S. Zhang, Y. Yan, F. Xia, A. Huang and Y. Xian, *ACS Appl. Mater. Interfaces*, 2017, **9**, 13415–13421.
- 155 R. van der Jagt, A. Vasileiadis, H. Veldhuizen, P. Shao, X. Feng, S. Ganapathy, N. C. Habisreutinger, M. A. van der Veen, C. Wang, M. Wagemaker, S. van der Zwaag and A. Nagai, *Chem. Mater.*, 2021, **33**, 818–833.
- 156 S. Royuela, E. Martínez-Periñán, M. P. Arrieta, J. I. Martínez, M. M. Ramos, F. Zamora, E. Lorenzo and J. L. Segura, *Chem. Commun.*, 2020, **56**, 1267–1270.
- 157 G. Zhao, H. Li, Z. Gao, L. Xu, Z. Mei, S. Cai, T. Liu, X. Yang, H. Guo and X. Sun, *Adv. Funct. Mater.*, 2021, **31**, 2101019.
- 158 X. Zhang, X. Cui, C. H. Lu, H. Li, Q. Zhang, C. He and Y. Yang, *Chem. Eng. J.*, 2020, **401**, 126031.
- 159 S. Qiao, S. Kang, Z. Hu, J. Yu, Y. Wang and J. Zhu, *J. Porous Mater.*, 2020, **27**, 237–247.
- 160 S. Liu, W. Chen and X. Zhou, *J. Porous Mater.*, 2021, **28**, 1155–1165.
- 161 M. Hasegawa, R. Tokunaga, K. Hashimoto and J. Ishii, *React. Funct. Polym.*, 2019, **139**, 181–188.
- 162 Y. Liao, J. Weber and C. F. J. Faul, *Macromolecules*, 2015, **48**, 2064–2073.
- 163 Z. Li, J. Zhou, R. Xu, S. Liu, Y. Wang, P. Li, W. Wu and M. Wu, *Chem. Eng. J.*, 2016, **287**, 516–522.
- 164 D. Tian, H. Z. Zhang, D. S. Zhang, Z. Chang, J. Han, X. P. Gao and X. H. Bu, *RSC Adv.*, 2014, **4**, 7506–7510.
- 165 H. Yao, N. Zhang, K. Shen, N. Song, K. Shi, S. Zhu, Y. Zhang and S. Guan, *Polymer (Guildf.)*, 2017, **115**, 176–183.
- 166 Y. Luo, B. Li, L. Liang and B. Tan, *Chem. Commun.*, 2011, **47**, 7704–7706.
- 167 A. Roy, S. Mondal, A. Halder, A. Banerjee, D. Ghoshal, A. Paul and S. Malik, *Eur. Polym. J.*, 2017, **93**, 448–457.
- 168 G. Li and Z. Wang, *Macromolecules*, 2013, **46**, 3058–3066.
- 169 F. Wang, X. Wu, X. Yuan, Z. Liu, Y. Zhang, L. Fu, Y. Zhu, Q. Zhou, Y. Wu and W. Huang, *Chem. Soc. Rev.*, 2017, **46**, 6816–6854.
- 170 R. Heimböckel, F. Hoffmann and M. Fröba, *Phys. Chem. Chem. Phys.*, 2019, **21**, 3122–3133.
- 171 J. S. M. Lee, T. H. Wu, B. M. Alston, M. E. Briggs, T. Hasell, C. C. Hu and A. I. Cooper, *J.*

- Mater. Chem. A*, 2016, **4**, 7665–7673.
- 172 Y. Jiang and J. Liu, *Energy Environ. Mater.*, 2019, **2**, 30–37.
- 173 Y. Wang, Y. Song and Y. Xia, *Chem. Soc. Rev.*, 2016, **45**, 5925–5950.
- 174 H. Wu, Q. Meng, Q. Yang, M. Zhang, K. Lu and Z. Wei, *Adv. Mater.*, 2015, **27**, 6504–6510.
- 175 X. Han, C. Chang, L. Yuan, T. Sun and J. Sun, *Adv. Mater.*, 2007, **19**, 1616–1621.
- 176 Z. Song, H. Zhan and Y. Zhou, *Angew. Chemie - Int. Ed.*, 2010, **49**, 8444–8448.
- 177 W. Luo, C. Bommier, Z. Jian, X. Li, R. Carter, S. Vail, Y. Lu, J. J. Lee and X. Ji, *ACS Appl. Mater. Interfaces*, 2015, **7**, 2626–2631.
- 178 D. Wu, Q. Xu, J. Qian, X. Li and Y. Sun, *Chem. - A Eur. J.*, 2019, **25**, 3105–3111.
- 179 Q. Xu, Y. Tang, X. Zhang, Y. Oshima, Q. Chen and D. Jiang, *Adv. Mater.*, 2018, **30**, 1706330.
- 180 J. Guo, C. Y. Lin, Z. Xia and Z. Xiang, *Angew. Chemie - Int. Ed.*, 2018, **57**, 12567–12572.
- 181 G. Singh, J. Lee, A. Karakoti, R. Bahadur, J. Yi, D. Zhao, K. Albahily and A. Vinu, *Chem. Soc. Rev.*, 2020, **49**, 4360–4404.
- 182 P. Atkins, J. de Paula and J. Keeler, *Atkins' Physical Chemistry*, Oxford University Press, Twelfth., 2022.
- 183 A. Nuhnen and C. Janiak, *Dalt. Trans.*, 2020, **49**, 10295–10307.
- 184 I. P. Jain, *Int. J. Hydrogen Energy*, 2009, **34**, 7368–7378.
- 185 S. Sharma and S. K. Ghoshal, *Renew. Sustain. Energy Rev.*, 2015, **43**, 1151–1158.
- 186 P. P. Edwards, V. L. Kuznetsov, W. I. F. David and N. P. Brandon, *Energy Policy*, 2008, **36**, 4356–4362.
- 187 H. Furukawa, N. Ko, Y. B. Go, N. Aratani, S. B. Choi, E. Choi, A. Ö. Yazaydin, R. Q. Snurr, M. O'Keeffe, J. Kim and O. M. Yaghi, *Science*, 2010, **329**, 424–428.
- 188 S. H. Sang, H. Furukawa, O. M. Yaghi and W. A. Goddard, *J. Am. Chem. Soc.*, 2008, **130**, 11580–11581.
- 189 M. P. Suh, H. J. Park, T. K. Prasad and D. W. Lim, *Chem. Rev.*, 2012, **112**, 782–835.
- 190 T. X. Wang, H. P. Liang, D. A. Anito, X. Ding and B. H. Han, *J. Mater. Chem. A*, 2020, **8**, 7003–7034.
- 191 Y. Chen, R. Luo, Q. Xu, W. Zhang, X. Zhou and H. Ji, *ChemCatChem*, 2017, **9**, 767–773.
- 192 R. R. Shaikh, S. Pornpraprom and V. D'Elia, *ACS Catal.*, 2018, **8**, 419–450.
- 193 F. Della Monica and A. W. Kleij, *Catal. Sci. Technol.*, 2020, **10**, 3483–3501.
- 194 V. Aomchad, À. Cristòfol, F. Della Monica, B. Limburg, V. D'Elia and A. W. Kleij, *Green Chem.*, 2021, **23**, 1077–1113.
- 195 Z. Wei and C. F. J. Faul, *Macromol. Rapid Commun.*, 2008, **29**, 280–292.
- 196 F. Qu, G. Zhu, H. Lin, W. Zhang, J. Sun, S. Li and S. Qiu, *J. Solid State Chem.*, 2006, **179**, 2027–2035.
- 197 P. Horcajada, C. Serre, M. Vallet-Regí, M. Sebban, F. Taulelle and G. Férey, *Angew. Chemie - Int. Ed.*, 2006, **45**, 5974–5978.
- 198 J. D. Xiao, L. G. Qiu, Y. P. Yuan, X. Jiang, A. J. Xie and Y. H. Shen, *Inorg. Chem. Commun.*, 2013, **29**, 128–130.
- 199 M. L. Huggins, *J. Phys. Chem.*, 1951, **55**, 619–620.
- 200 G. H. Brown, *Inorg. Chem.*, 1963, **2**, 431–432.
- 201 E. Stefanis and C. Panayiotou, *Int. J. Thermophys.*, 2008, **29**, 568–585.
- 202 C. M. Hansen, *Hansen solubility parameters: A user's handbook: Second edition*, 2007.
- 203 G. H. Brown, *Inorg. Chem.*, 1963, **2**, 431–432.
- 204 C. M. Hansen, in *Hansen Solubility Parameters: A Users Handbook, Second Edition*,

- 2nd edn., 2007.
- 205 J. Chen, T. Qiu, W. Yan and C. F. J. Faul, *J. Mater. Chem. A*, 2020, **8**, 22657–22665.
- 206 M. G. Kibria, J. P. Edwards, C. M. Gabardo, C. T. Dinh, A. Seifitokaldani, D. Sinton and E. H. Sargent, *Adv. Mater.*, 2019, **31**, 1–24.
- 207 C. Jia, K. Dastafkan, W. Ren, W. Yang and C. Zhao, *Sustain. Energy Fuels*, 2019, **3**, 2890–2906.
- 208 D.-H. Yang, Y. Tao, X. Ding and B.-H. Han, *Chem. Soc. Rev.*, 2022, **51**, 761–791.
- 209 R. M. Arán-Ais, D. Gao and B. Roldan Cuenya, *Acc. Chem. Res.*, 2018, **51**, 2906–2917.
- 210 M. Jouny, W. Luc and F. Jiao, *Ind. Eng. Chem. Res.*, 2018, **57**, 2165–2177.
- 211 E. E. Benson, C. P. Kubiak, A. J. Sathrum and J. M. Smieja, *Chem. Soc. Rev.*, 2009, **38**, 89–99.
- 212 D. R. Kauffman, J. Thakkar, R. Siva, C. Matranga, P. R. Ohodnicki, C. Zeng and R. Jin, *ACS Appl. Mater. Interfaces*, 2015, **7**, 15626–15632.
- 213 C. Costentin, M. Robert and J. M. Savéant, *Chem. Soc. Rev.*, 2013, **42**, 2423–2436.
- 214 D. T. Whipple and P. J. A. Kenis, *J. Phys. Chem. Lett.*, 2010, **1**, 3451–3458.
- 215 B. Kumar, J. P. Brian, V. Atla, S. Kumari, K. A. Bertram, R. T. White and J. M. Spurgeon, *Catal. Today*, 2016, **270**, 19–30.
- 216 J. Schneider, H. Jia, J. T. Muckerman and E. Fujita, *Chem. Soc. Rev.*, 2012, **41**, 2036–2051.
- 217 G. Li, X. Zhou and Z. Wang, *J. Phys. Chem. C*, 2020, **124**, 3087–3094.
- 218 Y. Liao, J. Weber and C. F. J. Faul, *Macromolecules*, 2015, **48**, 2064–2073.
- 219 M. Favaro, H. Xiao, T. Cheng, W. A. Goddard and E. J. Crumlin, *Proc. Natl. Acad. Sci. U. S. A.*, 2017, **114**, 6706–6711.
- 220 S. Xie, Q. Zhang, G. Liu and Y. Wang, *Chem. Commun.*, 2016, **52**, 35–59.
- 221 X. Chang, T. Wang and J. Gong, *Energy Environ. Sci.*, 2016, **9**, 2177–2196.
- 222 Y. Guan, J. Lai and G. Xu, *ChemElectroChem*, 2021, **8**, 2764–2777.
- 223 Q. Wang, Y. Zhang, H. Lin and J. Zhu, *Chem. - A Eur. J.*, 2019, **25**, 14026–14035.
- 224 Y. Zhao, L. Zheng, D. Jiang, W. Xia, X. Xu, Y. Yamauchi, J. Ge and J. Tang, *Small*, 2021, **17**, 2006590.
- 225 Z. He, J. Goulas, E. Parker, Y. Sun, X. dong Zhou and L. Fei, *Catal. Today*, 2023, **409**, 103–118.
- 226 Y. Fan, M. Chen, N. Xu, K. Wang, Q. Gao, J. Liang and Y. Liu, *Front. Chem.*, 2022, **10**, 942492.
- 227 C. Y. Lin, D. Zhang, Z. Zhao and Z. Xia, *Adv. Mater.*, 2018, **30**, 1703646.
- 228 X. Zhang, Y. Zhang, Q. Li, X. Zhou, Q. Li, J. Yi, Y. Liu and J. Zhang, *J. Mater. Chem. A*, 2020, **8**, 9776–9787.
- 229 X. Jiang, H. Li, J. Xiao, D. Gao, R. Si, F. Yang, Y. Li, G. Wang and X. Bao, *Nano Energy*, 2018, **52**, 345–350.
- 230 M. Perfecto-Irigaray, J. Albo, G. Beobide, O. Castillo, A. Irabien and S. Pérez-Yáñez, *RSC Adv.*, 2018, **8**, 21092–21099.
- 231 X. Tan, C. Yu, C. Zhao, H. Huang, X. Yao, X. Han, W. Guo, S. Cui, H. Huang and J. Qiu, *ACS Appl. Mater. Interfaces*, 2019, **11**, 9904–9910.
- 232 L. Jiao, W. Yang, G. Wan, R. Zhang, X. Zheng, H. Zhou, S. H. Yu and H. L. Jiang, *Angew. Chemie - Int. Ed.*, 2020, **59**, 20589–20595.
- 233 L. Ye, J. Liu, Y. Gao, C. Gong, M. Addicoat, T. Heine, C. Wöll and L. Sun, *J. Mater. Chem. A*, 2016, **4**, 15320–15326.
- 234 N. Kornienko, Y. Zhao, C. S. Kley, C. Zhu, D. Kim, S. Lin, C. J. Chang, O. M. Yaghi and P.

- Yang, *J. Am. Chem. Soc.*, 2015, **137**, 14129–14135.
- 235 X. Jiang, H. Wu, S. Chang, R. Si, S. Miao, W. Huang, Y. Li, G. Wang and X. Bao, *J. Mater. Chem. A*, 2017, **5**, 19371–19377.
- 236 S. Lin, C. S. Diercks, Y. B. Zhang, N. Kornienko, E. M. Nichols, Y. Zhao, A. R. Paris, D. Kim, P. Yang, O. M. Yaghi and C. J. Chang, *Science*, 2015, **349**, 1208–1213.
- 237 P. L. Cheung, S. K. Lee and C. P. Kubiak, *Chem. Mater.*, 2019, **31**, 1908–1919.
- 238 J. Yuan, S. Chen, Y. Zhang, R. Li, J. Zhang and T. Peng, *Adv. Mater.*, 2022, **34**, 2203139.
- 239 Z. Liang, H. Y. Wang, H. Zheng, W. Zhang and R. Cao, *Chem. Soc. Rev.*, 2021, **50**, 2540–2581.
- 240 H. Zhang, J. Li, Q. Tan, L. Lu, Z. Wang and G. Wu, *Chem. - A Eur. J.*, 2018, **24**, 18137–18157.
- 241 A. Al-Omari, Z. Yamani and H. Nguyen, *Molecules*, 2018, **23**, 2835.
- 242 T. N. Nguyen and C. T. Dinh, *Chem. Soc. Rev.*, 2020, **49**, 7488–7504.
- 243 S. Verma, B. Kim, H. R. M. Jhong, S. Ma and P. J. A. Kenis, *ChemSusChem*, 2016, **9**, 1972–1979.
- 244 C. Calabrese, F. Giacalone and C. Aprile, *Catalysts*, 2019, **9**, 325.
- 245 A. J. Kamphuis, F. Picchioni and P. P. Pescarmona, *Green Chem.*, 2019, **21**, 406–448.
- 246 C. Ngassam Tounzoua, B. Grignard and C. Detrembleur, *Angew. Chemie Int. Ed.*, 2022, **61**, e2021160.
- 247 B. Schöffner, F. Schöffner, S. P. Verevkin and A. Börner, *Chem. Rev.*, 2010, **110**, 4554–4581.
- 248 F. Ouhib, L. Meabe, A. Mahmoud, B. Grignard, J.-M. Thomassin, F. Boschini, H. Zhu, M. Forsyth, D. Mecerreyes and C. Detrembleur, *ACS Appl. Polym. Mater.*, 2020, **2**, 922–931.
- 249 X. D. Lang and L. N. He, *Chem. Rec.*, 2016, **16**, 1337–1352.
- 250 B. Yu and L. N. He, *ChemSusChem*, 2015, **8**, 52–62.
- 251 T. Kimura, K. Kamata and N. Mizuno, *Angew. Chemie - Int. Ed.*, 2012, **51**, 6700–6703.
- 252 R. Babu, A. C. Kathalikkattil, R. Roshan, J. Tharun, D. W. Kim and D. W. Park, *Green Chem.*, 2015, **18**, 232–242.
- 253 N. Aoyagi, Y. Furusho and T. Endo, *ChemInform*, 2014, **45**, 201414137.
- 254 N. Aoyagi, Y. Furusho and T. Endo, *Tetrahedron Lett.*, 2013, **54**, 7031–7034.
- 255 C. Martín, G. Fiorani and A. W. Kleij, *ACS Catal.*, 2015, **5**, 1353–1370.
- 256 Z. Z. Yang, L. N. He, C. X. Miao and S. Chanfreau, *Adv. Synth. Catal.*, 2010, **352**, 2233–2240.
- 257 X. Liao, Z. Wang, L. Kong, X. Gao, J. He, D. Huang and J. Lin, *Mol. Catal.*, 2023, **535**, 112834.
- 258 D. Kim, S. Subramanian, D. Thirion, Y. Song, A. Jamal, M. S. Otaibi and C. T. Yavuz, *Catal. Today*, 2020, **356**, 527–534.
- 259 L. Guo, K. J. Lamb and M. North, *Green Chem.*, 2021, **23**, 77–118.
- 260 A. Decortes, A. M. Castilla and A. W. Kleij, *Angew. Chemie - Int. Ed.*, 2010, **49**, 9822–9837.
- 261 R. Luo, X. Zhou, W. Zhang, Z. Liang, J. Jiang and H. Ji, *Green Chem.*, 2014, **16**, 4179–4189.
- 262 N. Zhang, B. Zou, G. P. Yang, B. Yu and C. W. Hu, *J. CO₂ Util.*, 2017, **22**, 9–14.
- 263 S. Ravi, J. Kim, Y. Choi, H. H. Han, S. Wu, R. Xiao and Y. S. Bae, *ACS Sustain. Chem. Eng.*, 2023, **11**, 1190–1199.
- 264 D. Ma, K. Liu, J. Li and Z. Shi, *ACS Sustain. Chem. Eng.*, 2018, **6**, 15050–15055.

- 265 J. Wu, L. Lin, F. J. Morvan, J. Du and W. Fan, *Inorg. Chem. Front.*, 2019, **6**, 2014–2023.
- 266 W. Wang, M. Zhou and D. Yuan, *J. Mater. Chem. A*, 2017, **5**, 1334–1347.
- 267 M. Fang, Q. Xiang, C. Yu, Z. Xia, X. Zhou, D. Cai, Z. Wang and H. Yu, *Greenh. Gases Sci. Technol.*, 2015, **5**, 210–221.
- 268 R. Sharma, A. Bansal, C. N. Ramachandran and P. Mohanty, *Chem. Commun.*, 2019, **55**, 11607–11610.
- 269 X. Chang, T. Wang and J. Gong, *Energy Environ. Sci.*, 2016, **9**, 2177–2196.
- 270 S. Yang, W. Hu, X. Zhang, P. He, B. Pattengale, C. Liu, M. Cendejas, I. Hermans, X. Zhang, J. Zhang and J. Huang, *J. Am. Chem. Soc.*, 2018, **140**, 14614–14618.
- 271 H.-J. Zhu, M. Lu, Y.-R. Wang, S.-J. Yao, M. Zhang, Y.-H. Kan, J. Liu, Y. Chen, S.-L. Li and Y.-Q. Lan, *Nat. Commun.*, 2020, **11**, 497.
- 272 L. Gong, Y. Gao, Y. Wang, B. Chen, B. Yu, W. Liu, B. Han, C. Lin, Y. Bian, D. Qi and J. Jiang, *Catal. Sci. Technol.*, 2022, **12**, 6566–6571.
- 273 Y. Liu, S. Wang, X. Meng, Y. Ye, X. Song and Z. Liang, *Mater. Chem. Front.*, 2021, **5**, 5319–5327.
- 274 J. Albo, D. Vallejo, G. Beobide, O. Castillo, P. Castaño and A. Irabien, *ChemSusChem*, 2017, **10**, 1100–1109.
- 275 L. Wang, W. Chen, D. Zhang, Y. Du, R. Amal, S. Qiao, J. Wu and Z. Yin, *Chem. Soc. Rev.*, 2019, **48**, 5310–5349.
- 276 Y. Pei, H. Zhong and F. Jin, *Energy Sci. Eng.*, 2021, **9**, 1012–1032.
- 277 Y. Oh and X. Hu, *Chem. Soc. Rev.*, 2013, **42**, 2253–2261.
- 278 S. C. Shit, N. S. Powar, P. Kalita, R. Paul, S. Xu, J.-W. Jung, C.-H. Cho, S.-I. In and J. Mondal, *Chem. Commun.*, 2022, **58**, 13716–13719.
- 279 B. B. Narzary, B. C. Baker, N. Yadav, V. D’Elia and C. F. J. Faul, *Polym. Chem.*, 2021, **12**, 6494–6514.
- 280 M. R. Liebl and J. Senker, *Chem. Mater.*, 2013, **25**, 970–980.
- 281 C. Sandford, M. A. Edwards, K. J. Klunder, D. P. Hickey, M. Li, K. Barman, M. S. Sigman, H. S. White and S. D. Minter, *Chem. Sci.*, 2019, **10**, 6404–6422.
- 282 A. H. Shah, W. Zaid, A. Shah, U. A. Rana, H. Hussain, M. N. Ashiq, R. Qureshi, A. Badshah, M. A. Zia and H.-B. Kraatz, *J. Electrochem. Soc.*, 2015, **162**, H115–H123.
- 283 H. J. Freund and M. W. Roberts, *Surf. Sci. Rep.*, 1996, **25**, 225–273.
- 284 P. A. Kempler and A. C. Nielander, *Nat. Commun.*, 2023, **14**, 1158.
- 285 C. Xiao and J. Zhang, *ACS Nano*, 2021, **15**, 7975–8000.
- 286 Y. Zhou, R. Zhou, X. Zhu, N. Han, B. Song, T. Liu, G. Hu, Y. Li, J. Lu and Y. Li, *Adv. Mater.*, 2020, **32**, 2000992.
- 287 Y. Gu, J. Wei, X. Wu and X. Liu, *Sci. Rep.*, 2021, **11**, 11136.
- 288 N. Huang, K. H. Lee, Y. Yue, X. Xu, S. Irle, Q. Jiang and D. Jiang, *Angew. Chemie Int. Ed.*, 2020, **59**, 16587–16593.
- 289 C. Lu, J. Yang, S. Wei, S. Bi, Y. Xia, M. Chen, Y. Hou, M. Qiu, C. Yuan, Y. Su, F. Zhang, H. Liang and X. Zhuang, *Adv. Funct. Mater.*, 2019, **29**, 1806884.
- 290 S. Raja, G. T. S. T. da Silva, E. A. Reis, J. C. da Cruz, A. Brunca Silva, M. B. Andrade, G. Periyasami, P. Karthikeyan, I. F. Perepichka, L. H. Mascaro and C. Ribeiro, *Energy & Fuels*, DOI:10.1021/acs.energyfuels.3c03268.
- 291 K. Zhao, Y. Liu, X. Quan, S. Chen and H. Yu, *ACS Appl. Mater. Interfaces*, 2017, **9**, 5302–5311.
- 292 D. Yang and X. Wang, *SmartMat*, 2022, **3**, 54–67.
- 293 M. M. F. Hasan, L. M. Rossi, D. P. Debecker, K. C. Leonard, Z. Li, B. C. E. Makhubela, C.

- Zhao and A. Kleij, *ACS Sustain. Chem. Eng.*, 2021, **9**, 12427–12430.
- 294 Q. Liu, L. Wu, R. Jackstell and M. Beller, *Nat. Commun.*, 2015, **6**, 5933.
- 295 P. Bhanja, A. Modak and A. Bhaumik, *ChemCatChem*, 2019, **11**, 244–257.
- 296 K. S. Song, P. W. Fritz and A. Coskun, *Chem. Soc. Rev.*, 2022, **51**, 9831–9852.
- 297 T. Kong, Y. Jiang and Y. Xiong, *Chem. Soc. Rev.*, 2020, **49**, 6579–6591.
- 298 L. Li, X. Li, Y. Sun and Y. Xie, *Chem. Soc. Rev.*, 2022, **51**, 1234–1252.
- 299 R. Sun, Y. Liao, S.-T. Bai, M. Zheng, C. Zhou, T. Zhang and B. F. Sels, *Energy Environ. Sci.*, 2021, **14**, 1247–1285.
- 300 X. Liu and L. Dai, *Nat. Rev. Mater.*, 2016, **1**, 16064.
- 301 D. Yadav, Subodh and S. K. Awasthi, *Mater. Chem. Front.*, 2022, **6**, 1574–1605.
- 302 M. Jia, J. Li, J. Gu, L. Zhang and Y. Liu, *Mater. Chem. Front.*, 2021, **5**, 1398–1404.
- 303 S. Meng, G. Li, P. Wang, M. He, X. Sun and Z. Li, *Mater. Chem. Front.*, 2023, **7**, 806–827.
- 304 T. Chen, W. Xiao, J. Yang, M. Qiu, C. Yi and Z. Xu, *J. Colloid Interface Sci.*, 2022, **622**, 202–208.
- 305 B. B. Narzary, B. C. Baker and C. F. J. Faul, *Adv. Mater.*, 2023, **35**, 2211795.
- 306 P. Cheng, X. Zhao and X. Zhan, *Accounts Mater. Res.*, 2022, **3**, 309–318.
- 307 K. S. W. Sing, *Pure Appl. Chem.*, 1985, **57**, 603–619.
- 308 R. Walczak, A. Savateev, J. Heske, N. V. Tarakina, S. Sahoo, J. D. Epping, T. D. Kühne, B. Kurpil, M. Antonietti and M. Oschatz, *Sustain. Energy Fuels*, 2019, **3**, 2819–2827.
- 309 H. M. Lee, I. S. Youn, M. Saleh, J. W. Lee and K. S. Kim, *Phys. Chem. Chem. Phys.*, 2015, **17**, 10925–10933.
- 310 S. Bhunia, R. A. Molla, V. Kumari, S. M. Islam and A. Bhaumik, *Chem. Commun.*, 2015, **51**, 15732–15735.
- 311 J. Chen, H. Li, M. Zhong and Q. Yang, *Green Chem.*, 2016, **18**, 6493–6500.
- 312 J. Liang, Y. B. Huang and R. Cao, *Coord. Chem. Rev.*, 2019, **378**, 32–65.
- 313 O. Buyukcakir, S. H. Je, S. N. Talapaneni, D. Kim and A. Coskun, *ACS Appl. Mater. Interfaces*, 2017, **9**, 7209–7216.
- 314 J. Roeser, K. Kailasam and A. Thomas, *ChemSusChem*, 2012, **5**, 1793–1799.
- 315 S. Ding, L. Sun, X. Ma, D. Cheng, S. Wu, R. Zeng, S. Deng, C. Chen and N. Zhang, *Catal. Letters*, 2020, **150**, 2970–2977.
- 316 Y. Zhi, P. Shao, X. Feng, H. Xia, Y. Zhang, Z. Shi, Y. Mu and X. Liu, *J. Mater. Chem. A*, 2018, **6**, 374–382.
- 317 G. H. Gunasekar, J. Shin, K.-D. Jung, K. Park and S. Yoon, *ACS Catal.*, 2018, **8**, 4346–4353.
- 318 X. Zhang, B. Qiu, Y. Zou, S. Wang, W. Mai, Y. Cao, Y. Wang, J. Chen and T. Li, *Microporous Mesoporous Mater.*, 2021, **319**, 110758.
- 319 X. Zhang, J. Wang, Y. Bian, H. Lv, B. Qiu, Y. Zhang, R. Qin, D. Zhu, S. Zhang, D. Li, S. Wang, W. Mai, Y. Li and T. Li, *J. CO₂ Util.*, 2022, **58**, 101924.
- 320 F. Zhou, Q. Deng, N. Huang, W. Zhou and W. Deng, *ChemistrySelect*, 2020, **5**, 10516–10520.
- 321 Y. Lu, Z. Chang, S. Zhang, S. Wang, Q. Chen, L. Feng and Z. Sui, *J. Mater. Sci.*, 2020, **55**, 11856–11869.
- 322 R. Sharma, A. Bansal, C. N. Ramachandran and P. Mohanty, *Chem. Commun.*, 2019, **55**, 11607–11610.
- 323 D.-H. Yang, Y. Tao, X. Ding and B.-H. Han, *Chem. Soc. Rev.*, 2022, **51**, 761–791.
- 324 J. Li, Y. Kuang, Y. Meng, X. Tian, W.-H. Hung, X. Zhang, A. Li, M. Xu, W. Zhou, C.-S. Ku,

- C.-Y. Chiang, G. Zhu, J. Guo, X. Sun and H. Dai, *J. Am. Chem. Soc.*, 2020, **142**, 7276–7282.
- 325 W. Guo, S. Liu, X. Tan, R. Wu, X. Yan, C. Chen, Q. Zhu, L. Zheng, J. Ma, J. Zhang, Y. Huang, X. Sun and B. Han, *Angew. Chemie Int. Ed.*, 2021, **60**, 21979–21987.
- 326 K. Liu, Z. Xu, H. Huang, Y. Zhang, Y. Liu, Z. Qiu, M. Tong, Z. Long and G. Chen, *Green Chem.*, 2022, **24**, 136–141.
- 327 X. Zhang, H. Zhang, B. Qiu, D. Zhu, S. Zhang, Y. Bian, J. Wang, D. Li, S. Wang, W. Mai, J. Chen and T. Li, *Fuel*, 2023, **331**, 125828.
- 328 Q. Shi, J. Wu, X. Wu, A. Peng and H. Huang, *Chem. - A Eur. J.*, 2020, **26**, 12510–12522.
- 329 R. Lenaerts, T. Cardeynaels, I. Sudakov, J. Kesters, P. Verstappen, J. Manca, B. Champagne, L. Lutsen, D. Vanderzande, K. Vandewal, E. Goovaerts and W. Maes, *Sol. Energy Mater. Sol. Cells*, 2019, **196**, 178–184.
- 330 R. S. Wilson-Kovacs, X. Fang, M. J. L. Hagemann, H. E. Symons and C. F. J. Faul, *Chem. - A Eur. J.*, 2022, **28**.
- 331 Y. J. Hwang, T. Earmme, B. A. E. Courtright, F. N. Eberle and S. A. Jenekhe, *J. Am. Chem. Soc.*, 2015, **137**, 4424–4434.
- 332 Q. Jiang, J. Zhang, Z. Mao, Y. Yao, D. Zhao, Y. Jia, D. Hu and Y. Ma, *Adv. Mater.*, 2022, **34**, 2108103.
- 333 D. Shukla, S. F. Nelson, D. C. Freeman, M. Rajeswaran, W. G. Ahearn, D. M. Meyer and J. T. Carey, *Chem. Mater.*, 2008, **20**, 7486–7491.
- 334 Y. Hu, Y. Qin, X. Gao, F. Zhang, C. A. Di, Z. Zhao, H. Li and D. Zhu, *Org. Lett.*, 2012, **14**, 292–295.
- 335 S. Chen, Z. Xue, N. Gao, X. Yang and L. Zang, *Sensors*, 2020, **20**, 917.
- 336 W. Zhou, G. Liu, B. Yang, Q. Ji, W. Xiang, H. He, Z. Xu, C. Qi, S. Li, S. Yang and C. Xu, *Sci. Total Environ.*, 2021, **780**, 146483.
- 337 C. Zhou, W. Xia, D. Huang, M. Cheng, H. Zhang, T. Cai, W. Xiong, Y. Yang, B. Song, W. Wang, M. Zhou and G. Zeng, *Environ. Sci. Nano*, 2021, **8**, 602–618.
- 338 S. Caby, L. M. Bouchet, J. E. Argüello, R. A. Rossi and J. I. Bardagi, *ChemCatChem*, 2021, **13**, 3001–3009.
- 339 Z. Zhong, X. Xu, A. Cao, W. You, Z. Tao and L. Kang, *J. Power Sources*, 2021, **489**, 229493.
- 340 J. D. B. Koenig, Z. Dubrawski, K. R. Rao, J. Willkomm, B. S. Gelfand, C. Risko, W. E. Piers and G. C. Welch, *ChemRxiv*, 2020, 1–76.
- 341 H. Banda, D. Damien, K. Nagarajan, A. Raj, M. Hariharan and M. M. Shaijumon, *Adv. Energy Mater.*, 2017, **7**, 1701316.
- 342 S. Seifert, D. Schmidt and F. Würthner, *Chem. Sci.*, 2015, **6**, 1663–1667.
- 343 T. Wang, L. Wang, D. Wu, W. Xia, H. Zhao and D. Jia, *J. Mater. Chem. A*, 2014, **2**, 8352–8361.
- 344 H. Wang, M. Li, J. Song, C. Li and Z. Bo, *Dye. Pigment.*, 2020, **183**, 108736.
- 345 S. E. Penty, M. A. Zwijnenburg, G. R. F. Orton, P. Stachelek, R. Pal, Y. Xie, S. L. Griffin and T. A. Barendt, *J. Am. Chem. Soc.*, 2022, **144**, 12290–12298.
- 346 L. Zhang, I. Song, J. Ahn, M. Han, M. Linares, M. Surin, H.-J. Zhang, J. H. Oh and J. Lin, *Nat. Commun.*, 2021, **12**, 142.
- 347 H. J. Cho, S. W. Kim, S. Kim, S. Lee, J. Lee, Y. Cho, Y. Lee, T. W. Lee, H. J. Shin and C. Song, *J. Mater. Chem. C*, 2020, **8**, 17289–17296.
- 348 L. Zong, Y. Xie, C. Wang, J. R. Li, Q. Li and Z. Li, *Chem. Commun.*, 2016, **52**, 11496–11499.

- 349 J. Royackers, A. Minotto, D. G. Congrave, W. Zeng, A. Patel, A. D. Bond, D. K. Bučar, F. Cacialli and H. Bronstein, *J. Org. Chem.*, 2020, **85**, 207–214.
- 350 G. S. Perez, S. Dasgupta, W. Żuraw, R. F. Pineda, K. Wojciechowski, L. K. Jagadamma, I. Samuel and N. Robertson, *J. Mater. Chem. A*, 2022, **10**, 11046–11053.
- 351 Y. Yu, N. Xue, C. Xiao, M. K. Ravva, Y. Guo, L. Wu, L. Zhang, Z. Li, W. Yue and Z. Wang, *J. Mater. Chem. C*, 2019, **7**, 12263–12269.
- 352 F. Ambroz, T. J. Macdonald, V. Martis and I. P. Parkin, *Small Methods*, 2018, **2**.
- 353 A. H. Berger and A. S. Bhowan, *Energy Procedia*, 2011, **4**, 562–567.
- 354 X. Li, S. Wang, L. Li, Y. Sun and Y. Xie, *J. Am. Chem. Soc.*, 2020, **142**, 9567–9581.
- 355 Y. Zou and S. Wang, *Adv. Sci.*, 2021, **8**, 2003579.
- 356 L. Jin and A. Seifitokaldani, *Catalysts*, 2020, **10**, 481.
- 357 L. Wang, B. Cheng, L. Zhang and J. Yu, *Small*, 2021, **17**, 2103447.
- 358 J. Heyes, M. Dunwell and B. Xu, *J. Phys. Chem. C*, 2016, **120**, 17334–17341.
- 359 D. M. Weekes, D. A. Salvatore, A. Reyes, A. Huang and C. P. Berlinguette, *Acc. Chem. Res.*, 2018, **51**, 910–918.
- 360 S. Liang, N. Altaf, L. Huang, Y. Gao and Q. Wang, *J. CO₂ Util.*, 2020, **35**, 90–105.
- 361 D. Wakerley, S. Lamaison, J. Wicks, A. Clemens, J. Feaster, D. Corral, S. A. Jaffer, A. Sarkar, M. Fontecave, E. B. Duoss, S. Baker, E. H. Sargent, T. F. Jaramillo and C. Hahn, *Nat. Energy*, 2022, **7**, 130–143.
- 362 J. P. J. Bow, V. Adami, A. Marasco, G. Grønnevik, D. A. Rivers, G. Alvaro and P. J. Riss, *Chem. Commun.*, 2022, **58**, 7546–7549.
- 363 C. Liu and S. M. Sadeghzadeh, *Catal. Letters*, 2021, **151**, 2807–2815.
- 364 P. S. Abbott, HSP Basics | Practical Solubility Science | Prof Steven Abbott, <https://www.stevenabbott.co.uk/practical-solubility/hsp-basics.php>, (accessed 13 March 2020).

Appendix 1

Procedure for calculating Hansen solubility parameters (HSPs):

1. Polymers must be ground to a fine powder using a mortar and pestle to obtain a better suspension of polymers in solvents.
2. Disperse an equal amount of finely ground powder (*e.g.*, 2 mg) into a constant volume of different solvents (*e.g.*, 13 different solvents or more).

Note: It is important to keep the amount of polymers and the volume of the solvents constant.

3. Put all the prepared suspensions into a sonication bath for 24 hours. After sonication, let the suspensions settle for 1-2 hours. During this time, turn on the UV-Vis and set up the software.
4. Pipette out the supernatant from the vial and measure the absorption after baseline correction with the same solvent.

For example, if **suspension A** contains polymers + DMF, then before recording absorption, baseline should be corrected with DMF and then record the absorption of **suspension A**.

Note: Baseline should be corrected with each solvent before recording the UV-Vis of each suspension. The solvent used for baseline correction should be the same one used to prepare the sample, *i.e.*, the solvent you kept in step 2 and record absorption for all the prepared suspensions.

5. After recording UV-Vis, plot the data using Origin as shown in **Figure A1S1**. Identify the maximum characteristic absorbance and record the intensity (referred to as Max. Absorbance below).

Table A1S1: Maximum absorbance of the suspension (BNPI-1) in various solvents

Sl No.	Solvents	Max. Absorbance (a.u.)
1	DMSO	1.22
2	DMF	1.16
3	Acetonitrile	1.13
4	NMP	1
5	1-methylimidazole	1.09
6	Dimethylacetamide	1.08

7	Propylene carbonate	1.12
8	Quinoline	0.98
9	Glycerol	0.37
10	Xylene	0.73
11	Toluene	0.1
12	Ethanol	0.62
13	Dioxane	0.23
14	Water	1.23

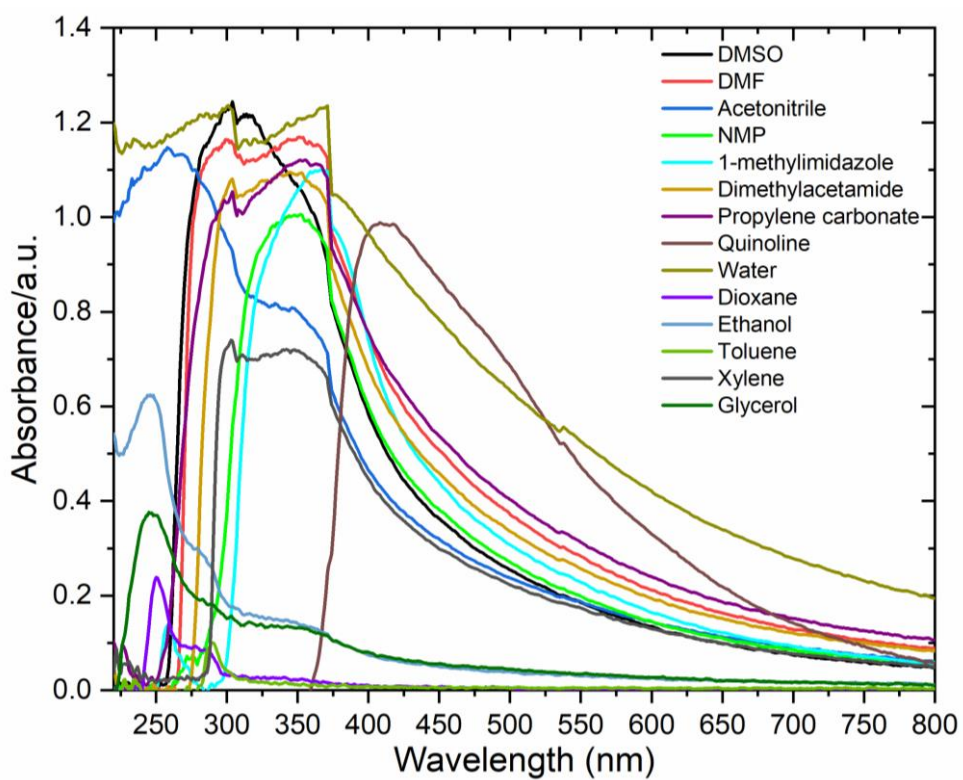


Figure A1S1: UV-Vis spectrum of suspension (BNPI-1) in various solvents

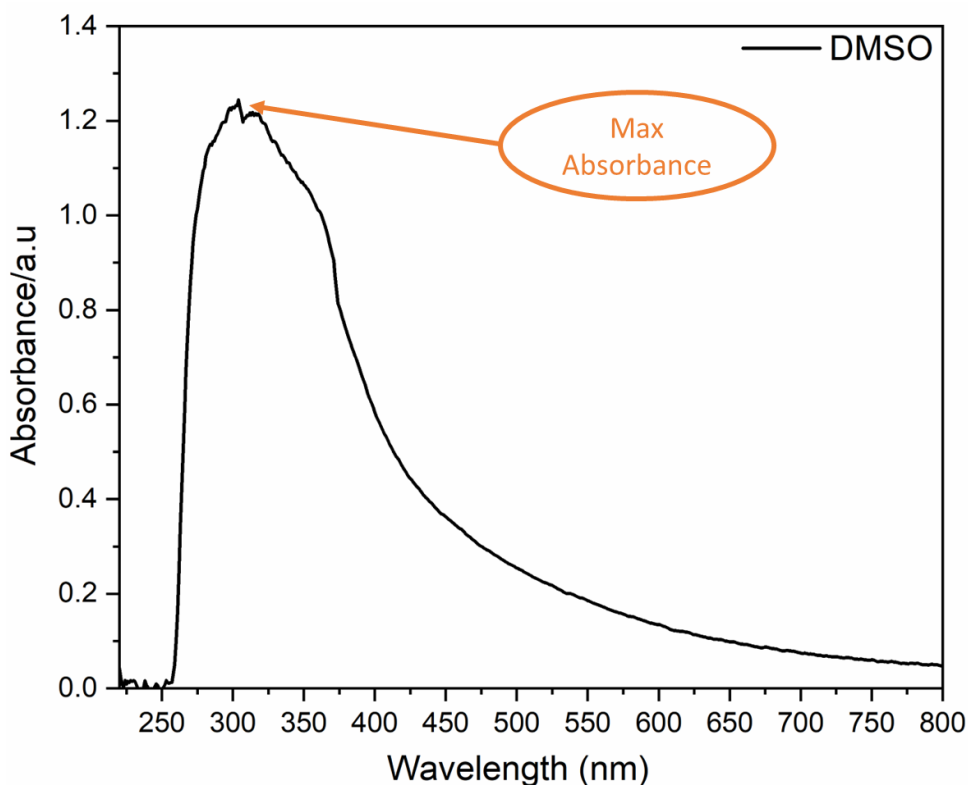


Figure A1S2: UV-Vis spectrum of suspension (BNPI-1) in DMSO

6. Get the HSPs of the solvents you applied in the study.
Sources: <https://www.stevenabbott.co.uk/practical-solubility/hsp-basics.php>
https://www.accudynetest.com/solubility_table.html?rd=self&
in the internet plenty of source available for HSPs of solvents.
7. Plot the absorbance maxima of polymers suspension against δ_D , δ_P , and δ_H of solvents.

Example: δ_D against Max. absorbance, δ_P against Max. absorbance and δ_H against Max. absorbance

Table A1S2: HSPs of the solvents

Sl No.	Solvents	$\delta_D^{[a]}$	$\delta_P^{[b]}$	$\delta_H^{[c]}$
		MPa ^{1/2}	MPa ^{1/2}	MPa ^{1/2}
1	DMSO	18.4	16.4	10.2
2	DMF	17.4	13.7	11.3
3	Acetonitrile	15.3	18	6.1
4	NMP	18	12.3	7.2
5	1-methylimidazole	20.6	14.9	11

6	Dimethylacetamide	16.8	11.5	9.4
7	Propylene carbonate	20	18	4.1
8	Quinoline	20	5.6	5.7
9	Glycerol	17.4	11.3	27.2
10	Xylene	17.8	1	3.1
11	Toluene	18	1.4	2
12	Ethanol	15.8	8.8	19.4
13	Dioxane	17.5	1.8	9
14	Water	15.5	16	42.3

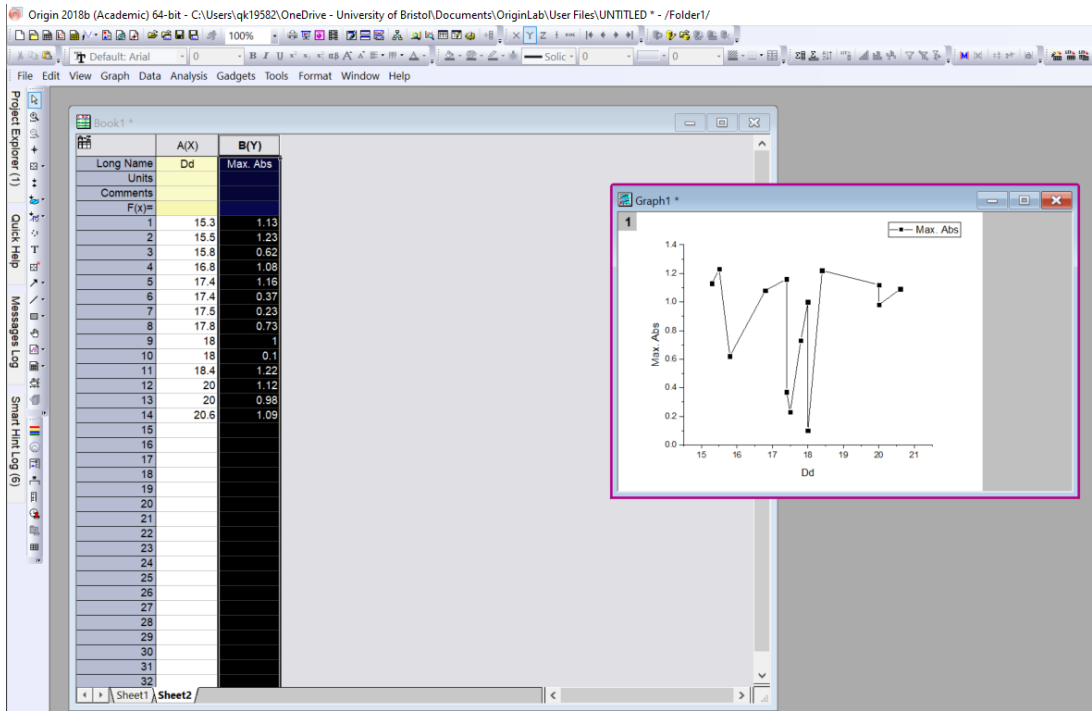
HSPs of solvent were adopted from the HSP basics by Prof Steven Abbott (<https://www.stevenabbott.co.uk/practical-solubility/hsp-basics.php>).³⁶⁴

- For B-spline fitting of δ_D against Max. absorbance, arrange δ_D in ascending order (small to big) which can be done Microsoft excel use sort function.

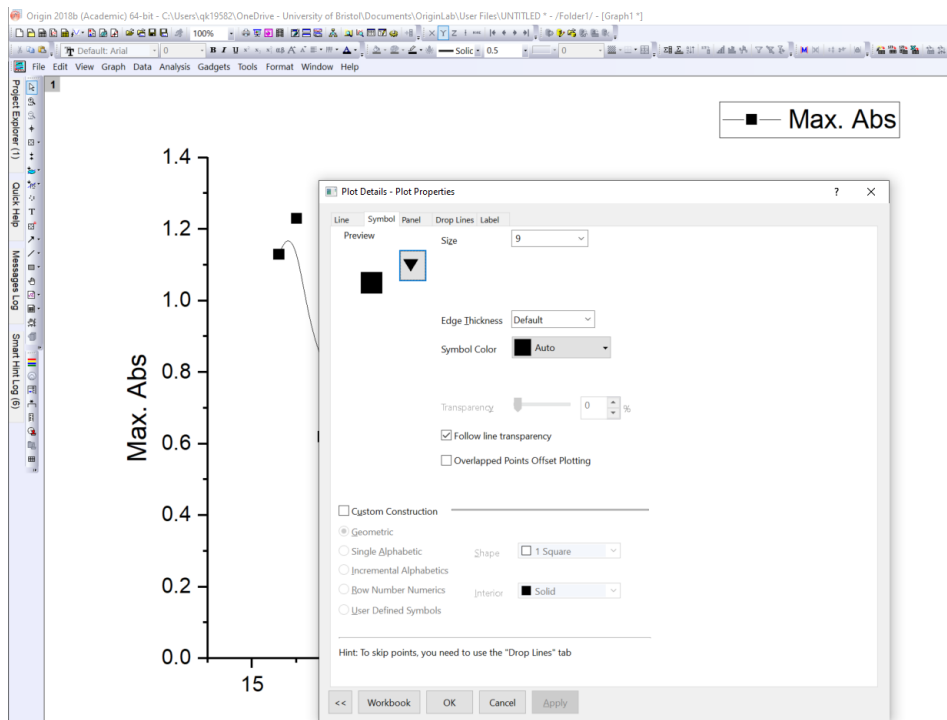
Example:

δ_D	Max. Abs
15.3	1.13
15.5	1.23
15.8	0.62
16.8	1.08
17.4	1.16
17.4	0.37
17.5	0.23
17.8	0.73
18	1
18	0.1
18.4	1.22
20	1.12
20	0.98
20.6	1.09

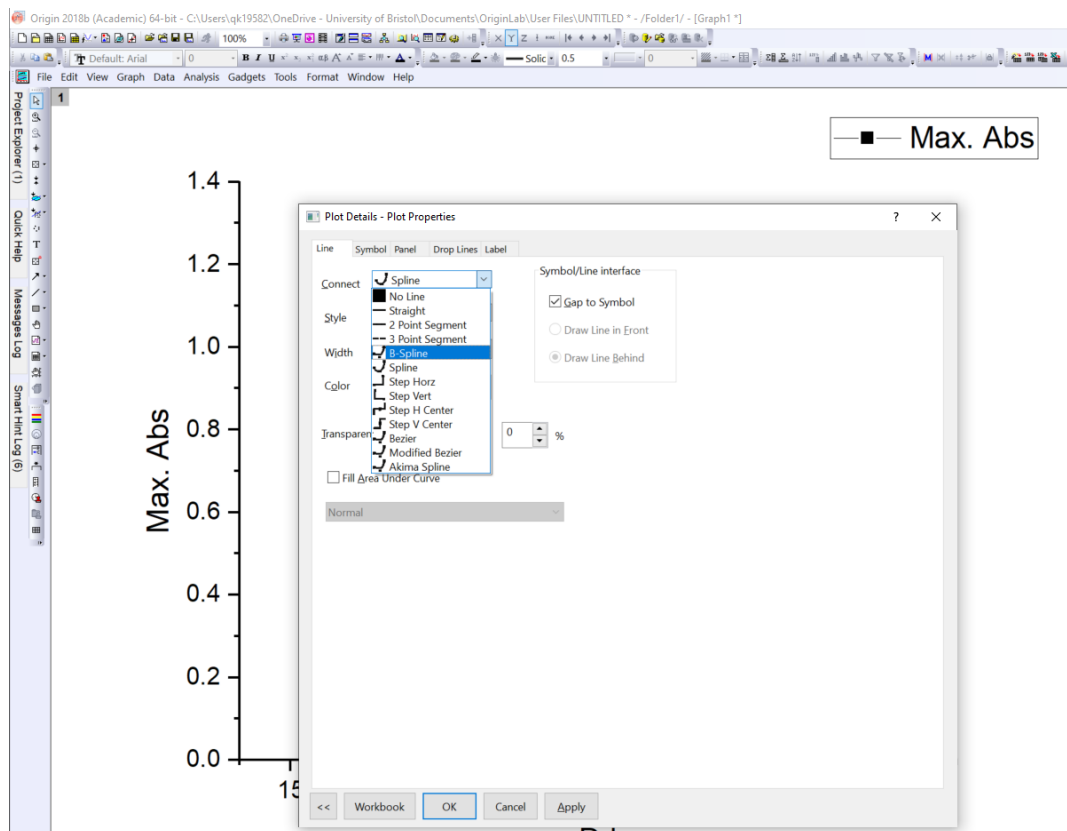
- Plot this in Origin. (line + symbol)



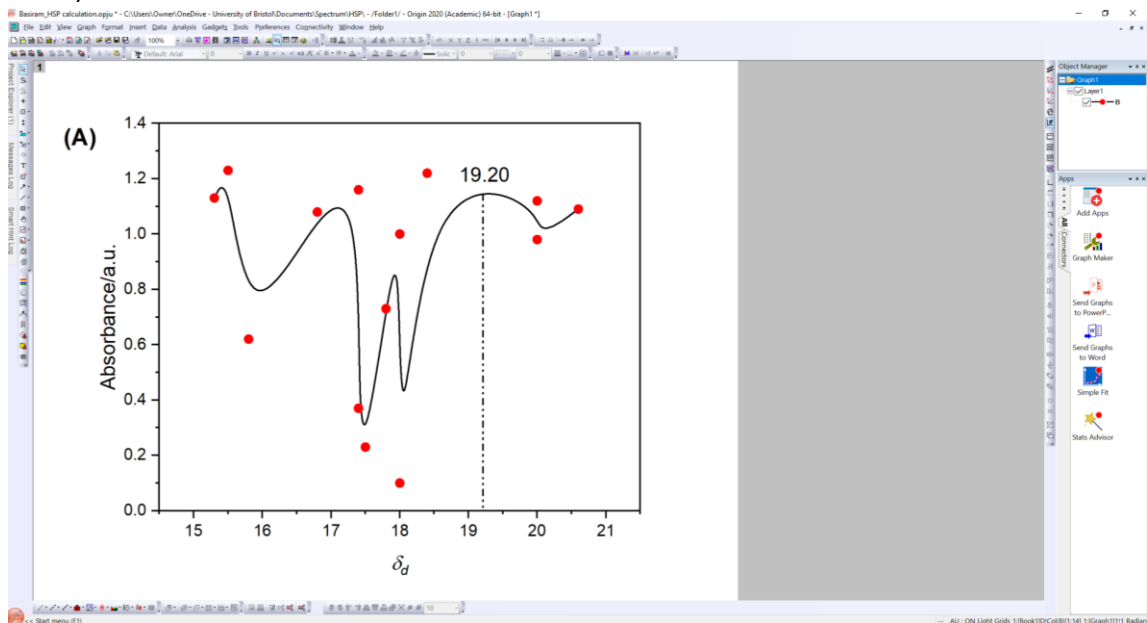
10. Double click on the plot to open Plot Details- Plot properties



11. Now click on Line and change Connect from straight to B-Spline

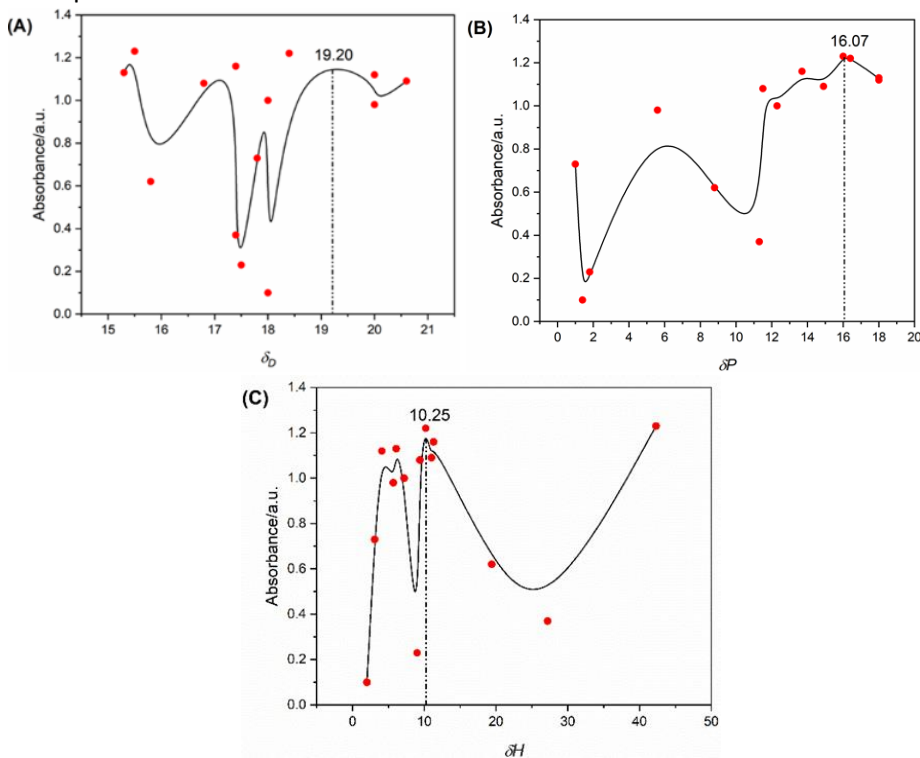


12. The maximum of the spline curve now corresponds to the δ_D of the polymers (BNPI-1, 19.20).



13. Similarly, we can find δ_P , and δ_H of the polymers.

Example:



Hence, the HSPs of BNPI-1 polymers used in this example are $\delta_D = 19.20 \text{ MPa}^{1/2}$, $\delta_P = 16.07 \text{ MPa}^{1/2}$, and $\delta_H = 10.25 \text{ MPa}^{1/2}$. The theoretical verification of experimental HSPs can be verified using the **equation**

$$1.4 (\delta_T^2 = \delta_D^2 + \delta_P^2 + \delta_H^2).^{43,205}$$

Unit conversion: $(1 \text{ cal}^{1/2} \text{ cm}^{-3/2} = (4.184 \text{ J})^{1/2} (10^{-2} \text{ m})^{-3/2} = (4.184 \text{ J})^{1/2} (0.01 \text{ m})^{-3/2} = 2.045483 \cdot 10^3 \text{ J}^{1/2} \text{ m}^{-3/2} = 2.045483 (10^6 \text{ J/m}^3)^{1/2} = 2.045483 \text{ MPa}^{1/2})$

Appendix 2

1. Equipment and materials

All chemicals used were purchased from Merck, and ThermoFisher Scientific and used as received.

Characterisation and measurements:

Fourier transform infrared (FT-IR) spectra were recorded on a Perkin Elmer Spectrum 100 spectrometer, with samples in powder form. Thermogravimetric analyses (TGA) were carried out on a TA TGA Q500 apparatus in a nitrogen atmosphere (flow rate 30 mL/ min) in the temperature range 30–800 °C (heating rate 20 °C/min). X-ray diffraction (XRD) patterns were obtained on a Bruker D8 Advance diffractometer (40 kV, 30 mA) using Cu K α radiation ($2\theta = 5\text{--}50^\circ$). Nitrogen adsorption/desorption measurements at 77.4 K were performed after degassing the samples on a Schlenk line for 24 hours and then under high vacuum at 150 °C for at least 20 hours on a Quantachrome Quadrasorb SI-MP apparatus. The specific surface areas were calculated by applying the Brunauer–Emmett–Teller (BET) model ($\frac{1}{x[(\frac{P_0}{P})-1]} = \frac{1}{x_m C} + \frac{C-1}{x_m C} (\frac{P}{P_0})$) to adsorption or desorption branches of the isotherms (N₂ at 77.4 K) using the QuadraWin 5.05 software package, with multipoint analysis used of the first 3 adsorption measurements ($< 0.15 P/P_0$). Analysis of the isotherms by commercialized quenched solid density functional theory (QSDFT)^{xviii} and Grand canonical Monte Carlo (GCMC)^{xix} methodologies were also undertaken using the QuadraWin 5.05 package. The pore size distribution (PSD) profiles of the pPIs were calculated from the adsorption branch of the isotherms with the non-local density functional theory (NLDFT) approach. ¹H NMR experiments were performed in D₂O using a Bruker cryo500 MHz NMR. UV-Vis-NIR spectroscopy measurements were carried out using a Shimadzu UV-2600 spectrometer fitted with an ISR-2600 integrating sphere attachment. Measurements were recorded in 10 mm path length quartz cuvettes.

Electrochemical measurements: All the electrochemical performance of BNPI-1 and BNPI-2 were investigated with an EG&G Princeton Applied Research Potentiostat Model 273A, using glassy carbon working electrode (0.38 cm² contact area of electrode), platinum (Pt) counter electrode and silver chloride (Ag/AgCl) reference electrode. All potentials were converted to the reversible hydrogen electrode (RHE) using $ERHE = E_{Ag/AgCl} + 0.059 \times pH + E^0_{Ag/AgCl}$, where ERHE is the converted potential vs. RHE, $E^0_{Ag/AgCl} = 0.1976$ at 25 °C, and $E_{Ag/AgCl}$ is the experimentally measured potential against Ag/AgCl reference.

Electrolyte preparation for NMR analysis after electrochemical reduction of CO₂ experiments. After CA experiments, the electrolyte (600 μ L) was collected from the cathodic side of the H-cell and product

detection was undertaken using cryo500 ^1H NMR spectroscopy. To determine the amount of product produced, which in turn allows the determination of the FE of the system, 1 mM maleic acid (10 μL) was added along with D_2O (180 μL) and mixture was analysed using ^1H NMR. FEs were calculated using the formula below;

$$\epsilon_{\text{Faradaic}} = \frac{z \cdot n \cdot F}{Q}$$

z: number of electrons required to produce a given product

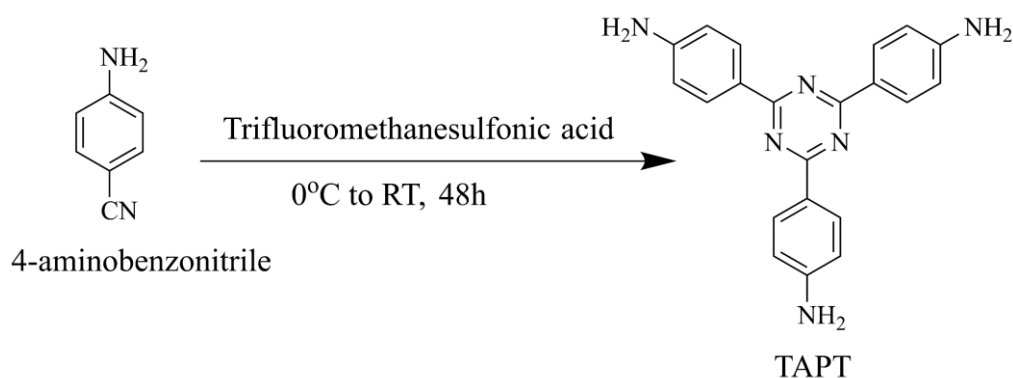
n: number of moles of the given product

F: Faraday's constant (96485.33 C/mol)

Q: total charged passed

1. Experimental procedure

Synthesis of 1,3,5-tris-(4-aminophenyl)triazine (TAPT):



A dried 100 mL two-neck round bottom flask was charged with 4-aminobenzonitrile (772.0 mg, 6.5 mmol) and placed in an ice bath at 0°C under inert atmosphere. Trifluoromethanesulfonic acid (2 mL) was added dropwise over 20 minutes, maintaining the temperature at 0°C. The resultant mixture was stirred for 48 h at room temperature. Distilled water (20.0 mL) was added, and the reaction mixture neutralized by 2 M NaOH solution. Initially, with an increase in pH, an orange precipitate dissolved to give a bright orange solution, which upon further increase in the pH gave a pale-yellow precipitate. The resultant product was filtered and washed with distilled water (3 x 250 mL) and ethanol (3x 50 mL). Yield: 80%

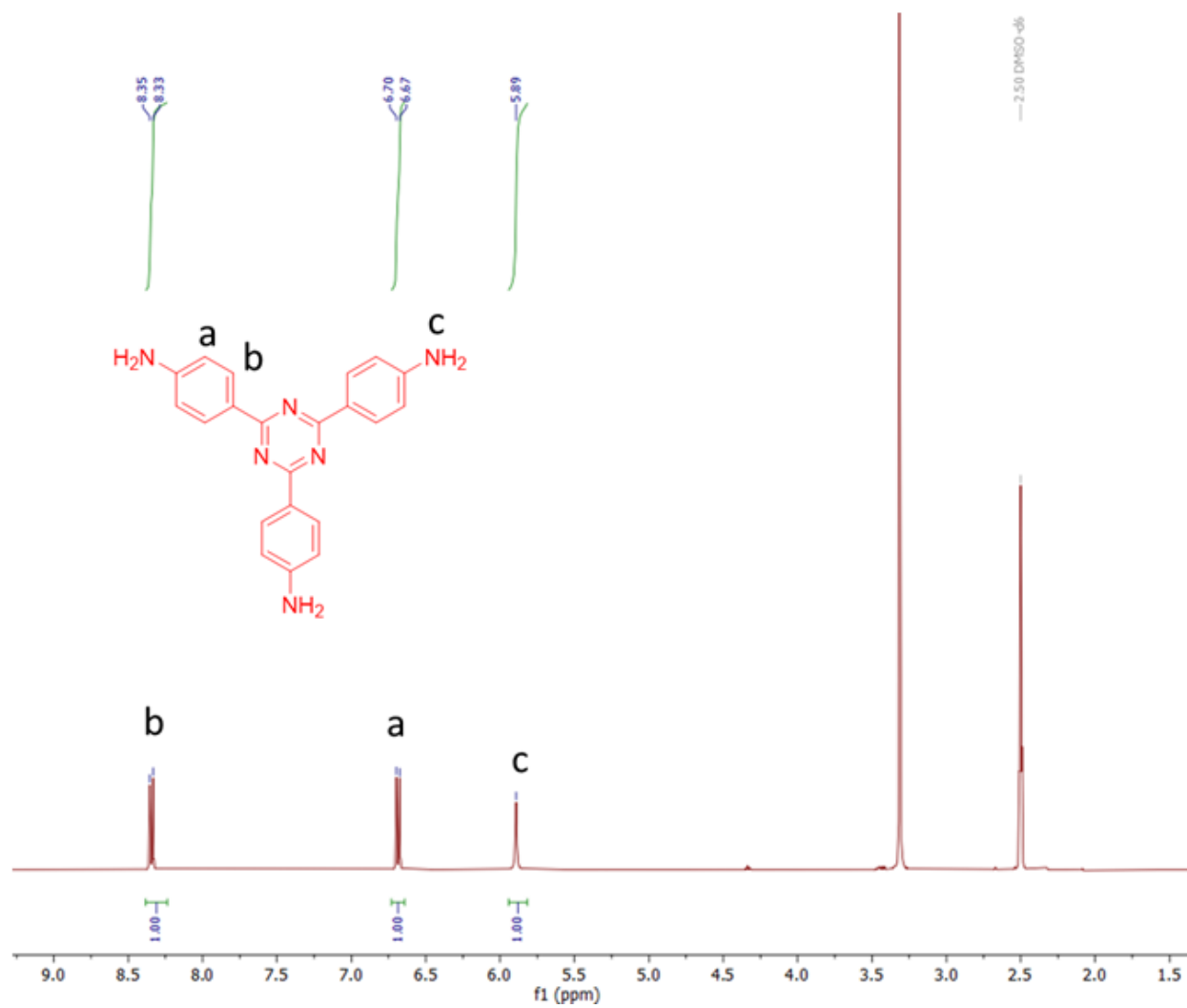


Figure A2S1: ^1H NMR of TAPT in DMSO-d_6

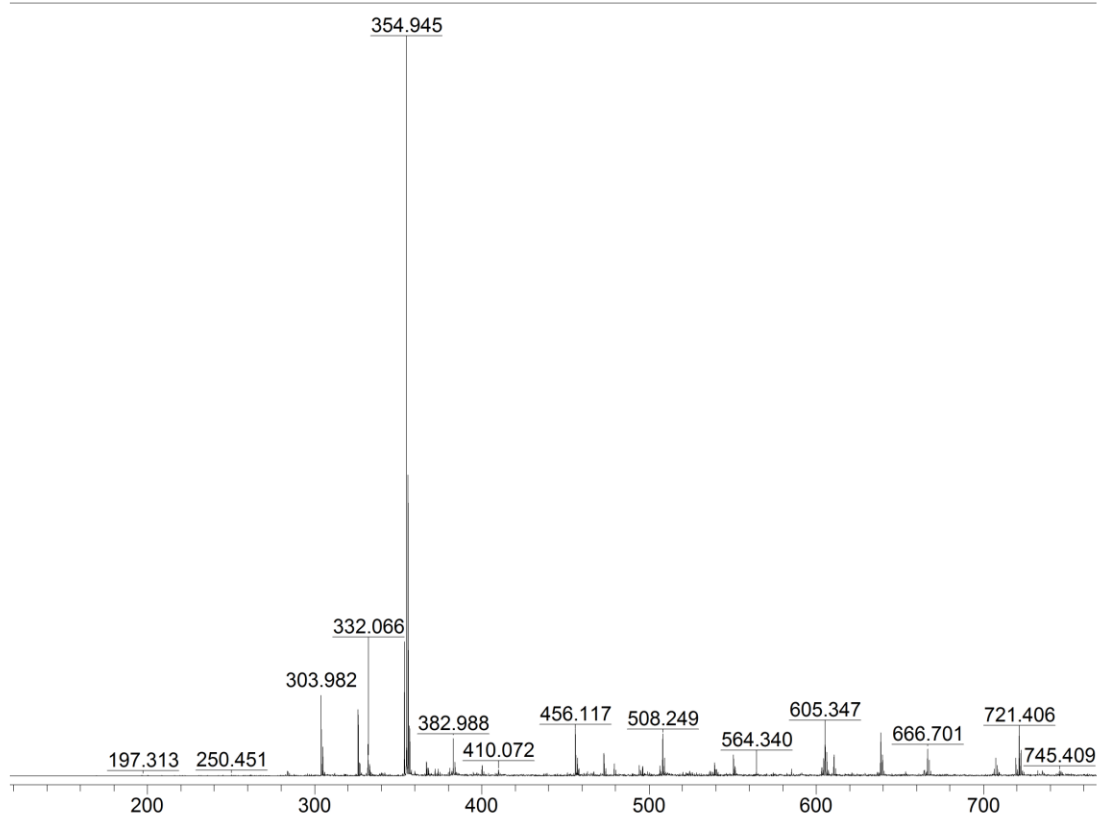


Figure A2S2: MALDI-TOF Mass Spectrum of TAPT

a. Synthesis of BNPI-1:

A dried round-bottomed flask equipped with mechanical stirring, nitrogen inlet, Dean-Stark trap and a reflux condenser and charged with DMSO (40 ml) and melamine (100 mg, 0.79 mmol). After 5 min of stirring 1,4,5,8,-naphthalenetetracarboxylic dianhydride (321 mg, 1.19 mmol) and salt (0.33, 0.66 and 0.99 mmol, respectively, were added and the reaction mixture stirred at room temperature for 30 min. The temperature was raised gradually to 180°C and held for 72 hours in a drysyn or high temperature oil bath. After cooling to 70°C, MeOH (50 ml) was added and the precipitate collected and washed with additional DMF and methanol, warm water and acetone (50ml x 3, each). The resulting product was dried at 80°C under vacuum for 24 hours. Yield: 40-50%

b. Synthesis of BNP-2:

A dried round-bottomed flask equipped with mechanical stirring, nitrogen inlet, Dean-Stark trap and a reflux condenser was charged with DMF (50 mL), tris(4-aminophenyl)triazine (280mg, 0.79mmol) and salt (0.33, 0.66, and 0.99 mmol, respectively). After 5 min of stirring 1,4,5,8,-naphthalenetetracarboxylic dianhydride (321mg, 1.19 mmol) was added and the reaction mixture stirred at room temperature for 30 min. The temperature was raised gradually to 150°C and held for

72 hours in a drysyn or high temperature oil bath. After cooling to 70°C, MeOH (50mL) was added and the precipitate collected and washed with additional DMF and methanol, water and acetone (3 x 50 mL each). The resulting product was dried at 80°C under vacuum for 24 h hours. Yield: 70-80%

1. Fourier Transform Infrared (FT-IR) Spectra

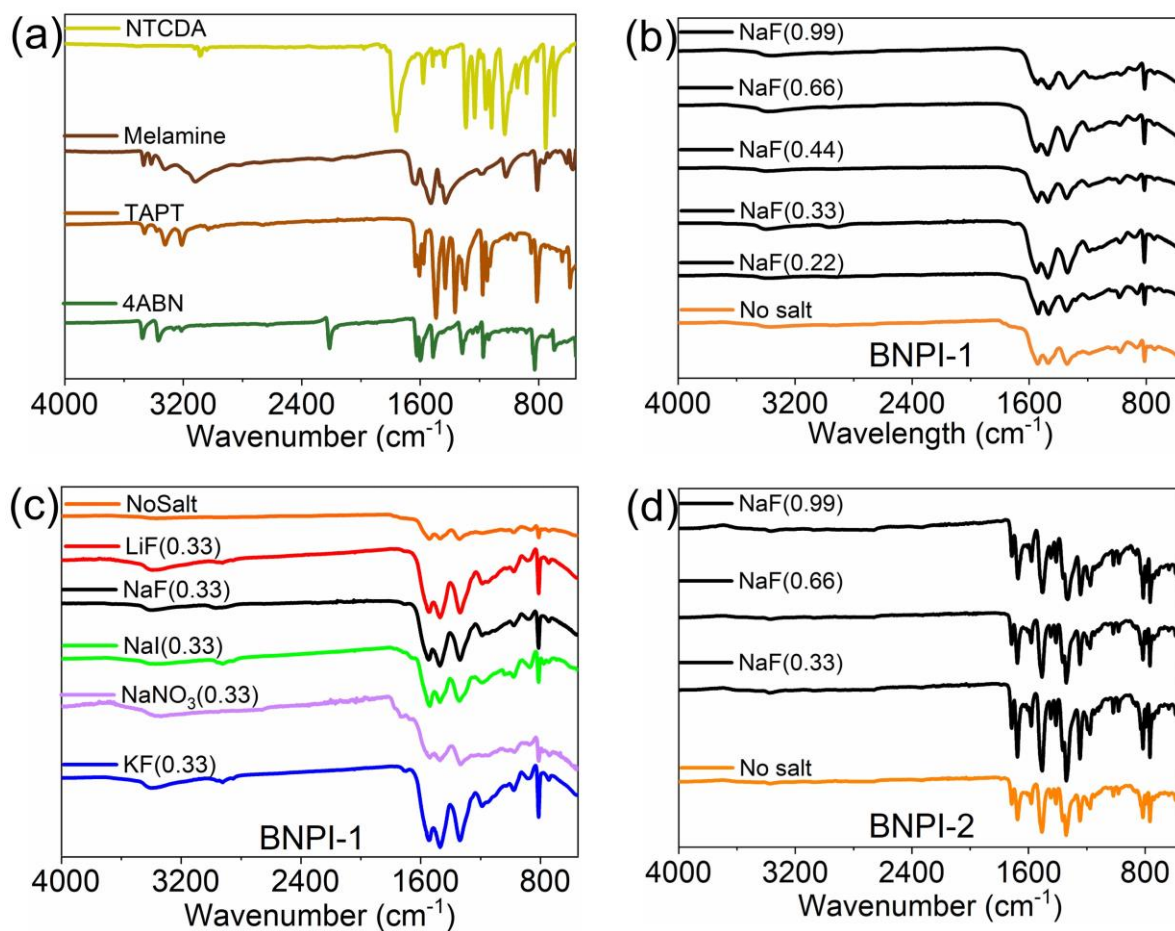


Figure A2S3: FTIR spectra of (a) starting materials, (b) BNPI-1 in DMSO with NaF concentrations, and (c) BNPI-1 with 0.33 mmol of different salt concentration (LiF, NaF, NaI, NaNO₃, KF) and (d) BNPI-2 in DMF with NaF concentrations.

2. PXRD, UV-Vis-NIR Data and Energy Dispersive X-Ray Analysis (EDX)

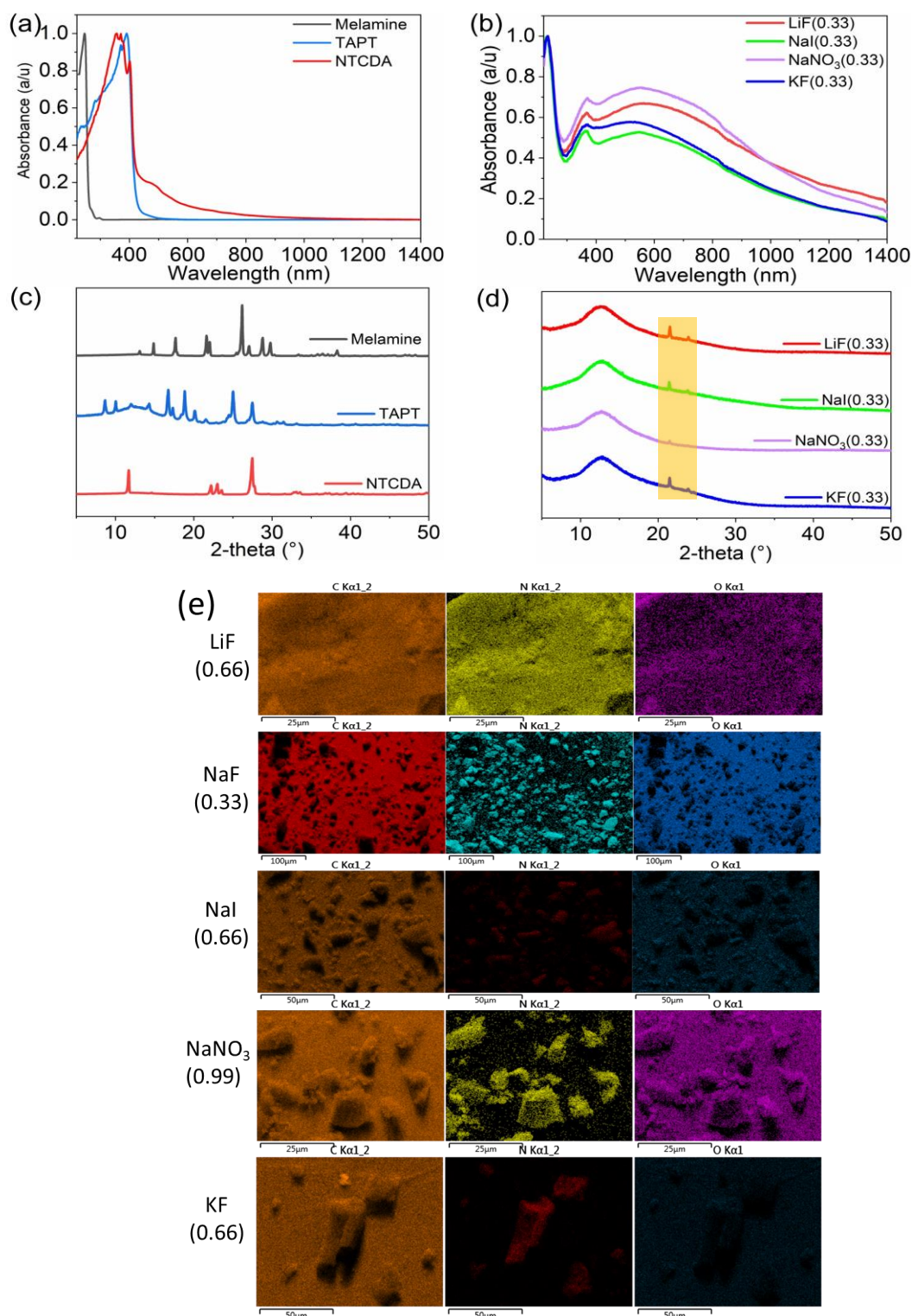


Figure A2S4: (a, b) UV-Vis-NIR spectra of starting material and BNPI-1 synthesised in DMSO with 0.33 mmol concentration of LiF, NaI, NaNO₃, KF and (c, d) PXRD spectra of starting material and BNPI-1 synthesised in DMSO with 0.33 mmol concentration of LiF, NaI, NaNO₃, KF, respectively. (The origin of the highlighted peak in (d) is from the paraffin wax used to fix samples to the sample holder during our XRD analysis.⁴) and (e) EDX analysis of BNPI-1 synthesised with LiF, NaF, NaI, NaNO₃ and KF.

3. TGA Analyses

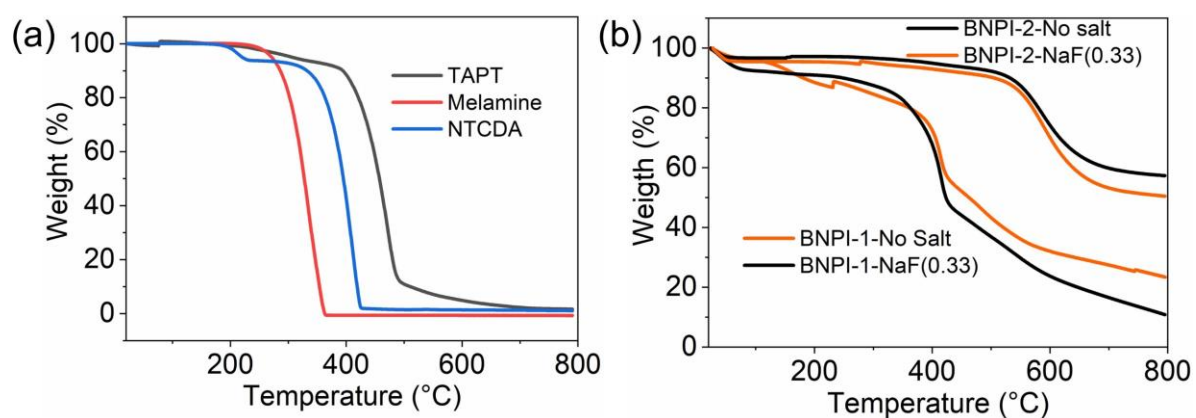


Figure A255: TGA data (a) starting materials (b) BNPI-1 and BNPI-2 synthesised in DMSO and DMF with and without NaF (0.33 mmol)

4. Sorption data

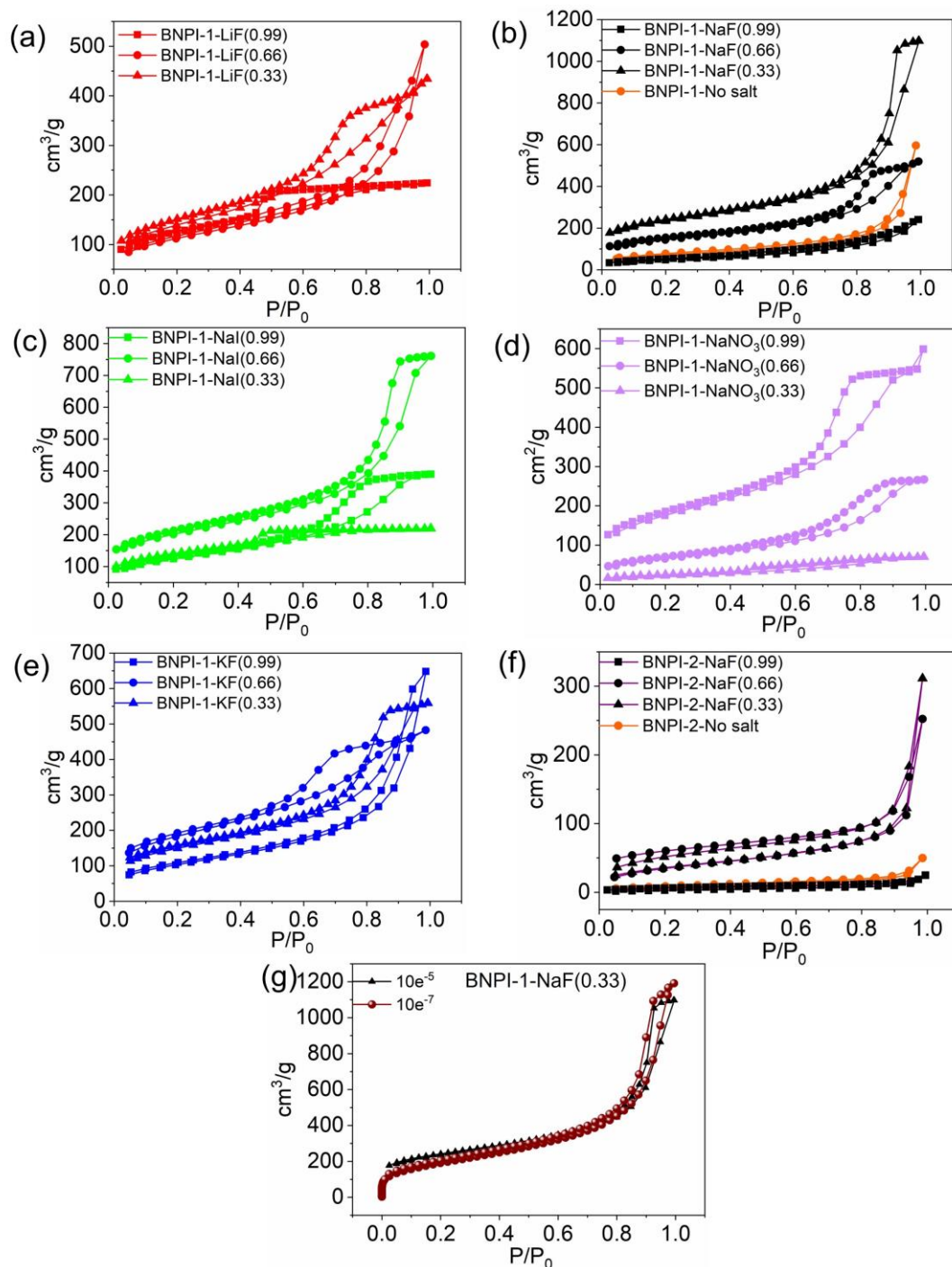


Figure A2S6: N_2 adsorption and desorption isotherms of BNPI-1 synthesised in DMSO with (a) LiF, (b) NaF, (c) NaI, (d) $NaNO_3$, (e) KF, additives and (f) BNPI-2 synthesised in DMF with NaF additives (numbers in brackets indicating mmol of additives) in the P/P_0 10^{-5} to 1 range and (g) comparison of BNPI-1-NaF(0.33) in the P/P_0 10^{-5} to 1 and 10^{-7} to 1 range.

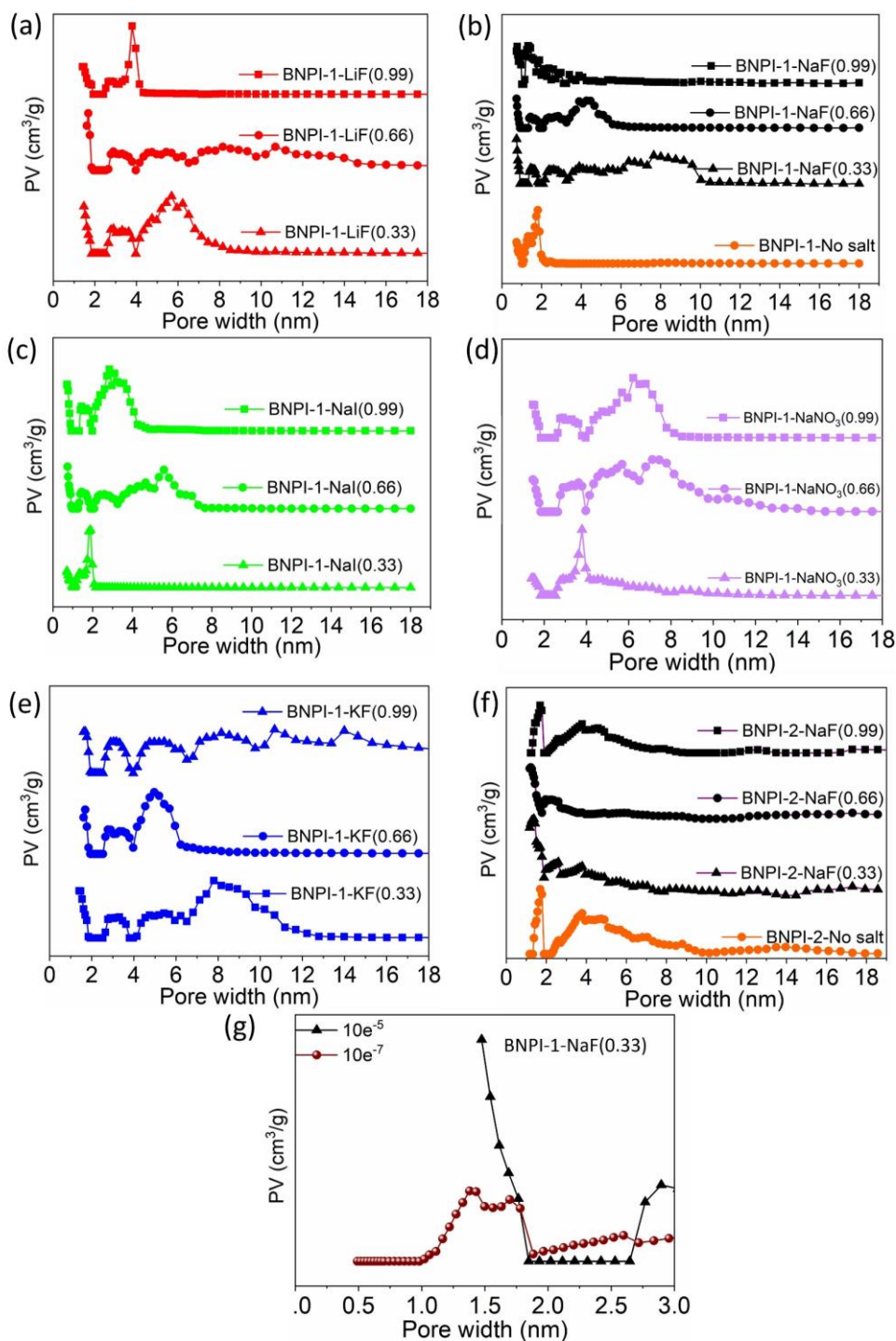


Figure A2S7: Pore size distribution calculated from NL-DFT of BNPI-1 synthesised in DMSO with (a) LiF, (b) NaF, (c) NaI, (d) NaNO₃, (e) KF, additives and (f) BNPI-2 synthesised in DMF with NaF additives (numbers in brackets indicating mmol of additives) in the P/P_0 10^{-5} to 1 range and (g) comparison of BNPI-1-NaF(0.33) in the P/P_0 10^{-5} to 1 and 10^{-7} to 1 range.

Table A2S1: Repeat surface area analysis of high performing pPIs

Sample	Surface area (m ² /g)		
	1	2	3
BNPI-1-No salt	406	349	402
BNPI-1-NaF(0.33)	846	836	737
BNPI-1-NaF(0.99)	54	47	70
BNPI-1-NaI(0.66)	728	664	656

Table A2S2: Surface area, Pore volume (PV), CO₂ uptake of BNPI-1 and BNPI-2

BNPI-1					BNPI-2				
Salt (mmol)	S_{BET} (m ² /g)	PV (cm ³ /g)	CO ₂ uptake (wt%)		Salt (mmol)	S_{BET} (m ² /g)	PV (cm ³ /g)	CO ₂ uptake (wt%)	
			273K	298K				273K	298K
Control	16	0.05	2.2	0.7	Control	15	0.03	3.7	*
No salt	406	0.25	6.8	4.0	No salt	26	0.05	4.5	3.0
NaF(0.33)	864	1.63	10.5	7.1	NaF(0.33)	132	0.34	5.3	2.5
NaF(0.66)	522	0.74	7.8	5.4	NaF(0.66)	102	0.30	5.2	2.9
NaF(0.99)	54	0.10	7.1	2.9	NaF(0.99)	11	0.2	6.0	3.7
LiF(0.33)	503	0.61	8	5.0					
LiF(0.66)	406	0.62	*	*					
LiF(0.99)	425	0.32	*	*					
NaI(0.33)	483	0.31	*	*					
NaI(0.66)	728	1.14	13.9	9.8					
NaI(0.99)	448	0.57	*	*					
NaNO ₃ (0.33)	79	0.09	*	*					
NaNO ₃ (0.66)	238	0.40	*	*					
NaNO ₃ (0.99)	633	0.80	9.7	5.5					
NaNO ₃ (1.20)	500	0.50	*	*					
KF(0.33)	536	0.82	*	*					
KF(0.66)	664	0.79	9.8	4.5					
KF(0.99)	374	0.21	*	*					

PV: pore volume, *: Not analysed

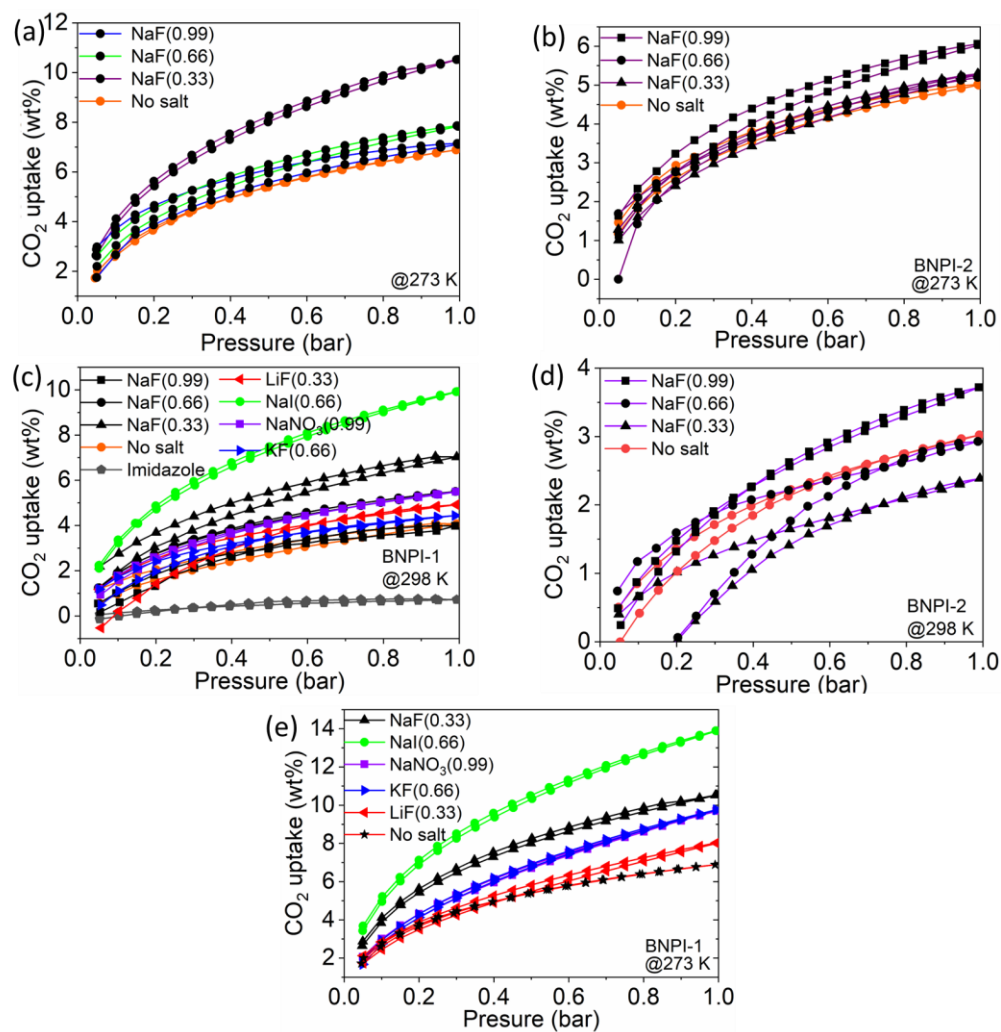


Figure A2S8: CO₂ uptake isotherm for (a) BNPI-1(NaF) at 273 K, 1 bar, (b) BNPI-2(NaF) at 273 K, (c) Selected BNPI-1 at 298 K, 1 bar, (d) BNPI-2(NaF) at 298 K and (e) BNPI-1 high surface area at 273 K, 1 bar. (numbers in brackets indicating mmol of additives).

5. HSPs calculation

The Hansen solubility parameters of pPIs were calculated according to the literature reported and can be found in **Appendix 1**.^{43,205}

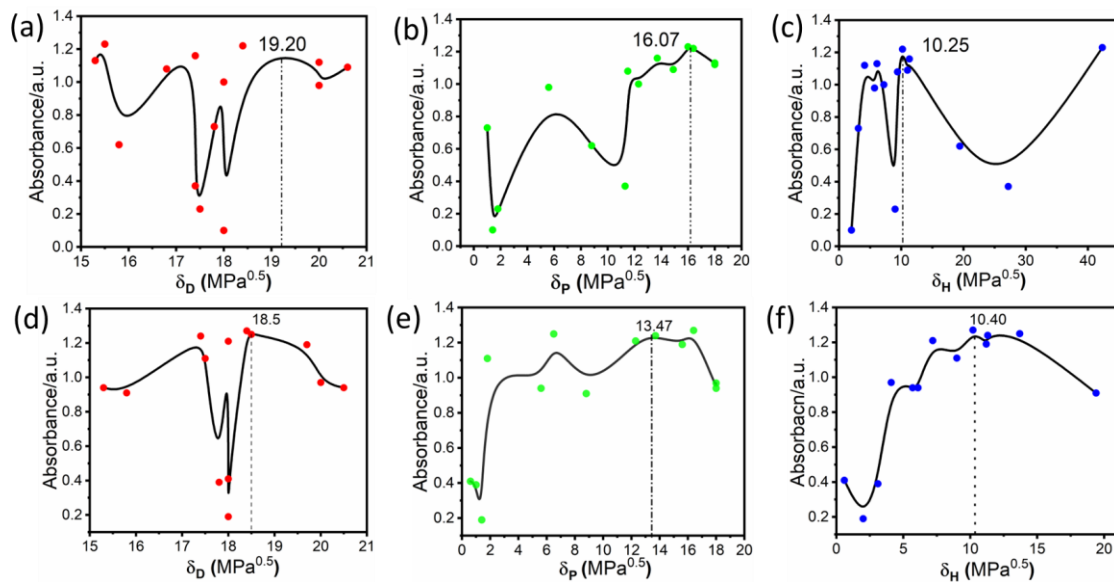


Figure A2S9: HSPs of BNPI-1 and BNPI-2: **(a)** and **(d)** dispersion-, **(b)** and **(e)** polar-, **(c)** and **(f)** hydrogen-bonding parameters, respectively.

Table S3: HSPs of BNP-1, BNPI-2, and compatible solvent (DMF and DMSO)

Name	δ_d	δ_p	δ_h
BNPI-1	19.2	16.07	10.25
DMSO	18.4	16.4	10.2
BNPI-2	18.5	13.4	10.4
DMF	17.4	13.7	11.3

6. Electrochemical studies

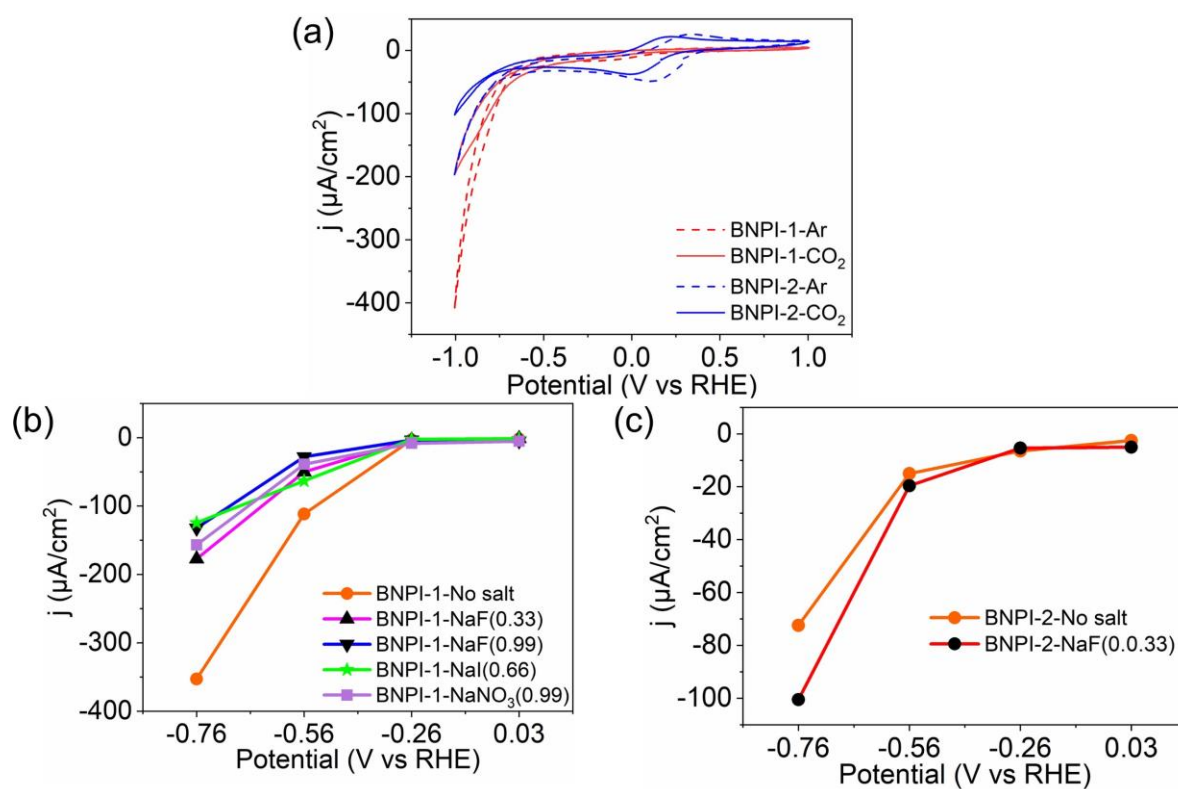


Figure A2S10: (a) Cyclic voltammetry studies of BNPI-1 and BNPI-2 in 0.1 M Ar- and CO_2 -saturated KHCO_3 electrolyte at a scan rate of 20 mV/s. (b and c) Plot of potential vs current density (j) of BNPI-1 and BNPI-2, respectively, (numbers in brackets indicating mmol of additives).

Table A2S4: Electrochemical potentials for CO₂ reduction reaction in aqueous medium.^{11,275}

Possible half-cell electrochemical CO ₂ reduction	Electrode potential (E° (V) vs SHE) at pH 7
$\text{CO}_{2(\text{g})} + 2\text{H}^+ + 2\text{e}^- \rightarrow \text{CO}_{(\text{g})} + \text{H}_2\text{O}_{(\text{l})}$	-0.53
$\text{CO}_{2(\text{g})} + 2\text{H}^+ + 2\text{e}^- \rightarrow \text{HCOOH}_{(\text{l})}$	-0.61
$\text{CO}_{2(\text{g})} + 4\text{H}^+ + 4\text{e}^- \rightarrow \text{HCHO}_{(\text{l})} + \text{H}_2\text{O}_{(\text{l})}$	-0.48
$\text{CO}_{2(\text{g})} + 6\text{H}^+ + 6\text{e}^- \rightarrow \text{CH}_3\text{OH}_{(\text{l})} + \text{H}_2\text{O}_{(\text{l})}$	-0.38
$\text{CO}_{2(\text{g})} + 8\text{H}^+ + 8\text{e}^- \rightarrow \text{CH}_{4(\text{g})} + 2\text{H}_2\text{O}_{(\text{l})}$	-0.24
$2\text{CO}_{2(\text{g})} + 8\text{H}^+ + 8\text{e}^- \rightarrow \text{CH}_3\text{COOH}_{(\text{g})} + 2\text{H}_2\text{O}_{(\text{l})}$	-0.26
$2\text{CO}_{2(\text{g})} + 12\text{H}^+ + 12\text{e}^- \rightarrow \text{C}_2\text{H}_5\text{OH}_{(\text{g})} + 3\text{H}_2\text{O}_{(\text{l})}$	-0.32
$2\text{CO}_{2(\text{g})} + 12\text{H}^+ + 12\text{e}^- \rightarrow \text{C}_2\text{H}_4_{(\text{g})} + 4\text{H}_2\text{O}_{(\text{l})}$	-0.34
$3\text{CO}_{2(\text{g})} + 18\text{H}^+ + 18\text{e}^- \rightarrow \text{C}_3\text{H}_7\text{OH}_{(\text{l})} + 5\text{H}_2\text{O}_{(\text{l})}$	-0.31
$2\text{H}^+ + 2\text{e}^- \rightarrow \text{H}_{2(\text{g})}$	-0.42

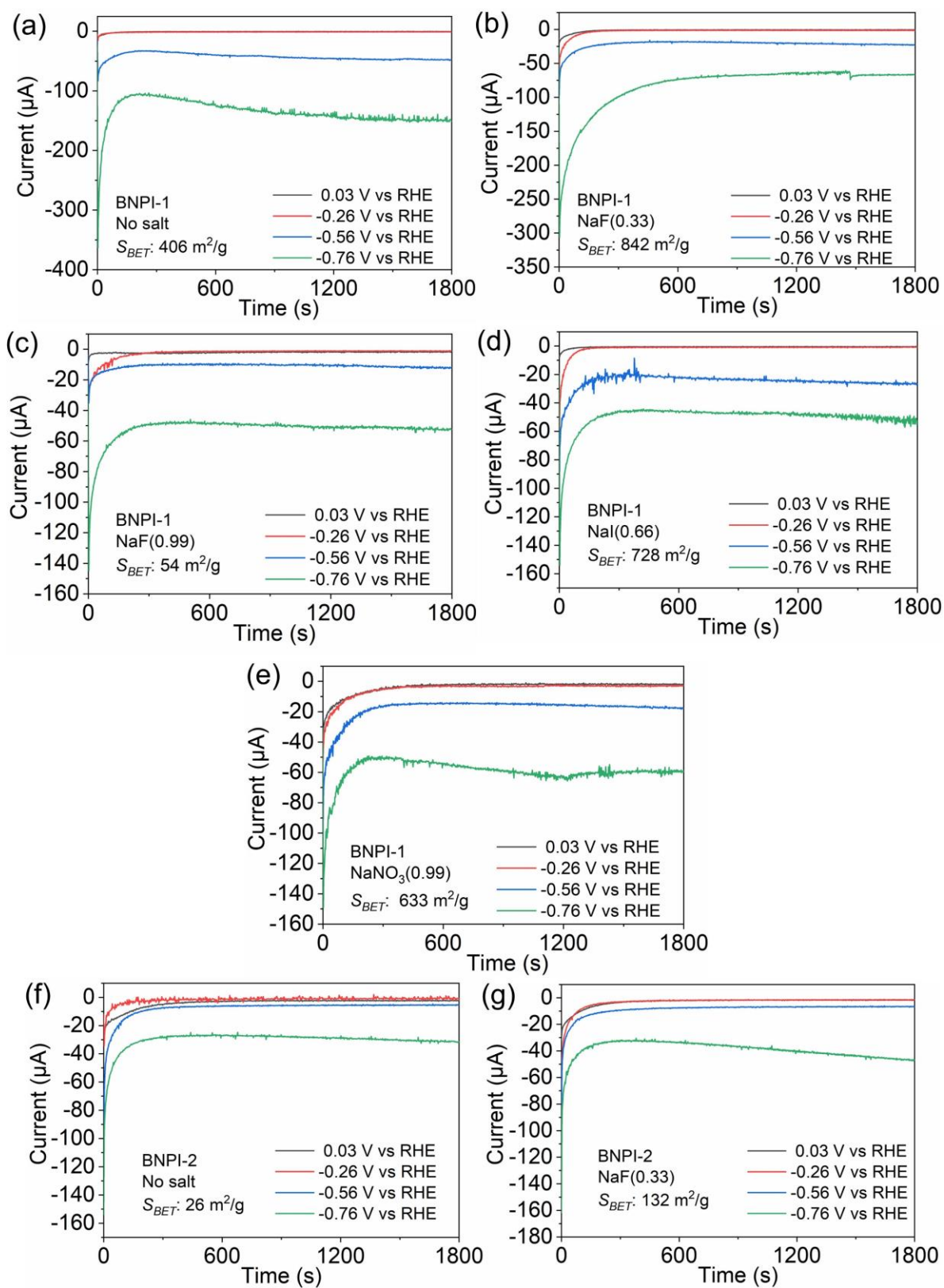


Figure A2S11: Chronoamperometry data of (a-e) BNPI-1 and (f-g) BNPI-2, in CO_2 -saturated 0.1 M KHCO_3 electrolyte for 30 min, (numbers in brackets indicating mmol of additives).

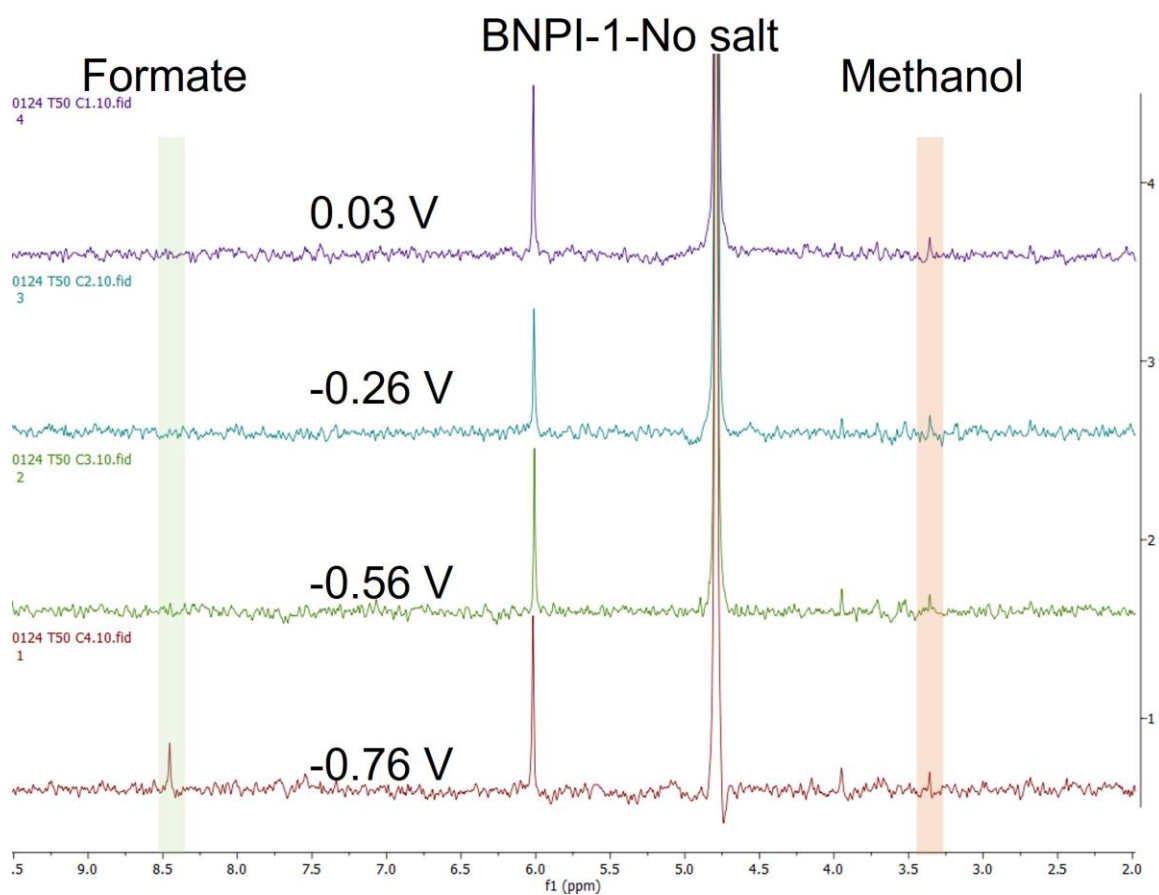


Figure A2S12: NMR of electrolyte BNPI-1-No salt after CA investigations for 30 min in CO₂-saturated 0.1 M KHCO₃ electrolyte.

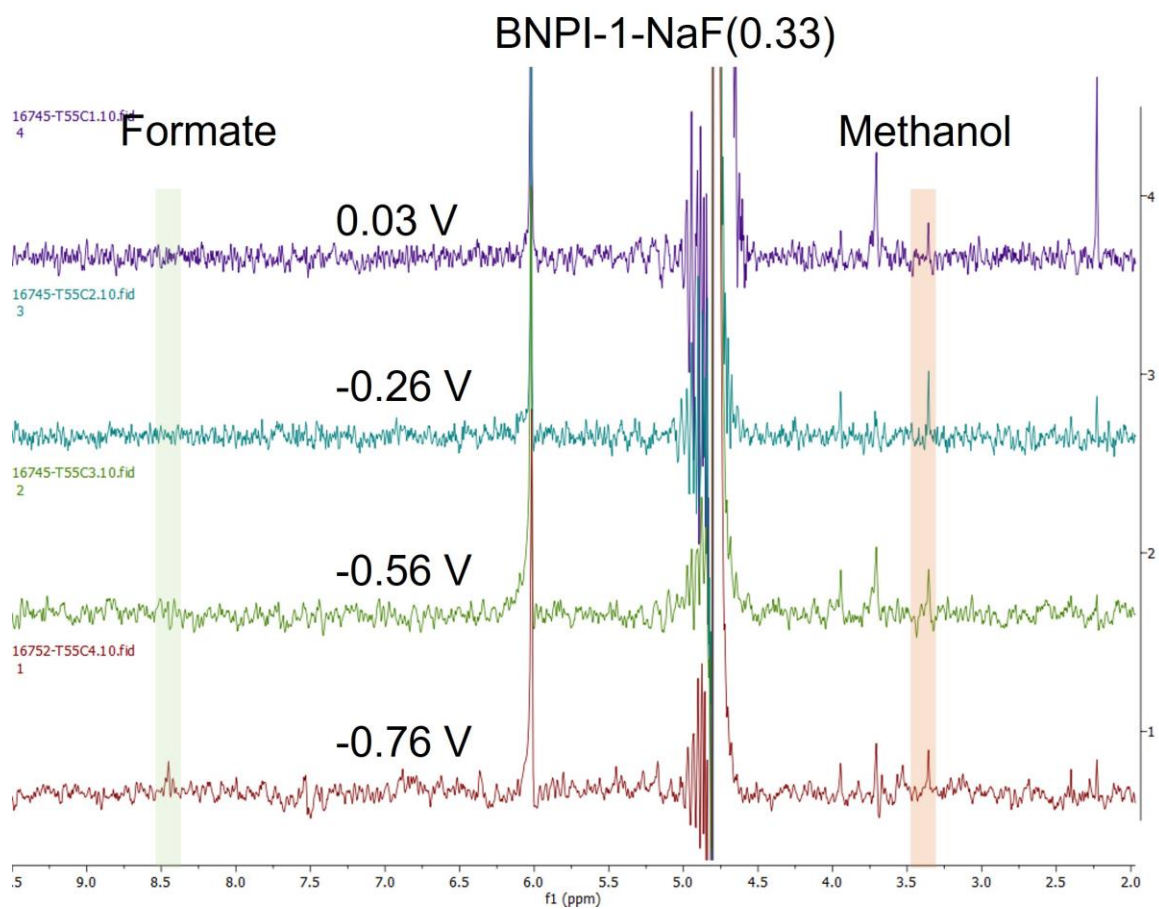


Figure A2S13: NMR of electrolyte BNPI-1-NaF(0.33) after CA investigations for 30 min in CO₂-saturated 0.1 M KHCO₃ electrolyte.

BNPI-1-NaF(0.99)

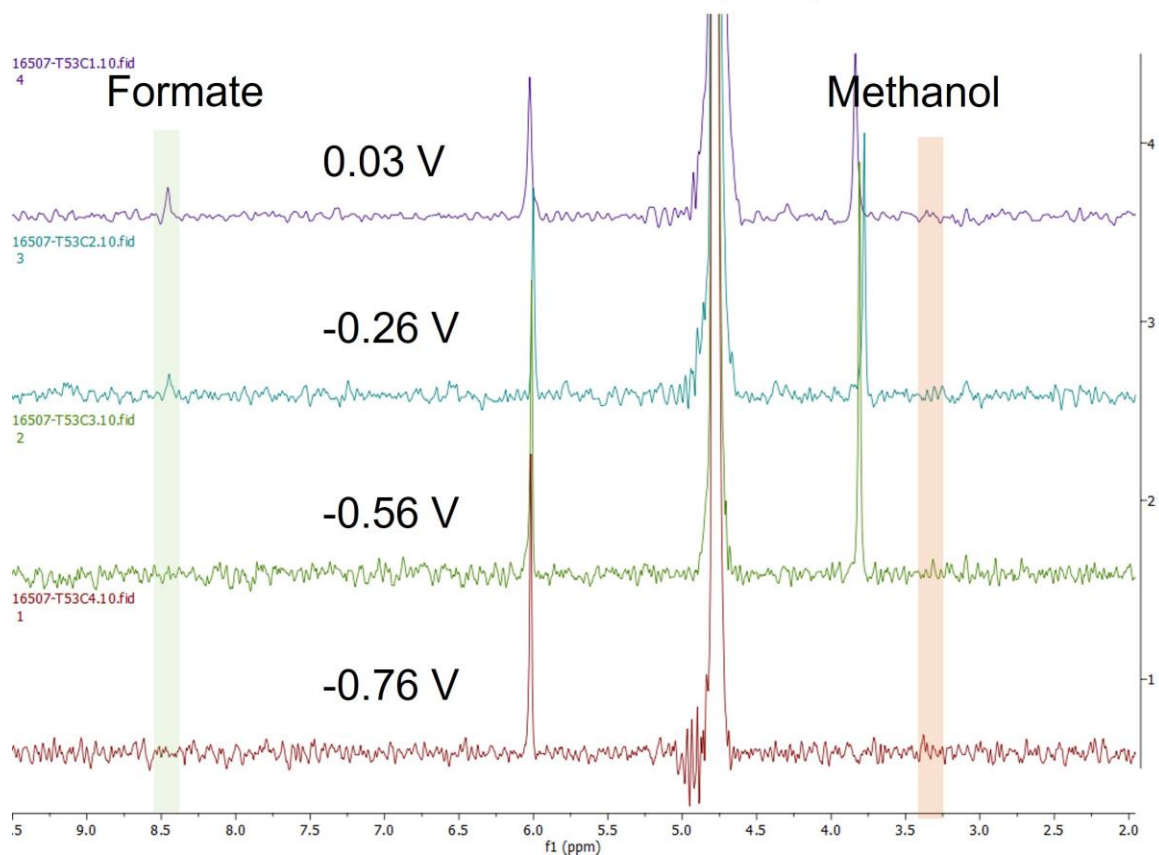


Figure A2S14: NMR of electrolyte BNPI-1-NaF(0.99) after CA investigations for 30 min in CO₂-saturated 0.1 M KHCO₃ electrolyte.

BNPI-1-NaI(0.66)

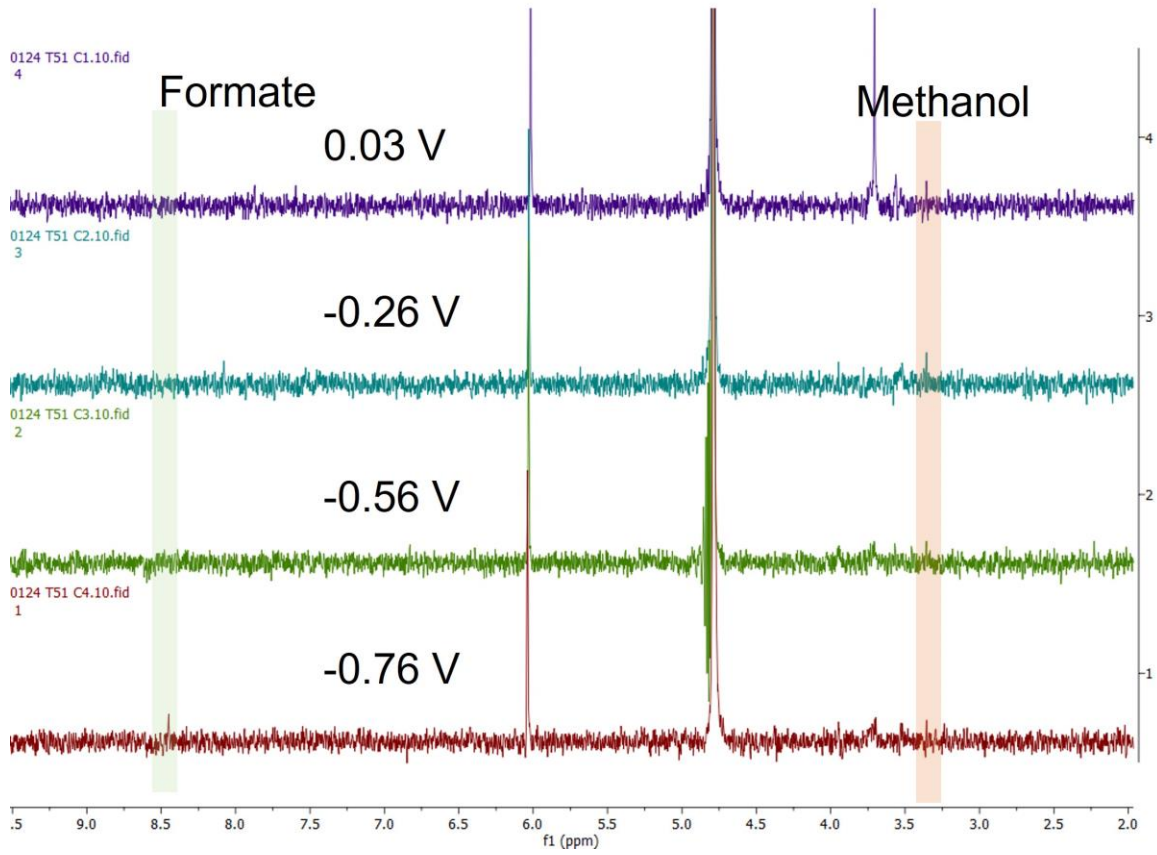


Figure A2S15: NMR of electrolyte BNPI-1-NaI(0.66) after CA investigations for 30 min in CO₂-saturated 0.1 M KHCO₃ electrolyte.

BNPI-1-NaNO₃(0.99)

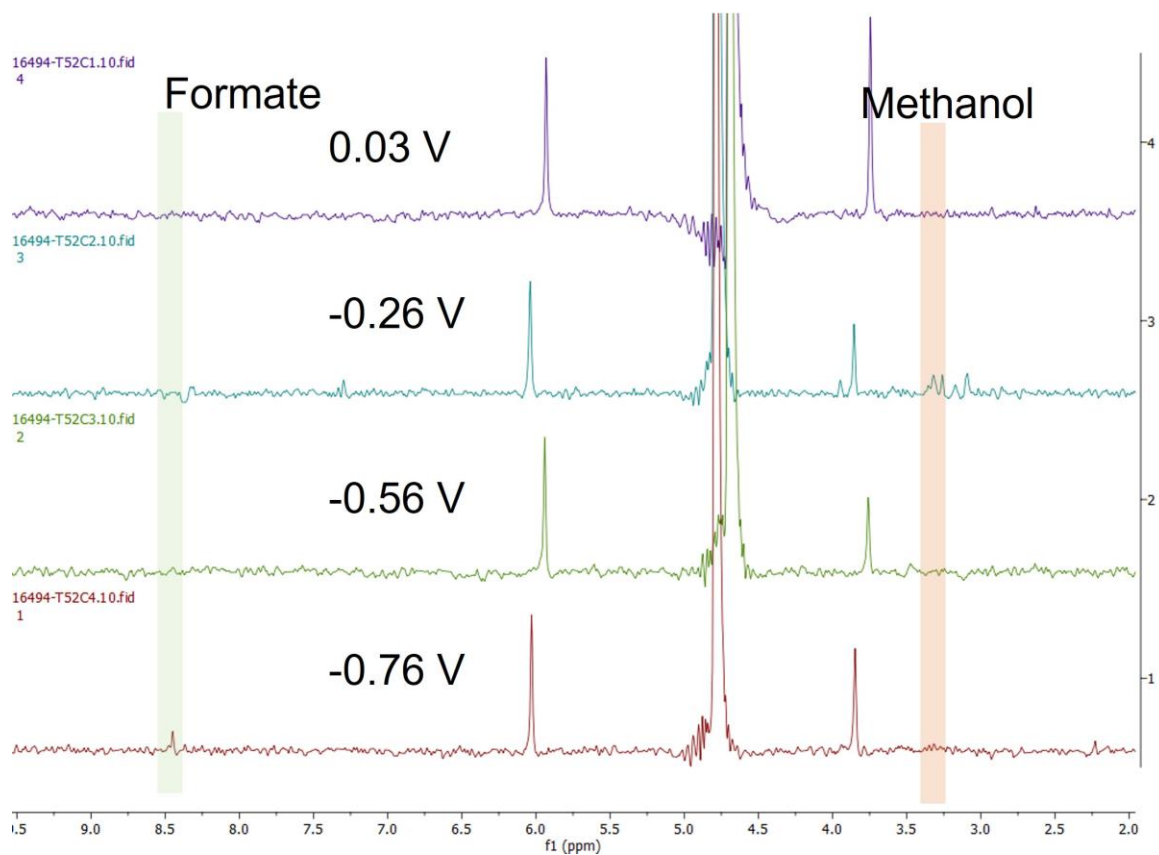


Figure A2S16: NMR of electrolyte BNPI-1-NaNO₃(0.99) after CA investigations for 30 min in CO₂-saturated 0.1 M KHCO₃ electrolyte.

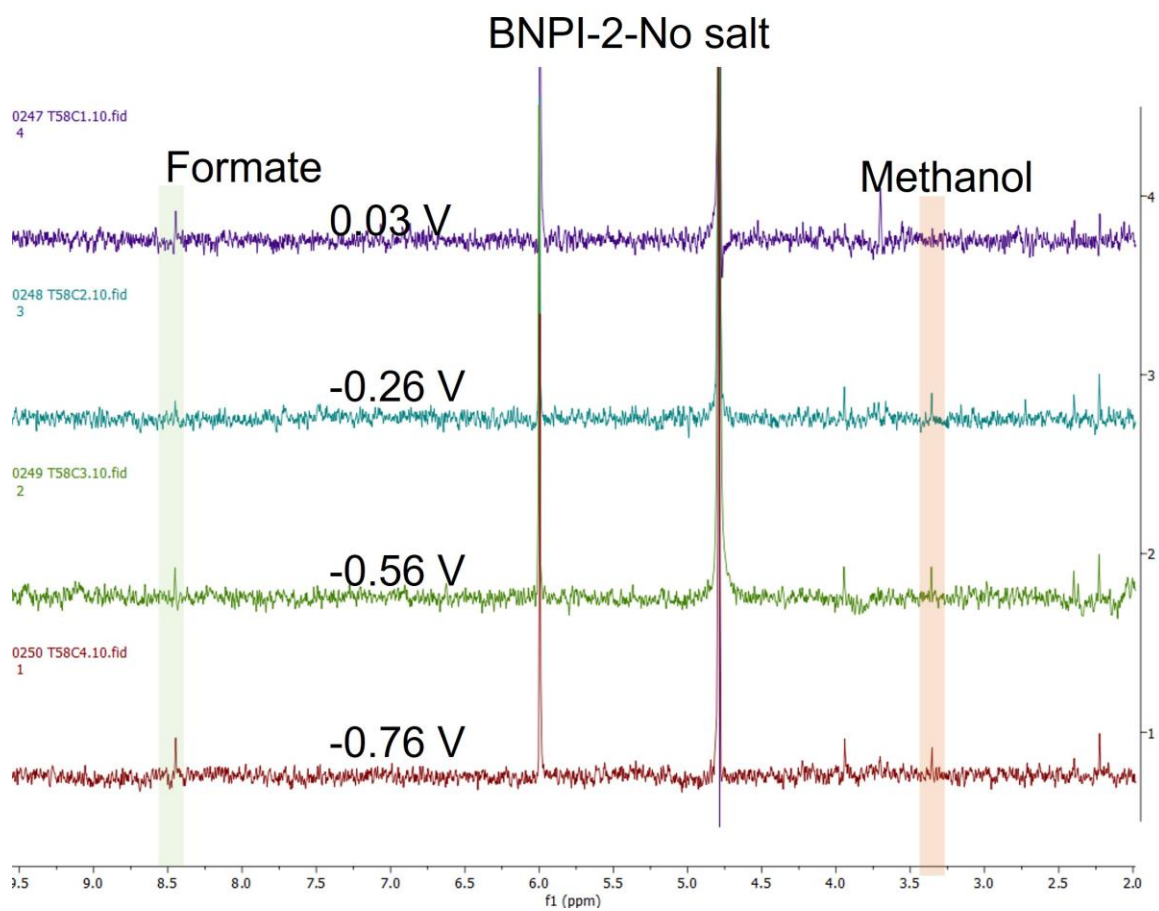


Figure A2S17: NMR of electrolyte BNPI-2-No salt after CA investigations for 30 min in CO₂-saturated 0.1 M KHCO₃ electrolyte.

BNPI-2-Na F(0.33)

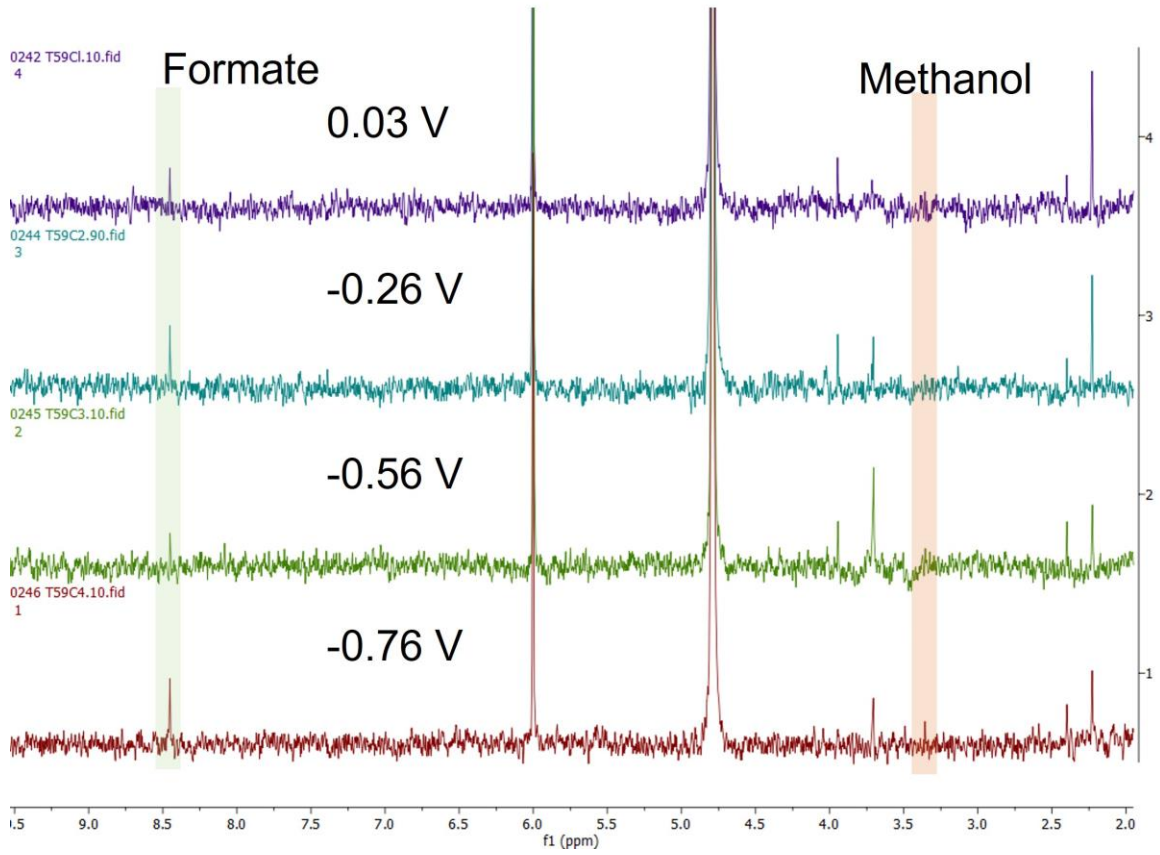


Figure A2S18: NMR of electrolyte BNPI-2-NaF(0.33) after CA investigations for 30 min in CO₂-saturated 0.1 M KHCO₃ electrolyte.

Appendix 3

1. Equipment and materials:

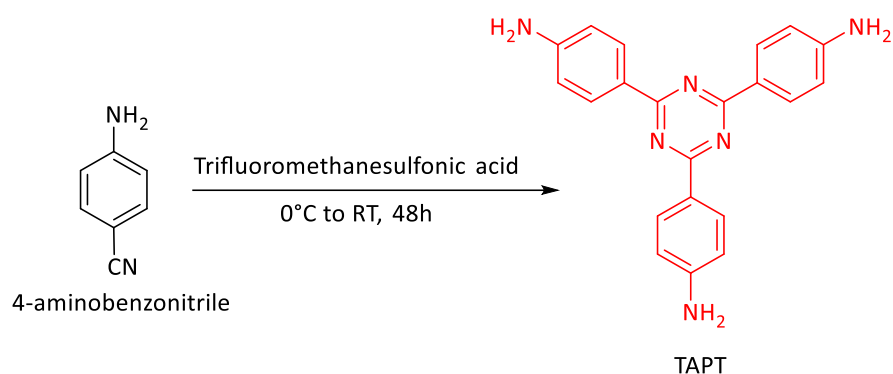
All the chemical used were purchased from Merck and ThermoFisher Scientific and used as received.

Characterisation and measurements: Fourier transform infrared (FT-IR) spectra were recorded on a Perkin Elmer Spectrum 100 spectrometer, with samples in powder form. Thermogravimetric analyses (TGA) were carried out on a TA TGA Q500 apparatus in a nitrogen atmosphere (flow rate 30 mL/ min) in the temperature range 30–800 °C (heating rate 20 °C/min). X-ray diffraction (XRD) patterns were obtained on a Bruker D8 Advance diffractometer (40 kV, 30 mA) using Cu K α radiation ($2\theta = 5\text{--}50^\circ$). Nitrogen adsorption/desorption measurements at 77.4 K were performed after degassing the samples on a Schlenk line for 24 hours and then under high vacuum at 180 °C for at least 20 hours on a Quantachrome Quadrasorb SI-MP apparatus. The specific surface areas were calculated by applying the Brunauer–Emmett–Teller (BET) model to adsorption or desorption branches of the isotherms (N₂ at 77.4 K) using the QuadraWin 5.05 software package. Analysis of the isotherms by commercialized quenched solid density functional theory (QSDFT)^{xviii} and Grand canonical Monte Carlo (GCMC)^{xix} methodologies were also undertaken using the QuadraWin 5.05 package. The pore size distribution (PSD) profiles of the pPIs were calculated from the adsorption branch of the isotherms with the non-local density functional theory (NLDFT) approach. ¹H NMR experiments were performed in chloroform-d or D₂O or DMSO-d₆ using a Bruker 400 and cryo500 MHz NMR. UV-Vis-NIR spectroscopy measurements were carried out using a Shimadzu UV-2600 spectrometer fitted with an ISR-2600 integrating sphere attachment. Measurements were recorded in 10 mm path length quartz cuvettes. X-ray photoelectron spectroscopy (XPS) measurements were conducted at the Bristol NanoESCA Facility. Powdered samples were pressed into indium foil, subsequently loaded onto carbon tape, and mounted on a Ta plate for analysis. The XPS analysis employed monochromatic Al K α radiation at 270 W. To counteract the charging effects on non-conducting pPIs, a charge neutraliser was employed. The electron analyser used was an Argus analyser, operating at a pass energy of 100 eV for the survey scans and 50 eV for high-resolution scans. The emission angle was set at 35°.

Electrochemical measurements: All the electrochemical performance of pPI-1 and pPI-2 were investigated with an EG&G Princeton Applied Research Potentiostat Model 273A, using glassy carbon working electrode (0.38 cm² contact area of electrode), platinum (Pt) counter electrode and silver chloride (Ag/AgCl) reference electrode. All potentials were converted to the reversible hydrogen electrode (RHE) using $ERHE = E_{Ag/AgCl} + 0.059 \times pH + E^0_{Ag/AgCl}$, where ERHE is the converted potential vs.

RHE, $E_{\text{Ag}/\text{AgCl}}^0 = 0.1976$ at 25 °C, and $E_{\text{Ag}/\text{AgCl}}$ is the experimentally measured potential against Ag/AgCl reference.

1. Syntheses:



Synthesis of 1,3,5-tris-(4-aminophenyl)triazine (TAPT):

A dried 100 mL two-neck round bottom flask charged with 4-aminobenzonitrile (772.0 mg, 6.5 mmol) and placed in an ice bath at 0°C under inert atmosphere. Trifluoromethanesulfonic acid (2 mL) was added dropwise over 20 minutes, maintaining the temperature at 0°C under an inert atmosphere. The resultant mixture was stirred for 48 h at room temperature. Distilled water (20.0 mL) was added, and the reaction mixture was neutralized by 2 M NaOH solution until the pH 7. Initially, with an increase in pH, an orange precipitate dissolved to give a bright orange solution, which upon further increase in pH gave a pale-yellow precipitate. The resultant product was filtered and washed with distilled water (3 x 250 mL) and ethanol (3x 50 mL). Yield: 80%

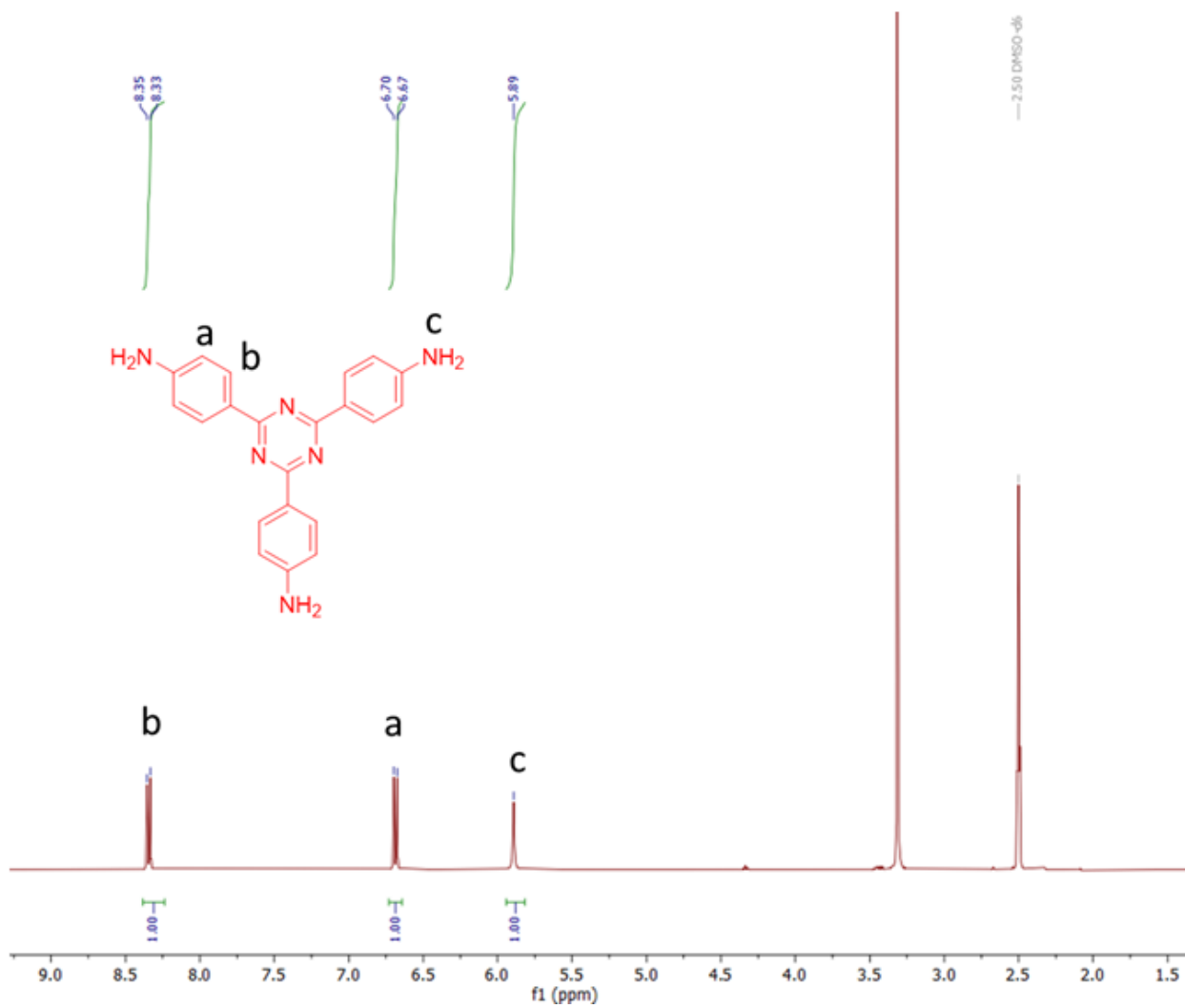


Figure A3S1: ^1H NMR of TAPT in DMSO-d_6 .

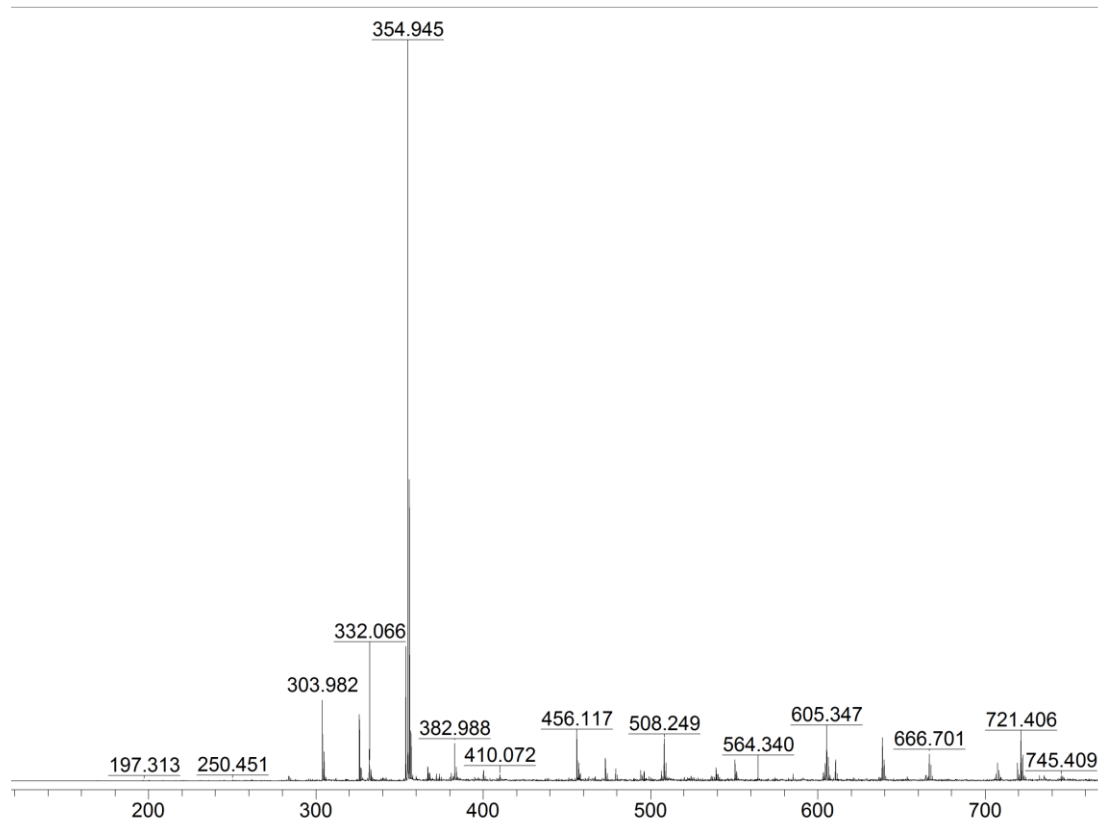


Figure A3S2: MALDI-TOF mass spectrum of TAPT.

Synthesis of **pPI-1**:

A dried round-bottomed flask equipped with mechanical stirring, nitrogen inlet, Dean-Stark trap and a reflux condenser was charged with 1-methyl-imidazole (40 ml), and perylene-3,4,9,10-tetracarboxylic dianhydride (PTCDA) (466 mg, 1.19 mmole). After 30 min of stirring at room temperature melamine (100 mg, 0.79 mmol) was added and the reaction mixture stirred at 180°C for 72 hours. After cooling to 70°C, MeOH (50 ml) was added and the precipitate was collected and washed with additional DMF and methanol, warm water and acetone (50ml x 3, each). The resulting product was dried at 80°C under vacuum for 24h. Yield: 60-70%

Synthesis of **pPI-2**:

A dried round-bottomed flask equipped with mechanical stirring, nitrogen inlet, Dean-Stark trap and a reflux condenser was charged with 1-methyl-imidazole (40 ml), and perylene-3,4,9,10-tetracarboxylic dianhydride (PTCDA) (297 mg, 0.76 mmol). After 30 min of stirring at room temperature TAPT (135 mg, 0.38 mmol) was added and the reaction mixture stirred at 180°C for 72 hours. After cooling to 70°C, MeOH (50 ml) was added and the precipitate was collected and washed with additional DMF and methanol, warm water and acetone (50ml x 3, each). The resulting product was dried at 80°C under vacuum for 24h. Yield: 80-90%

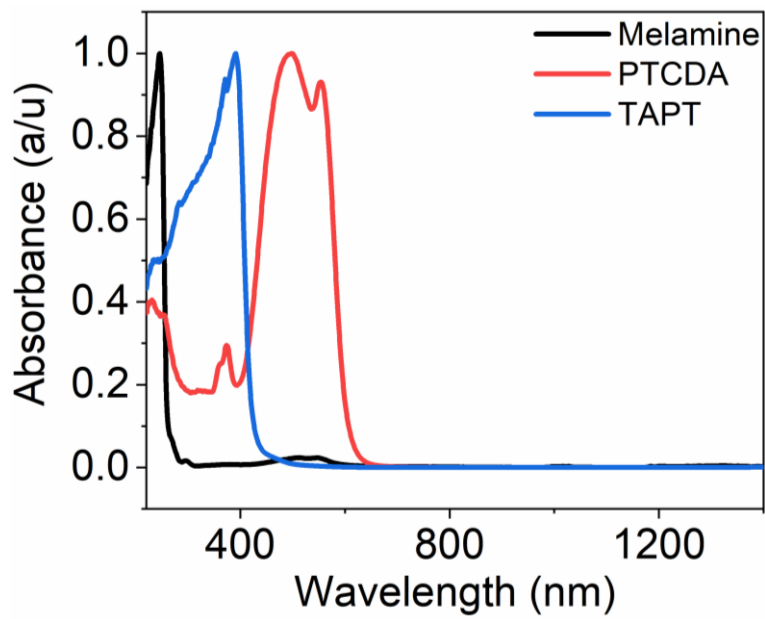


Figure A3S3: Solid-state UV-Vis-NIR spectra of melamine, PTCDA and TAPT.

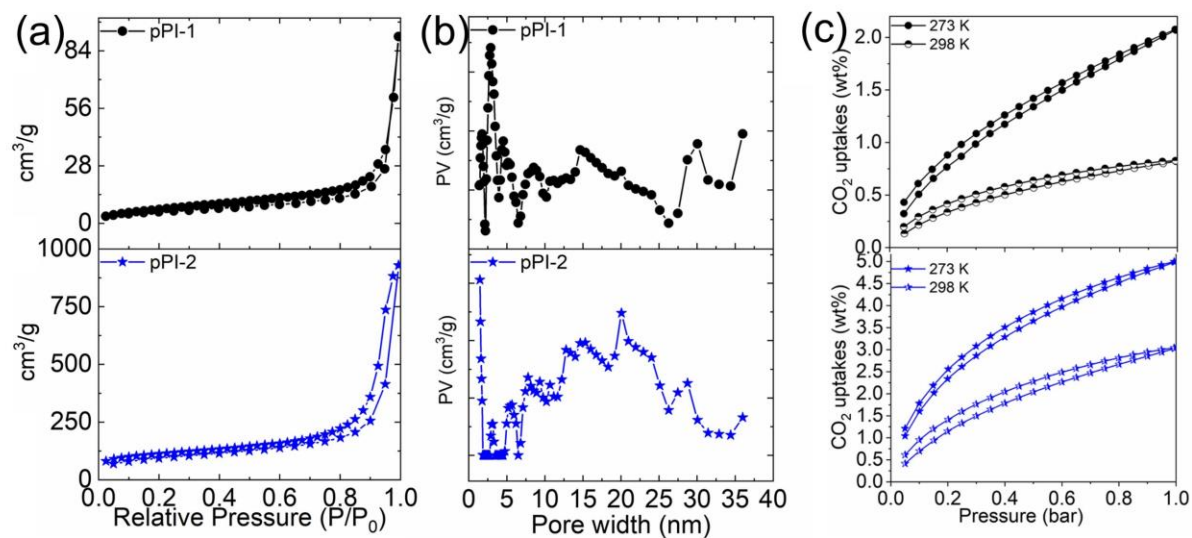
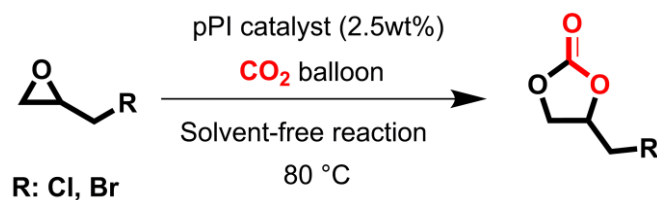


Figure A3S4: (a) The N_2 sorption isotherms of **pPI-1** and **pPI-2**, (b) Pore size distribution calculated from NLDFT, (c) CO_2 uptake measurement at 273 K and 298 K at 1 bar.

Cyclic carbonate synthesis:



Epoxide (1.0 mL, 0.0127 mol) was loaded in a round bottom Schlenk flask. The pPI (5wt%, 30 mg) to be studied as a catalyst was added to the flask. A balloon filled with CO₂ (approx. 1.5–2 L) was connected to the Schlenk flask and the reaction solution flushed with CO₂ to replace air from flask. Silicon grease and Parafilm were applied to the joints of the flask to prevent any leakage of CO₂ and the reaction stirred at 80 °C. The reaction was performed for 24 hours, 48 hours, and 72 hours, and reaction progress followed using ¹H NMR.

Cyclic carbonate conversion calculated using ¹H NMR.

$$\text{Conversion (\%)} = \frac{\text{Integration (b) from cyclic carbonate}}{\text{Integration (b) from cyclic carbonate} + \text{Integration (d) from epoxide}} \times 100\%$$

See NMR spectra below for integral **b** from cyclic carbonate and integral **d** from epoxide.

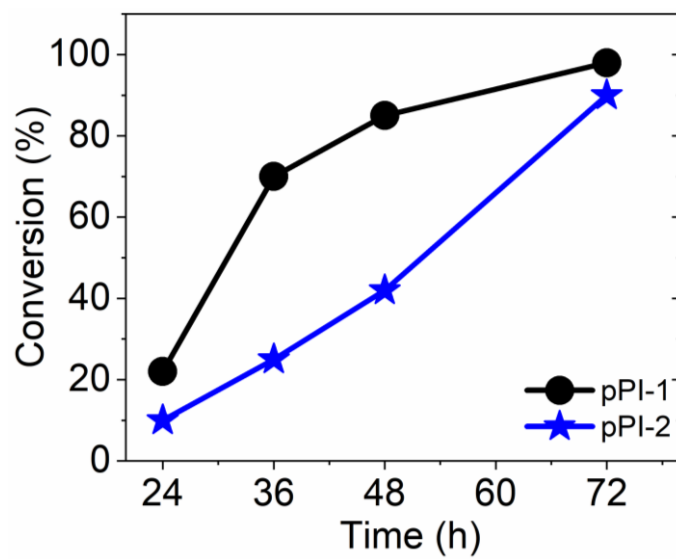
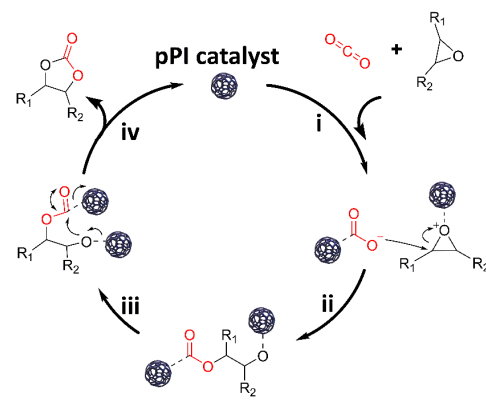
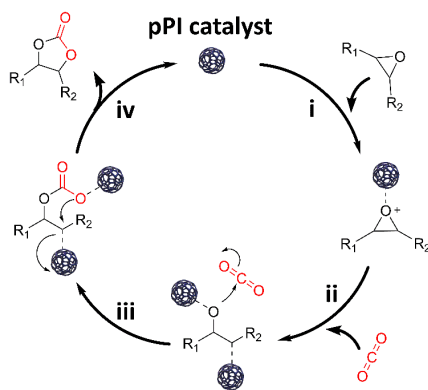
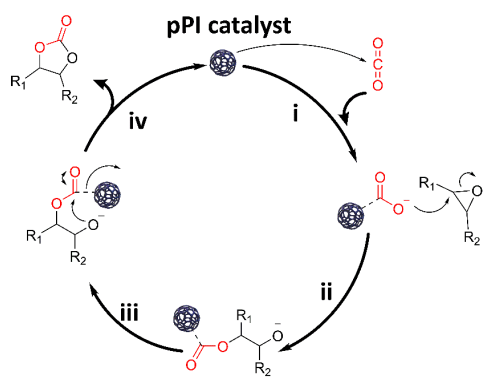


Figure A3S5: Time-dependent percentage conversion of ECH at 80 °C for **pPI-1** and **pPI-2**.



Scheme A3S1: Plausible mechanism for cyclic carbonate synthesis using pPIs (see detailed explanation in the **Chapter 1, Section 1.8**).

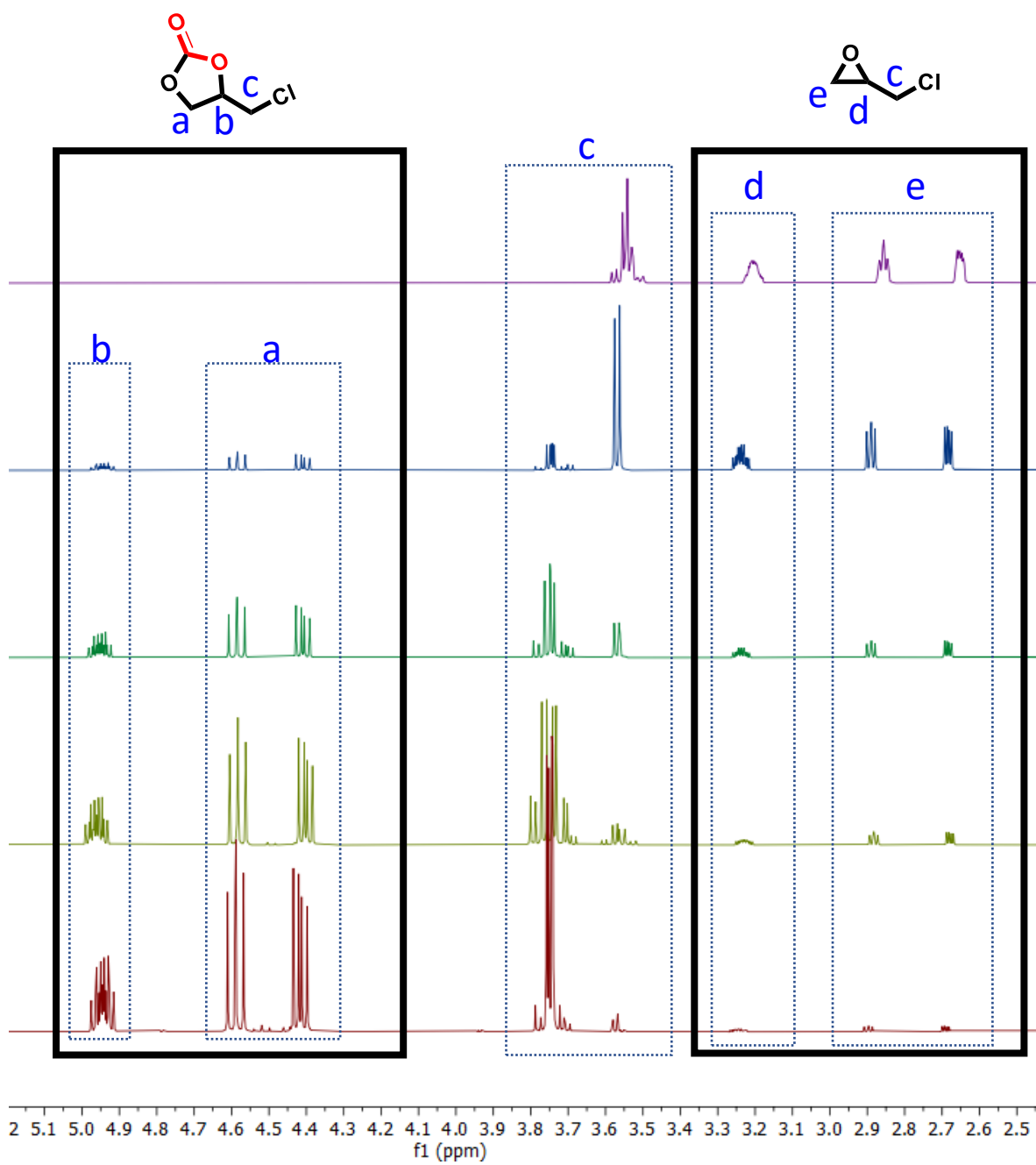


Figure A3S6: ^1H NMR for 4-(chloromethyl)-1,3-dioxolan-2-one using **pPI-1** from ECH.

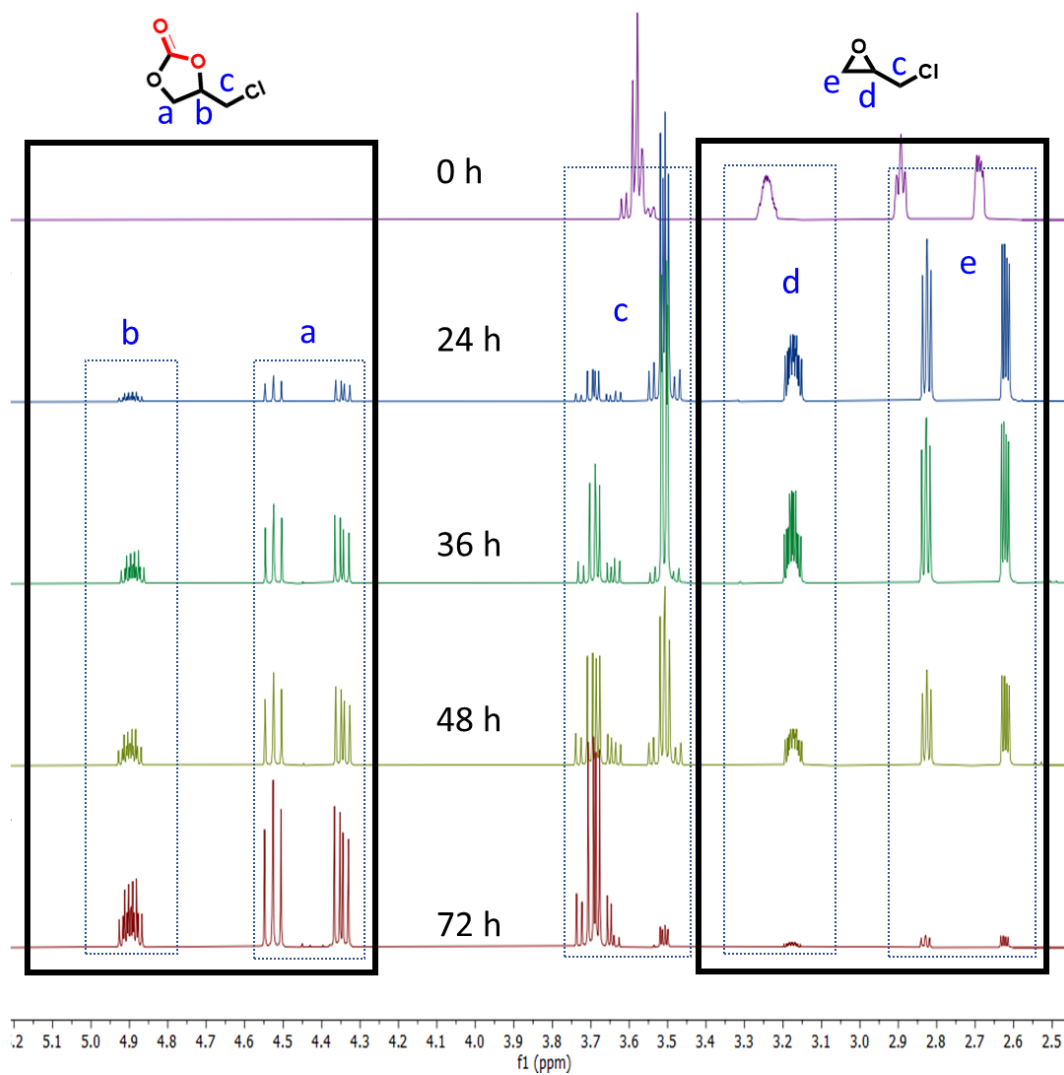


Figure A3S7: ^1H NMR for 4-(chloromethyl)-1,3-dioxolan-2-one using **pPI-2** from ECH.

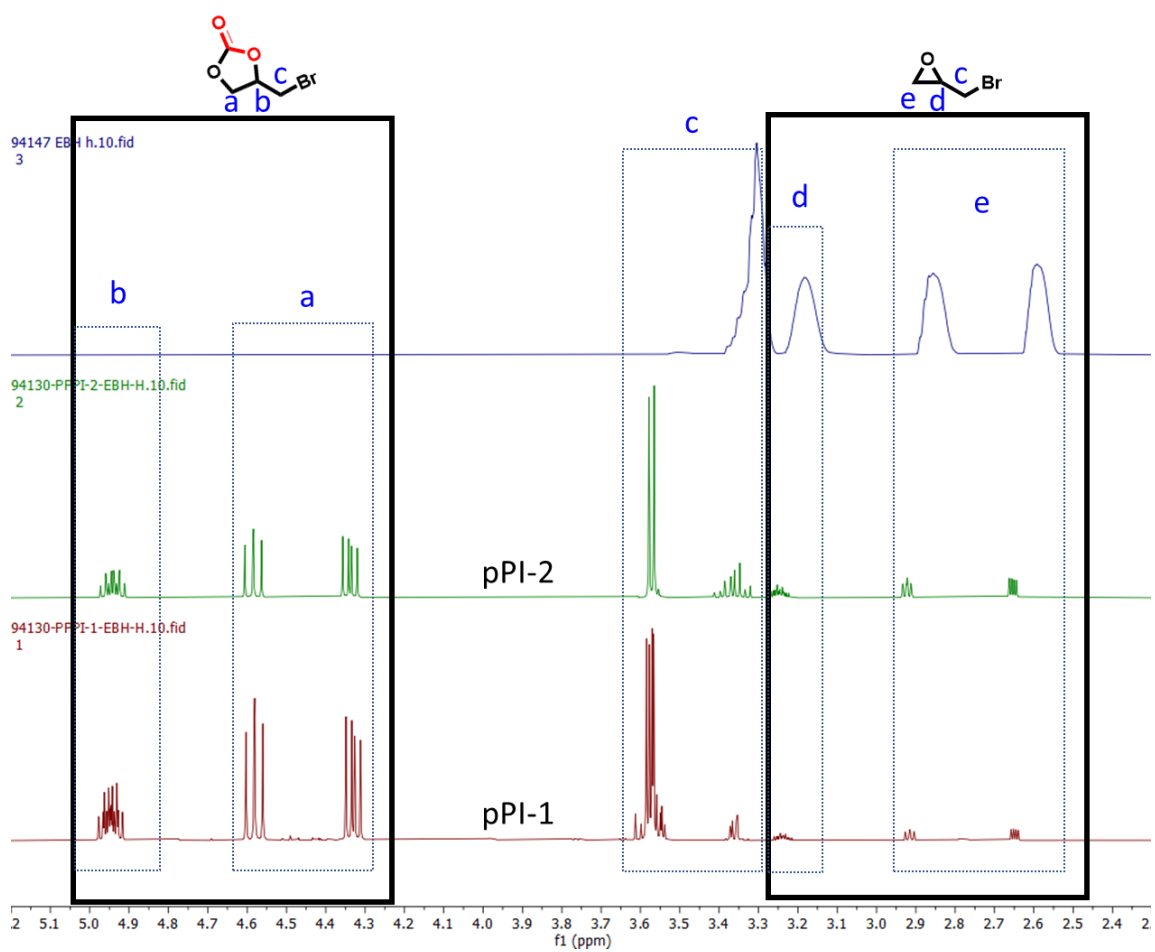


Figure A3S8: ^1H NMR for 4-(bromomethyl)-1,3-dioxolan-2-one using **pPI-1** and **pPI-2** from EBH (72 hours).

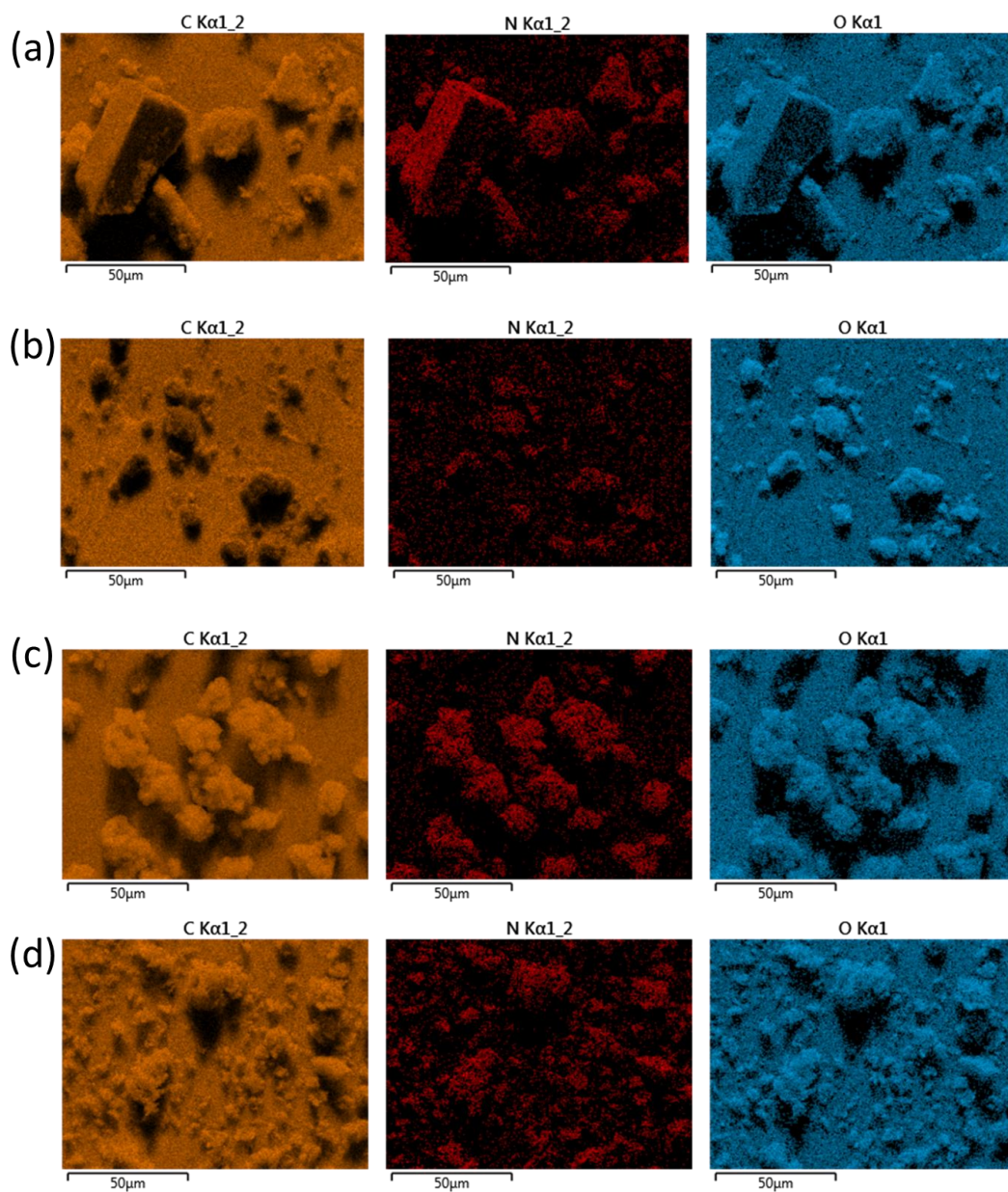


Figure A3S9: Energy-dispersive X-ray spectroscopy (EDX): (a) **pPI-1**, (b) **pPI-1** after 5 cycles, (c) **pPI-2** and (d) **pPI-2** after 1 cycle.

Table S1: Elemental analysis results of **pPI-1** and **pPI-2** (before and after catalytic cycle).

Name	C%	N%	O%
pPI-1	79.7	6.8	13
pPI-1 after 5 cycles	84	1.7	13.3
pPI-2	83	5.7	10.4
pPI-2 after 1 cycle	82.1	5.0	12.1

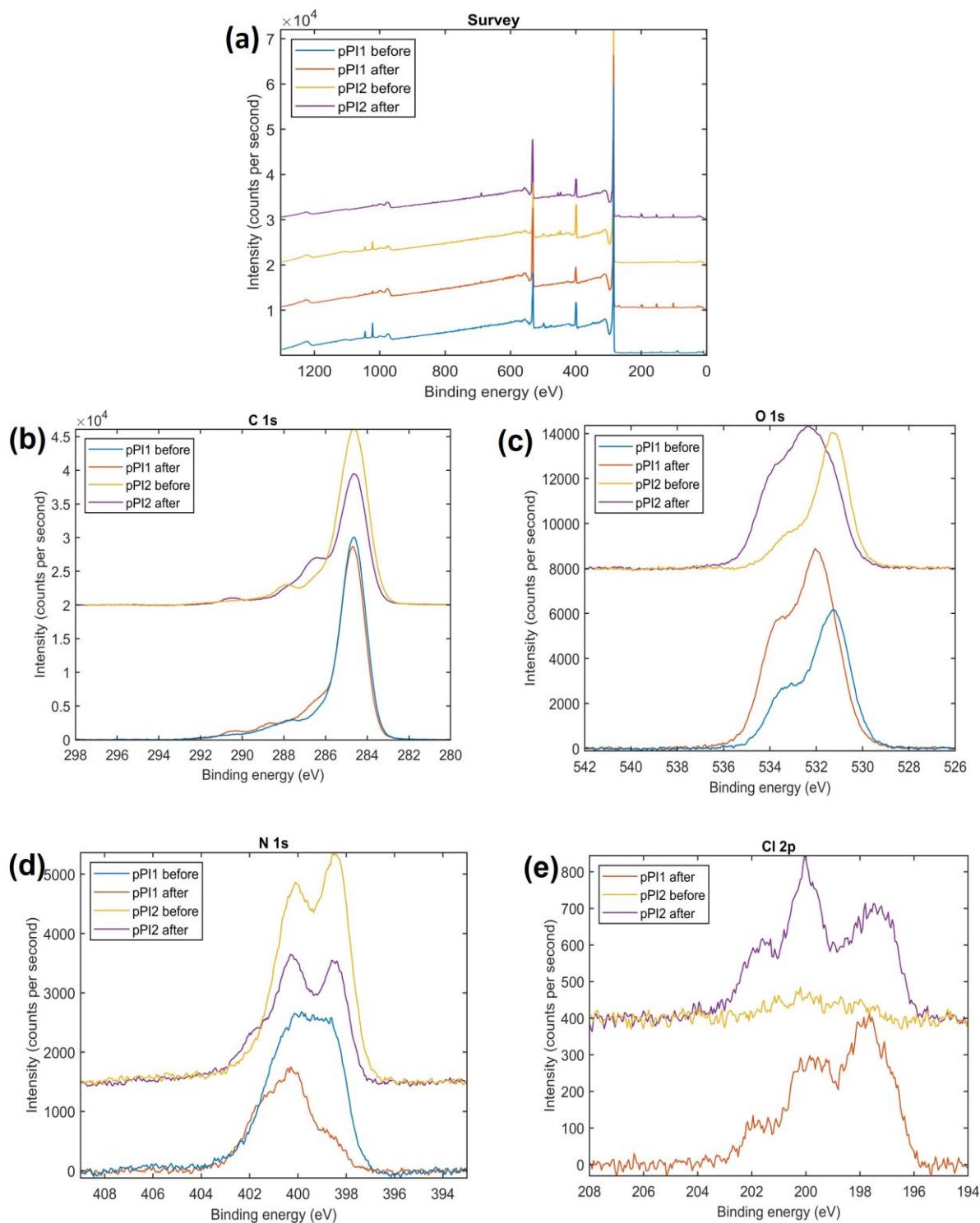


Figure A3S10: X-ray photoelectron spectroscopy (XPS) spectra: (a) pPI-1 and pPI-2, before and after cycle 1, (b) C 1s, (c) O 1s, (d) N 1s and (e) Cl 2p, of pPI-1 and pPI-2 (before and after cycle 1).

2. Electrochemical CO₂ reduction

Electrode preparation:

pPis (1.5 mg) were ground to fine powder and sonicated in isopropanol (500 μ L) for 2-3 hours. Nafion (10 μ L) was added to the suspension and sonicated for 30 min. The suspension (20 μ L) was drop-cast on a clean glassy carbon working electrode. The electrode was dried at room temperature vacuum oven for overnight and used for electrochemical studies.

Electrolyte preparation for NMR analysis after electrochemical reduction of CO₂ experiments

After CA experiments, the electrolyte (600 μ L) was collected from the cathodic side of the H-cell and product detection was undertaken using cryo500 ¹H NMR spectroscopy for methanol and formate, respectively. To determine the amount of methanol and formate produced, which in turn allows the determination of the FE for each product in the system, 1 mM maleic acid (10 μ L) was added along with D₂O (180 μ L) and mixture was analysed using ¹H NMR. FEs were calculated using the formula below;

$$\varepsilon_{Faradaic} = \frac{z \cdot n \cdot F}{Q}$$

z: number of electrons required to produce a given product

n: number of moles of the given product

F: Faraday's constant (96485.33 C/mol)

Q: total charged passed (C)

*Note**: The faradaic efficiency is calculated for each product individually, not the sum of all products formed.

Standard deviation (σ) was calculated using the equation:

$$\sigma = \sqrt{\frac{\sum (xi - \mu)^2}{N}}$$

Where N=3, xi = the faradaic efficiencies calculated for methanol and formate respectively and μ = the mean value of the calculated faradaic efficiencies for methanol and formate respectively.

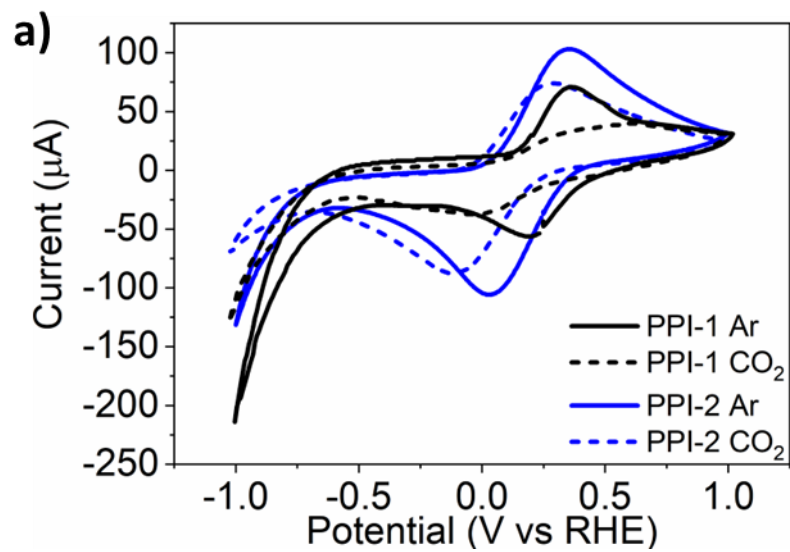


Figure A3S11: Cyclic voltammogram of **pPI-1** and **pPI-2** in the applied potential range from -1–1 V vs RHE, scan rate 20 mV/s, 20 cycles.

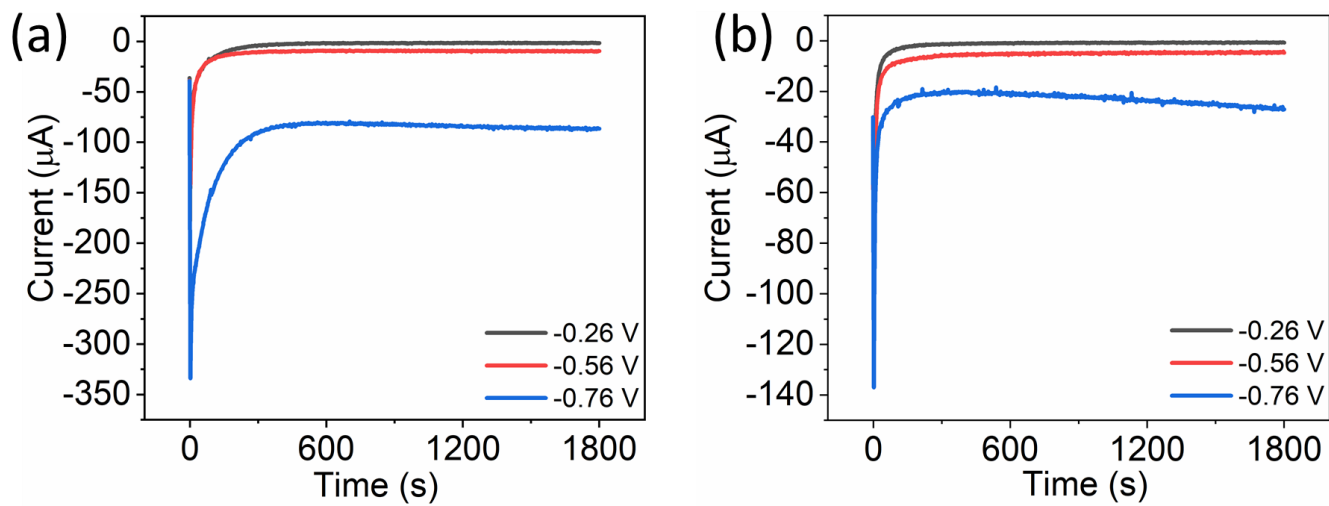


Figure A3S12: Chronoamperometry studies of (a) **pPI-1** and (b) **pPI-2**, in CO_2 -saturated 0.1 M KHCO_3 electrolyte for 30 min.

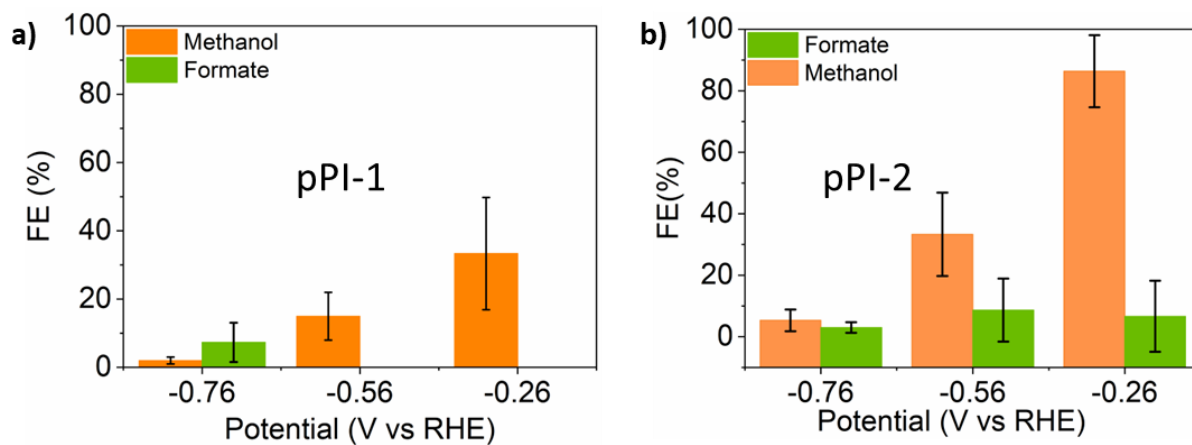


Figure A3S13: Graphs showing FEs, including error bars, for: (a) **pPI-1** and (b) **pPI-2**, respectively.

Table S2: Faradaic efficiency of **pPI-1** and **pPI-2** in three runs.

	V vs RHE	Methanol (FE%)			Formate (FE%)		
		Run1	Run2	Run3	Run1	Run2	Run3
pPI-1	-0.26	21	52	27	0	0	0
	-0.56	8	15	22	0	0	0
	-0.76	1	2	3	4	4	14
pPI-2	-0.26	91	73	95	0	20	0
	-0.56	25	26	49	20	0	6
	-0.76	5	2	9	2	2	5

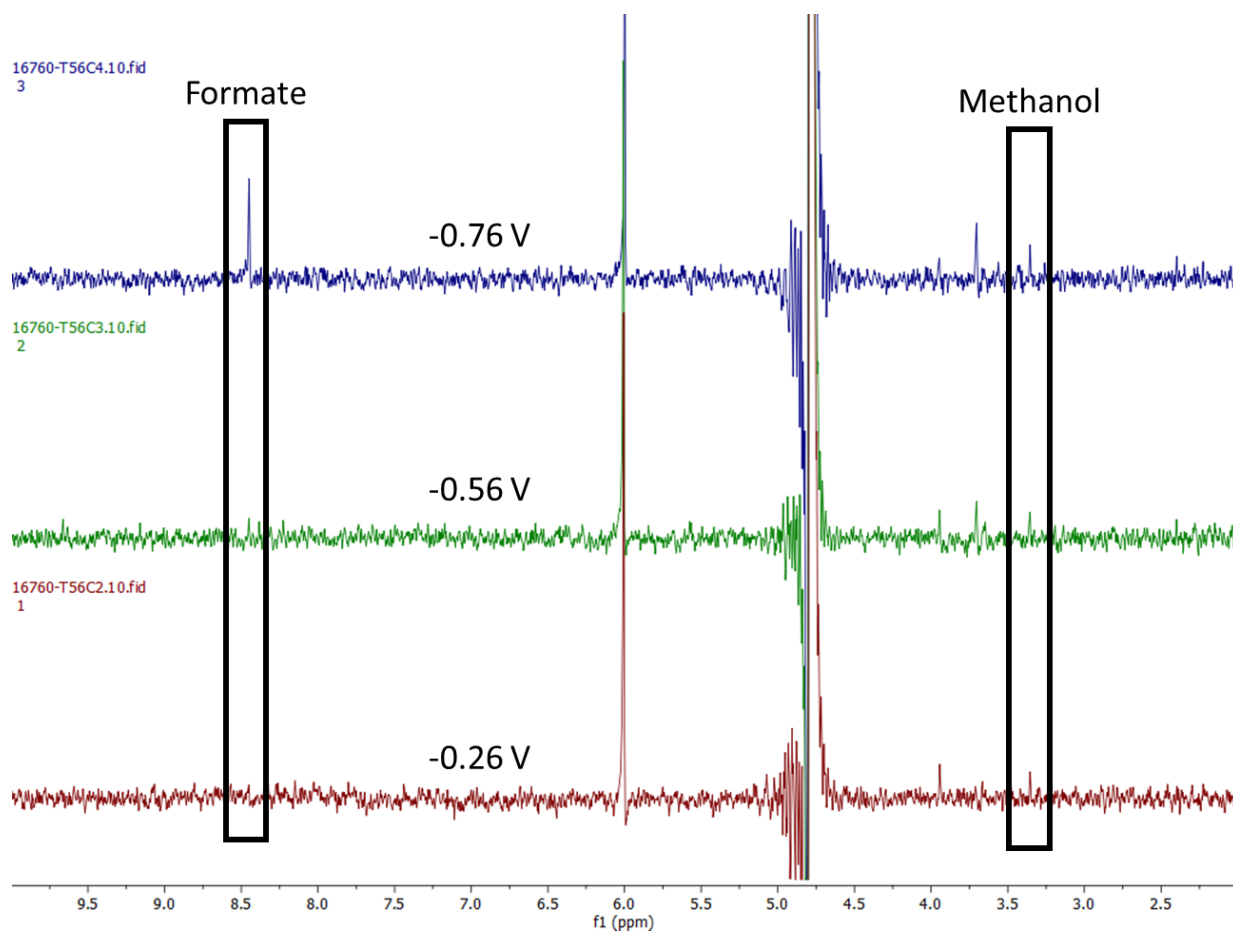


Figure A3S14: ^1H NMR of electrolyte for **pPI-1** after CA investigations for 30 min in CO_2 -saturated 0.1 M KHCO_3 electrolyte.

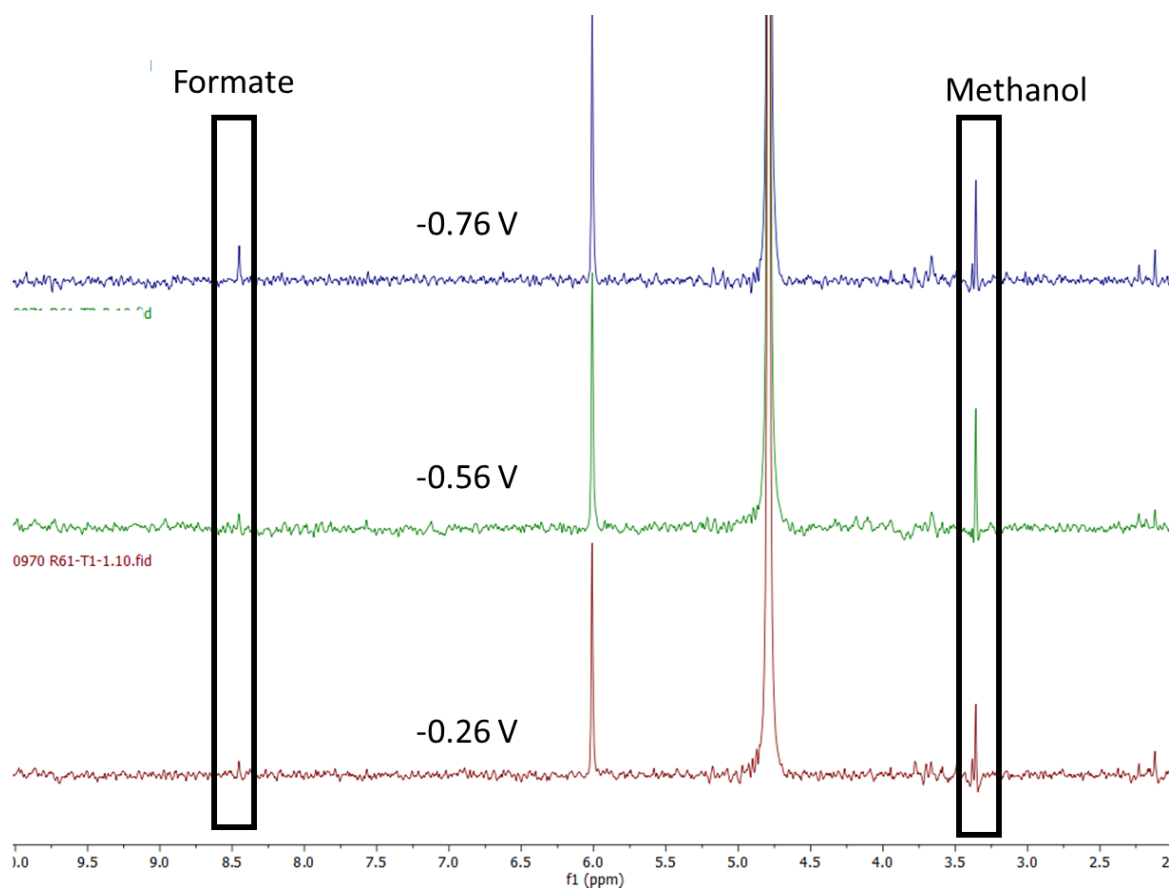


Figure A3S15: ^1H NMR of electrolyte for pPI-2 after CA investigations for 30 min in CO_2 -saturated 0.1 M KHCO_3 electrolyte.

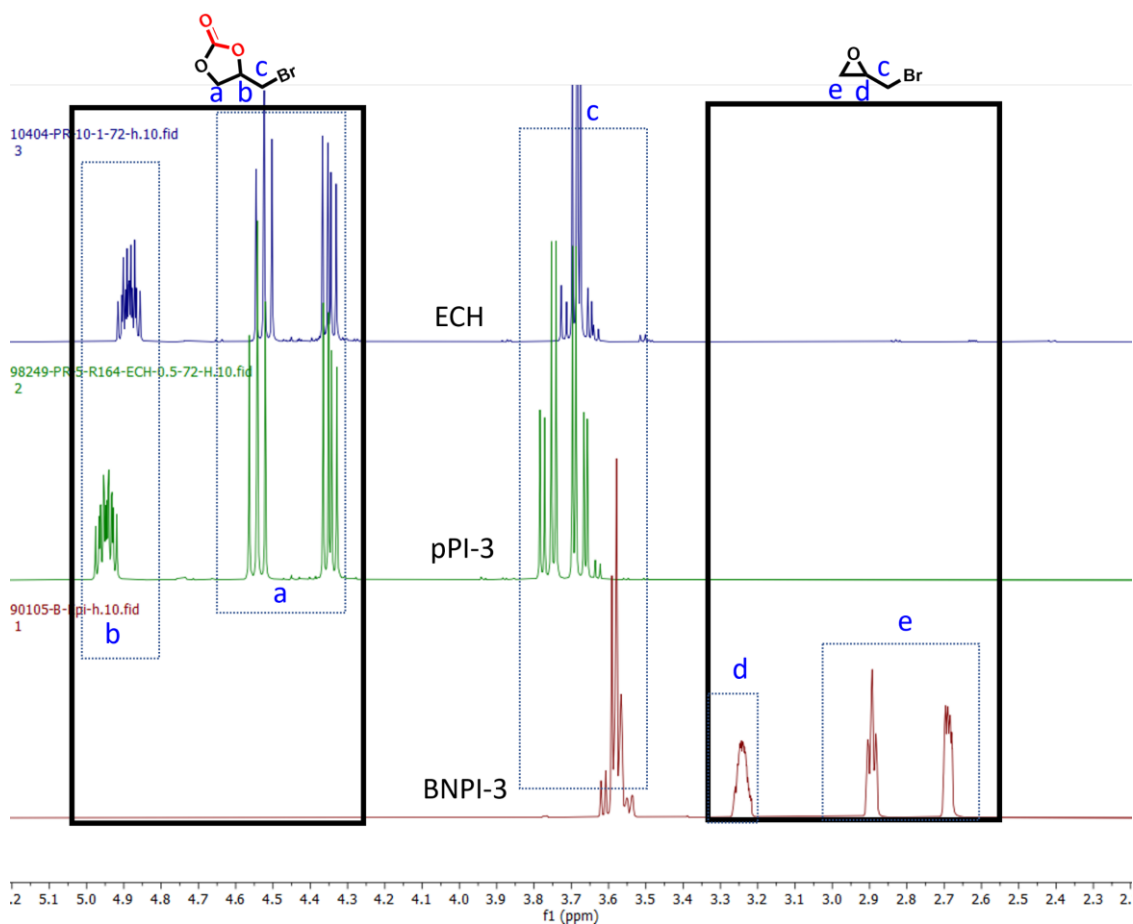


Figure A3S16: ^1H NMR for 4-(chloromethyl)-1,3-dioxolan-2-one using **BNPI-3** and **pPI-3** from ECH (100 °C, 72 h and 0.25 bar gauge CO_2).

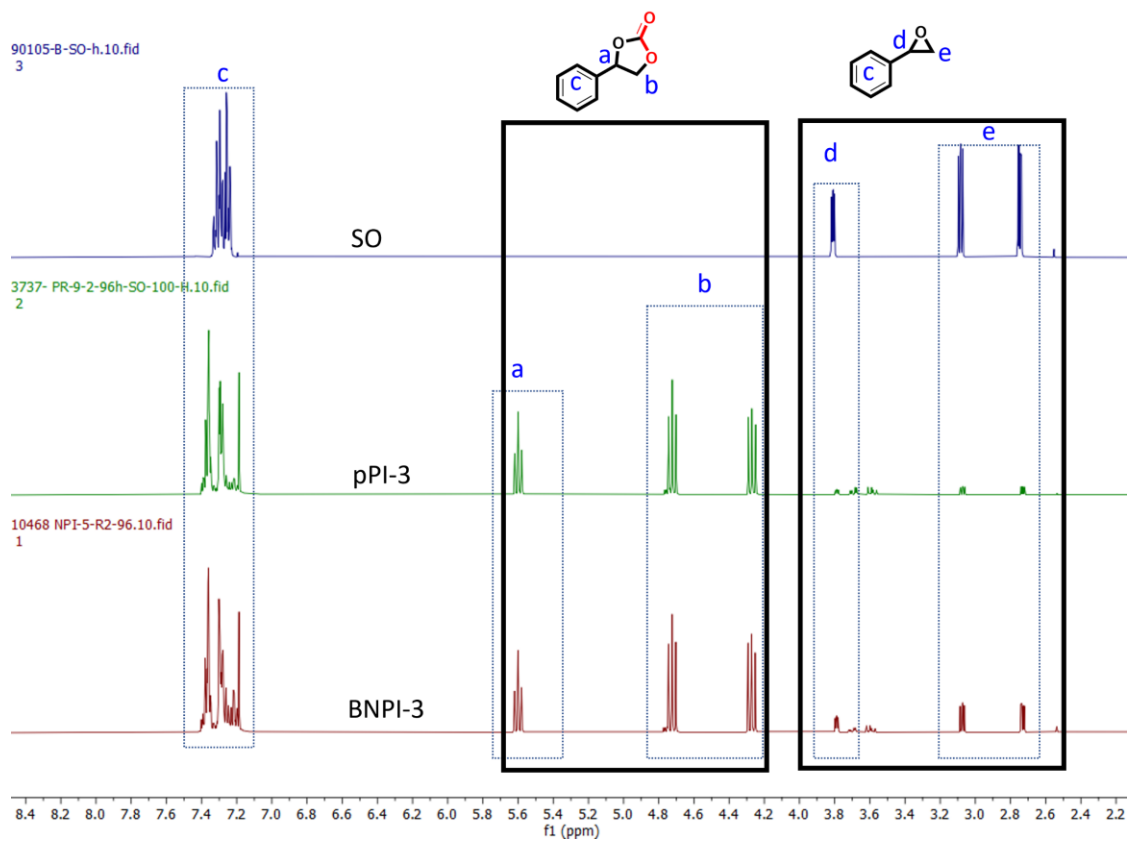


Figure A3S17: ^1H NMR for styrene carbonate using **BNPI-3** and **pPI-3** from SO (100 °C, 96 h and 0.25 bar gauge CO_2).

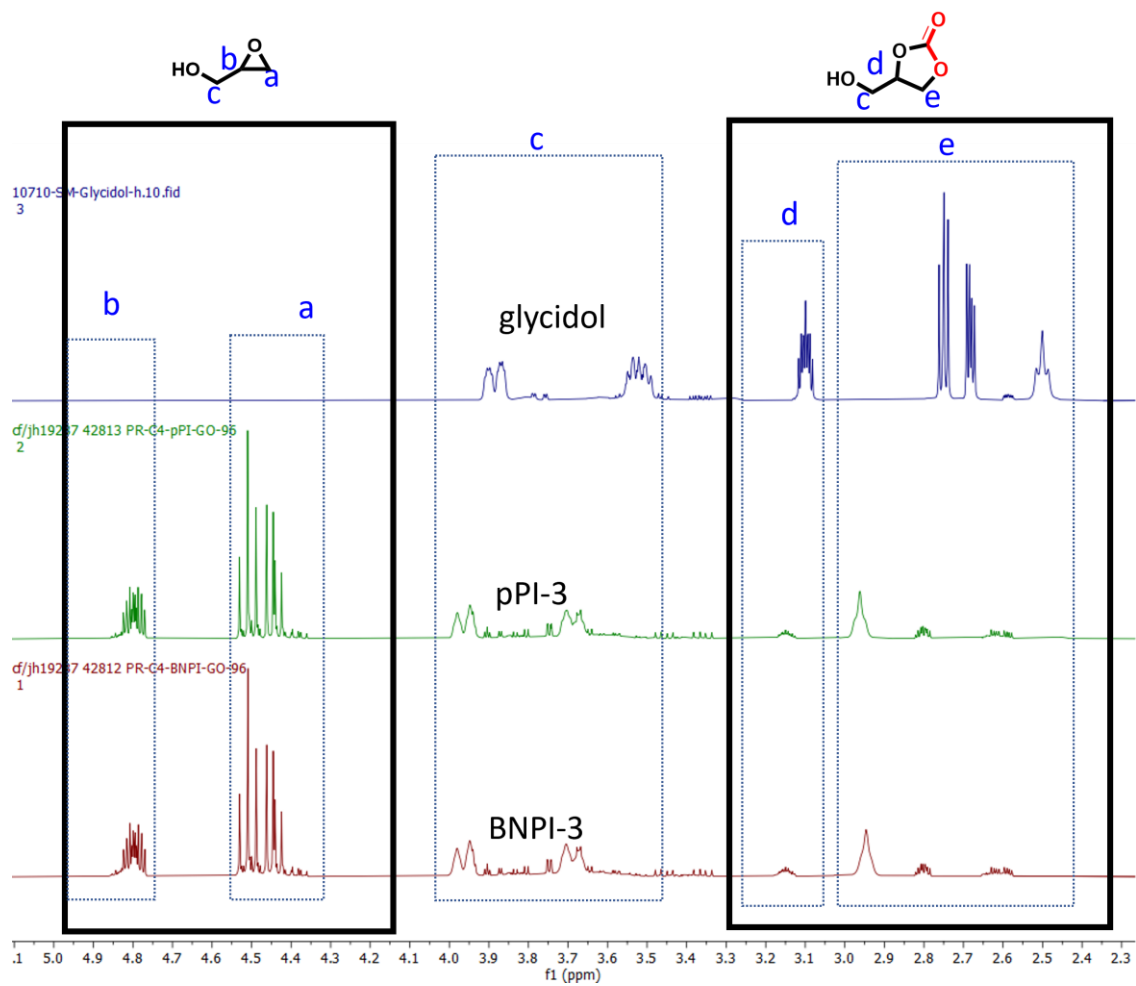


Figure A3S18: ^1H NMR for glycerol carbonate using **BNPI-3** and **pPI-3** from glycidol (100 °C, 96 h and 0.25 bar gauge CO_2).

